Bioimage informatics for understanding the effects of chemotherapy on cellular signaling, structure, and function

by

Simon Gordonov

B.S., Rutgers University (2010)
M.Phil., University of Cambridge (2011)

Submitted to the Department of Biological Engineering
in partial fulfillment of the requirements for the degree of

Doctor of Philosophy in Biological Engineering

at the

MASSACHUSETTS INSTITUTE OF TECHNOLOGY

September 2017

Author ..... Signature redacted .....
Department of Biological Engineering
August 11, 2017

Certified by ..... Signature redacted .....
Douglas A. Lauffenburger
Professor of Biological Engineering, Chemical Engineering, and Biology
Thesis Supervisor

Certified by ..... Signature redacted .....
Mark Bathe (co-supervisor)
Associate Professor of Biological Engineering
Thesis Supervisor

Accepted by ..... Signature redacted .....
Mark Bathe
Chairman, Graduate Program Committee

Bioimage informatics for understanding the effects of chemotherapy on cellular signaling, structure, and function

by

Simon Gordonov

Submitted to the Department of Biological Engineering
on August 11, 2017, in partial fulfillment of the
requirements for the degree of
Doctor of Philosophy in Biological Engineering

Abstract

Chemotherapy is widely used in the treatment of solid tumors, but its effects are often associated with cancer relapse, metastasis, and drug resistance. The biological mechanisms that drive the structural and functional changes in cancer cells associated with these features of disease progression remain poorly understood. Consequently, quantitative characterization of molecular signaling pathways and changes in cancer cell phenotypes induced by chemotherapy through the use of *in vitro* model systems would expand our understanding of drug mechanisms and provide for putative strategies to counteract drug-induced cancer progression.

Toward this end, I develop bioimage informatics tools to characterize changes in signaling, structure, and function of cancer cells from fluorescence microscopy data. I first present a generally-applicable probabilistic time-series modeling framework to classify cell shape dynamics. Times-series models draw quantitative comparisons in cell shape dynamics that are used to distinguish and interpret cellular responses to diverse drug perturbations.

Next, I investigate the effects of doxorubicin, a DNA-damaging chemotherapeutic drug, on breast cancer cell signaling and phenotype. Bioinformatics analyses of phosphoproteomics data are first used to infer biological processes downstream of DNA damage response signaling networks altered by doxorubicin treatment. These analyses reveal changes in phosphoproteins associated with the actomyosin cytoskeleton and focal adhesions. Live-cell imaging of cell morphology, motility, and apoptosis dynamics reveals a link between doxorubicin-induced cytoskeletal signaling and morphological elongation, directional migration, and enhanced chemo-tolerance. These findings imply that sub-maximal tumor killing can exacerbate disease progression through adaptive resistance to primary chemotherapy treatment through DNA damage response-regulated cytoskeletal signaling.

Finally, I combine the results of the phosphoproteomic analysis with phenotypic profiling to characterize doxorubicin-induced changes in actomyosin signaling that affect cancer cell shape and survival. I additionally describe a generally-applicable multiplexed fluorescence imaging framework that uses diffusible nucleic acid probes to detect nearly a dozen subcellular protein targets within the same biological sample. Taken together, these methodologies reveal previously-unappreciated effects of chemotherapy on breast cancer signaling and phenotype, and demonstrate the value of combining bioinformatics analyses of -omics data with quantitative fluorescence microscopy as a general strategy in biological mechanism discovery.

Thesis Supervisor: Douglas A. Lauffenburger
Title: Professor of Biological Engineering, Chemical Engineering, and Biology

Thesis Supervisor: Mark Bathe (co-supervisor)
Title: Associate Professor of Biological Engineering

Acknowledgments

I am indebted to the many extraordinary people who have made my graduate school years at MIT a defining moment of inspiration and growth, both professionally and personally:

- My thesis advisors, Profs. Doug Lauffenburger and Mark Bathe, who have enabled me to realize my scientific pursuits through their excellent mentorship, guidance, and positive encouragement; they instilled in me important core values and offered valuable perspectives.
- Members of my thesis committee, Profs. Frank Gertler, Alan Wells, and Roger Kamm, who have been instrumental in guiding my work and injecting important scientific insights and suggestions.
- Dr. Mun Kyung Hwang and Prof. Michael Yaffe who have played a key part in the planning, development, and execution of the core themes and experiments in this thesis, in what was a highly productive interdisciplinary collaboration across multiple laboratories.
- Members of the Lauffenburger, Griffith, Bathe, and Gertler laboratories, including other staff and colleagues at MIT, who have been unlimited sources of inspiration, guidance, and camaraderie. They have been fundamental to my intellectual growth at MIT and have provided me with a broad set of skills and perspectives on a multitude of topics, scientific or otherwise.
- My wife, Elayne, who has been an unending source of support and encouragement.
- My family, especially my sister, mother, and uncle, who always lend an ear and provide useful advice on the many angles of a graduate student's life.
- My father, who has been my internal guiding light and motivator to push boundaries, work hard, help others, and persevere through uncertainty and hardship.

This doctoral thesis has been examined by a Committee of the Department of Biological Engineering as follows:

Professor Roger D. Kamm .....
Chairman, Thesis Committee
Professor of Biological Engineering and Mechanical Engineering, MIT

Professor Douglas A. Lauffenburger .....
Thesis Supervisor
Professor of Biological Engineering, Chemical Engineering, and Biology, MIT

Professor Mark Bathe .....
Thesis Supervisor
Associate Professor of Biological Engineering, MIT

Professor Frank B. Gertler .....
Member, Thesis Committee
Professor of Biology, MIT

Professor Alan Wells .....
Member, Thesis Committee
Professor of Pathology, University of Pittsburgh

Contents

List of Figures

List of Tables

Chapter 1

Introduction

1.1 Chemotherapy in the treatment of breast cancer

Chemotherapy is commonly used in the treatment of solid tumors, including those of breast tissue origin. Despite many examples of successful clinical response in cancer patients over the past decades, chemotherapy has posed considerable challenges related to efficacy and toxicity. Chemotherapy carries many unfavorable side effects and can lead to drug resistance. Doxorubicin is a widely used drug in breast cancer treatment, and although is can be highly effective upon primary application, subsequent treatments commonly exhibit reduced tumor response. What are the reasons for these unfortunate clinical observations of reduced drug efficacy that manifest from multiple rounds of treatment? Incomplete tumor eradication upon primary treatment leaves behind surviving cancer cells that are exposed to sub-lethal doses of the drug. These remaining cells can undergo pronounced genetic, epigenetic, transcriptional, or protein-level signaling changes that drive important structural and functional alterations in cancer cells. These alterations may contribute to reduced efficacy following multiple rounds of treatment. Using *in vitro* model systems, this thesis combines phosphoproteomics, quantitative imaging, and molecular biology approaches to investigate the effects of doxorubicin on breast cancer cell signaling, structure, and function. The goal of this work is to expand our understanding into how protein-level signaling networks and subsequent phenotypic changes contribute to cancer cell response to this important clinical agent.

Doxorubicin is a natural product derived from *Streptomyces peucetius* and is part of a class of DNA damaging agents called anthracyclines. This drug was first introduced in the late 1960s and by the 1970s was considered among the most effective compounds for breast cancer treatment [24, 176]. Therapies combining doxorubicin with other agents such as 5-fluorouracil and cyclophosphamide became standard treatment regimens for both metastatic and adjuvant disease [243]. During the 1970s and 1980s relatively few new chemotherapeutic drugs were developed that could achieve a substantial improvement in therapeutic efficacy [241]. The turning point occurred with the development of microtubule-targeting taxanes, such as paclitaxel and docetaxel, which showed therapeutic effects comparable to, if not better than, those of doxorubicin [86]. Despite the growing use of taxanes, clinical trials showed that inclusion of doxorubicin in combination treatment regimens with cyclophosphamide and 5-fluorouracil, for instance, were more effective than those that excluded doxorubicin,

highlighting the importance of this drug in the treatment of breast cancer [73, 81, 94, 87]. Subsequent studies showed that doxorubicin monotherapy was as effective as combination therapies in terms of overall patient survival. As a result, sequential rounds of doxorubicin monotherapy were reinstated for the treatment of the majority of breast cancer patients [242, 34], and anthracyclines continue to be used as a standard post-operative therapy in the early stages of the disease [105].

In addition to the prevalent use of doxorubicin and other cytotoxic chemotherapies in the clinic, targeted therapies are also highly effective in particular types of breast cancer. Gene expression profiling and histopathological staining have enabled tumor subtype classification – an early chapter in the story of "personalized medicine". The development of targeted therapies has enabled physicians to match molecular characteristics of tumors in patients to specific courses of treatment. Although molecular subtyping for therapy customization continues to improve, there are a number of core categories of breast cancers for which therapeutic options have been specifically defined and are commonly used in the clinic [253]. Targeted therapies have proven highly effective against breast cancers that express particular combinations of receptors: estrogen (ER), progesterone (PR), or HER2. HER2 is a transmembrane receptor tyrosine kinase (RTK) that propagates intracellular signals responsible for regulating cell proliferation and migration, among other processes. Estrogen and progesterone receptors also drive tumor growth. Consequently, anti-estrogen therapy, such as Tamoxifen or Raloxifene, is highly effective in treating ER+ tumors. Tumors with HER2 amplifications, which occur in approximately 15% of diagnosed patients, often have poor clinical outcomes, but are frequently treated with targeted antibody-based therapies, such as trastuzumab, an anti-HER2 antibody that is often used in combination with chemotherapeutic agents [240, 239, 103]. For ER+/PR- tumors that overexpress HER2, aromatase inhibitors have been effective in postmenopausal women, which block the conversion of androgen into estrogen, thus producing anti-growth effects similar to those of hormone therapy [198].

Although breast cancers that express particular receptors such as ER or HER2 that drive tumor growth are amenable to targeted therapies, cancers that fail such therapies are commonly treated with chemotherapy as a second-line option. Another common subtype of the disease, referred to as "triple-negative breast cancer" (TNBC) does not respond to targeted therapies. TNBC typically presents as ER/PR negative with normal levels of HER2, making cytotoxic chemotherapy the frontline treatment option. This subtype of breast cancer is arguably one of the most aggressive forms for the disease [207], and has been shown to exhibit high levels of intercellular variability in response to chemotherapy [198]. TNBC is generally responsive to chemotherapy, but favorable treatment outcomes are often short, with average survival remaining at around 2 years. As a result, the study of chemotherapy effects on breast cancer are particularly important in TNBC subtypes, for which few other therapeutics options are currently available. Although a distinctive feature of TNBC is lack of ER/PR and normal HER2 levels, this subtype also generally exhibits mesenchymal-like characteristics that confer pro-invasive, metastatic properties to tumor cells [156, 205]. As a result, the study of cytoskeletal, morphological, and migratory changes in cancer cells, which often characterize metastatic disease, in addition to the signaling mechanisms that regulate them, is important for rational therapy design and selection in the treatment of TNBC.

1.1.1 Clinical considerations of drug efficacy and toxicity

One key clinical consideration in the use of doxorubicin chemotherapy treatment regimens is drug toxicity. The most prominent toxic side effects of doxorubicin treatment are cardiotoxicity, neuropathy, myelosuppression, and alopecia [198, 28]. Cumulative doses of the drug that exceed 450 mg/m^2 (m^2 corresponds to patient surface area), dramatically increase the chance of congestive heart failure. Numerous strategies to ameliorate doxorubicin toxicity have been developed, many of which are used in the clinic. Liposomal formulation of doxorubicin (e.g. Doxil^{TM}) improves the pharmacokinetic properties and intratumoral distribution of the drug. This formulation makes the drug more permeable within the tumor and increases drug retention, while partially alleviating doxorubicin-associated cardiotoxicity [248, 267, 187]. Unfortunately, approval for clinical use of this formulation is currently in place only for the treatment of certain types of ovarian cancers. Doxorubicin metabolism and binding with intracellular iron produces reactive oxygen species (ROS) that can damage healthy tissue [28, 198]. Dexrazoxane, an iron chelator that reduces doxorubicin-induced oxygen radicals, is used clinically to reduced cardiotoxicity associated with doxorubicin in breast cancer treatment [266].

Combination treatments with chemotherapeutics can improve tumor killing, but must be carefully chosen in order to avoid increased toxicity. For example, trastuzumab is an effective therapy in breast cancer with HER2 amplification, but, like doxorubicin, is cardiotoxic, making combinations of anthracyclines and trastuzumab problematic [172, 198, 28]. Because trastuzumab is often used in combination with anthracyclines such as doxorubicin, which are in themselves cardiotoxic, great care must be taken to avoid excessive toxicity and make the combination therapeutically justified. Moreover, combining anthracyclines with taxanes (e.g., doxorubicin and paclitaxel/docetaxel) has shown to be highly effective, but often leads to increased levels of cardiomyopathy [83]. A combination of paclitaxel and doxorubicin, for instance, elevates cardiac toxicity, likely due to paclitaxel interactions with doxorubicin metabolites. Combined and sequential administration of these agents is therefore typically avoided [244]. These data emphasize the potential advantage of monotherapies and show the challenges associated with combination treatments – combinations are guided not only by a need to improve efficacy, but must also be carefully selected to minimize toxicity.

Furthermore, chemotherapy dosing and scheduling are additional key variables that determine therapeutic response and toxicity. The use of multiple treatment cycles of doxorubicin with shorter (e.g., 2 week versus 3 week) drug-free intervals, called dose-dense regimens, can elicit better therapeutic response based on the Norton-Simon hypothesis [115, 50]. Unfortunately, these regimens are also associated with increased toxicity, such as myelosuppression, while more frequent but lower doses are less toxic [255]. As a result, typical doxorubicin monotherapy regimens consistent of multiple rounds of treatment – single doses range from 50 to 75 mg/m^2, with multiple I.V. administrations every 3 weeks, or use lower doses of the drug in a dose-dense regimen. This approach – multiple rounds of treatment with weeks of no drug treatment in between rounds – may constitute a temporal window for tumor adaptation to therapy in the context of incomplete tumor eradication (discussed below), a process that is explored in this thesis in Chapter 3 using an *in vitro* model system of TNBC.

Selection of therapeutic strategies is particularly important in breast cancer, as medical

imaging has revealed that many patients may not even require treatment to manage the disease [198]. This additional variable opens the door for over-treatment of cancer that exacerbates patient mortality and morbidity. Maximizing drug efficacy, which pertains to tumor killing, while reducing toxicity associated with doxorubicin treatment, are principal goals. The consequences of over-treatment and the tradeoffs between efficacy and toxicity (i.e., the "benefit-to-risk ratio") collectively demonstrate that despite decades of progress, much work still remains to better understand the factors that constitute and promote breast cancer progression in the context of chemotherapy treatment. Part of the solution may be to identify and validate better prognostic biomarkers for improved personalized treatment that is tailored to specific patients. Another important angle is the use of relevant *in vitro* and animal model systems to explore the vast therapeutic parameter space on the cellular level in order to optimize treatment combinations, dosing, and scheduling.

1.1.2 The many paths to cancer drug adaptation and resistance

Despite the progress in the development and implementation of targeted therapies and chemotherapies, drug resistance in breast cancer is common, leading to disease relapse and recurrence [118]. One phenomenon that drives resistance is genetic evolution. In 1943, Luria and Delbrück published their seminal paper describing two principal modes of bacterial resistance to viral infection [161]. They postulated two competing hypotheses that could lead to bacterial resistance to bacteriophage: (1) mutation to immunity, and (2) acquired immunity. In essence, their studies demonstrated the Darwinian principles of natural selection at work by showing that random mutagenesis inherent to a growing population of organisms can provide a survival advantage in a competitive microenvironment or confer resistance to exogenous insult. Since then, many studies have shown that these modes of resistance – instrinsic or acquired – are also at play in pathophysiological systems, including tumors. Therapy-resistant subpopulations of cancer cells, or clones, can be present in a tumor prior to any treatment. When these subpopulations comprise the bulk of a tumor, "intrinsic" resistance is present. Intrinsic resistance manifests as poor response to primary treatment (Fig. 1-1a).

In addition to intrinsic resistance, later work offered alternative possibilities of cancer cell adaptation to drug treatment through "acquired" resistance [198, 253] (Fig. 1-1b-c). In acquired resistance that has a genetic basis, a rare subpopulation of resistant cells that arises from random genetic mutations survives the initial treatment, even though the overall tumor may die off and shrink below detectable size [113]. Although acquired resistance can constitute progressive selection of resistant clones which harbor mutations that confer resistant properties, a variety of other possible mechanisms exists. These mechanisms include bypass signaling through alternative biochemical and signal transduction pathways [113], signaling network rewiring through altered proteolytic shedding [178], drug efflux through transmembrane transporters, or altered drug metabolism [253]. For instance, previous studies have shown that redundant RTK signaling pathways can drive cancer cell proliferation and survival, so targeted inhibition of a specific RTK leads to activation and bypass signaling through another [113]. Proteolytic shedding of RTKs at the cell surface is a key modulator of receptor signaling, enabling bypass mechanisms and signaling cross-talk that contribute to resistance [178].

The delineation between predisposed, or intrinsic, resistance and one that is acquired

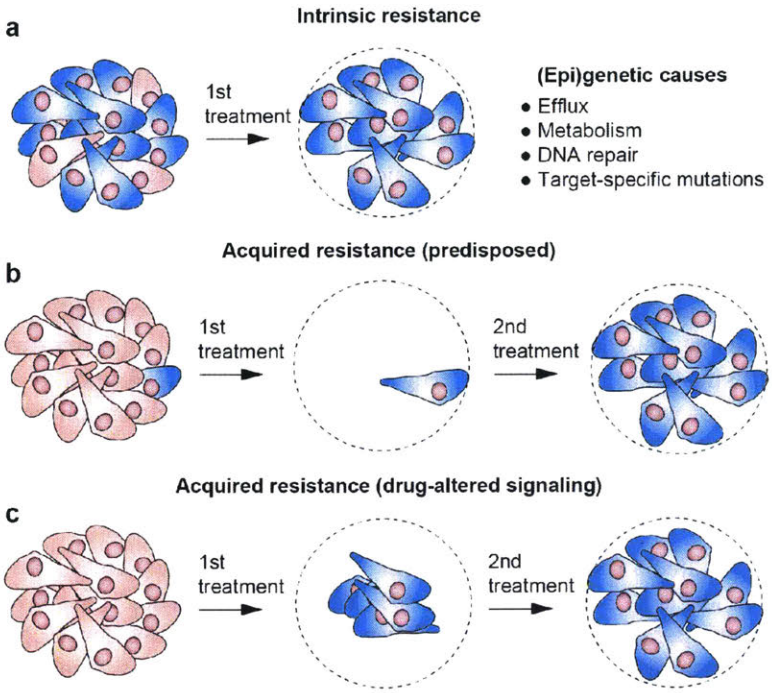

Figure 1-1: Tumor cell resistance to multiple rounds of therapy has various paths. **(a)** Pre-existing intrinsic resistance in the bulk of the tumor leads to poor primary response. **(b)** Rare drug-resistant clones within the tumor are selected for by primary treatment, which grow out due to eradication of drug-sensitive cells that comprise the bulk of the tumor prior to treatment. In (a) or (b), genetic or epigenetic factors play a dominant role in drug resistance. **(c)** Drug-induced acquired resistance results from activation or rewiring of cellular signaling networks through post-translational modifications. Sub-lethal doses of the drug at the tumor core are insufficient to induce cell death, but nonetheless alter signaling and phenotype of survivors that can lead to drug tolerance or resistance.

can often lead to philosophical "chicken and egg" arguments. One can argue that even in the case of acquired resistance through bypass RTK signaling, there is a predisposed propensity for a resistance mechanism. Nonetheless, one distinction between the two resistance modes can be established from a clinical response perspective. In intrinsic resistance, a drug has little or no effect at the beginning of treatment without resistant clone selection, while in acquired resistance lack of drug efficacy is observed progressively over time after multiple rounds of treatment. Another important distinction is related to whether the resistance is permanent or reversible. Intrinsic resistance to a specific drug derived through random mutagenesis within a genomically heterogeneous population prior to treatment is more likely to be permanent since reversion of a specific genomic locus to a previous state by chance is unlikely. On the other hand, drug adaptation, which can be thought of as one mode of acquired resistance, is a more dynamic process. An adaptive response to a drug, which is investigated in this thesis in Chapter 3, constitutes rewiring of signaling networks that depend on many intracellular (e.g., altered phospho-signaling) or extracellular (e.g., stromal cells) inputs, all of which can change substantially over the lifetime of a cell. Numerous strategies have been developed to identify and target drug resistance, including

drug transport inhibitors and drugs that target the DNA repair machinery in cancer cells [198, 28]. Although *in vitro* studies have shown promise, their clinical efficacy has been minimal, largely due to the multifactorial nature of resistance and the capacity of cancer cells to adapt to treatment through a variety of acquired bypass mechanisms [285].

A unique feature of DNA damaging chemotherapy like doxorubicin is that, unlike targeted therapies like monoclonal antibodies or RTK inhibitors, these drugs promote genomic instability that can increase tumor cell mutagenesis [198]. As a result, submaximal tumor killing can actually exacerbate the disease in some cases by increasing the chance of an acquired resistance genotype. Pharmacokinetics also play an important role in drug resistance. Limitations on maximal tolerable dose of cytotoxic chemotherapy due to high toxicity leads to sub-lethal doses of the drug in some tumor cells, especially at the core of larger tumor masses where the diffusion profile results in lower drug concentration at the tumor core than at the periphery. This sub-lethal dose can still initiate doxorubicin-induced signaling (discussed in the next section), but is insufficient to induce apoptosis, which can drive a stress response that leads to drug adaptation.

Interestingly, clinical data has shown that the use of anthracyclines, like doxorubicin, results in higher levels of recurrent metastatic disease in patients that have been previously treated post-operatively with these drugs [105]. Remarkably, lower levels of partial or complete response in patients that have had prior chemotherapy treatment relative to patients who are treated for the first time with a particular drug, is not unique to anthracyclines. Randomized clinical trials have shown that mitotic inhibitors (e.g., taxanes), anti-metabolites (e.g., capecitabine and gemcitabine), alkylating-like agents (e.g., cisplatin), and hydroxyquinolones (e.g., mitoxanthrone), are all less effective in patients who have undergone previous chemotherapy treatment (see Table 34.5 in [198]). These data demonstrate a serious challenge in the use of state-of-the-art chemotherapy regimens for breast cancer, in that promising early response turns into resistant and progressive disease in subsequent cycles of treatment. By the clinical definition, this constitutes tumor adaptation and acquired resistance. In Chapters 3 and 4 of the thesis, I investigate and describe one such adaptive response mechanism that is driven by the DNA damage response networks induced by sub-lethal doses of doxorubicin in an *in vitro* model system of TNBC.

1.1.3 Doxorubicin: a frontline chemotherapy with broad effects on cellular signaling

As discussed above, doxorubicin is widely used as a frontline therapy for TNBC, either alone, in combination, or in sequence with other chemotherapeutics or targeted agents. This therapy often leads to acquired resistance, but the mechanisms that lead to this resistance remain largely unknown. The most well-characterized and intended mode of action of doxorubicin in the treatment of cancer is the inhibition of topoisomerase II, a nuclear enzyme involved in DNA replication and transcription. Topoisomerase II inhibition leads to DNA damage that activates the DNA damage response – intracellular protein networks that result in cell cycle arrest. Successful repair of drug-induced DNA lesions can result in cell cycle re-entry and cell survival, whereas irreparable damage in tumor cells leads to cell death [113] (Fig. 1-2). Doxorubicin also reacts with intracellular iron to form the doxorubicinol derivative, leading to reactive oxygen species (ROS) production [266, 28]. High level of ROS can damage cellular macromolecules including proteins and lipids, but ROS also act

as important signaling molecules. ROS, and hydrogen peroxide (H_2O_2) in particular, act as second messengers that inactivate tyrosines phosphatases, leading to increased RTK signaling. ROS also activate a variety of signals including p38MAPK, Src kinase, and the Rho GTPase family member, Rac [116, 142]. These proteins are hub kinases that mediate cellular cytoskeletal organization and morphogenesis, proliferation, survival, and migration. As a result, sub-cytotoxic levels of doxorubicin chemotherapy can dramatically alter the signaling and phenotypic landscape of cells, the properties of which are studied in this thesis.

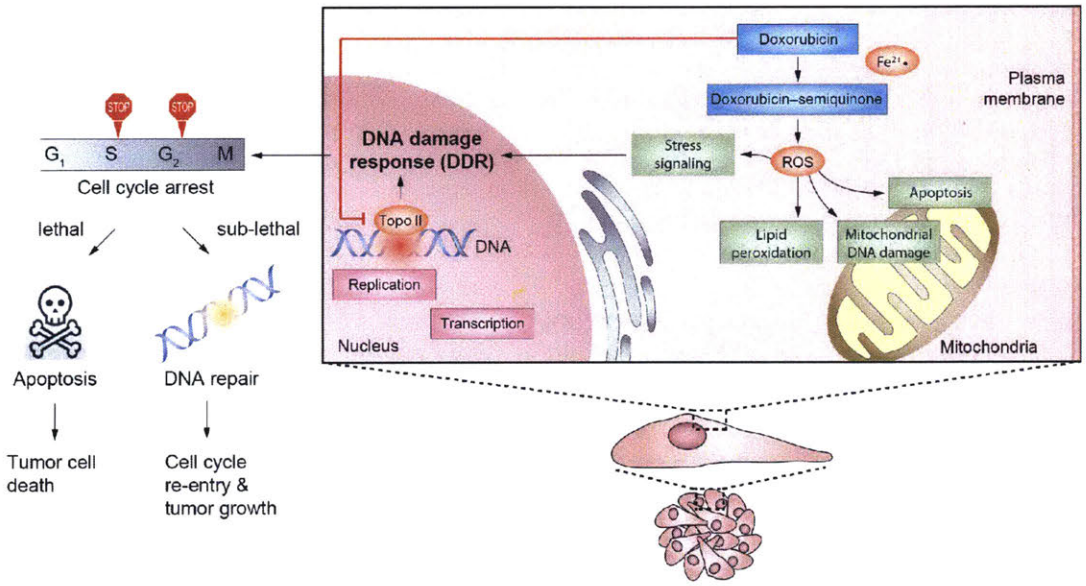

Figure 1-2: Doxorubicin has multiple modes of action that contribute to its toxicity and efficacy. Reactive oxygen species (ROS) produced by doxorubicin react with intracellular iron, which leads to mitochondrial dysfunction and macromolecular damage that produce toxicity in healthy organs like the heart. DNA damage response signaling networks are activated in cancer cells by doxorubicin-induced inhibition of topoisomerase II (Topo II) function, leading to cell cycle arrest that blocks tumor growth. Irreparable DNA damage leads to cell death, while DNA repair results in cell cycle re-entry and continued tumor growth.

Two-dimensional cell culture systems, which are used in this thesis, are typically limited in capturing *in vivo* microenvironmental context of surrounding stromal cells, extracellular matrix composition, or tissue architecture, but nonetheless provide an experimental model system for studying the signaling and phenotypic landscape of cells. These 2-D cultures provide a well-defined system in which microenvironmental variables (e.g., cell density, drug dose, etc.) can be reliably controlled and measurements can be made specifically from the cell type of interest. Such systems are particularly amenable for high-throughput characterization of single-cell phenotypic changes from hundreds of cells that provide enough data for robust statistical analyses and data modeling, and are commonly used for mechanistic studies. The findings from 2-D systems can set the stage for additional experiments with added complexity that aim toward specific *in vivo*-like conditions to be tested.

Collectively, the multitude of mechanisms by which doxorubicin alters cellular struc-

ture and function complicates the delineation of specific pathways that may confer tolerance and resistance to chemotherapy. The DNA damage response, stress signaling through serine/threonine kinases, altered metabolism, and ROS damage and signaling, may all play a role in the poorly characterized process of doxorubicin resistance in cancer and toxicity in healthy tissues. The complexity of these intertwined mechanisms is further complicated by the prevalent use of combination therapies that pair doxorubicin with other chemotherapeutic drugs and targeted therapies. The interactions among drugs in combination treatments are critical determinants of the efficacy and toxicity for a given regimen, making it even more important to understand the modes of action of each individual therapeutic component. Clarifying these mechanisms may shed light into alternative synergistic combination treatments that have favorable risk-to-benefit ratios for patients. Guided by clinical findings and therapeutic strategies, the discovery and characterization of these mechanisms along with the cellular phenotypes they control falls into the domain of biomolecular investigation.

In addition to the utilization of -omics technologies (e.g., genomics, transcriptomics, proteomics) for biomolecular studies, fluorescence imaging enables characterization of cellular signaling and phenotype on a single-cell level, capturing the heterogeneity of cellular responses to external cues. Imaging provides a means for quantifying cytoskeletal structure and cellular morphology, which are critical properties that regulate a variety of cellular functions, including cell motility, division, and death – key processes that reflect tumor response to drugs. As a result, fluorescence imaging and the complementary computational informatics approaches are critical research tools that enable the generation of specific biological hypotheses and their detailed validation, which are discussed next.

1.2 Bioimage informatics: analysis of signaling and phenotype with single-cell resolution

Bioimage informatics refers to the application of computer vision methods to the analysis and interpretation of quantitative measurements extracted from biological images. The bioimage informatics field draws concepts, theories, and algorithms from computer vision, which is a subfield of computer science that integrates image processing and analysis methodologies with statistical modeling used to understand and manipulate visual data in the real world [58]. Computer vision has been largely applied to areas such as process manufacturing and quality control, satellite image interpretation, automated vehicle navigation, and medical image segmentation, among many others. In the field of molecular and cellular biology, which is the domain of this thesis, bioimage informatics has defined the application of computer vision to the study of cellular structure and function from light microscopy data. As discussed in Section 1.1, extracellular perturbations such as chemotherapeutic drugs can produce a variety of signaling and phenotypic alterations among individual cells, leading to heterogeneous cellular responses that can contribute to drug resistance. Integral to the proper characterization of this cellular heterogeneity is the ability to analyze cellular structure and function on the single-cell level. Population-level central tendency measures often mask properties of rare subpopulations and can miss underlying modes, or classes, of responses. These classes, which could be cells that upregulate a certain receptor or not, or are migratory versus immobile, are important to capture and quantitatively characterize in order to rationalize effective therapeutic strategies. A key aim of this thesis is therefore

to develop and apply bioimage informatics tools to characterize changes in cellular signaling, structure, and function in order to better understand the mechanisms and phenotypic consequences of sub-lethal doxorubicin chemotherapy in TNBC.

1.2.1 Mechanisms of cellular morphology and motility regulation

Migration is the defining process in cancer cell dissemination and metastasis that is a key determinant of patient morbidity and mortality [190, 284]. It is therefore no surprise that considerable attention has been given to gaining a deeper understanding of the interconnectedness between cancer therapies, altered signaling mechanisms, cell morphology and motility. This thesis principally deals with actin cytoskeleton signaling processes and the changes in cell shape and motility that these processes regulate, with an emphasis on understanding how sub-lethal chemotherapy influences these features of signaling and phenotype.

Central to the initiation and propagation of cell movement is the concerted reorganization of subcellular signaling pathways and cytoskeletal structure under the influence of extrinsic factors. This asymmetric intracellular localization of signals and resulting differences in cytoskeletal organization define a polarized migratory cell state [41]. The polarization in signals and local shape is highly dynamic, and results in a cell migration "cycle" of protrusion, de/adhesion, and retraction that together orchestrate cell movement [20] (Fig. 1-3). Although protrusion, retraction, and substrate interaction events are common to all motile cells, the identities of and spatial patterns of sub-cellular signals determine the steps and physical manifestations of the migration cycle for a given cell [138]. Signaling networks transduce biochemical and mechanical information from the local surroundings into asymmetric physical changes in morphology that lead to orientation and directionality of movement. The morphological properties that a migratory cell adopts and its mode of migration are reflective of cell type, local identities and concentrations of pericellular stimuli, such as soluble (chemotactic) and extracellular matrix (ECM) protein (haptotactic) gradients, intercellular interactions, and local ECM topology, dimension, and stiffness (durotactic) variations [41, 20, 53, 59].

Modes of cell migration can be broadly broken down into mesenchymal and amoeboid [200]. Amoeboid movement, which is a major mode of motility of leukocytes, is relatively rapid and is characterized by squeezing of cells through pores in 3D matrices via cycles of contraction and relaxation, regulated predominantly by the actomyosin machinery, in which F-actin filaments associate and slide across myosin motors to generate contractile force. The mesenchymal mode of migration leads to slower cell speeds, and involves actin polymerization at the front, association of the cell with the extra-cellular matrix (ECM) through focal adhesions, and the activity of intracellular and secreted proteases for substrate de-adhesion and matrix degradation, respectively [199, 200]. The mesenchymal mode of migration is also less well understood with regard to spatial asymmetry in signaling molecules and the generation of highly dynamic and spatially segregated cytoskeletal structures, making it of considerable interest to study in the context of migratory cell polarity [15].

Considerable progress has been made in the migration field to dissect the individual intracellular signaling pathway components (signals) that play particular roles in different regions of a polarized cell [12, 132, 289, 97]. It is important to emphasize that both the identities of the nodes (signals) and regulatory interactions (edges/arrows) in canonical actin

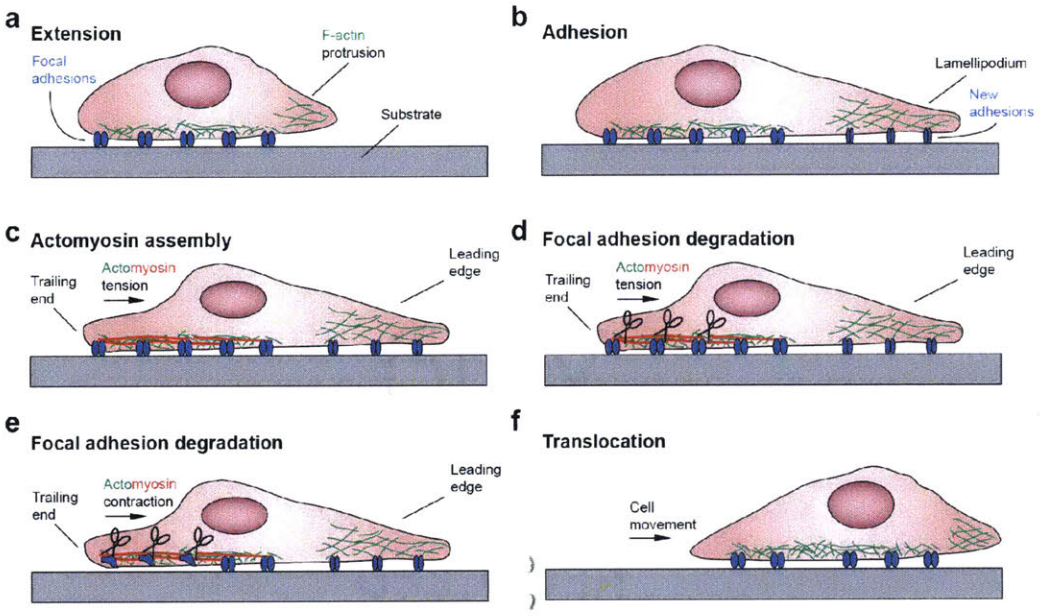

Figure 1-3: Motility cycle of mesenchymal cell migration. **(a)** Actin polymerization at the leading edge forms protrusions that extend at the front of the migrating cell. **(b)** Protrusions adhere to the substrate through nascent focal adhesions. **(c)** Actin assembles with myosin II to form actomyosin contractile units at the back of the migrating cell, producing intracellular tension that pulls on mature focal adhesions in the trailing end of the cell. This leads to morphological elongation of the migrating cell. **(d)** and **(e)** Proteases, such as m-calpain, cleave multiple molecular components of focal adhesions in the back of the cell. **(f)** Actomyosin tension coupled with focal adhesion degradation leads to retraction of the trailing end producing translocation of the cell body in the direction of cell motion.

regulatory signaling networks represent only a small subset of a broader set of heavily studied fraction of the actual multitude of molecular players, interactions, and spatial topologies of networks regulating cell shape and cytoskeletal organization. Most biological studies focus on the specific roles of 1 to 2 molecular species in the context of only a single cell type and extracellular cue. However, cell morphology and migration is a highly complex process that employs the spatiotemporal coordination of dozens of signal and structural proteins on a systems level. Consequently, we next describe a subset of highly-studied signaling species, transduction events, and cytoskeletal structures that have been shown to regulate cell morphology and motility.

Signaling and cytoskeletal structures at the leading edge

Unlike highly polarized cells such as leukocytes that have a clearly defined actin-rich protrusive front, mesenchymal cell protrusions are highly dynamic. These protrusions, such as filopodia and lamellipodia, are variable in structure and molecular composition and are used by the cell to probe the surrounding environmental cues and generate traction during migration. Local gradients in these cues activate transmembrane receptors asymmetrically within the cell leading to localized subcellular signaling. In addition, integrin-based adhe-

sions sense substrate cues, and the study of their compositional and spatial differences is of profound interest given their role in bi-directional signaling at the cell-ECM interface and regulation of cytoskeletal organization [277, 15, 180, 287, 227].

Ligand binding to RTKs leads to conformational changes and phosphorylation of cytoplasmic domains that recruit adapter proteins that transduce the local signal [148]. At the leading edge, various temporally regulated signaling pathways lead to the formation of lamellipodia – sheet-like protrusions driven by both linear and branched actin polymerization [138]. The Rho family of GTPases, including various isoforms of Rho, Rac, and cdc42, are key regulators of polarization and morphology of leading edge structures [164]. Within seconds of ligand binding to an RTK, cdc42 directs phospholipase C gamma (PLCγ) to the cell front and its activation leads to cleavage of phosphoinositide-(4,5)-bisphosphate, PI(4,5)P2, into inositol trisphosphate (IP3) and diacyl-glycerol (DAG) [46]. This cleavage leads to de-sequestration of F-actin severing proteins such a cofilin and gelsolin, and formins, such as profilin, that generate new barbed ends and actin polymerization producing outward protrusion of the plasma membrane [47, 270, 186]. IP3 and DAG also lead to the activation of various isoforms of protein kinase C (PKC), which have been shown to spatially segregate during migratory polarization and result in directed cell movement in the presence of chemo- and hapto-tactic cues [67, 71].

Persistent lamellipodial protrusion that characterizes a dominant leading edge has been shown to be regulated in part by phosphoinositide 3-kinase (PI3K). PI3K phosphorylates PI(4,5)P2 at the 3' position on the inositol ring, which, following dephosphorylation at the 5' phosphate by SHIP2, leads to protein kinase B (Akt) activation and binding of lamellipodin to PI(3,4)P2 [11]. These events, together with Rac GTPase function through WAVE lead to activation of the Arp 2/3 complex that initiates nascent polymerizing actin branches that produce lamellipodia [288]. Cdc42 can also activate Arp 2/3 complex to produce lamellipodia through WASP. Moreover, smaller-scale actin-rich structures, filopodia, are generated by cells to sense the local environment that can prime persistent directed movement. These structures are composed of linear actin filaments bundled by fascin and regulated by Ena-VASP proteins [217]. Both lamellipodia and filopodia comprise a multitude of structural and signaling species whose identities and functions are a topic of continued investigation in the cell migration community.

Signaling and cytoskeletal organization in the trans-cellular body and trailing end

In addition to actin polymerization at the migratory cell front that generate forward force, contractility of the body and de-adhesion of the cell rear is required for productive cell movement [277]. Contractility of the cell is induced by stress fibers – bundles of F-actin associated with non-muscle myosin II, with or without tropomyosin and α-actinin bridges, depending on myosin isoform. Motor function of myosin II is regulated by phosphorylation of the myosin light chain (MLC) on S19 and T18 through various kinases, such as Rho-associated kinase (ROCK), which is activated by RhoA, and PKCδ [119, 274]. MLC phosphorylation is positively regulated by myosin light chain kinase (MLCK) and ROCK, and negatively regulated by myosin light chain phosphatase (MLCP), a multimeric complex. Importantly, MLCP is recruited to myosin through the myosin phosphatase targeting subunit 1 (MYPT1) in a wide variety of cell types, and post-translational modifications of

MYPT1 alter its association with MLCP. Stress fibers extend to the cell rear and are sites of stable focal adhesions that link the cytoskeleton with the underlying ECM. Following protrusion and contractility, a migratory cell attains an elongated morphology with a pointed trailing end due to substrate attachment. At this stage, calpain cysteine proteases, of which m-calpain is a key isoform, cleave focal adhesion proteins that link the actin cytoskeleton to transmembrane integrins that bind ECM. The localization of m-calpain activity to the trailing end has been shown to be regulated by transient Erk activity and PI(4,5)P2 binding [147]. Calpain activation leads to disengagement of the cytoskeleton from the ECM, and, due to the tension from transcellular actomyosin contraction, the trailing end rapidly retracts from the ECM [75].

1.2.2 Image-based analysis of cellular morphology and molecular signaling

Measurement of sub-cellular signal localization and cytoskeletal structure through fluorescence microscopy has been paramount in the study of migratory cell shape regulation. Live fluorescent reporter constructs typically employ stable or transient ectopic expression of a specific protein of interest that can be imaged in live cells. In addition to overall expression, FRET-based sensors have been used to measure activation of cytoskeleton regulators, such as Rho GTPases. For example, Machacek et al. used FRET sensors to study the temporal profiles of Rho GTPase activity through computational multiplexing, which links signals of different probes in different cells through similarities in leading edge boundary dynamics [163]. Fluorescent protein-fused binding domains have been used to detect various phosphoinositides, such as GFP-PH-domains of Akt for PI(3,4)P2 detection, as by Johnson and Haugh to detect PI3K activity in lamellipodia of randomly migration fibroblasts [122]. A number of computational techniques have been developed to quantify local boundary dynamics, such as level sets [163] and electrostatic contour migration method [265], the former using partial differential equation modeling to propagate points through time and space for tracking points at the leading edge. Tsygankov and coworkers developed a software package for quantifying protrusion dynamics and identifying filopodia using shape skeletonization [261].

Despite the prevalent use and advantage of acquiring dynamic signaling measurements, live reporters have a number of disadvantages. Although live-cell imaging captures rich temporal dynamics of cellular processes, time-lapse imaging and generation of cell lines of ectopically expressing fluorescent proteins is low throughput. It requires cloning, transfection/transduction, cell sorting, and maintenance of live cultures for long periods of imaging time. In addition, ectopic expression leads to the observer effect – fluorescent protein variants used for imaging can compete with the endogenous cellular pool of the protein, changing the stoichiometry and local concentrations that are critical for signaling network behavior [106]. The fluorescent probes fused to the protein of interest may also interfere with protein-protein interaction interfaces. Photobleaching of fluorophores, stage drift over time, temperature fluctuations, and cellular phototoxicity are some of the many additional unfavorable features that have been identified that introduce measurement artifacts and perturb cell function in live imaging.

As a result, many cell morphology and migration studies have used fixed-cell immunocytochemistry techniques for measuring signal localization and cell shape description. Un-

fortunately, the vast majority of studies focusing on cytoskeletal structure and assessment of signal localization in fixed cells have been largely descriptive and qualitative in nature, hampering the ability to draw definitive, quantifiable differences in experimental conditions of interest. For instance, a study looking at localization of PKC isoforms during fibroblast chemotaxis used arbitrary, undescribed, qualitative means of assessing signal localization to the leading edge [67]. Many studies also use arbitrary judgment in assessing changes in cytoskeletal morphology and stress fiber formation [268]. Without live imaging that enables unequivocal detection of shape dynamics, identification of polarized cytoskeletal structures are but a subjective human evaluation. Such subjectivity introduces user bias and is likely a confounding factor in the attempt to make cross-study comparisons of cell shape regulation mechanisms.

To address this need, researchers have turned to high-content imaging screens (HCS) to quantitatively characterize cell shape and capture intracellular signals from images of thousands of cells [294, 124, 211, 203]. Image-based cell shape description and quantification of immunofluorescence images of signaling proteins has gained significant popularity and utility in HCS. These screens comprise the following main steps: (1) cell staining and image acquisition using high-throughput imaging platforms, (2) data storage and annotation, (3) cell or subcellular object segmentation, (4) feature extraction, (5) generation of multivariate phenotypic profiles, and (6) statistical modeling and machine learning approaches to compare, visualize, and interpret phenotypic profiles between treatment conditions (discussed in the next section). A key challenge in such imaging screens is the difficulty of measuring more than 4 targets in the same cell population, largely due to spectral limits imposed by overlap in fluorophore emission and excitation spectra. In Chapter 5 of the thesis, I describe a framework that provides an effective way to overcome this challenge by realizing multiplexed fluorescence imaging using diffusible probes. Although steps (1)-(3) above are generally common to many types of fluorescence imaging studies, the foundational principle of HCS is to measure hundreds or even thousands of shape, intensity, and texture parameters, or features, from single cells with the goal of capturing biological properties that can be used to categorize cells into phenotypic classes based on feature similarity. Comparing frequencies of phenotypic classes of cells following treatment with perturbagens, such as drugs or gene knockdowns through RNAi or CRISPR/Cas9, reveals similarities in drug action and signaling protein function that can be used to generate testable mechanistic hypotheses [123].

1.2.3 Extracting biological insights: computational modeling applied to imaging data

As discussed in Section 1.1, dosing and scheduling are critical parameters that are often evaluated in randomized clinical trials designed to study and optimize the myriad of variables that can be altered in a therapeutic regimen. Clinical trials are expensive and put patient lives at risk, and although *in vitro* and animal models of cancer have their drawbacks, they provide a powerful platform for evaluating and comparing therapeutic strategies. Various technologies are currently used to profile cellular changes in the (epi)genome, transcriptome, proteome, and metabolome under experimental pertubations in model systems. Genome sequencing, microarrays and RNA sequencing, and mass spectrometry, are but a few of the core tools used to measure these cellular changes in bulk populations. In addition, cellular

imaging with light microscopy is widely used to study cellular signaling, structure, and function on the single-cell level. A key challenge with microscopy measurements is how to properly analyze and interpret the information-rich content of these types of data. One powerful way to convert image-based measurements into interpretable biological insights is through machine learning. Machine learning is a rapidly growing field within computer vision that is used to detect patterns in data used for comparing cells or treatment conditions to each other (unsupervised learning) or to classify cells or treatment conditions based on previously-categorized instances (supervised learning) [98, 169, 114].

Another important advancement in machine learning applied to bioimage informatics is data visualization. HCS typically produces hundreds to thousands of image-derived features, making their interpretation and summarization challenging. Many features may carry little information content, masking the important measured properties of cells that convey biologically meaningful changes across cells. The need to summarize and visualize multivariate data has motivated the application of dimensionality reduction techniques like principal component analysis (PCA), which is used in this thesis to identify morphological features of cells that vary most between treatment conditions (Appendix A.5), and is commonly applied by others in the field [294, 224, 232]. Other nonlinear dimensionality reduction techniques like multidimensional scaling [258] and t-distributed Stochastic Neighbor Embedding (t-SNE) [162], have also facilitated the visualization and comparison of single-cell measurements derived from flow cytometry and microscopy experiments. Representing image-derived cellular features and their inter-relationships as network graphs, scatter plots, and Glyph-based plots has also aided in microscopy data consolidation and visualization [225]. Central to these approaches is the facile usability by non-expert users who can rapidly interpret HCS results that help guide follow-up studies.

In addition to HCS-based analysis of fixed cells, live-cell imaging screens can be used to characterize cellular phenotypes that capture drug response (e.g., morphology, migration, apoptosis, proliferation) over time. These assays can be used to screen different combination regimens and administration sequences using *in vitro* model systems in which many such conditions can be studied. Although substantial progress has been made in HCS assay development and data analysis, these screens typically miss the rich temporal dynamics of cellular processes that are integral to studying the dynamics of drug response. A key focus of this thesis (Chapter 2) is therefore to develop computational modeling tools that can be used to objectively characterize and summarize the dynamics of image-derived cellular measurements, thus leveraging time-series data to compare the effects of experimental treatments on cellular structure and function. In this thesis, probabilistic time series modeling is applied to classify single-cell shape dynamics as discrete morphological states explored in time, which can be applied to other phenotypic or signaling measurements derived from imaging data as well. In a case study, the framework reveals important similarities and identifies key differences in shape dynamics following inhibition of molecular regulators of cytoskeletal organization in breast cancer cells. Accounting for temporal dynamics of individual cells within heterogeneous populations helps to distinguish and interpret cellular response to diverse drug perturbations. This temporal characterization and summarization of multivariate features typically measured in HCS experiments also helps with interpretation as to which cellular properties vary most between different treatments, shedding light on putative molecular mechanisms of action involved.

1.3 Motivation, overview, and structure of the thesis

In Section 1.1, I discussed that the chemotherapeutic drug doxorubicin is a frontline clinical therapy for triple-negative breast cancer (TNBC), a subtype of the disease for which few other drugs offer an effective treatment response. Cytotoxic levels of doxorubicin activate DNA damage response networks that lead to cell cycle arrest and cell death. Unfortunately, although high doses of chemotherapy are more effective at killing cancer cells, they also adversely affect normal physiology. Clinically, high dosing of doxorubicin is principally limited by toxicity, which can lead to incomplete tumor eradication. These consequences lead to an important question: what effect do doses that fail to completely eradicate a tumor have on surviving cancer cells?

This thesis develops and applies informatics approaches to investigate this question using an *in vitro* model system of TNBC. In Chapter 2, I develop live- and fixed-cell fluorescence image processing and analysis tools to measure, model, and interpret cellular structure and function. The overarching goals of such imaging-based cellular characterization in this system is two fold:

1. To generate testable hypotheses from measured morphological changes in cells in order to hone in on putative molecular mechanisms involved.
2. Directly characterize and establish relationships between cell structure (morphology) and function (migration and apoptosis), to explore whether doxorubicin-induced changes in the cytoskeleton manifest downstream, and in the longer-term, as phenotypes associated with drug resistance and disease progression.

Toward achieving these goals, I present a broadly-applicable statistical time-series modeling framework called SAPHIRE (Stochastic Annotation of Phenotypic Individual-cell Responses), which combines live-cell imaging, image processing, multivariate data analysis, and hidden Markov modeling to characterize cell shape dynamics on a single-cell level. A proof-of-principle shape profiling study demonstrates that temporal dynamics modeled with SAPHIRE are better able to classify actomyosin-altering drugs based on mechanism-of-action compared to existing approaches. This framework can be broadly applied to other cell types and live-cell phenotyping applications as open-source software (http://saphire-hcs.org), capturing rich dynamic features of cellular responses that are missed in fixed-cell assays.

In Chapter 3, I characterize changes in cell signaling and infer putative biological processes altered by doxorubicin from phosphoproteomics data using bioinformatics and data visualization tools. This data captures the effects of doxorubicin on the phosphoproteome regulated by checkpoint kinases MK2, Chk1, and Chk2, three key mediators of the DNA damage response. Additionally, I explore the checkpoint kinase substrate regulation network using targeted phosphoproteomics data that quantifies the effects of selective knockdown of each checkpoint kinase individually in the context of doxorubicin treatment. I further present the follow-up validation of numerous protein species whose phosphorylation is altered by chemotherapy.

In the remainder of Chapter 3, I characterize TNBC cell morphology, motility, and apoptosis dynamics following doxorubicin treatment using the image processing and feature extraction modules of SAPHIRE. Using multiple fluorescent reporters enables simultaneous

tracking of cell nuclei (H2B-mCherry), F-actin (LifeAct-eGFP), and apoptosis (AnnexinV-Alexa647), which I use to relate cellular morphodynamics with the corresponding migration and death rates within the same population upon doxorubicin treatment.

In Chapter 4, I combine the results from the SAPHIRE development experiments and the fixed/live-cell doxorubicin studies, to show that morphological changes associated with ROCK and myosin II ATPase inhibition, but not MLCK, phenocopy those of low-dose doxorubicin treatment, suggesting that myosin II activity may be affected by the drug. In support of this hypothesis, I find that phosphorylation of the myosin II regulatory light chain (MLC) activating site (S19) is reversibly reduced in MDA-MB-231 cells after 24 hours of doxorubicin treatment. Application of a Rho-activating compound reverses the doxorubicin-induced reduction in pMLC and enhances apoptosis of doxorubicin-treated cells. This observation suggests that low doses of doxorubicin may lead to deregulated actomyosin contractility, a crucial biophysical process involved in cell migration, and that reduced pMLC may be associated with altered cellular morphology and viability upon drug exposure.

In Chapter 5, I describe the development of a multiplexed fluorescence imaging approach that uses nucleic acid barcoding of antibodies and peptides to detect a large number (approximately a dozen) different sub-cellular protein targets within a given sample. This approach provides the methodological foundation to expand molecular profiling of cellular specimens beyond the spectral limitations imposed by conventional imaging systems. It sets the stage for building relationships between altered subcellular signaling (e.g., Chapters 3 and 4) and changes in cellular phenotypes (e.g., Chapter 2), enabling the study of signaling-to-phenotype relationships on a single-cell level.

Finally, in Chapter 6, I conclude by summarizing the key findings presented in the thesis and describe future directions of interest for additional applications and extensions of bioimage informatics in drug discovery. I highlight the value of using -omics data analyses to hone in on biological processes that may be altered in the system under study. These putative processes can then be used to design structural and functional assays (e.g., using fluorescence imaging) to capture the associated phenotypic properties with finer detail. This thesis demonstrates that findings from phenotypic assays, when coupled with bioinformatics analyses of -omics data, can help guide follow-up mechanistic studies to narrow down and identify putative modes of drug action. Such approaches may be particularly useful in identifying mechanisms of action (e.g., altered cytoskeletal signaling and phenotypes) of non-targeted therapies like chemotherapeutic drugs that may have consequential effects on tumor response and disease progression in the clinic.

Taken together, this thesis advances the state-of-the-art in quantitative profiling of live- and fixed-cell phenotype and signaling from fluorescence imaging data sets (Chapters 2 and 5), and explores in depth the detailed mechanisms that coordinate previously-unappreciated changes in cancer cell morphology, migration, and survival induced by sub-lethal DNA-damaging chemotherapy (Chapters 3 and 4).

Chapter 2

Probabilistic time-series modeling of live-cell shape dynamics for categorizing mechanisms of cytoskeletal regulation

The contents of this chapter were published as:

S. Gordonov, M. K. Hwang, A. Wells, F. B. Gertler, D. A. Lauffenburger, and M. Bathe. Time series modeling of live-cell shape dynamics for image-based phenotypic profiling. *Integrative Biology*, 8(1):73–90, 2016.

2.1 Abstract

Live-cell imaging can be used to capture spatio-temporal aspects of cellular responses that are not accessible to fixed-cell imaging. As the use of live-cell imaging continues to increase, new computational procedures are needed to characterize and classify the temporal dynamics of individual cells. For this purpose, here we present the general experimental–computational framework SAPHIRE (Stochastic Annotation of Phenotypic Individual-cell Responses) to characterize phenotypic cellular responses from time series imaging datasets. Hidden Markov modeling is used to infer and annotate morphological state and state-switching properties from image-derived cell shape measurements. Time series modeling is performed on each cell individually, making the approach broadly useful for analyzing asynchronous cell populations. Two-color fluorescent cells simultaneously expressing actin and nuclear reporters enabled us to profile temporal changes in cell shape following pharmacological inhibition of cytoskeleton-regulatory signaling pathways. Results are compared with existing approaches conventionally applied to fixed-cell imaging datasets, and indicate that time series modeling captures heterogeneous dynamic cellular responses that can improve drug classification and offer additional important insight into mechanisms of drug action. The software is available at http://saphire-hcs.org.

2.2 Introduction

High-content imaging (HCI) is widely used to perform quantitative *in vitro* cell phenotyping in a broad range of applications from RNAi and drug screening to prediction of stem cell differentiation fates [80, 159, 258, 271]. In contrast to population-level assays that measure concentrations and activities of molecular species pooled over heterogeneous cellular populations, HCI has the advantage of profiling cells *in situ* in a manner that captures both overall cellular morphology as well as sub-cellular features such as protein localization and their relative levels [92, 171]. Shape is the most common property used to characterize cellular phenotype in part due to the ease of image-based quantification enabled by cytoskeletal staining and the importance of morphology in a wide variety of cellular processes. In practice, fixed-cell imaging is typically performed because it avoids large-scale handling of live cultures during imaging or generation of fluorescent reporter cell lines, and enables quantification of large numbers of cells at a single time point, increasing statistical power for comparing cellular phenotypes across experimental conditions [280, 189]. Multivariate statistical modeling of fixed-cell image features has been effective in phenotype-based drug classification, providing important insight into signaling pathways involved in cellular morphogenesis [9, 197]. Single-cell analysis using imaging has been particularly instrumental in identifying and deciphering cellular phenotypes in disease states [32]. User-defined shape categories coupled with supervised learning such as support vector machines, as well as unsupervised methods such as principal component analysis (PCA), have been used to generate quantitative profiles for comparing experimental perturbations and inferring spatial signaling mechanisms of shape regulation [123, 294, 139, 157].

However, fixed-cell assays, while relatively simple to perform through fluorescent staining and imaging, suffer from several important limitations. Principal among these is the loss of information regarding cellular dynamics in response to long-term or transient drug treat-

ments. In addition, imaging artifacts may occur due to cell fixation and permeabilization, which may distort spatially resolved protein distributions [228]. For these reasons, live-cell imaging is increasingly being used to characterize cellular phenotypes, particularly in the subcellular analysis of cell shape dynamics and polarization. For example, computational tools for cell boundary tracking [25, 261, 13], morphodynamics profiling [163, 260, 61, 272], measurement of fluorescent reporters [283, 60], and quantitative morphology and subcellular protein distribution analyses [262] in live cells have become an integral component of high-resolution analyses of cell shape and its regulation, particularly in the context of cell migration. In cell migration studies, live-cell shape and signaling analyses have been complemented by direct quantification of motility properties such as cell speed and persistence of motion to establish links between molecular mechanisms and migratory phenotypes [131, 15, 154, 281, 282, 109].

In these applications, the relative strengths of high-resolution, live-cell imaging versus fixed-cell HCI assays are apparent: the former captures rich, dynamic properties of single-cell behavior while the latter enables large-scale screening of hundreds to thousands of cells. In an effort to bridge this gap, several mathematical approaches have been developed to infer dynamic properties of cell populations from fixed-cell measurements in HCI studies. For example, ergodic rate analysis based on differential equation modeling has been used to infer transition rates through cell cycle stages from images of molecular reporters that define various mitotic phases in individual fixed cells [128]. Additionally, Bayesian network modeling of shape parameters coupled with RNAi knockdown of cytoskeleton-regulatory proteins has been used to infer shape state transitions of migratory cells and reveal underlying regulatory signaling modules [224, 232]. However, these approaches assume quasi-steady-state of the cell population, assign cells into pre-defined phenotypic categories, and, in the case of Bayesian networks, face difficulties in modeling repetitive processes such as motility cycle stages in migrating cells. Moreover, they are not directly applicable to the analysis of live cells over time to monitor individual cellular responses to drug perturbations.

To address these limitations, here we present a live-cell HCI framework that captures the dynamics of a large number of cells on the scale of a phenotypic screen. The approach combines high-content live imaging, image processing, multivariate data analysis, and probabilistic modeling to characterize cell shape dynamics in a drug-screening context. Inspired by existing methods for modeling cell cycle stages from time series images [108, 298], our framework employs hidden Markov modeling to describe shape dynamics as temporal sequences of morphological states that are observed as noisy, multivariate image data. Describing temporal trajectories of multivariate shape measurements as a finite set of states that is limited in number by Bayesian model selection that penalizes model complexity, results in an efficient description of time-dependent shape categories explored by a cell. This approach provides a means of modeling the shape dynamics of hundreds of individual cells, capturing temporal evolution in cell morphology directly from live images without assumptions of steady-state cell populations or predefined shape categories assumed by fixed-cell analyses. We show here in a proof-of-principle study that drug-response profiles derived from these models can be used for phenotypic drug comparisons and can reveal spatially distinct and pathway-specific roles that drug-targeted species play in modulating shape dynamics. Our computational framework is available as open source for the computational cell biology community to apply using MATLAB at http://saphire-hcs.org.

2.3 Results

We developed a framework to characterize single-cell shape dynamics for large collections of cells from live-imaging assays (Fig. 2-1). Fluorescent cells treated with a variety of drug perturbations are imaged in a multi-well format followed by image processing and analysis to track and outline individual cells over time. Image-derived features, or descriptors, of cell shape are extracted to generate a data cube for the entire imaging screen, with the three dimensions corresponding to shape features, individual cells, and time points. PCA is used for dimensionality reduction along the shape feature axes to generate temporal "shape-space" trajectories of individual cells in principal component (PC) space. HMM is then used to annotate each cell shape trajectory using a small set of shape states that are determined using Bayesian model selection, revealing important time-dependent features of cell morphology while substantially reducing live-cell data size and complexity. Features extracted from temporal model annotations of hundreds of cells are then used for clustering and classifying perturbations. In the following sections we detail the steps of the framework and present a proof-of-principle study in profiling the heterogeneity in cell shape dynamics from a small-scale drug screen.

2.3.1 Live imaging enables temporally-resolved readout of cell phenotypes

We first generated a triple negative breast cancer cell line, MDA-MB-231, with stable expression of two fluorescent reporters, LifeAct-eGFP and histone H2B-mCherry, for concurrent imaging of actin and nuclear dynamics, respectively. This enabled the unambiguous identification, isolation, and tracking of individual cells using the segmented nuclei, while the actin reporter enabled quantitative characterization of cytoskeletal morphology. MDA-MB-231 cells were chosen for their mesenchymal-like properties and lack of epithelial-type intercellular junctions, making this cell line particularly amenable to studying phenotypic behavior on the single-cell level. The two-color fluorescent reporter cells were seeded in 96-well plate format and treated with different drugs that target distinct components of the actomyosin cytoskeleton-regulatory pathways including ROCK (Rho-associated protein kinase), myosin II, EGFR (epidermal growth factor receptor), calpain, MLCK (myosin light chain kinase), and MEK (mitogen-activated protein kinase kinase), to probe their effects on cell shape dynamics in two independent imaging experiments (Appendix A.1).

In one experiment, we included two controls in order to set a baseline for cell behavior under no drug treatment: one of growth media only and the other with 0.1% v/v DMSO in growth media to assess effects of DMSO alone since it was used to dissolve drug stock. We also included two different doses for the ROCK and MLCK inhibitors to assess drug concentration effects on cell shape dynamics characterized in our framework. In an additional experiment, we expanded the panel of drug treatments and used a different microscope, culture media, and cell passage number to assess these factors on reproducibility of experiments and subsequent analyses. Epifluorescence 2-D microscopy using a 10x/0.3NA air objective offered a suitable tradeoff between field-of-view and resolution, enabling us to maximize the number of cells captured with sufficient detail to characterize individual cell morphologies over approximately eighteen hours for each treatment condition.

Visual inspection of the compiled time series movies revealed asynchronous populations

of dividing, apoptotic, and migratory cell phenotypes (see online Supplementary Videos S1-S3 in [96]). For cells not undergoing division or death, we observed a broad range of shape changes, with some cells changing shape rapidly with pronounced cell body protrusions and retractions, while others exhibited less noticeable morphodynamic activity. Although the cells generally exhibited autonomous behavior that was largely independent of one another, we observed frequent contact and spatial overlapping of some cells in addition to entry and exit of cells into and out of the imaging fields of view. Collectively, the large quantity of imaging data and phenotypic cell behaviors rendered fully manual data parsing and analysis intractable, thereby motivating the need for an automated computational analysis pipeline for processing the time-series images.

2.3.2 Automated processing with quality control ensures accurate parsing of image data

A priority in formulating our probabilistic modeling approach was to ensure that any data input into the model accurately captures cell shape properties. We therefore developed an image processing pipeline to segment and track cells with as many automated, user-free steps as possible to increase throughput and minimize user subjectivity (see Materials and Methods A.1; Fig. 2-2A). Automated image parsing, cell segmentation, and tracking were first performed for all acquired image time series (see examples in online Supplementary Videos S1-S3 in [96]). A major challenge, however, involved the treatment of variations in image illumination between fields and within fields over time, as well as variability in fluorescent reporter levels between cells, leading to occasional image processing errors such as over- or under-segmentation of cells (Fig. 2-2B). We therefore developed a GUI-based quality control (QC) module that enabled manual validation and modification of segmented regions and cell tracks. Here, user input is desirable because cell boundaries can be defined unambiguously by the human eye while automated segmentation is notoriously sensitive to image properties. This module was used to discern and correct artifacts introduced during image acquisition and automated processing steps. The QC module also enabled us to identify and label dividing and dying cells, which were removed from subsequent analyses (Fig. 2-2C).

2.3.3 Drug treatments diversify morphologies of MDA-MB-231 cells

The automated image processing and QC pipeline resulted in a collection of accurately segmented and tracked cell trajectories. We next extracted a set of eighteen morphological features from segmentation masks of each cell and time point (Table B.1). Following z-score normalization of each feature across cells, we applied PCA to the data in order to capture and visualize the variability in shape between all cell images from the imaging experiment with the expanded panel of drug treatments (Fig. 2-3A, see Appendix A.5). Here, we call the basis of the projected data onto the first two PCs the "shape-space". The first two PCs captured over 80% of the shape variability in the observations. In order to assess how PCA distributes and orients morphological properties of cells in shape-space, we selected random time snapshots from four different cells in seven regions of PC space and visualized the overlaid actin and nuclei images (Fig. 2-3B). This visualization revealed that morphologies of MDA-MB-231 cells across all seven drug treatments vary from large and spread (Fig.

2-3B, panel d), to round cells with pronounced cortical actin at the cell periphery (Fig. 2-3B, panels e and f), as well as polarized cells with varying degrees of elongation (Fig. 2-3B, panels a, b and g), and branched morphologies (Fig. 2-3B, panel c).

To visualize how morphologies vary in different directions and radial distances away from the data mean in shape-space, we created a polar representation of the two PCs. The polar shape-space was subdivided into twelve equal angular bins, with each bin subdivided further into quartiles. Fig. 2-3C shows the representative cell shapes in each radial quartile of the angular bins as well as the contributions of the original eighteen shape features to the values of the two PCs. The highest variance in shape, along the first PC, predominantly captures cell elongation and branching, while the second PC captures cell spreading area and roundness. Features such as major axis length, geodesic diameter, and maximum Feret length capture similar length properties of cells and therefore have similar PC coefficients and directions in shape-space. These features are anti-correlated with solidity, circularity, and extent, which point in the opposite direction for both PCs, showing that branched and elongated morphologies have smaller solidities and circularities, as expected. As captured mainly by the second PC, cells with longer minor axes and larger areas have generally lower eccentricities and smaller ratios of major to minor axis lengths.

Furthermore, we found that cells are densely packed around the data mean at the origin in shape-space, with the point density dissipating radially (Fig. 2-3A). This suggests that although MDA-MB-231 morphologies are visually distinct, shape properties of the population as a whole vary on a continuum, with no clearly distinguishable groups. Interestingly, however, when we plotted cell shape trajectories one at a time we found increased grouping and clustering of points. We applied k-means clustering to individual cells and to the cell population as a whole for k = 2 to k = 10 clusters, and computed average silhouette values in order to quantify the degree to which points form well separated, or cohesive, groups (Fig. 2-3D). As may visually be discerned in Fig. 2-3A, example cell trajectory i forms 2 groups while cell trajectory j forms 3 groups, which is confirmed by the maximum silhouette value that occurs for k = 2 and k = 3 clusters, respectively. On average, points from individual cell trajectories had higher cluster cohesion than did random samples with the same number of points as the trajectories or the entire cell population as a whole.

2.3.4 Probabilistic modeling of morphological states reveals heterogeneity in cell shape dynamics

Having observed that individual cell trajectories form more cohesive clusters than the population as a whole, we next sought to develop a principled and reproducible means of modeling morphological dynamics on a single-cell basis. We reasoned that the higher cluster cohesiveness within individual trajectories signifies the presence of underlying "states" that the cell explores in shape-space over time. Although Gaussian mixture modeling (GMM) is a highly useful approach for unsupervised, model-based data clustering that would eliminate subjective, user-defined delineation of states [298], it typically ignores the temporal nature of data. Including temporal information during model inference is reasonable a priori because GMM inherently assumes that observations are independent [74], which is not necessarily satisfied for sequential time series measurements from the same cell, whose shape may be highly correlated in time. We therefore applied an HMM framework in which temporal dependencies are directly incorporated during model inference, using a modified approach

developed for annotating modes of single-particle motion in live cells [184]. Within this HMM framework, the "hidden" underlying states correspond to cell shape states that produce observable emissions that are associated with the measureable cell shapes computed in PC shape-space (see Materials and Methods A.1). Additionally, Bayesian model selection enables us to penalize models with greater numbers of underlying shape states to fit the set of time series points satisfying Occam's razor or the Principle of Parsimony [206, 209].

To compare our approach with GMMs that ignore dependencies in time series data, we simulated shape-space trajectories from underlying hidden Gaussian states to explore differences with HMM-based annotation using SAPHIRE. Specifically, we sought to compare state identification capability of the two methods, with SAPHIRE using Bayesian model selection and GMM using the Bayesian information criterion to penalize model complexity. Our two-state model simulations revealed that SAPHIRE is more likely to choose the model with the correct number of states and has better accuracy in inferring locations of state means compared with GMM due to SAPHIRE's incorporation of temporal dependencies in the data during the state inference steps (Fig. 2-9).

Next, we applied SAPHIRE to experimental observations of cells in the two-dimensional PC shape-space to infer a time series model for each cell individually. The inferred model specifies the most probable number of hidden shape states, which is unknown *a priori*, as well as the state parameters. Each state is a symmetric, bivariate Gaussian distribution in shape-space with two variables corresponding to the two PCs. The inferred parameters for each Gaussian distribution are the standard deviation and the mean, which capture temporal shape variation and average morphology of the cell within the state, respectively. The model also specifies a state transition probability matrix that describes the probability of transitions between shape states. Each cell is annotated in time with the most probable, or maximum likelihood, shape state sequence, enabling us to determine the most likely state that the cell exists in at each point in time. We first compared shape state inference of our approach with that of commonly-used GMM under different model constraints. Allowing for elliptically-shaped Gaussian states in the GMM led to undesirable grouping of cell shapes with visually-dissimilar morphologies into the same state (Fig. 2-10), and, similar to the results of the numerical simulations (Fig. 2-9), SAPHIRE was better able to capture distinct morphological phases of cells that gradually move between distinct regions of shape-space (Fig. 2-11). In certain cases of cells moving between two visually distinguishable underlying states, the state annotations of cell trajectories were similar for SAPHIRE and GMM (Fig. 2-12). Moreover, from all modeled cell trajectories we found that a larger fraction of cells exists in two to three underlying states, while fewer cells explore either a single state or four or more states (Fig. 2-13).

Despite some similarities in the numbers of states explored by cells, the inferred parameters of transition dynamics and state annotations varied considerably between cells. These variations not only existed for cells across different drugs, but also across cells within a given treatment and for cells with the same number of shape states. Fig. 2-4 shows the inferred shape states for two example cells treated with the same drug having the same number of inferred states, but with notable heterogeneity in state parameters and transition dynamics. Some cells exhibited rapid back-and-forth switching between states corresponding to periodicity in actin protrusions and retractions, resulting in shapes that are elongated, rounded, or those in between (Fig. 2-4A). Other cells exhibited individual instances of state transitions, progressively changing shape in a given direction in shape-space, such as going

from larger and more spread to smaller and rounder morphologies (Fig. 2-4B). The maximum likelihood state annotations capture different phases in the morphodynamic history of a cell, with state transition parameters derived from the state sequence providing useful insights into its dynamic behavior. For instance, the model for the cell in Fig. 2-4A reveals that the cell is more likely to stay in state 1 ($p = 0.19$) or state 2 ($p = 0.29$) than transition to other states, and that direct transitions between elongated (state 1) and a rounded (state 3) morphology without going through an intermediate shape (state 2) is not likely ($p = 0$).

2.3.5 Shape state annotations serve as phenotypic readouts of drug action

Our probabilistic modeling framework produced annotated sequences of shape dynamics for all individual cell trajectories from the inhibitor screen, with each trajectory comprised of morphological states evolving in PC shape-space over time. We next explored how shape dynamics compare between cells treated with the distinct compounds. We first generated phenotypic signatures from the annotated state sequences for each cell. These signatures capture where in PC shape-space states are located, how long a cell spends in its inferred states, and how frequently and in what directions in PC space a cell makes shape transitions (Fig. 2-5A).

We next assessed how the distribution of cellular shape states in polar PC space was affected by the experimental treatment conditions (Fig. 2-5B). Cells in the DMSO and growth media controls were positioned closely and were fairly evenly distributed around the mean of the shape-space data without exhibiting biased morphologies in any particular direction compared with the morphologies induced by drugs. The ROCK and myosin II inhibitors pushed cells predominantly towards highly elongated and branched morphologies with longer dwell times in these states. On the other hand, MLCK inhibition had the opposite effect, biasing cells toward smaller and rounder morphologies along the negative first PC axis. In the experiment with the expanded panel of drugs, both MEK inhibitors tested led to a broader variety of states, predominantly either rounder, or more elongated, shapes, although no strong biases of shape state location or state dwell time were observed upon MEK inhibition (Fig. 2-14A). Similarly, EGFR inhibition led to a broader and relatively more uniform distribution of morphological states around shape-space, albeit with a noticeable shift towards less elongated morphologies, whereas calpain inhibition biased cells into more elongated morphologies. Further, doubling the dose of the myosin II inhibitor shifted cells slightly towards more branched morphologies while diminishing elongated states, whereas an increase in dose of the MLCK inhibitor appeared to accentuate the bias towards smaller and more rounded shapes (Fig. 2-5B). For either drug, however, the overall distributions of cellular shape states and state dwell times were similar across both doses tested, as well as between the two imaging experiments.

Live-cell analysis also enables the determination of whether drugs differentially affect the trajectories that cells take through shape-space when they transition between distinct morphological states. To our surprise, state transition directions were similar across the drugs tested, with cells moving between two relatively narrow angular ranges, 120 to 180 degrees or 300 to 360 degrees in shape-space (Fig. 2-5C and Fig. 2-14B) that correspond to decreased elongation with increased roundness versus increased elongation and decreased roundness, respectively (Fig. 2-3C). This finding suggests that most of the dynamics in shape that MDA-MB-231 cells undergo are along this morphological axis of increasing or

decreasing elongation, regardless of drug treatment, which may be indicative of cytoskeletal protrusion and retraction cycles, while transitions toward larger, spread morphologies, for example, are quite rare for this cell type. Despite the similarity in the directions of state transitions taken by cells across drugs, ROCK and myosin II inhibition led to larger magnitudes and slightly broader distributions in state transitions, suggesting that these drugs induce more pronounced variations along the roundness-elongation axis of cell shape, likely by reducing transcellular actomyosin tension.

Moreover, readouts of shape state locations and state transitions can be used to group treatments based on similarities in induced phenotype dynamics. We derived a dynamic shape state "profile" for each treatment from the shape state and state transition histograms (Fig. 2-5B,C and Fig. 2-14A,B) and hierarchically clustered the treatments using profile similarities for each imaging experiment separately (Fig. 2-6A,B). As anticipated based on the preceding results, the two MEK inhibitors clustered closest together, as did the DMSO and growth media controls. These results serve as internal controls to validate the HMM annotation and phenotypic drug comparison procedure proposed here. The MEK inhibitors were also found to have dynamic shape state profiles more similar to those of the EGFR and calpain inhibitors than to the MLCK, ROCK, and myosin II inhibitors. Myosin II inhibition with Blebbistatin produced phenotypes most similar to those with ROCK inhibition. Perhaps surprisingly, MLCK inhibition, which is known to alter myosin II activity, induced shape dynamics more similar to those under MEK and EGFR inhibition than under myosin II and ROCK inhibition. Overall, the computational analyses from these imaging experiments demonstrate that temporal dynamics of individual cells can be combined into quantitative profiles that serve as useful readouts for phenotypic drug comparison and for inferring shape-regulatory roles of targeted signaling molecules.

2.3.6 State-space temporal modeling of cell morphology improves drug classification over existing image-based profiling methods

SAPHIRE generates phenotypic profiles of experimental treatments from single-cell models of HMM-annotated morphological state trajectories in shape-space. This approach differs from existing fixed-cell HCI profiling methods, which, instead of modeling cellular properties of a given cell over time, characterize cellular properties for different cells in a population at a given time point. Therefore, we sought to assess the benefit that live-cell temporal modeling on a per-cell basis has in comparison with fixed-cell approaches [197, 249, 238, 296] in classifying treatment conditions in our screen (Fig. 2-7). We chose four profiling methods that have previously been compared amongst one another and have shown high drug classification accuracies in a large-scale drug screen study (see [157] and Materials and Methods A.1). To make a fair comparison with live-cell analyses, we used live-cell population data from our inhibitor screen at five different time points post-treatment for the fixed-cell analysis methods in order to mimic a fixed-cell time course experiment. We additionally profiled the dynamics of individual cells but without the HMM that is used in SAPHIRE to assess the value of the HMM state-space shape representation for classifying treatments.

For the three treatments tested that were amenable to the classification analysis approach as in [157], of the four fixed-cell methods the "Factor Analysis + Means" profiles performed best, correctly classifying 5 of 6 treatments (Fig. 2-7A,B). This approach has

also previously been shown to have good classification performance in a large-scale screen of dozens of drugs from different mechanistic classes [157, 296]. Profiles generated using Gaussian mixtures [238] and the K–S statistic [197] correctly classified 4 of 6 treatments, whereas the simplest "Means" [249] approach only classified 2 of 6 treatments correctly. Treatment profiles generated using SAPHIRE resulted in correct classification of all 6 treatments, demonstrating improvement over the fixed-cell profiling methods tested. Moreover, the HMM annotation of morphological states using SAPHIRE appears to be critical for improving correct treatment classification, as profiles derived from single-cell temporal dynamics without the HMM misclassified 2 of the 6 treatments.

To further understand which properties of the state-space treatment profiles generated using SAPHIRE improve treatment classification, we separately considered the use of features that capture state transitions versus features that only consider properties of the states themselves (Fig. 2-7C). Treatment classification confusion matrices using these state features separately revealed that state transitions correctly classify all six treatments, whereas exclusion of temporal transition information leads to misclassification of a treatment, yielding a classification performance similar to the fixed-cell "Factor Analysis + Means" profiling approach.

Collectively, these results demonstrate that all of the methods implemented, with the exception of the "Means" approach, correctly classify the MLCK and myosin II inhibitors, but fail to differentiate between cells treated with MEK inhibitor versus control, or those treated with ROCK versus myosin II inhibitors. Thus, as shown in Fig. 2-7D, when the shape distributions of two treatments differ, both state-space modeling of individual cells over time and existing fixed-cell profiling methods that measure features of different cells at multiple time points, can correctly classify and resolve treatment effects on cell shape. When shape distributions of two treatments are similar, however, state-space modeling of single-cell temporal transitions within the population distributions can improve discriminability and classification of treatments compared with existing methods that only capture shape properties of distinct cells within a population. Therefore, annotation of cell morphologies with a state-space representation using HMM, and in particular capturing state transition dynamics on a per-cell basis, can improve the accuracy of classifying treatment conditions in an HCI experiment.

2.4 Discussion

Here, we presented a computational framework that applies probabilistic time series modeling to characterize shape dynamics of individual cells under the action of drug perturbations assayed using live-cell imaging. Modeling temporal dynamics of cell shape using HMM condenses complex multivariate imaging data into simpler sequences of morphological states that evolve over time. Advantages of our approach over existing methods that are designed for fixed-cell imaging applications were explored. Quantitative features extracted from HMM state sequences using our approach serve as temporal signatures for comparing morphodynamic behaviors between cells, which are not available from fixed-cell analysis procedures. Temporal signatures from multiple identically treated cells are combined to serve as phenotypic profiles for clustering and classifying experimental perturbations.

It has been proposed that cell populations can assume either discrete or continuous

morphological landscapes, principally determined by cell type, extracellular environment, types of perturbations, and the particular phenotype captured [295]. For example, in cases when particular morphologies are reached under effect of genetic perturbations, cells may exhibit more stable steady-state morphologies leading to discrete shape states [294]. Our results suggest, however, that shorter-term responses to pharmacological perturbation of highly asynchronous cell populations fall on a more continuous, finely graded morphological spectrum of shapes that conceals more cohesive and well separated shape state clusters within temporal trajectories of individual cells (Fig. 2-3). Consequently, two different approaches to cell profiling, one using commonly-applied fixed-cell analyses of populations of distinct cells and the other using temporal modeling of individual live cells presented here, may collectively serve as a powerful combined approach to reveal idiosyncrasies in phenotypic effects of different molecular perturbations (Fig. 2-8).

In particular, within the context of image-based phenotypic profiling, our results illustrate that state-space temporal modeling of cell shape using HMM can improve the resolution of cellular classification in response to distinct drug treatments. This result, shown in Fig. 2-7D, highlights an important practical outcome of this work in the context of HCI. Existing phenotypic profiling methods correctly classified some treatments and misclassified others in the actomyosin cytoskeleton-focused drug screen. Our analyses demonstrate that modeling morphological transitions over time on an individual cell basis using HMM can provide useful live-cell phenotypic information for discriminating between treatment effects. Some of these effects are not captured by simply modeling cell shape distribution properties of different cells in a population, even if the same population is profiled over time. This suggests that the framework presented offers additional information beyond fixed-cell profiling in image-based classification using morphological data. An interesting application of temporal modeling would be to complement fixed-cell assays that utilize immunofluorescence staining in order to augment phenotypic profiling and better resolve underlying molecular differences driving distinct cellular drug responses assayed using live imaging.

In addition to investigating the utility of temporal shape modeling in HCI applications, we characterized differential cell shape dynamics induced by small-molecule inhibitors in order to infer relationships between actomyosin signaling mechanisms and shape phenotypes. Similarities in shape dynamics between DMSO and non-DMSO controls, between the two MEK inhibitors, and under different doses of the same drugs, validates the morphological states and state transitions as fundamentally reflecting target-specific effects. Similar dynamic responses in cell shape induced by EGFR, MEK, and calpain inhibition suggest that these species function along a common signaling axis of cell shape regulation in MDA-MB-231 breast cancer cells (Fig. 2-6B). This result is in concordance with previous molecular mechanistic studies performed in fibroblasts, which showed that m-calpain activity is directly regulated by Erk by altering its spatial localization and association with PI(4,5)P2 at the plasma membrane [147]. This process can be mediated by EGFR signaling through PLC-γ, which depletes PI(4,5)P2 at the leading edge resulting in localization and activation of m-calpain at the trailing end that plays an important role in migratory cell polarization. The increased elongation phenotype induced by calpain inhibition revealed from our analysis (Fig. 2-14A) reflects the role of m-calpain in adhesion remodeling, the inhibition of which leads to trailing end retraction defects [91, 75].

Moreover, our observation that ROCK and myosin II inhibitors biased cells toward branched and elongated morphologies is consistent with reported effects of increased acto-

myosin tension promoting cell polarization and limiting the formation of new protrusions [64, 257, 274, 273]. The increased elongation and branching dynamics we observed reflect the impairment in actomyosin contractility and loss of cell polarity upon ROCK and myosin II inhibition, leading to multiple competing protrusions extending outwards around the cell periphery. Given that MLCK and ROCK are both known to induce myosin II phosphorylation and activation, we may have expected their inhibition to promote similar shape dynamics. Instead, the surprisingly dissimilar and near-opposite morphologies that their inhibition produced (Fig. 2-5B) suggests that MLCK and ROCK differentially affect cytoskeletal dynamics; this notion is supported by previous studies which showed that MLCK and ROCK have spatially distinct roles in regulating myosin II activity, and whose activities have opposite effects on the number of lamellipodial protrusions, cell elongation, and polarization [257, 160]. The MDA-MB-231 cell shapes induced by MLCK inhibition in our work are reflective of single-front motile cell morphologies for which formation of additional lamellipodial protrusions is limited (see Video S3 in [96]), as has been suggested to also occur in keratocytes at different stages of development [160]. The differential effects of ROCK and MLCK inhibition on shape dynamics that we identified through our analyses (Fig. 2-8) may have consequential effects on overall cell polarization and migratory behavior in cancer that warrants further investigation in future work.

More generally, the plasticity and variability in shape revealed in our analyses reflects the highly dynamic cytoskeletal changes characteristic of protrusion and retraction events, such as those of migratory cells undergoing directional changes or motility cycles. In light of this, further exploration of interest would be to characterize and understand what cellular functions the morphological states captured by HMM annotation may represent. Qualitative visual inspection suggests that cells in rounder states have higher amounts of cortical actin, whereas those in more elongated states are polarized and may therefore be migratory (Fig. 2-2B and see Videos S1–S3 in [96]). Future studies will focus on characterizing morphological state properties in more depth by quantifying cytoskeletal organization in addition to whole-cell shape, incorporating signaling status from live or fixed-cell fluorescent reporters in post-capture analysis [283, 136], and combining model-annotated state-space dynamics with motility measurements to establish temporal relationships between morphology and migratory behavior [131, 158, 231].

Notwithstanding, the current work demonstrates that phenotypic information derived from imaging-based models of temporal shape dynamics reflects underlying signaling pathway activities that regulate cell shape, which enables hypothesis generation for more in-depth, mechanistic follow-up studies. *In vitro* profiling of phenotype dynamics is also relevant in the context of early-phase drug discovery. In that context, time series modeling of live-cell phenotypes can complement existing fixed-cell imaging methods as well as genetic and biochemical approaches for understanding cellular drug responses, particularly with the advent of genome editing approaches such as CRISPR/Cas9 [82, 173, 192, 54, 165]. The collective implementation and application of these approaches will become an increasingly important component of integrative drug profiling and holistic understanding of cell function.

2.5 Acknowledgements

We would like to acknowledge Shannon Hughes for guidance on experimental elements of this work, and Nilah Monnier, Syuan-Ming Guo, Zachary Barry, and Russell McConnell for helpful discussions. We are grateful to the assistance of staff from the Imaging and Flow Cytometry cores of the Swanson Biotechnology Center at the MIT Koch Institute for Cancer Research. This work was supported by NIGMS grant GM69668 (Alan Wells, Douglas Lauffenburger), NSF PoLS PHY 1305537 (Mark Bathe), and the Ludwig Postdoctoral Fellowship (Mun Kyung Hwang).

2.6 Figures

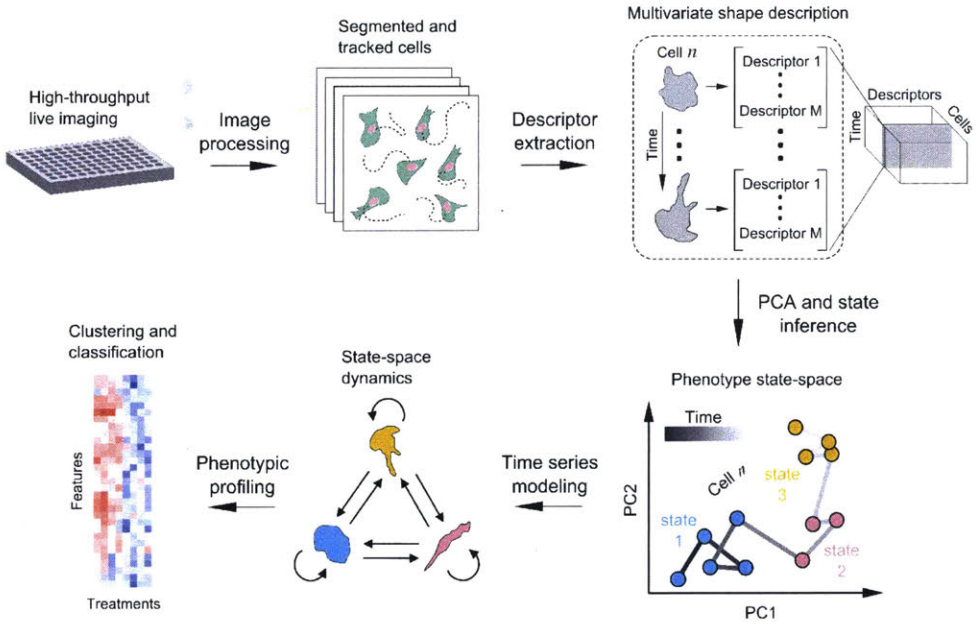

Figure 2-1: Schematic of SAPHIRE (acronym) for live imaging-based modeling of cellular phenotypes. Live fluorescent cells treated with drugs or other perturbations are imaged in multi-well format on a microscope with an incubation system. Temporal image acquisition is followed by image processing and analysis to segment and track individual cells over time. Cell shape descriptors are extracted to generate a data "cube" with dimensions corresponding to [shape features] $\times$ [individual cells] $\times$ [time-points] for the entire imaging screen. Principal component analysis is applied to generate the temporal "shape-space" trajectories of individual cells. For each cell trajectory, probabilistic time series modeling is applied to infer the most likely underlying model of phenotypic states (e.g. blue, pink, and yellow) and its parameters, which are used to annotate a temporal sequence of states and state transitions. Model-derived temporal features of single-cell dynamics from multiple cells are then used to generate phenotypic profiles for drug clustering and classification.

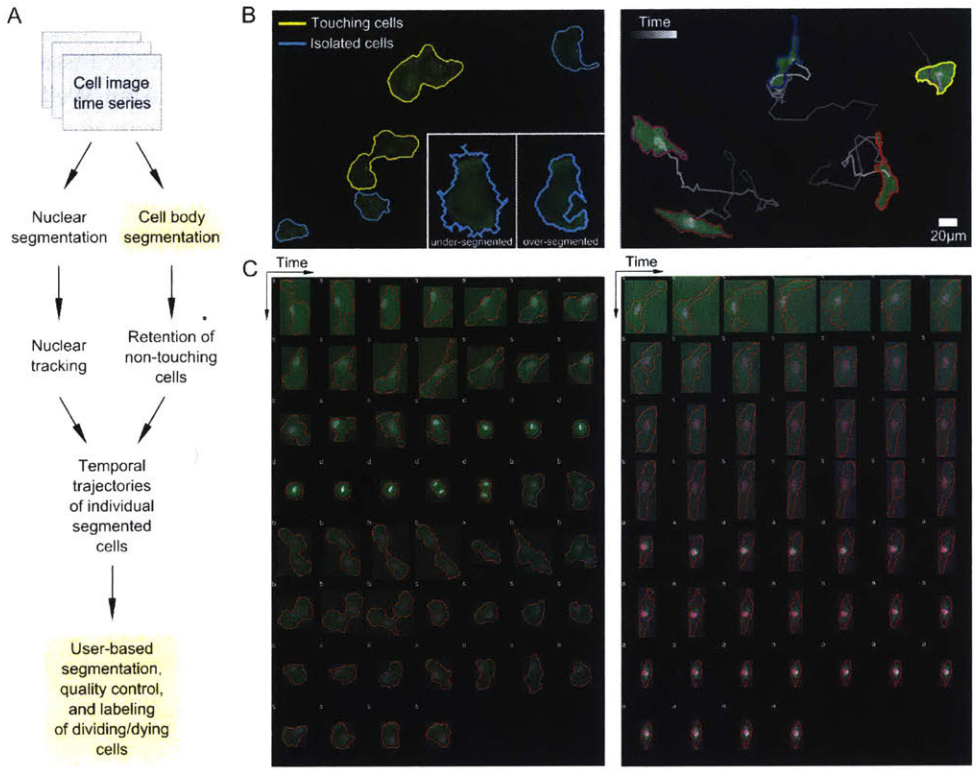

Figure 2-2: Processing and analysis of two-color fluorescent cell movies for segmentation, tracking, phenotype annotation, and quality control. (A) Schematic of the image time series processing workflow used to generate tracked cell outlines in multi-well imaging experiments. Boxes in yellow indicate steps with user input. (B) Left, an example image time series field of view showing touching (yellow) and isolated (non-touching) cells (cyan) automatically identified in the processing pipeline. Inset shows automatic thresholds that may lead to under- or over-segmentation that are subsequently adjusted by the user with a GUI tool. Right, example of individual cells segmented and tracked using the pipeline in (A) from time series imaging over approximately sixteen hours. (C) Quality control and phenotype labeling of processed cell image time series. Two example cell trajectories imaged for eighteen hours at 20 minute intervals are shown, one undergoing cell division (left), characterized by cell rounding in mitosis followed by cytokinesis, and another undergoing death (right), with progressive cytoskeletal shrinking, non-uniformity in actin structure (green), and disruption of nuclear morphology (pink). Isolated cells are automatically labeled `s` while cells touching others or the image boundary are labeled `b`. Dividing or dying cells are interactively labeled `d` and `a`, respectively.

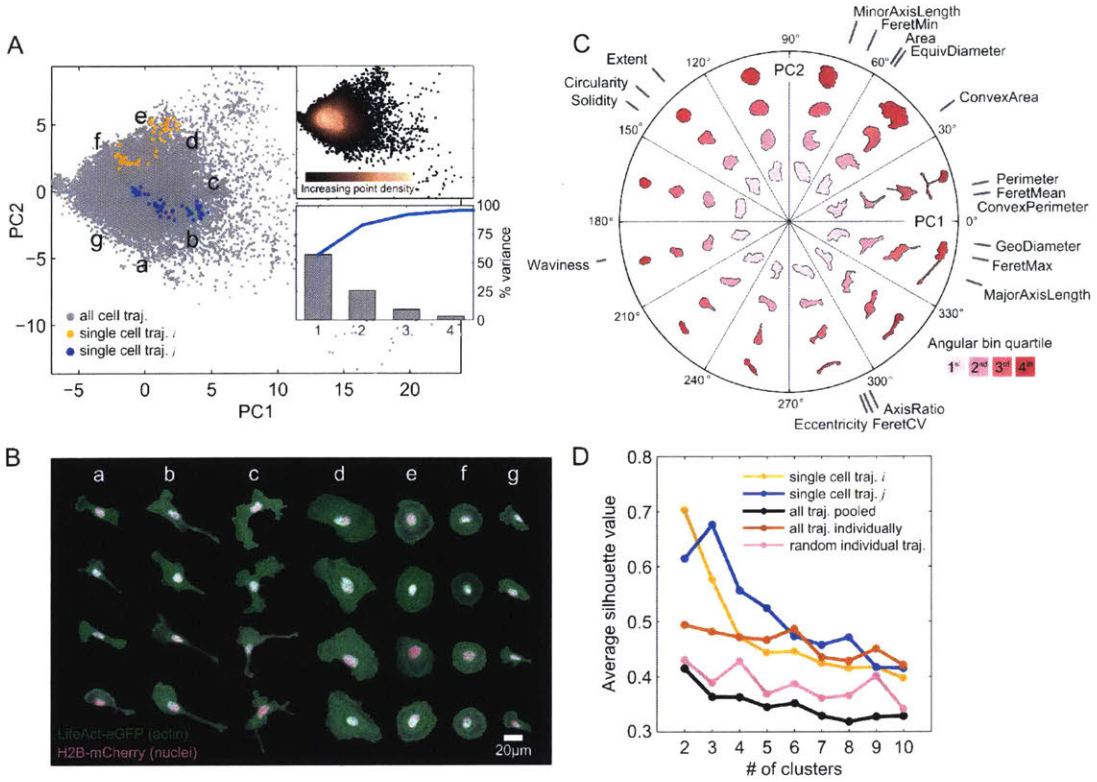

Figure 2-3: Visualization and clustering of live-cell shape features reveals a morphologically diverse shape-space following drug treatments. (A) PCA of approximately 20,000 temporal snapshots (gray points) from live imaging of 293 cells treated with seven drugs (inhibitors of: EGFR, Calpain, MEK (2), Myosin II, ROCK, and MLCK). Two PCs explain over 80% of the variability in the original shape features (upper right panel). Inset shows a continuous shape-space with highest point density around the mean of the data for the cell population, while single-cell trajectories form more well separated clusters in time. (B) Visualization of 28 live-cell snapshots randomly chosen in different regions (a-g) of shape-space in (A). Under the influence of the seven drugs, shapes vary from large and spread, to round with cortical actin, to varying degrees of elongation, to branched morphologies. (C) Polar coordinate PC shape-space visualization. Shapes are shown in different angular bins and radial distances from the mean of the data, which is the origin of the two PC axes in (A). Cell shapes are colored based on the radial distance quartiles within each angular bin. The orientations of the original shape features that contribute to each PC are shown. Lengths of gray lines for each feature correspond to the relative magnitudes of their PC coefficients. (D) K-means clustering of morphologies in shape-space on individual cell trajectories (examples, yellow and blue) reveals clusters that are tighter and better separated on average for all imaged trajectories (orange) compared with clustering of cells pooled together (black) or of random single-cell trajectories of the same lengths (pink).

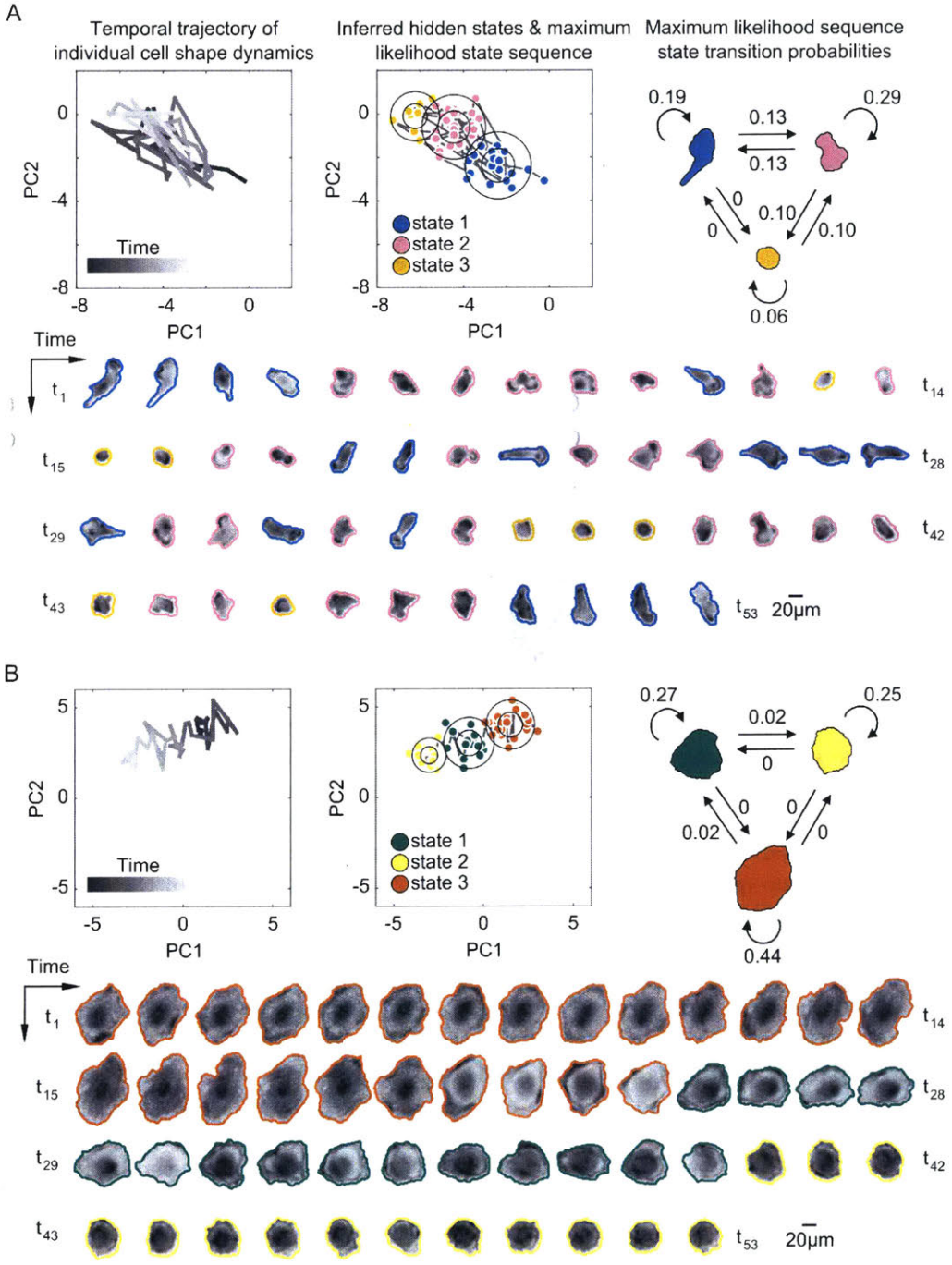
A
Temporal trajectory of individual cell shape dynamics
Inferred hidden states & maximum likelihood state sequence
Maximum likelihood sequence state transition probabilities
PC2
PC1
Time
state 1
state 2
state 3
0.19
0.29
0.13
0.13
0
0
0.10
0.10
0.06
t_1
t_{14}
t_{15}
t_{28}
t_{29}
t_{42}
t_{43}
t_{53}
20μm
B
0.27
0.25
0.02
0
0.02
0
0
0.44

Figure 2-4: Probabilistic modeling of temporal shape-space trajectories captures heterogeneous dynamic transitions in cell morphology. (A) A cell exhibiting repetitive back-and-forth switching between three inferred morphological states of increasing elongation of the cell body from yellow to pink to blue. Top left, the temporal trajectory of the cell through PC shape-space. Top center, Gaussian shape states inferred by Bayesian HMM in SAPHIRE with circles corresponding to one and two standard deviations from the mean (circle center), respectively. Trajectory time points are colored based on the maximum likelihood (ML) hidden state inferred from the model. Top right, a diagram of the dynamic state transitions derived from the ML state sequence with numbers next to arrows corresponding to transition frequencies between, or within, states. Live-cell actin reporter images are outlined with the cell body mask boundaries and colored according to their ML states. (B) A cell with switch-like transitions between three morphological states, changing shape continuously from larger and spread to smaller and round. Shape modeling of this cell trajectory is performed independently of the cell in (A).

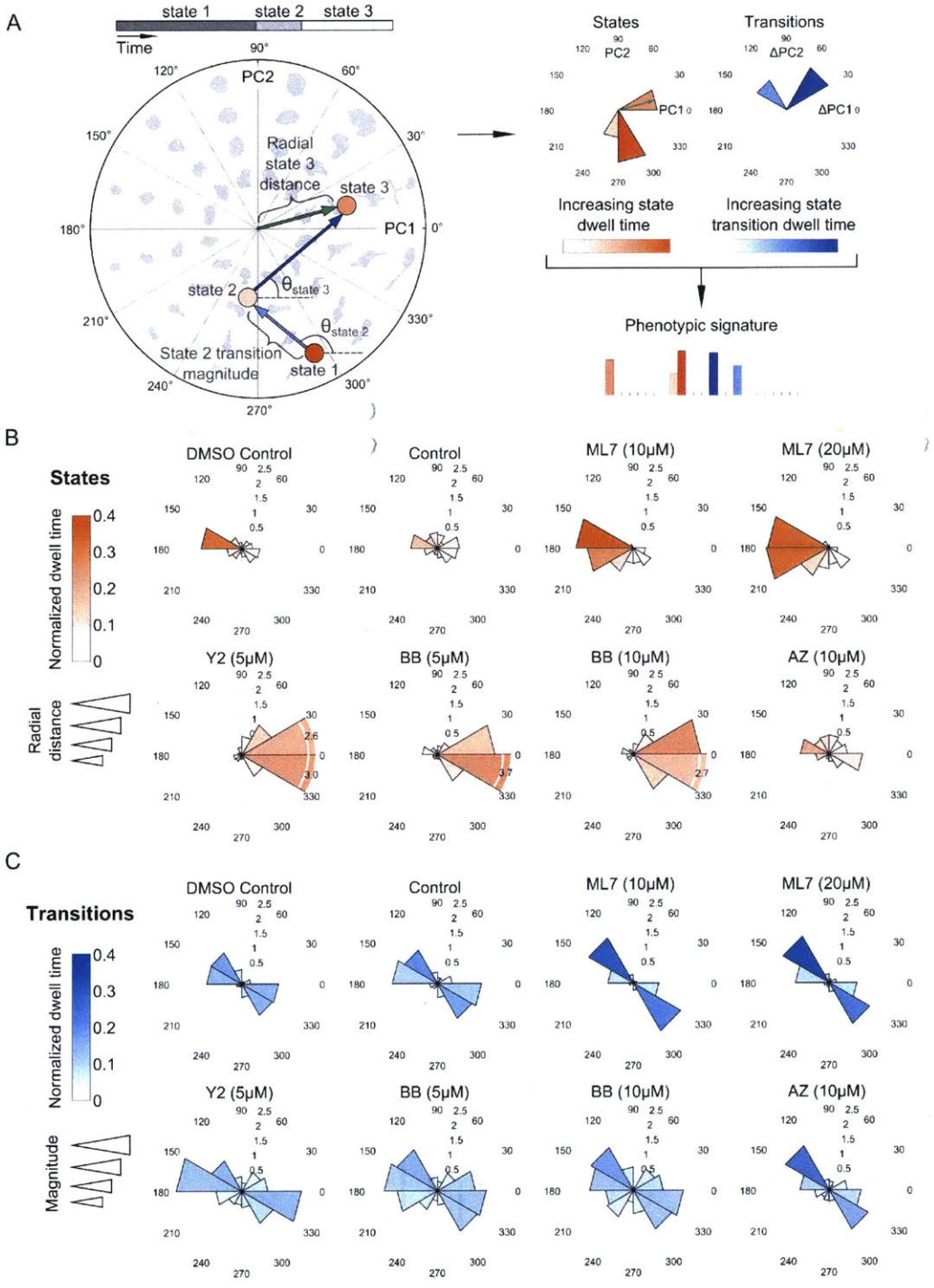
A
state 1
state 2
state 3
Time
PC2
PC1
Radial state 3 distance
state 3
state 2
θstate 3
θstate 2
State 2 transition magnitude
state 1
States
Transitions
ΔPC2
ΔPC1
Increasing state dwell time
Increasing state transition dwell time
Phenotypic signature
B
States
Normalized dwell time
Radial distance
DMSO Control
Control
ML7 (10μM)
ML7 (20μM)
Y2 (5μM)
BB (5μM)
BB (10μM)
AZ (10μM)
C
Transitions
Magnitude

Figure 2-5: Dynamic features of model-annotated shape state sequences from multiple cells enable phenotypic comparisons between experimental treatment conditions. (A) Traversal of a hypothetical cell through polar shape-space showing shape state and state transition features for deriving a phenotypic signature of a cell trajectory. Circles are locations of inferred state means, blue arrows are state transitions, and the green arrow is an example of a radial distance of a particular state from the shape-space center. State transitions capture direction of cellular shape changes over time regardless of state location, whereas state locations capture the particular morphological properties of a cell in a given region of shape-space where the state resides. States and transitions are used to generate a phenotypic signature for each cell individually to enable comparisons between cells. (B) Polar distributions of combined states from all single-cell trajectory models for treatments tested in the imaging screen. Rose plot petals correspond to directional bins in polar shape-space as in (A), but represent average responses of all cells in a given treatment. Longer petals signify radial distances that are further from the shape-space origin. Petal color depth relates to state dwell time of cells in a given slice of polar shape-space, normalized to total trajectory length. (C) Effects of drugs on directions of cellular transitions in polar shape-space. Rose plot petals are average state transition directions of cells in a given treatment. Longer petals signify larger transition magnitudes between states, meaning that state means are farther apart. Petal color depth relates to dwell times of the target states normalized to total trajectory length.

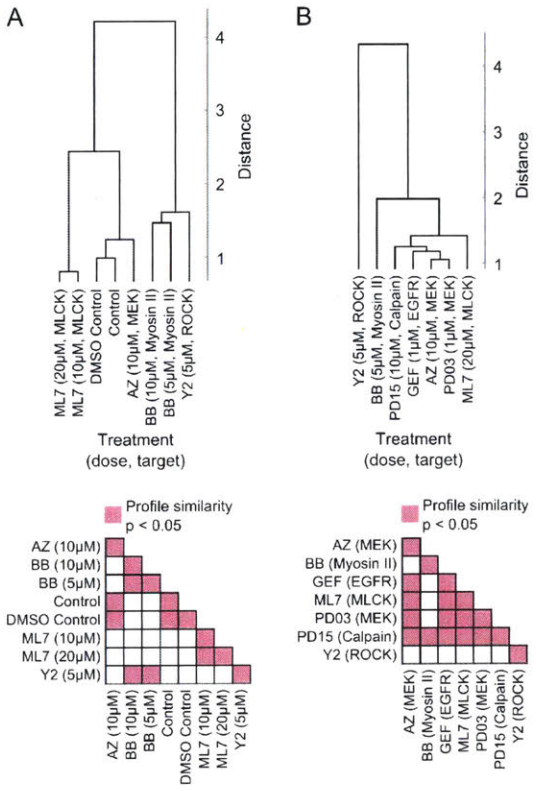

Figure 2-6: Comparisons of drug effects on morphological states and state transition dynamics. (A) Top, hierarchical clustering of phenotypic profiles derived from single-cell models of shape dynamics under the effect of small-molecule inhibitors that target molecular species involved in regulating actomyosin organization. Increasing Euclidean distance indicates decreasing similarity between treatments that are grouped in the dendrogram using average linkage. Bottom, permutation tests indicate statistical significance of pairwise similarities between treatment profiles. (B) Clustering of model-derived phenotypic profiles, as in (A), of cell shape dynamics in response to treatment with an expanded panel of inhibitors.

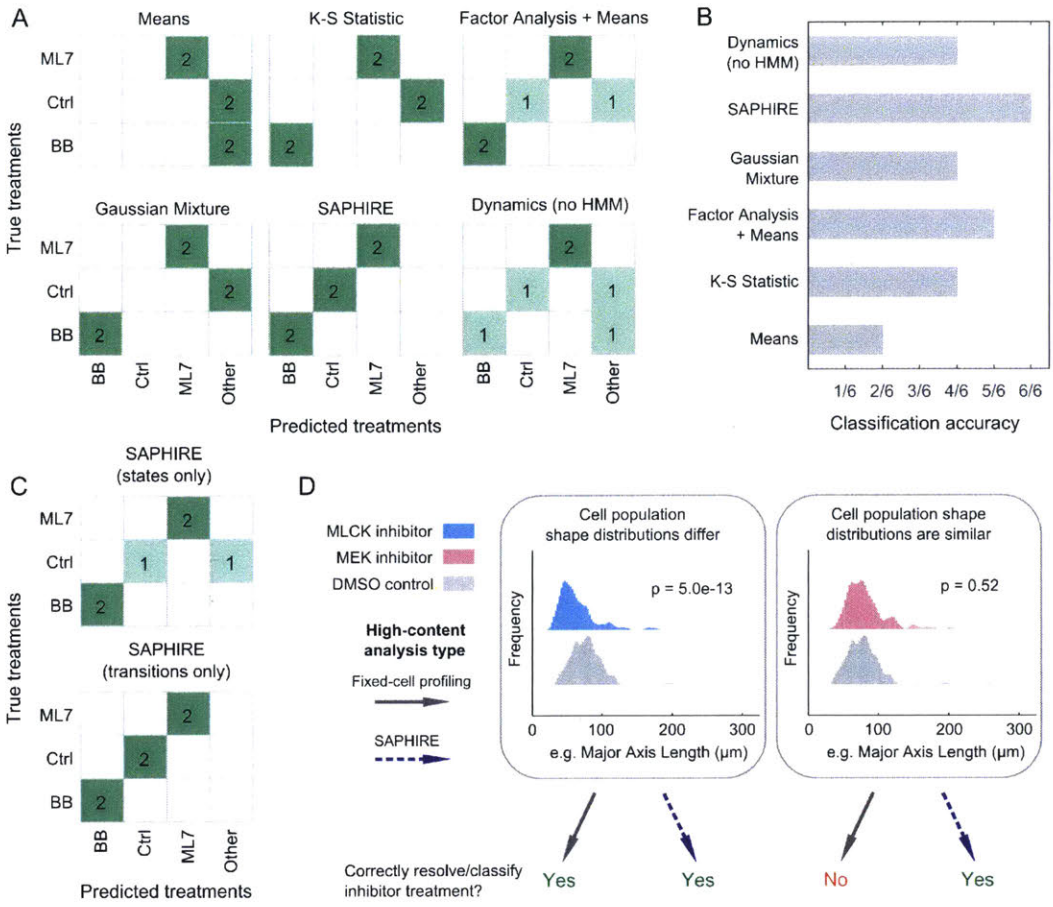

Figure 2-7: State-space modeling of cellular shape dynamics improves drug classification performance compared to existing image-based profiling methods. (A) Confusion matrices showing nearest-neighbor classifications of individual treatments in the inhibitor screening experiment using existing fixed-cell drug profiling methods and the dynamic modeling approach presented in this work. The myosin II and MLCK inhibitor (BB and ML7, respectively) treatments are comprised of two different doses tested for each drug, "Ctrl" comprises the DMSO and non-DMSO controls, and "Other" comprises Y-27632 (ROCK inhibitor) and AZD6422 (MEK inhibitor) treatments that were only tested at a single dose and therefore not used for classification comparisons. (B) Overall treatment classification performances of the proposed and existing phenotypic profiling methods. Classification accuracy reflects the number of correctly predicted treatments out of six true treatment comparisons made in (A). (C) Confusion matrices showing treatment classification performance of SAPHIRE using either state features alone or temporal state transition features alone for generating profiles used in classification. (D) Utility of single-cell temporal modeling in phenotypic profiling depends in part on similarities of cellular feature distributions between treatments. Cellular distributions of a highly varying shape property between cells, major axis length, are shown for pairwise treatment comparisons illustrating the benefits of single-cell temporal modeling in drug profiling and classification. Each distribution comprises individual cells measured at 1, 4, 8, 12 and 16 hours post-treatment. *P*-values correspond to Kolmogorov–Smirnov tests with the null hypothesis that the distributions of two treatments being compared are the same.

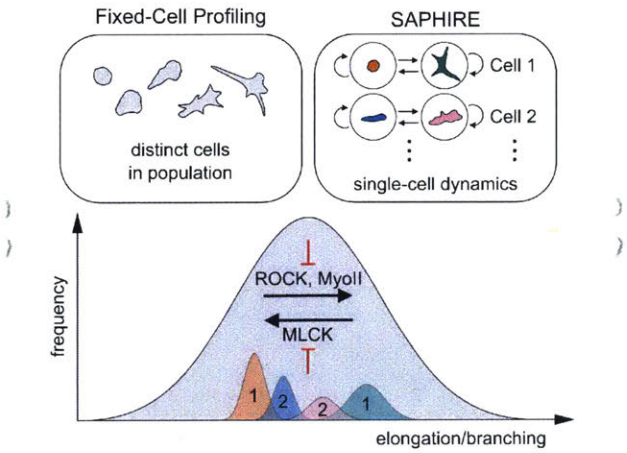

Figure 2-8: Schematic of the conceptual difference between fixed-cell analyses versus SAPHIRE, and their combined insights into molecular mechanisms of cell shape regulation. The distribution of morphologies of drug-treated MDA-MB-231 breast cancer cells falls on a continuum, illustrated in gray. The extent of cell elongation and branching is the dominantly varying morphological property of the breast cancer cell line analyzed in our drug screen (Fig. 2-3). Fixed-cell profiling captures the morphological landscape of distinct cells in the population at a given time point. In contrast, SAPHIRE captures the morphological evolution of individual cells over time. SAPHIRE uses an HMM framework to detect the presence of morphological states (e.g. orange and green states for one cell, blue and pink states for another) used to model the temporal dynamics of each cell independently within the population. Application of both of these approaches to live-cell shape profiling reveals that MLCK inhibition decreases, while ROCK and myosin II inhibition increases, cellular elongation and branching.

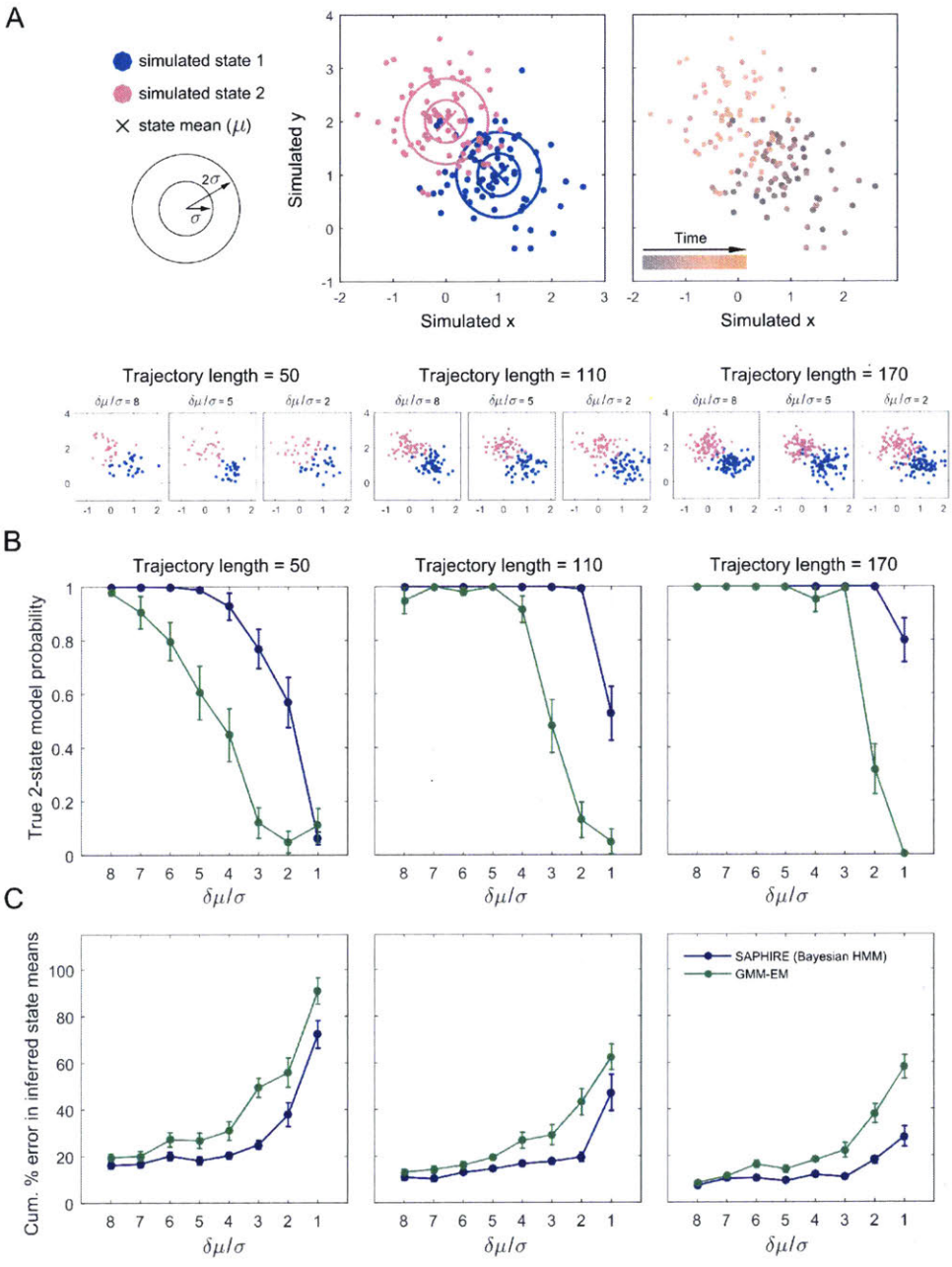
A
simulated state 1
simulated state 2
× state mean (μ)
2σ
σ
Simulated y
Simulated x
Time
Simulated x
Trajectory length = 50
Trajectory length = 110
Trajectory length = 170
δμ/σ = 8
δμ/σ = 5
δμ/σ = 2
B
Trajectory length = 50
Trajectory length = 110
Trajectory length = 170
True 2-state model probability
δμ/σ
C
Cum. % error in inferred state means
SAPHIRE (Bayesian HMM)
GMM-EM
δμ/σ

Figure 2-9: Simulations demonstrating differences in model selection and parameter estimation of Bayesian HMM in SAPHIRE versus GMM under varying degrees of state discriminability. (A) Two bivariate Gaussian states (blue and pink) with equal variances along x and y (left panel) were used to create temporal trajectories with a single state transition. In practice, the states are unknown and must be inferred from a time series cellular trajectory of coordinates (right panel). State circles represent one and two true standard deviations from the mean (circle centers) and points are random samples drawn from the states. Simulated trajectories of different lengths (different number of samples drawn from the states) and varying resolvability of the states (how well separated the states are, $\delta\mu/\sigma$) are shown. (B) Comparison between Bayesian HMM and GMM ability to infer the correct 2-state model (versus a 1-state, or 3-state models) as a function of how well separated the two states are ($\delta\mu/\sigma$) for different trajectory lengths. Here, $\delta\mu$ is the Euclidean distance between the means (centers) of the two states and σ is the standard deviation of each state, set to be the same for the two states in the simulations. Error bars represent +/- standard error of the mean for 20 state-drawn samples for each $\delta\mu/\sigma$. Inclusion of temporal information in the true two-state trajectories enables the Bayesian HMM in SAPHIRE to infer the correct 2-state model with higher probability (purple curve) compared to GMM with expectation maximization (green curve), which does not take temporal information of the trajectory into account. For both the Bayesian HMM and GMM inference methods, longer trajectories and larger separation of underlying states improved inference of the correct 2-state model. (C) The percent error in inferred state means for the Bayesian HMM and GMM. Cumulative percent error in the state means was calculated as

$$\%\ \text{error} = 100 \sum_{s} (|\mu_{s_a,x} - \mu_{s_i,x}| + |\mu_{s_a,y} - \mu_{s_i,y}|)/\delta\mu$$

where s_a is the actual (true) state (two states in these simulations), $|\cdot|$ denotes absolute value, and s_i is the inferred state closest to the true state s_a, for all 2-state inferred models, regardless of whether they are the most probable model or not.

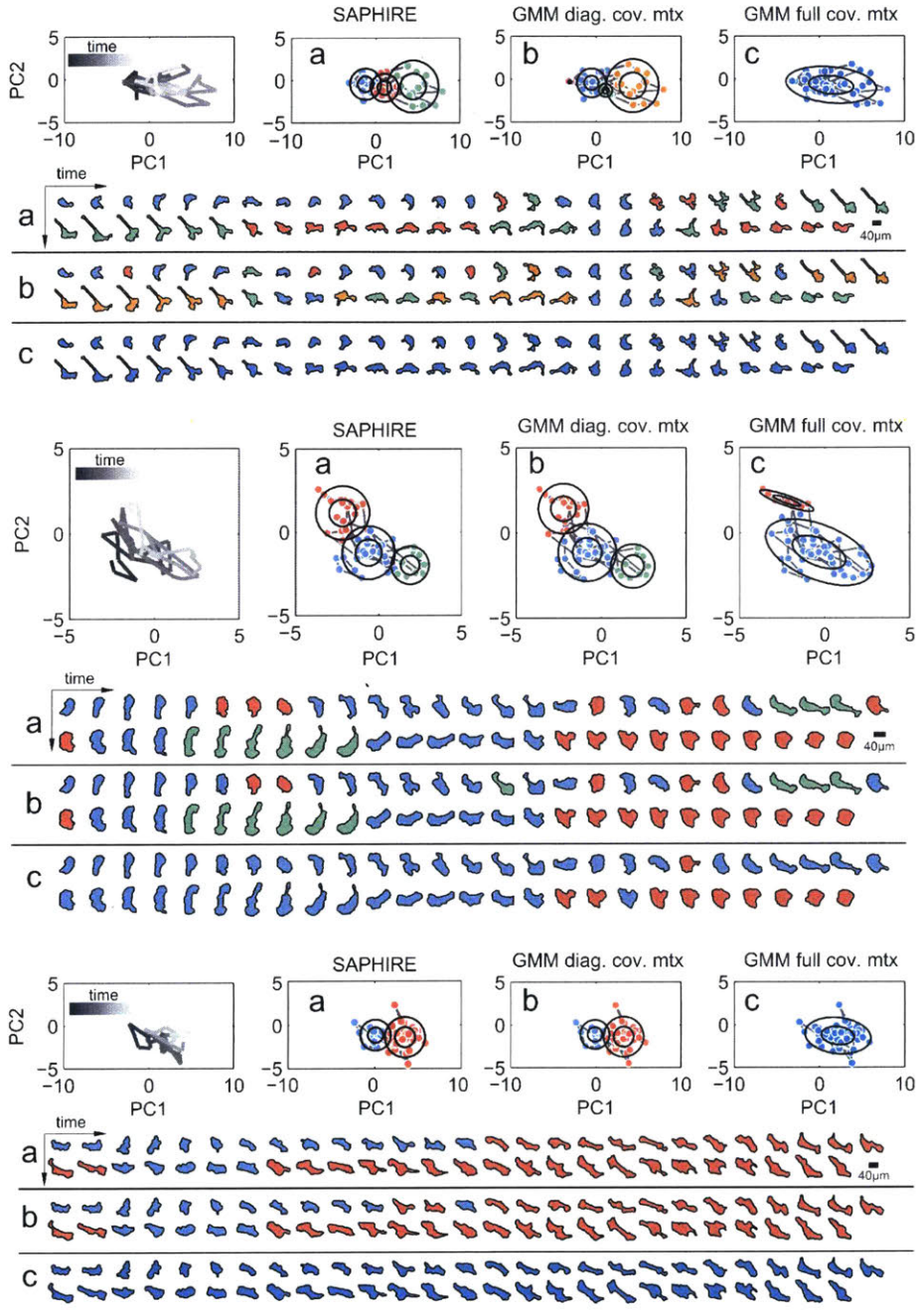
SAPHIRE
GMM diag. cov. mtx
GMM full cov. mtx
time
PC2
PC1
a
b
c
40μm

Figure 2-10: Gaussian mixture modeling (GMM) with full covariance matrix specification leads to state under-fitting and undesirable grouping of diverse morphologies into the same state. Three examples of individual cell shape trajectories from the expanded drug panel imaging experiment modelled with SAPHIRE to derive annotated underlying shape state sequences from PCA shape-space trajectories (a). The same cell shapes over time are classified into groups using GMM with a diagonal, equal-variance constraint for the covariance matrix (b) or full covariance matrix (c), with BIC used for the GMMs to find the most probable shape state model for each cell trajectory individually, independent of other cells. The full covariance matrix GMM lumps cell with heterogeneous morphologies (e.g., rounder, elongated, branched) into similar groups, showing that Gaussian states with diagonal, equal variances (circles as opposed to ellipses) better resolve and describe the underlying morphological states of MDA-MB-231 cells in shape-space.

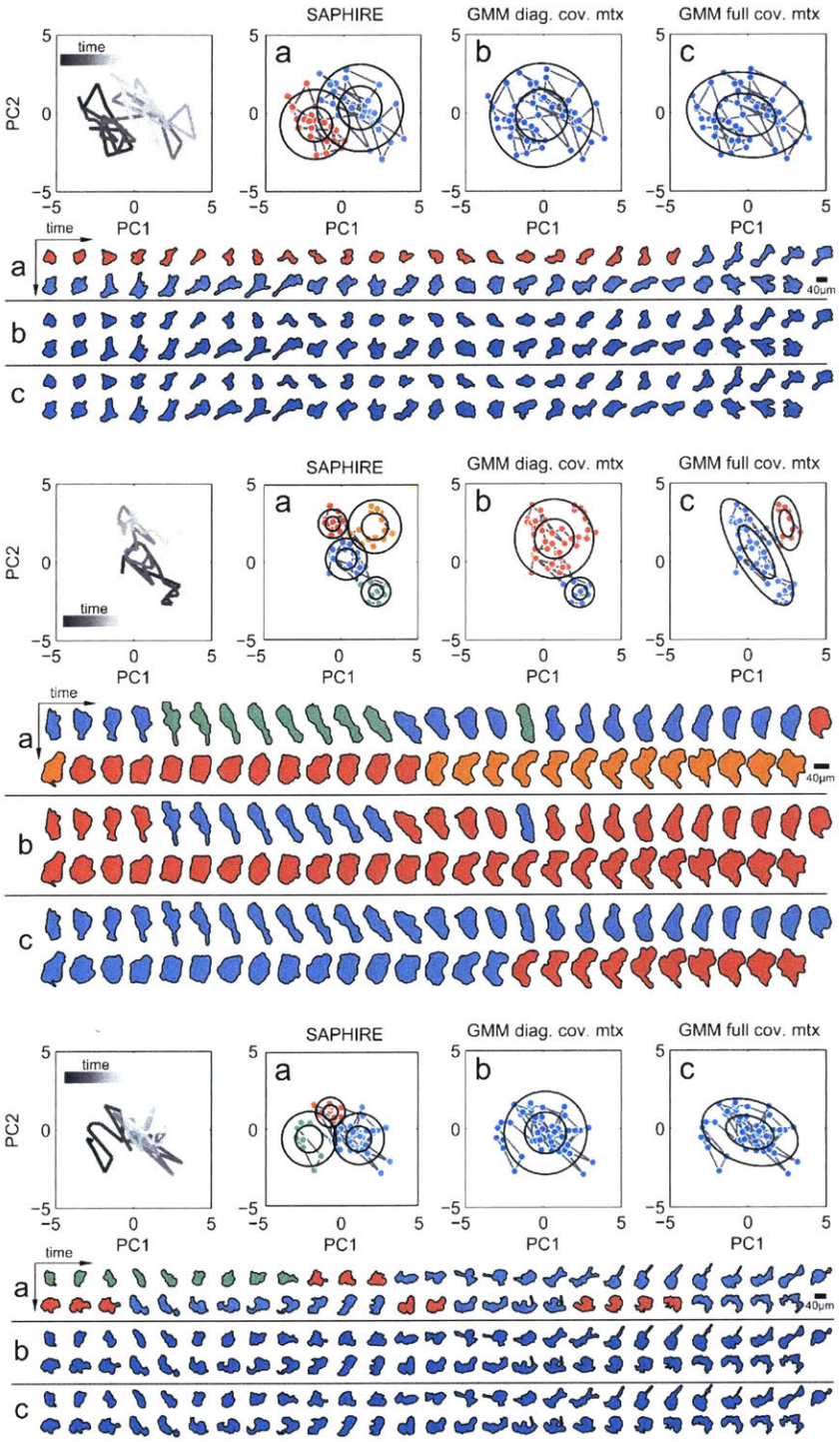
SAPHIRE
GMM diag. cov. mtx
GMM full cov. mtx
time
PC1
PC2
a
b
c
40μm

Figure 2-11: Probabilistic time series modeling using SAPHIRE better resolves cell shape states compared to GMM when cells progressively explore shape-space over time. Three PCA shape-space cell trajectories are shown, with annotation with the most likely shape state model and state sequence using SAPHIRE (a), and GMM using diagonal, equal-variance constraint on the covariance matrix (b) or full covariance matrix (c) using BIC to select the most likely model for the GMMs. The cells shown generally move through shape-space continuously in given directions over time (e.g., left to right for the first cell in the upper panel), with SAPHIRE able to capture these states and state transitions, whereas the GMM is unable to resolve them. This is consistent with numerical simulations (Fig. 2-9) showing that time series information taken into account by SAPHIRE, which is neglected by the GMM, is better able to resolve, model, and annotate the underlying temporal shape state behavior of individual cells. The inability to properly resolve and capture shape states by GMM leads to under-fitting of the number of states and improper grouping of morphologically dissimilar shapes into the same state.

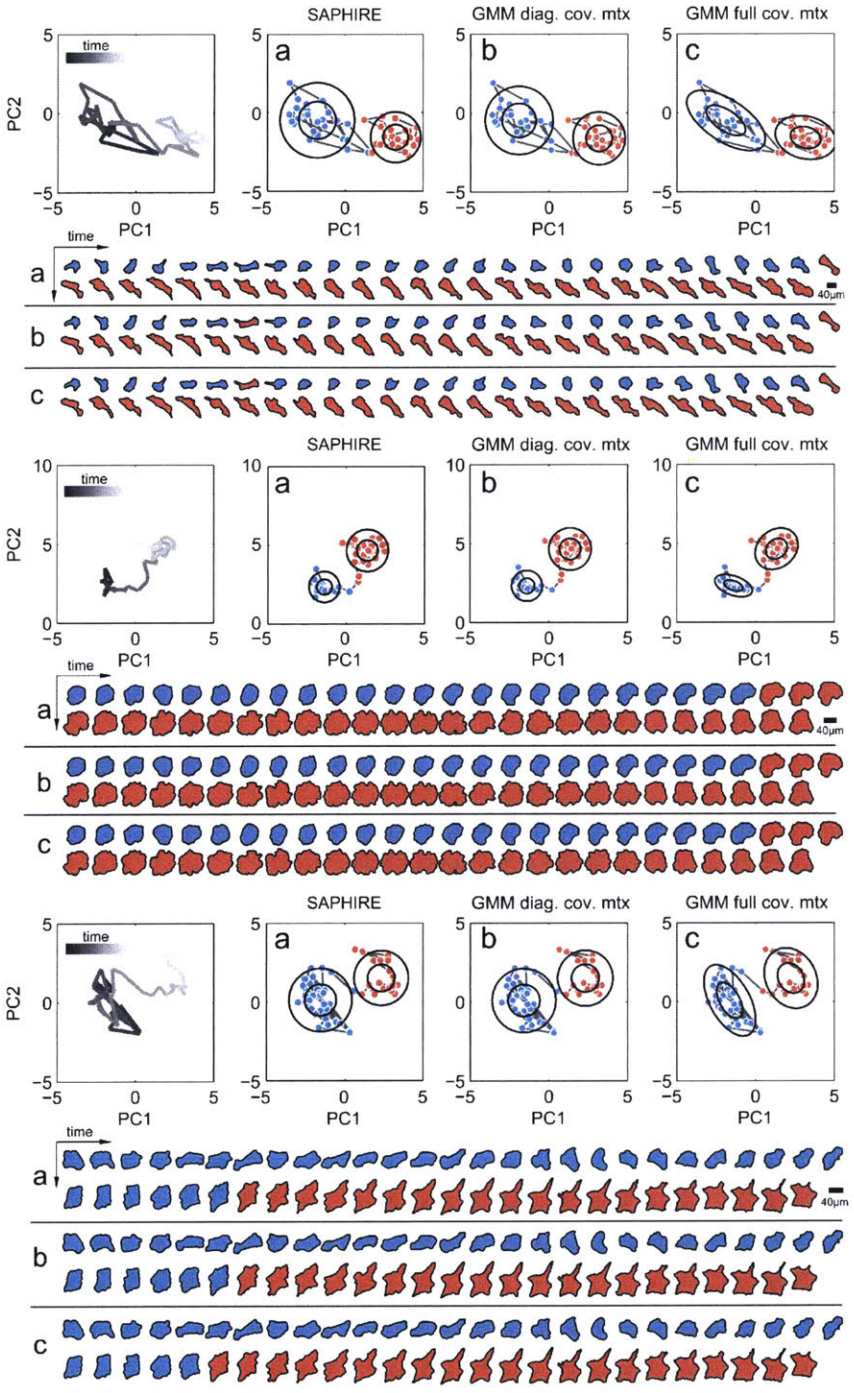
SAPHIRE
GMM diag. cov. mtx
GMM full cov. mtx
time
PC1
PC2
a
b
c
40μm

Figure 2-12: Examples of cells with similar SAPHIRE and GMM shape state annotations. Cell trajectories in shape-space were annotated with the most likely shape state model and state sequence using Bayesian HMM (a), and GMM using diagonal, equal-variance constraint on the covariance matrix (b) or full covariance matrix (c). For the GMMs, the BIC was used to select the most likely state model. When a cell moves progressively through shape-space over time and resides in well-separated shape-space regions (early time in black and later time in gray/white in left panels), Bayesian HMM and GMM categorize morphologies using the same number of states, with state transitions (blue to red) found to occur at similar points in time.

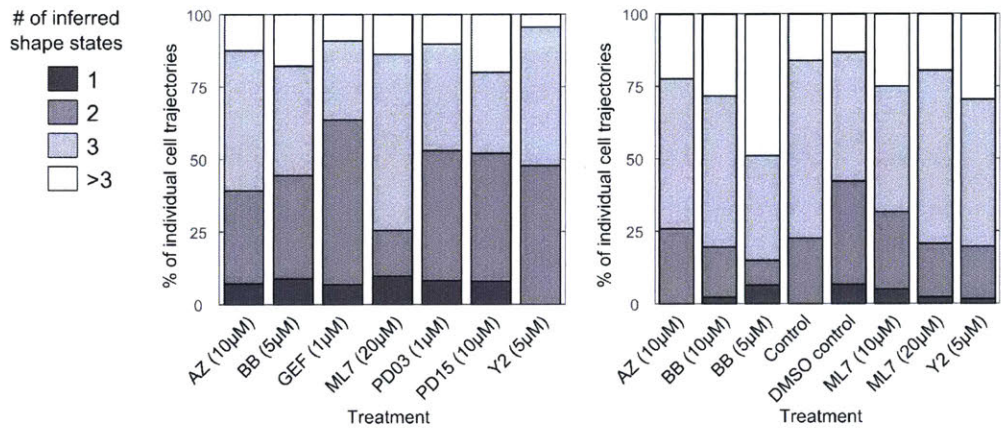

Figure 2-13: Effects of treatments on the number of morphological states explored by cells. Percentage of individual cells with given numbers of explored shape states as inferred from the probabilistic models across different treatment conditions for the two imaging experiments. Modeling was applied separately for each temporal shape-space trajectory to infer the *a priori* unknown number of hidden shape states explored by each cell.

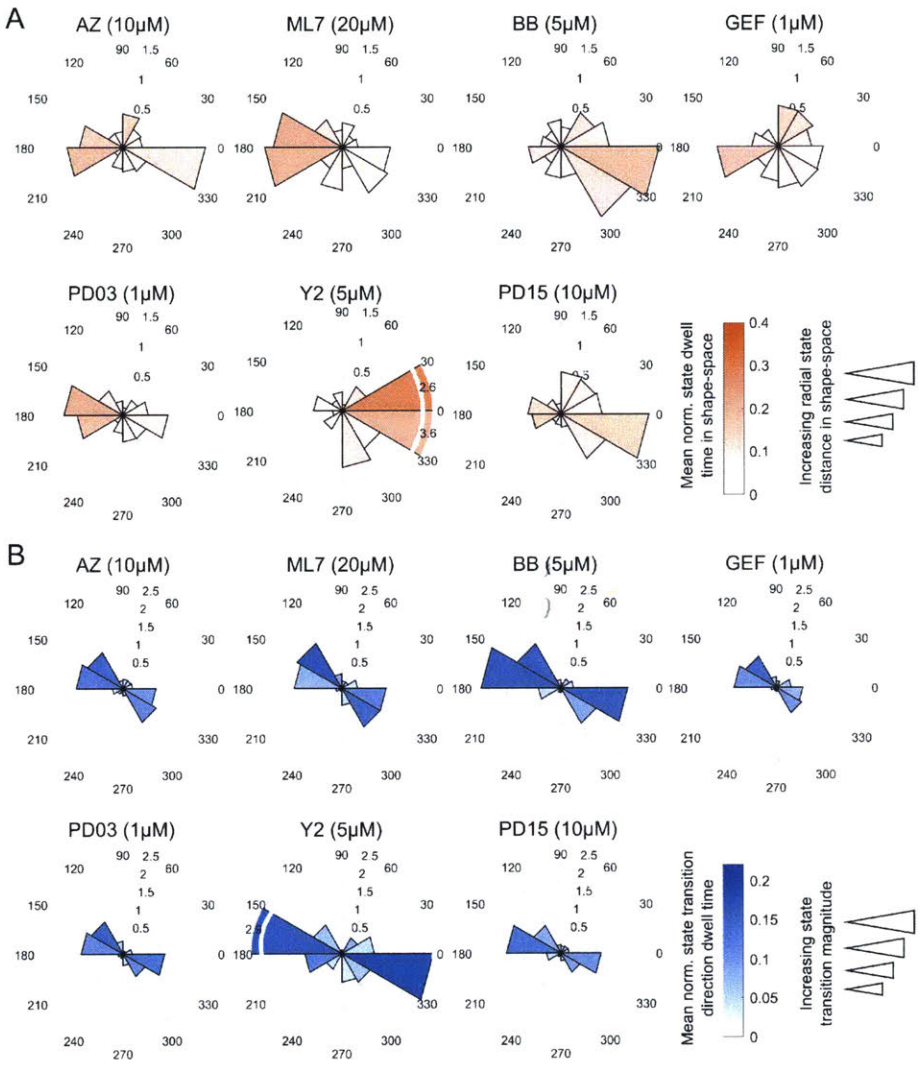

Figure 2-14: Phenotypic comparisons of an expanded panel of drugs that target actomyosin-regulatory proteins using model-annotated profiles of cell shape dynamics. (A) Effects of the expanded panel of drugs targeting various molecular species involved in regulating actomyosin dynamics on model-inferred cellular shape state locations in polar shape-space (as in Fig. 2-5B). (B) Effects of the expanded panel of drugs on cellular state transitions in shape-space (as in Fig. 2-5C).

Chapter 3

The checkpoint kinase-regulated phosphoproteome drives a cytoskeleton-associated adaptive response to doxorubicin chemotherapy

Contributions

This chapter comprises work derived from equal and joint contribution of the author and his collaborator Dr. Mun Kyung Hwang from the laboratory of Dr. Michael Yaffe at the Massachusetts Institute of Technology. Mun Kyung Hwang designed and conducted experiments, including phosphoproteomics and cell population-level assays. The author designed and conducted imaging experiments, performed bioinformatics analysis of mass spectrometry data, and processed and analyzed imaging data.

3.1 Abstract

Conventional cytotoxic chemotherapy activates a DNA damage response (DDR) that induces cell cycle arrest and apoptosis, but can also lead to drug resistance. To identify novel targets of the DDR, we performed a phosphoproteomic analysis for substrates of three DDR checkpoint kinases, MK2, Chk1, and Chk2, following treatment with doxorubicin, a cancer drug used in the clinic. Intriguingly, functional annotation analyses showed that a large number of checkpoint kinase phospho-substrates induced at 12 hours after doxorubicin treatment were cytoskeleton-associated proteins that modulate the structure and function of actomyosin and focal adhesions. Doxorubicin altered cancer cell morphology, migration, and focal adhesion organization, which were associated with prolonged cell survival and anoikis resistance. We demonstrate that checkpoint kinases can activate targets with diverse functions, which collectively link the DDR, cytoskeleton, and adhesome in an adaptive cellular response to chemotherapy to enhance drug tolerance, likely contributing to disease progression.

3.2 Introduction

Cytotoxic chemotherapy alters a variety of biological processes in normal and tumor cells through signal transduction pathways that mediate protein post-translational modifications [16]. The DNA damage response (DDR) constitutes one such signaling network that not only senses and responds to chromatin lesions, but also coordinates downstream responses including transcriptional activation, cell cycle arrest, recruitment of DNA repair machinery, and induction of apoptosis or senescence following genotoxic stress [120, 48, 216]. In response to DNA damage by chemotherapeutic drugs, cells activate three major checkpoint effector kinases: Chk1, Chk2, and MK2. These three kinases share a common core substrate phosphorylation motif [166], but appear to play distinct and separable roles in the DDR [215, 14]. Chk1 and Chk2 function primarily in the nucleus at early times after DNA damage to initiate cell cycle arrest, while MK2, in contrast, participates in the prolonged maintenance of cell cycle checkpoints by acting on substrates in the cytoplasm [214]. Chk1, Chk2, and MK2 are known to share a few common direct substrates such as the mitotic phosphatases Cdc25B and C (reviewed in ref. [129]).

In addition, Chk1 and MK2 bind to and/or phosphorylates different proteins that share related molecular functions including chromatin organization [21, 230], transcriptional control [21, 221] and RNA processing/stability [22, 213, 33]. For example, Chk1 phosphorylates RBM7, a targeting subunit of the RNA exosome, leading to the release of non-coding RNAs after DNA damage, while MK2 phosphorylates the RNA binding protein hnRNPA0, to stabilize p27Kip1 and Gadd45α mRNAs, resulting in sustained G1/S and G2/M arrest in p53-defective cells [214, 22, 33]. Despite these functional similarities and differences, only a limited number of downstream substrates of these important kinases are known [21, 22, 254, 299], particularly at later times after genotoxic stress. Clarifying the identities, differential regulation, and function of checkpoint kinase substrates on a global scale would provide a more comprehensive, mechanistic understanding of DDR pathways that determine cellular response to chemotherapy treatment.

We therefore set out to characterize the phospho-substrate landscape of three checkpoint kinases, Chk1, Chk2, and MK2, in cancer cells treated with doxorubicin, a DNA-damaging chemotherapeutic agent widely used in the clinic for treatment of cancer. We applied Stable Isotope Labeling with Amino acids in Cell culture (SILAC) quantitative phosphoproteomics using three metabolic labels [167], together with targeted enrichment for checkpoint kinase substrate motifs, in order to characterize this signaling/substrate landscape. We further assessed whether the differential regulation of specific phosphosites induced by doxorubicin is dependent on each checkpoint kinase by using inducible RNAi knockdowns of each kinase in the SILAC screen. Unexpectedly, we found that, in addition to canonical DDR processes such as DNA repair and chromatin modulation, the checkpoint kinase-regulated phosphoproteome is highly enriched in proteins that participate in cytoskeletal regulation, particularly actin and focal adhesion remodeling. We show that sub-lethal doses of doxorubicin alter cancer cell morphology, motility, and survival – three interdependent processes that constitute an adaptive response to chemotherapy regulated in part by checkpoint kinase signaling.

3.3 Results

3.3.1 Phosphoproteomic profiling elucidates the doxorubicin-induced checkpoint kinase effector signaling network

In response to DNA damage, the protein kinases Chk1, Chk2 and MK2 phosphorylate a variety of downstream effector molecules that control the subsequent cellular response, including cell cycle arrest, DNA repair, or cell death. To examine phosphorylation-dependent modification of the proteome of human U2OS osteosarcoma cells downstream of these effector kinases, we first profiled their kinetics of activation in response to doxorubicin-induced DNA damage. As shown in Fig. 3-8, both Chk1 and Chk2 were maximally activated within 30-60 min, and remained active for up to 12 hrs, albeit at lower levels. In contrast, in this experiment robust MK2 activation was not observed until 6 hrs with maximal activation at 12 hrs.

The 12 hr time point was selected for subsequent phosphoproteomic analyses to maximize the identification of MK2 substrates, while still maintaining some ability to identify Chk1 and Chk2 targets. U2OS cells were selectively SILAC labeled with medium or heavy isotopes of Lys and Arg at least five passages to fully convert all unlabeled Arg and Lys residues to isotope-labeled ones. After labeling, cells were treated with 5 μM doxorubicin for 12 hrs or with DMSO as a vehicle control using two biological replicates with a SILAC labeling swap (Fig. 3-1a). To enrich for substrates of these checkpoint effector kinases, we used a tandem pooled phospho-specific antibody enrichment approach based on the common Chk1/Chk2/MK2 substrate motif LxRxxpS/pT (where x is any amino acid)[166] for peptide immunoprecipitation (IP). To preserve motif sequences, samples were digested with LysC prior to IP and subsequently digested with trypsin, then separated by HPLC and analyzed by tandem mass spectrometry (MS/MS) (Fig. 3-1b). These replicate SILAC phosphoproteomic screens identified 413 and 962 unique phosphosites, respectively, together spanning 711 different proteins, with 280 phosphosites detected in both replicates, spanning 227 different proteins. The screen showed high reproducibility in phosphosite regulation after doxorubicin treatment across both biological replicates (Fig. 3-1c). Of the 280 phosphosites, 208 were upregulated and 31 were downregulated consistently in both replicates.

3.3.2 Doxorubicin induces a multifunctional phosphoproteome enriched in cytoskeleton-remodeling proteins

Phosphoproteins were ranked for doxorubicin-induced upregulation and tested for enrichment in gene ontology (GO) annotations using Gene Set Enrichment Analysis (GSEA) [245]. Because our ranked list of 711 proteins input into GSEA was much shorter than genome-wide lists typically used for analysis, we chose a less conservative false discovery rate (FDR) threshold to define enriched GO terms (Fig. 3-1d). A network visualization of the enriched GO terms (Fig. 3-1e) revealed a number of expected annotations for checkpoint kinase-mediated DDR pathways, including DNA repair, DNA/chromatin organization, cell cycle regulation, and RNA processing. Surprisingly, however, we also found numerous enriched GO terms relating to cytoskeletal organization, including proteins that localize to cell-extracellular matrix junctions such as focal adhesions and those that regulate microtubule dynamics (Fig. 3-1e (i), orange). Under the premise that phosphosites detected in both SILAC screen replicates are more likely to be true positives, we defined a set of high-confidence "hits" whose phosphorylation on Chk1/Chk2/MK2 consensus sites was up-

regulated following doxorubicin treatment (Fig. 3-1f). Singular enrichment analysis (SEA) was then performed on these proteins to identify GO term gene sets in which the "hits" were over-represented (Fig. 3-1g). As shown in Fig. 3-1h, in agreement with the GSEA results, SEA-enriched GO terms related largely to cytoskeleton regulation. Notably, "hit" proteins FLNA, DOCK7, and CLASP1, which are known regulators of actin and microtubule dynamics, occurred in the majority of enriched GO terms identified by SEA. Collectively, these findings suggest that substrates of these checkpoint kinases that remain phosphorylated 12 hrs following doxorubicin treatment participate in a variety of diverse biological processes, and are unexpectedly enriched in proteins that mediate cytoskeletal organization.

3.3.3 Doxorubicin treatment alters cell shape and F-actin organization

To directly assess whether doxorubicin treatment of U2OS cells induced alterations in the cytoskeleton, we used fluorophore-conjugated phalloidin to visualize the actin fiber network along with accompanying changes in cell morphology. Untreated cells contained a large number of pronounced F-actin stress fibers throughout the cell, while doxorubicin treatment resulted in stress fiber loss in central regions of the cell with retention of cortical actin bundles, producing noticeable changes in overall cell shape (Fig. 3-9a). Although our phosphoproteomic screen was performed in U2OS cells, a cell line typically used in studies of DNA damage signaling [117, 70, 2], the morphological phenotypes of these cells proved difficult to characterize on a larger scale, since these cells tend to grow in clusters, making detailed single-cell morphology analyses challenging. We therefore turned to the triple negative breast cancer cell line, MDA-MB-231, to further characterize changes in cell morphology induced by doxorubicin. This tumor tissue type is clinically treated with doxorubicin as a component of anti-cancer chemotherapy, and MDA-MB-231 cell line is widely used to study cytoskeleton-mediated processes such as cell migration [78]. As observed with U2OS cells, doxorubicin caused a loss of central stress fiber formation in the MDA-MB-231 cells, and a markedly elongated morphology after 24 hrs of treatment, particularly at lower doxorubicin doses (Fig. 3-2a). At high doses, the cells displayed a rounded up morphology and evidence of PARP cleavage, consistent with apoptosis (Fig. 3-2f, described below). To validate doxorubicin-induced changes in phosphorylation of checkpoint kinase substrates in U2OS cells identified in the SILAC screen, and to confirm similar signaling effects in MDA-MB-231 cells, we performed Western blotting on a subset of proteins with commercially-available, phospho-specific antibodies. The phosphorylation of FLNA, PEA15, YAP1, PPP1R12A, and HSP27, were affected similarly by doxorubicin treatment in both the U2OS and MDA-MB-231 cells. Importantly, the doxorubicin-dependent phosphorylation of these cytoskeletal proteins was easily observable after sub-lethal doses of doxorubicin at 0.5 μM and 5 μM in MDA-MB-231 and U2OS cells, respectively (Fig. 3-9b).

To quantify the observed cell shape changes, we performed a high-throughput automated analysis to characterize the effects of various doxorubicin doses on cell morphology on a large number of cells. As shown in Fig. 3-2b, c and d, doses of the drug below 5 μM shifted the cell populations toward a more elongated morphological phenotype, as captured by the major axis length of the cells. The distributions of cell elongation across doses were skewed right. There was no obvious presence of multiple modes (Fig. 3-2b), arguing against the binary activation an on/off switch that leads to elongation in a specific subpopulation of cells. Moreover, the increase in cell elongation induced by doxorubicin at multiple doses was irreversible upon drug washout up to 24 hrs (Fig. 3-10). Interestingly, although doxorubicin progressively inhibited cell proliferation in a dose- and time-dependent manner (Fig.

3-2e), the intermediate doses that promoted morphological elongation showed no noticeable PARP cleavage, an early marker of apoptosis, while a 5 μM dose did (Fig. 3-2f). Finally, we confirmed that the sub-lethal 0.5 μM dose of doxorubicin was sufficient to activate DDR at 24 hrs in MDA-MB-231 cells, as assessed by staining for the DNA damage marker γH2AX (S139) (Fig. 3-9c), indicating that the observed whole-cell elongation changes occur in the context of DDR signaling at sub-cytotoxic doxorubicin concentrations.

3.3.4 Alterations in cell phenotype and checkpoint kinase signaling are induced by other chemotherapeutic drugs and in other breast cancer cell lines

We next asked whether the observed morphological changes in MDA-MB-231 cells could be induced by other chemotherapeutic drugs. Like doxorubicin, the topoisomerase inhibitor camptothecin also increased cell elongation. In contrast paclitaxel, a microtubule stabilizing drug, led to a rounded cell morphology (Fig. 3-11a), consistent with its known mechanism of action with cell arrest in mitosis [125]. Etoposide and irinotecan had minimal effects on cell elongation at the doses tested (Fig. 3-11b). Consistent with these results, flow cytometric analysis of the cell cycle revealed that doxorubicin and camptothecin both arrested MDA-MB-231 cells predominantly in S phase, while paclitaxel treatment led to M phase arrest (Fig. 3-11c). In addition, doxorubicin and camptothecin both activated at least one checkpoint kinase among MK2 and Chk1, while paclitaxel, a microtubule poison, did not appreciably activate any of the checkpoint kinases (Fig. 3-11d). Collectively, the similarities in the morphologies, drug sensitivities, stage of cell cycle arrest, and checkpoint kinase signaling induced by doxorubicin and camptothecin further point to the broader potential role that the DDR may play in regulating cytoskeletal processes in response to sub-lethal doses of DNA damaging chemotherapy.

Furthermore, we assessed whether the morphologies of other breast cancer cell lines were also altered by sub-lethal doses of doxorubicin. In addition to MDA-MB-231 cells, other triple-negative breast cancer cell lines with a mesenchymal-like pattern of gene expression displayed a similar elongated phenotype after low-dose doxorubicin treatment, while MCF7 breast cancer cells, a luminal subtype with a more epithelial-like pattern of gene expression [40, 250], did not (Fig. 3-12a). Interestingly, the 0.5 μM dose of doxorubicin did not activate either MK2 or Chk1 in MCF7 cells, using phosphorylation as a surrogate readout for checkpoint kinase activation (Fig. 3-12b). Conversely, in cell lines that became more elongated, doxorubicin induced activation of at least one of the checkpoint kinases (Fig. 3-12b), further suggesting a link between chemotherapy-induced checkpoint kinase signaling and morphological changes across multiple cell lines.

3.3.5 Morphological changes induced by doxorubicin are coupled with changes in cell motility

Cell morphology and migratory behavior are functionally connected [182], particularly in mesenchymal cell types like MDA-MB-231, which migrate as single cells through successive stages of protrusion, adhesion, and retraction. To assess whether the observed doxorubicin-induced changes in cell shape also affected cell motility, we next used live-cell fluorescence microscopy to image MDA-MB-231 cells stably co-expressing LifeAct-eGFP and H2B-mCherry, as markers of cytoskeletal rearrangement and cell movement, respectively (Fig. 3-3a). Live-cell imaging confirmed that doxorubicin induced visually-discernible increases

in elongation in a large subset of cells over time, in agreement with our previous fixed-cell shape analyses (Fig. 3-3b, orange box). Importantly, this increase in elongation was associated with altered cell migration trajectories (Fig. 3-3b, blue box). Sub-lethal doses of doxorubicin, and in particular 0.5 μM treatment, caused increased cell elongation beginning at 12 hrs following drug addition, which appeared to be driven largely by impaired or delayed retraction of the trailing ends of migrating cells.

To quantitatively characterize the relationship between cell shape changes and migration response in a large number of cells, we measured a variety of commonly used morphological features and correlated them to three different motility metrics: distance, displacement, and persistence, for each cell. This analysis revealed that the net migratory displacement was highly correlated with persistence, a measure of how directionally efficient motility is for a given cell, while these two metrics were uncorrelated with total distance travelled (Fig. 3-3c, top three panels). Cells that attained more elongated morphologies (larger major axis lengths) travelled more persistently largely due to increased migratory displacement (Fig. 3-3c, bottom three panels). This relationship suggests that differences in cell elongation dynamics are coupled to cell migration directionality in this cell type. Interestingly, doxorubicin treatment increased morphological elongation (Fig. 3-3d (i)), slightly decreased migration distance (Fig. 3-3d (ii)), and increased total migratory displacement (Fig. 3-3d (iii)) of the cell population, on average, over time. These alterations resulted in pronounced induction of persistent cell movement under doxorubicin treatment, particularly at the 0.5 μM dose (Fig. 3-3d (iv)). These findings collectively demonstrate that doxorubicin treatment enhanced cell migration directionality, which is tightly linked to morphological elongation induced by the drug.

3.3.6 Cytoskeleton-associated phosphosites induced by doxorubicin are differentially regulated by the checkpoint kinases Chk1, Chk2, and MK2

To assess the dependence of doxorubicin-induced substrate phosphorylation detected in our SILAC screen on each of the DNA damage-activated checkpoint kinases, we performed additional SILAC phosphoproteomic experiments using the same substrate motif enrichment strategy and U2OS cell type as in Fig. 3-1, but with inducible shRNA-mediated knockdown of either MK2, Chk1, or Chk2. Because checkpoint kinases perform essential functions, and the murine homozygous Chk1 knockout in particular is embryonic lethal [151], we explicitly avoided stable knockdown or CRISPR knockout of the checkpoint kinases to limit adaptive re-wiring. Instead, we used a lentiviral vector containing a miR30-based short hairpin under the TRE promoter that tightly regulates target protein expression in a doxycycline-inducible manner (Fig. 3-4a). Four days of doxycycline treatment was sufficient to reduce checkpoint kinase expression in cells transduced with each kinase-specific hairpin, as assessed by Western blotting (Fig. 3-4a). This also confirmed that each checkpoint kinase-specific inducible knockdown minimally affected the activation of other checkpoint kinases and efficiently reduced on-target checkpoint kinase activation, as assessed by phosphorylation of MK2, Chk1, or Chk2 (Fig. 3-13). Cells were labeled with different SILAC isotopes, treated either with DMSO or doxorubicin for 12 hrs, and two LC-MS/MS runs were each performed twice, as technical replicates, with each run analyzing three treatment and knockdown conditions (Fig. 3-4b).

This analysis identified 473 unique phosphosites that were identified in both replicates of the two separate MS runs. Among these sites, 156 were at least 2-fold up- or down-

regulated, including classical DDR players, such as TP53BP1 (pS1317), MCM3 (pS160), and RAP80 (pS330), in addition to numerous other proteins not known to be involved in the DDR. As described in the legend to Fig. 3-4c, kinase-specific "hits" were identified as phosphosites that were both statistically significantly upregulated by doxorubicin and whose phosphorylation was dependent on a particular checkpoint kinase (boxed regions in Fig. 3-4c). MK2-regulated phosphosites had the largest number of "hits" (46, cyan circles), while Chk1- and Chk2-regulated sites (31 and 15, pink and brown circles, respectively) had fewer.

To assess the cellular processes in which the checkpoint kinase-regulated phosphosite "hits" participate, we built a kinase-substrate regulatory network for each of the three kinases (Fig. 3-4d). As expected from our previous analysis (Fig. 3-1), the majority of substrates in the network were cytoskeleton-associated proteins. We found that a number of phosphosites on TNS1, FLNA, AHNAK, PALLD, and MAP2, proteins known for their role in cytoskeletal organization, were dependent on all three checkpoint kinases and showed higher upregulation following doxorubicin treatment compared to other shared sites. Notably, a number of other well established cytoskeleton regulators, including ENAH, LMO7, and PPP1R12A (MYPT1), were dependent on Chk1 and MK2, but not on Chk2, signaling. Gene ontology analysis (GSEA) of these phosphoprotein substrates, ranked based on their checkpoint kinase dependence following doxorubicin treatment, revealed that the phosphoproteins specifically regulated by MK2, in comparison with Chk1 and Chk2 substrates, were significantly enriched in actin and cytoskeletal binding GO terms (Fig. 3-4e).

3.3.7 MK2 or Chk1 inhibition abrogates doxorubicin-induced changes in cell shape and migration

We next applied pharmacological and genetic perturbations to directly assess the contributions of MK2 and Chk1, respectively, to the morphological changes induced by doxorubicin in MDA-MB-231 cells. We used pharmacological inhibitors against both MK2 or its upstream activator p38MAPK, and confirmed their lack of effect on Chk1 kinase activity using IP kinase assays (Fig. 3-5a,b). Treatment with either the p38MAPK or MK2 inhibitor dramatically attenuated the increase in cell elongation induced by doxorubicin, as measured by changes in the cellular major axis length (Fig. 3-5c). We next used siRNA to block MK2 or Chk1, and confirmed the efficiency and specificity of the knockdowns in this cell type by immunoblotting (Fig. 3-5d). Similar to what was observed with the p38MAPK and MK2 small molecule inhibitors, knockdown of MK2 with siRNA resulted in a marked inhibition of doxorubicin-induced cell elongation (Fig. 3-5e). Although our inducible shRNA SILAC-based mass spectrometry screen for Chk1 substrates did not show a statistically significant enrichment of cytoskeletal-containing GO terms by GSEA-based phosphosite ranking, Chk1 was nonetheless activated under chemotherapy treatment conditions that produced a morphologically elongated cell phenotype, (Figs. 3-11d and 3-12b) and Chk1 phosphorylated numerous cytoskeletal proteins that overlapped with those phosphorylated by MK2 (Fig. 3-4d). We therefore also tested the effect of Chk1 depletion on doxorubicin-induced change in cell morphology. As shown in Fig. 3-5f, knockdown of Chk1 with siRNA markedly diminished the increase in cell elongation induced by doxorubicin, as measured by changes in the cell major axis length, similar to the effects seen upon MK2 depletion.

We also assessed whether MK2 or Chk1 were involved in doxorubicin-induced changes in cell migration, given their effects on cell morphology. Live-cell imaging and cell tracking in the presence or absence of MK2 or Chk1 siRNA knockdown revealed that the enhanced

migratory displacement and persistence seen following doxorubicin treatment in wild-type cells, was reduced in the MK2- or Chk1-depleted cells (Fig. 3-5g-i). Taken together with the kinase-specific phosphoproteomics data above (Fig. 3-4d), these assays confirm an important role for MK2 and Chk1 kinases in regulating cytoskeletal processes following doxorubicin treatment, which contributes to changes in both cell morphology and motility induced by sub-lethal concentrations of this DNA-damaging agent.

3.3.8 Doxorubicin alters adhesome organization and signaling, and enhances anoikis resistance

Changes in cell morphology and migration are highly dependent on interactions between the actin cytoskeleton and the extracellular matrix, mediated largely through focal adhesions (FAs) [287, 227, 36]. Rapid assembly of FAs occurs at the leading edge of migrating cells, with concomitant disassembly at the lagging edge. Since doxorubicin treatment induced trailing-end retraction defects in migrating cells, and GO terms related to cell-substrate interactions were highly enriched in our phosphoproteomic screen (Fig. 3-1e (i)), we next asked whether the structure and dynamics of FAs was altered by chemotherapy. Immunofluorescence staining of phospho-FAK (Y397), a key component and regulator of focal adhesion signaling and organization, revealed that doxorubicin-treated cells had larger, more elongated FAs around the cell periphery than did control DMSO-treated cells, which instead showed a larger number of smaller FAs (Fig. 3-6a). Quantification of the images confirmed that doxorubicin treatment significantly increased the total focal adhesion area per cell (Fig. 3-6b). The presence of fewer but larger FAs, in combination with the elongated shape of the cells with adherent trailing ends suggested that sub-lethal doxorubicin exposure might lead to impaired FA turnover [188]. FA disassembly was therefore directly examined using the nocodazole washout method [66, 72]. This assay is based on the finding that nocodazole-induced microtubule depolymerization results in stabilization of FAs by a variety of mechanisms, such as GEF-H1 release/RhoA activation to enhance FA assembly [72], and/or loss of kinesin-1 mediated transport of FA disassembly factors along microtubules [188], among others. Following nocodazole washout, rapid microtubule regrowth and synchronous FA disassembly allows cellular recovery to the pre-nocodazole-treated state. As shown in Fig. 3-6c and d, FA disassembly in DMSO-treated control cells was nearly complete by 15 min of nocodazole washout (top row). In contrast, during this same washout period there was little FA disassembly in the doxorubicin-treated cells (bottom row). These findings are consistent with reduced FA disassembly after doxorubicin exposure, contributing to the observed increase in focal adhesion area, the increased cell elongation, and the enhanced migratory persistence.

To further explore connections between doxorubicin-induced checkpoint kinase-regulated phosphoproteins identified in our SILAC screen and those induced upon cell-matrix adhesion, we compared our list of phosphosites to a published list of adhesosome proteins whose phosphorylation was induced upon cell attachment to fibronectin [220]. Remarkably, many proteins and phosphosites were shared between the two lists, including the actin-binding protein filamin A (FLNA) and the regulatory/targeting subunit of myosin phosphatase PPP1R12A (MYPT1), which were highly upregulated by doxorubicin in a checkpoint kinase-dependent manner (Fig. 3-4d), and for which phospho-specific antibodies were available (Fig. 3-9f). As shown in Fig. 3-6f, modestly increased levels of these phosphorylated proteins were detectable up to 48 hrs after a brief 4 hr doxorubicin pulse, and intriguingly, this phosphorylation was even maintained when the cells were then re-plated

on poly-HEMA (P.H.)-coated plates, conditions in which matrix attachment is blocked. These findings suggest that in addition to affecting adhesion number and size, doxorubicin treatment results in the sustained phosphorylation of multiple adhesome components even upon loss of active cell attachment to the surrounding ECM.

Focal adhesions not only function as physical linkers of a cell to the extra-cellular matrix (ECM), but also contribute to cell survival [90]. FA signaling plays a particularly important role in resistance to anoikis, a mechanism of apoptotic cell death induced upon loss of ECM adhesion [5]. Consistent with the observed increase in phosphorylation of adhesome proteins after low dose doxorubicin treatment, cells treated with 0.5 μM doxorubicin for 4 hrs showed increased survival when plated on P.H.-coated non-adherent tissue culture plates (Fig. 3-6g). Collectively, these findings demonstrate that doxorubicin-induced phosphorylation of molecular components of the adhesome by DNA damage-activated checkpoint kinases enhances adhesion signaling and may enhance ECM-independent cell survival.

3.3.9 Morphological elongation induced by doxorubicin is associated with prolonged cell survival following higher dose exposure

The finding that a sub-lethal dose of doxorubicin treatment enhanced cell viability in the absence of cell adhesion (Fig. 3-6g), led us to ask whether the alterations in cell elongation (Figs. 3-2 and 3-3), focal adhesion turnover, and adhesome signaling (Fig. 3-6a,b) were correlated with increased resistance to doxorubicin when the cells were grown on a highly adherent substrate (tissue culture plastic coated with Collagen I and Matrigel). To quantify the relationship between doxorubicin-induced cell elongation and the subsequent induction of cell death, we tracked individual MDA-MB-231-LifeAct/H2B-expressing cells over 3 days in the presence of a fluorescent apoptosis reporter, AnnexinV-AlexaFluor647, after a prolonged 24 hr treatment with 1 μM doxorubicin (Fig. 3-6h). Using the morphologies of untreated cells (DMSO control) as baseline, a threshold was established (see A.2) to identify cells that became elongated during the 1 μM doxorubicin treatment, and those that did not (Fig. 3-6i). As shown in the bottom panel of Fig. 3-6j, cells that did not become elongated within the first 24 hrs died over a wide range of times following drug treatment, with a median time to death of 43 hrs. Remarkably, cells that became elongated within the first 24 hrs of drug treatment died at later times, with a median time to death of 49 hrs, and a distribution of cell death kinetics that was markedly skewed left (Fig. 3-6j, top panel).

3.3.10 Doxorubicin pre-treatment with a sub-lethal dose confers enhanced cell elongation and long-term drug tolerance to secondary treatment

To evaluate whether the observed doxorubicin-induced changes in cell shape, adhesion-related signaling, and delayed cell death conferred a long-term survival advantage in response to subsequent drug exposure, we performed a two-stage doxorubicin treatment protocol with a prolonged period of drug washout and recovery in between treatments (Fig. 3-7a,b). Sub-confluent MDA-MB-231 cells were pre-treated with 0.5 μM doxorubicin or DMSO for 24 hrs. Drug or vehicle was then washed out, and the cells allowed to recover by culturing them in serum-containing growth media without drug for a month. Many of the pre-treated cells died over the first 2 weeks, but a subpopulation survived, and began to proliferate after 3 weeks in culture. By one month in culture the growth rate of these sur-

viving doxorubicin-pre-treated cells was comparable to the growth rate of control cells that had not been pre-treated with the drug (Fig. 3-7b and c, treatments (iii) and (i), respectively). Furthermore, both the doxorubicin-pre-treated and control cells after one month in culture had similar morphologies at baseline (Fig. 3-7d). The cells were then secondarily treated with DMSO or with increasing doses of doxorubicin (0.5-5 μM), and assayed for survival 48 hrs later. As shown in Fig. 3-7e, the population of pre-treated cells consistently demonstrated increased tolerance to a secondary doxorubicin treatment compared to the population of non-pre-treated cells (Fig. 3-7b, treatments (iv) and (ii), respectively), but had no survival advantage after treatment with the microtubule-targeting drug docetaxel.

To explore the dynamics of response at the single-cell level, cells were transduced to co-express H2B-mCherry and LifeAct-eGFP, and analyzed for changes in proliferation and cell shape by fluorescence microscopy over the ensuing 48 hrs in response to an intermediate (1 μM) dose of doxorubicin (Fig. 3-7a). The media was supplemented with fluorophore-conjugated AnnexinV, allowing concurrent live cell imaging-based measurements of apoptosis. These single-cell measurements confirmed that both the pre-treated and non-pre-treated cells showed similar proliferation rates at baseline (DMSO treatment) (Fig. 3-7f, treatment conditions (iii) and (i), respectively), consistent with the previous population based measurements (Fig. 3-7c). Both the pre-treated and control cells ceased to proliferate after secondary treatment with 1 μM doxorubicin (Fig. 3-7f, treatment conditions (iv) and (ii), respectively), and a subset of both types of cells became elongated following doxorubicin treatment, producing similar morphologies in the pre-treated and control cell populations (Fig. 3-7g). Importantly, cells that were pre-treated with the drug one month earlier showed a significantly increased percentage of cells that subsequently became elongated in response to secondary treatment, compared to the control DMSO pre-treated cells (Fig. 3-7h).

In addition to the increased percentage of cells that became elongated, the cells that had been pre-treated with 0.5 μM doxorubicin showed a significant reduction in the kinetics of apoptotic cell death, as evaluated by live-cell AnnexinV staining as a function of time, compared to cells that had not been pre-treated, despite the one month period of time that had elapsed between treatments (Fig. 3-7i). In agreement with the population level measurements (Fig. 3-7e), the single-cell assay verified that the pre-treated cells contained a larger total fraction of non-apoptotic (AnnexinV-negative) cells at 48 hrs after the secondary doxorubicin treatment (Fig. 3-7j). Finally, to determine whether the observed increased tolerance to doxorubicin was directly connected to the drug-induced elongation phenotype, the population of individually tracked cells was grouped into those that died or survived within the 48 hrs. As shown in Fig. 3-7k and l, cells that survived for 48 hrs were the ones that became elongated. Taken together, these data suggest that changes in doxorubicin-induced cytoskeletal and focal adhesion signaling (Fig. 3-6) underlie a morphological response that is associated with drug tolerance.

3.4 Discussion

Here we presented a quantitative phosphoproteomics study to profile DNA damage-induced checkpoint kinase substrates in cells treated with a chemotherapeutic agent, doxorubicin. We demonstrated that DNA damage checkpoint kinase signaling regulates cytoskeletal organization and remodeling. Fluorescence imaging and other phenotypic assays showed that these signaling changes induced by sub-lethal chemotherapy are associated with altered cellular morphology, migration, focal adhesion organization, and chemo-tolerance (Fig. 3-7m).

Previous large scale phosphoproteomic and smaller detailed mechanistic studies have shown that, in addition to their role in regulating cell cycle progression, DNA repair, and apoptosis, DDR-activated kinase signaling pathways also control other cellular processes, including chromatin structure and transcriptional regulation through RNA binding proteins [16, 196, 168]. In agreement with these studies, our phosphoproteomics screen revealed that checkpoint kinase-regulated substrates were highly enriched in RNA-related GO terms that included, among others, "RNA binding" (Fig. 3-1e (ii)) and "Transcriptional regulation by RNA polymerase II" (Fig. 3-1e (iii)). More unexpectedly, however, our screen also revealed that doxorubicin chemotherapy alters adhesion- and actomyosin cytoskeleton-associated pathways through checkpoint kinase signaling (Fig. 3-1e (i), (iii) and Fig. 3-4d,e).

Regulation of the cytoskeleton requires the spatio-temporal control of many structural and signaling proteins. Therefore, multiple checkpoint kinases and their substrates (Fig. 3-4d) may collectively coordinate the morphological and migratory properties of doxorubicin-treated cells (Fig. 3-5). Although doxorubicin-induced topoisomerase II inhibition, mitochondrial dysfunction, and reactive oxygen species production are well documented (reviewed in ref. [28]), previous studies have shown that doxorubicin can also alter actomyosin and myofibril organization in cardiac cells in a kinase signaling-dependent manner [247, 226]. Shi and coworkers demonstrated that doxorubicin alters focal adhesion organization and stress fiber formation in part through ROCK1 in mouse embryonic fibroblasts, illustrating that chemotherapy can influence cytoskeletal structure through the actomyosin-regulatory machinery [246, 234]. In the current work, we found that doxorubicin altered the phosphorylation of many adhesion- and actomyosin-associated protein substrates of checkpoint kinases in cancer cells (Fig. 3-1h and 3-4d, Fig. 3-9b), including FLNA, a cytoskeleton-membrane linker involved in actomyosin-mediated adhesion maturation; PPP1R12A, a myosin phosphatase subunit regulated by RhoA/ROCK that participates in actomyosin contractility-driven adhesion remodeling; and TNS1, a substrate of calpain-II proteinase localized in focal adhesions that crosslinks actin filaments. In particular, we speculate that altered phosphorylation of adhesion-associated proteins could affect their proteolytic cleavage by calpain-II [37, 38, 35] or their endocytic recycling [reviewed in ref. [185]], resulting in impaired cellular de-adhesion and trailing-end retraction, a defining phenotype of doxorubicin-treated cells that was observed. Although we do not explore these or other potential mechanisms here, our phosphoproteomics screen provides a resource that lays the groundwork for future follow-up studies to determine the contributions of individual phosphoprotein species to the cytoskeletal changes mediated by DDR signaling.

Furthermore, although selective pressure from doxorubicin treatment can promote the outgrowth of invasive or resistant subpopulations of cells [93, 264, 259, 1, 31], our phosphoproteomics data suggest an alternate mechanism – DNA damage-induced cytoskeletal signaling could generate a pro-invasive cell phenotype in the absence of selection. For instance, doxorubicin has been reported to induce migration and block apoptosis of MDA-MB-231 cells through p38/NF-κB-dependent signaling [193]. Other drugs, such as the microtubule-targeting chemotherapeutics paclitaxel and vincristine, have also been shown to enhance cell motility, invasiveness, and metastasis through altered signaling [208, 276, 63]. In the case of doxorubicin within our system, we speculate that delayed trailing-end retraction both reduced focal adhesion disassembly (Fig. 3-6c,d), and resulted in larger focal adhesions (Fig. 3-6a,b and Fig. 3-14). These phenomena likely contribute collectively to the morphological elongation and migratory persistence induced by the drug (Fig. 3-3b,d). Indeed, average cell elongation and migratory persistence were positively correlated (Fig. 3-3c), in agreement with the established notion that focal adhesion disassembly is a criti-

cal step in the motility cycle of migratory cells [145]. Consequently, doxorubicin-induced adhesome signaling could alter focal adhesion dynamics that results in cell elongation and a directionally-persistent migratory phenotype, which could provide for more productive cancer cell motility and enhanced metastatic potential. Moreover, changes in cell morphology and motility are also a defining feature of an epithelial-to-mesenchymal transition (EMT) that confers pro-invasive characteristics [292, 293]. Previous studies have reported a link between chemotherapy treatment and induction of transcription factors associated with EMT. For example, doxorubicin can promote EMT through the induction of Twist-1 [149], while sub-lethal doses of cisplatin can induce Snail [68]. It would be interesting to investigate in follow-up studies whether induction of EMT-related markers is associated with DDR-regulated cytoskeletal and adhesome signaling in response to chemotherapy.

Interestingly, we also found that the morphological changes induced by sub-lethal doxorubicin were associated with enhanced chemo-tolerance (Fig. 3-6h-j and Fig. 3-7e,g-l), which could constitute an adaptation to therapy through a variety of possible mechanisms. For instance, breast cancer cells can adopt a transient and reversible $CD24^{high}/CD44^{high}$ state that confers adaptive resistance to chemotherapy, which is different from a $CD24^{low}/CD44^{high}$ state typically associated with EMT [95]. Alternatively, cells can also transition from a proliferative state to an invasive state that alters drug sensitivity [130]. For example, it has been shown that proliferative melanomas are sensitive to B-Raf inhibitors, while non-proliferative melanomas become resistant and more invasive [111]. Recent work has demonstrated that the transition from a proliferative to an invasive state requires cell cycle arrest [170]. As a result, doxorubicin-treated cells in our system may also have undergone such a transition, since sub-lethal doses of the drug induced cell cycle arrest (Fig. 3-11c) that blocked proliferation (Fig. 3-2e), while promoting cytoskeletal reorganization (Fig. 3-2a-d), persistent migration (Fig. 3-3d), and drug tolerance (Fig. 3-6h-j and 3-7e,g-l). Finally, cells in non-proliferating tumors can also exist in quiescent or dormant states that have been linked to therapy resistance [62] and metastatic burst [194]. For example, activation of p38MAPK, an upstream regulator of the checkpoint kinase MK2 that we studied here, has been shown to enhance survival of dormant tumor cells under therapy- or microenvironment-induced stress [256, 212]. Whether sub-lethal doses of chemotherapy induce tumor dormancy through the p38MAPK/MK2 signaling axis in our system is not known, but is of interest to investigate in future studies.

One of our most intriguing findings was that sub-lethal doses of doxorubicin enhanced cell survival under no-adhesion conditions, which may constitute an escape from anoikis (Fig. 3-6g). Cells treated with doxorubicin maintained higher levels of phosphorylation of adhesion-associated proteins like FLNA and PPP1R12A under no-adhesion conditions (Fig. 3-6f). This suggests that doxorubicin-induced DDR signaling may activate cellular functions typically mediated by focal adhesion signaling, but in the absence of extracellular matrix-regulated signal transduction or cell-substrate interactions. Functionally, proteins such as FAK that regulate focal adhesion-mediated signaling can promote cell survival and chemotherapy resistance [252, 29, 79]. Since anoikis is initiated by loss of cellular engagement with the extracellular matrix, as would be the case for disseminating cancer cells in the bloodstream, DNA damage-induced activation of adhesome signaling under such conditions could support cancer cell viability and confer anoikis resistance during metastasis.

Taken together, our findings suggest that the checkpoint kinase-regulated phosphoproteome activated by DNA damage in the context of sub-maximal tumor killing can alter cytoskeletal organization and migratory behavior, as well as enhance cancer cell survival that could influence the course of residual disease. The capacity of doxorubicin-treated

cells to attain elongated morphologies and better tolerate secondary treatment appears to be retained even weeks after primary drug exposure (Fig. 3-7e-l). This phenomenon could constitute an adaptive cellular response to chemotherapy that may adversely affect therapeutic efficacy and exacerbate disease progression in clinical regimens involving multiple rounds of treatment.

3.5 Acknowledgements

This work was funded by grants from the Charles and Marjorie Holloway Foundation, the Ovarian Cancer Research Foundation, and the STARR Cancer Consortium to Prof. Michael Yaffe (M.B.Y.), NIH grants R01-ES015339 and R01-GM104047 to M.B.Y., and R01-GM069668 to Profs. Douglas Lauffenburger and Alan Wells. Dr. Mun Kyung Hwang was supported by a Ludwig Postdoctoral Fellowship. Simon Gordonov was partially supported by a Whitaker Health Sciences Fund Fellowship. We acknowledge the Koch Institute Swanson Biotechnology Center, specifically the Microscopy and Flow Cytometry core facilities, for technical support. Amanda M. Del Rosario from the Koch Institute contributed to peptide identification and phosphosite assignment of the phosphoproteomics data. Albrecht Moritz and Sean A. Beausoleil (Cell Signaling Technology) assisted with mass spectrometry experiments and data analysis. Frank Gertler (MIT), Johanna Ivaska (Turku Centre for Biotechnology), and Ian Cannell (Koch Institute) are acknowledged for useful discussions and review of this work.

3.6 Figures

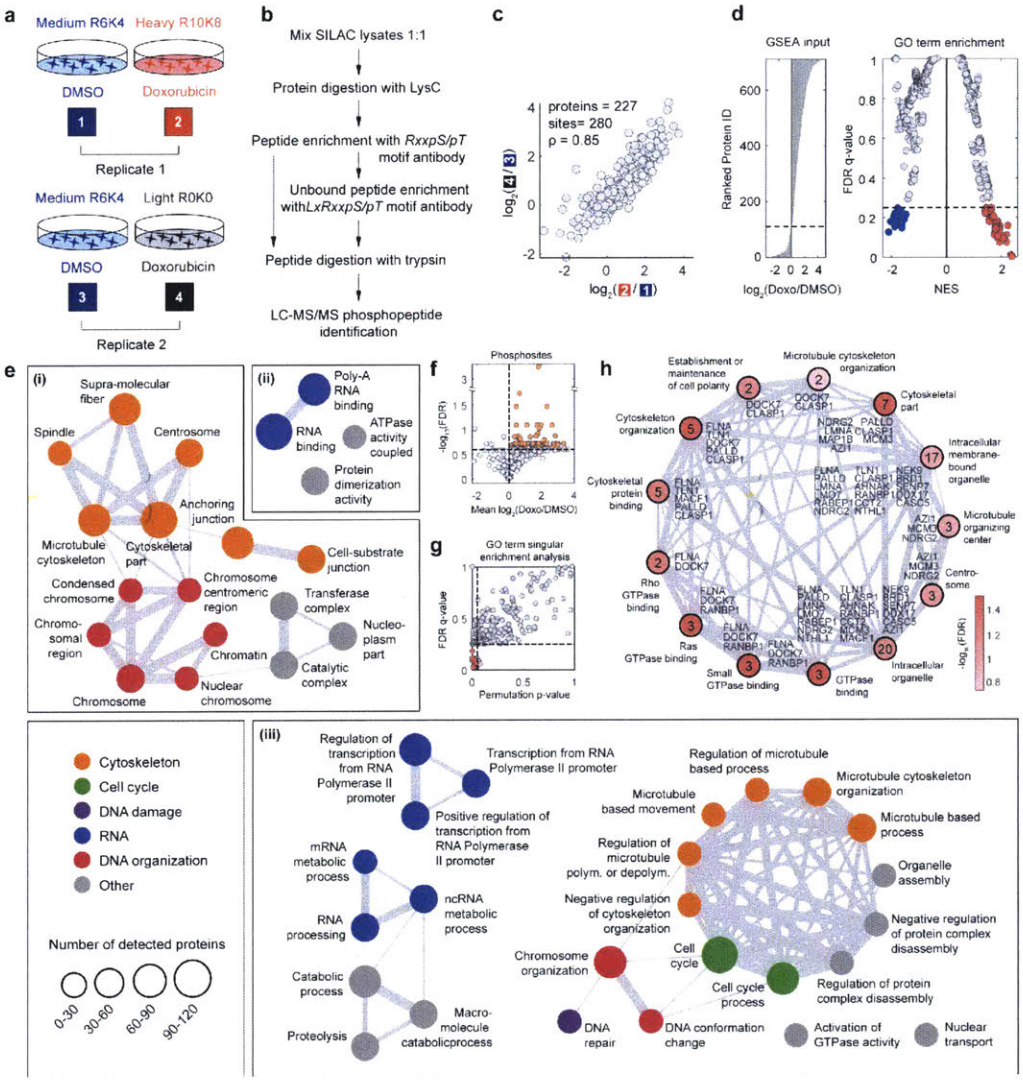
a
Medium R6K4
Heavy R10K8
DMSO
Doxorubicin
1
2
Replicate 1
Medium R6K4
Light R0K0
DMSO
Doxorubicin
3
4
Replicate 2
b
Mix SILAC lysates 1:1
Protein digestion with LysC
Peptide enrichment with RxxpS/pT motif antibody
Unbound peptide enrichment withLxRxxpS/pT motif antibody
Peptide digestion with trypsin
LC-MS/MS phosphopeptide identification
c
proteins = 227
sites= 280
p = 0.85
log2(2/3)
log2(2/1)
d
GSEA input
GO term enrichment
Ranked Protein ID
log2(Doxo/DMSO)
FDR q-value
NES
e
(i)
Supra-molecular fiber
Spindle
Centrosome
Anchoring junction
Microtubule cytoskeleton
Cytoskeletal part
Cell-substrate junction
Condensed chromosome
Chromosome centromeric region
Chromo-somal region
Chromatin
Nucleo-plasm part
Transferase complex
Catalytic complex
Nuclear chromosome
Chromosome
(ii)
Poly-A RNA binding
RNA binding
ATPase activity coupled
Protein dimerization activity
f
Phosphosites
-log2(FDR)
Mean log2(Doxo/DMSO)
g
GO term singular enrichment analysis
FDR q-value
Permutation p-value
h
Establishment or maintenance of cell polarity
Microtubule cytoskeleton organization
Cytoskeleton organization
Cytoskeletal part
Cytoskeletal protein binding
Intracellular membrane-bound organelle
Microtubule organizing center
Rho GTPase binding
Centro-some
Ras GTPase binding
Small GTPase binding
GTPase binding
Intracellular organelle
-log2(FDR)
Cytoskeleton
Cell cycle
DNA damage
RNA
DNA organization
Other
Number of detected proteins
0-30
30-60
60-90
90-120
(iii)
Regulation of transcription from RNA Polymerase II promoter
Transcription from RNA Polymerase II promoter
Positive regulation of transcription from RNA Polymerase II promoter
mRNA metabolic process
RNA processing
ncRNA metabolic process
Catabolic process
Proteolysis
Macro-molecule catabolicprocess
Regulation of microtubule based process
Microtubule cytoskeleton organization
Microtubule based movement
Microtubule based process
Regulation of microtubule polym. or depolym.
Organelle assembly
Negative regulation of cytoskeleton organization
Negative regulation of protein complex disassembly
Chromosome organization
Cell cycle
Cell cycle process
Regulation of protein complex disassembly
DNA repair
DNA conformation change
Activation of GTPase activity
Nuclear transport

Figure 3-1: Cytoskeleton-associated proteins predominantly define the checkpoint kinase-mediated phosphosignaling response to doxorubicin. **(a)** Schematic of the mass spectrometry SILAC labeling strategy to profile doxorubicin effects on the phosphoproteome. **(b)** Experimental workflow of the phosphoproteomic screen focused on substrates with checkpoint kinase target motifs. **(c)** Scatterplot showing doxorubicin effects on 280 phosphosites spanning 227 proteins from two biological replicates (ρ, Pearson correlation). **(d)** Left, list of 711 proteins detected in at least one replicate ranked by doxorubicin-induced upregulation used for gene set enrichment analysis (GSEA). Right, scatterplot of gene ontology (GO) terms (data points) showing GSEA normalized enrichment scores (NES) and their corresponding false discovery rate (FDR) q-values. GO terms deemed significantly enriched in doxorubicin-induced proteins (FDR < 0.25) with positive and negative NES are colored red and blue, respectively. **(e)** Network maps of significant GO terms identified in (d) showing enrichment (node size), categorical annotation (node color), and gene set overlap (edge thickness) in cellular components **(i)**, molecular functions **(ii)**, and biological processes **(iii)**, of phosphoproteins upregulated by doxorubicin. Network edges with gene set overlap coefficients > 0.4 are shown. **(f)** Volcano plot of the 280 phosphosites common to both replicates in (c) used to identify 83 "hits" spanning 68 proteins (colored orange). "Hits" are phosphosites upregulated by doxorubicin (x-axis, mean across replicates) with FDR q-value < 0.25 (Benjamini-Hochberg multiple test-corrected t-test p-values). **(g)** Scatterplot of GO terms (data points) showing results of singular enrichment analysis (SEA) that tests over-representation of "hits" identified in (f) within each GO term gene set. GO terms with FDR < 0.25 (Fisher's exact test following Benjamini-Hochberg multiple test correction) and permutation test $p < 0.05$ for non-hit enrichment were deemed significant (colored red). **(h)** Network of significant GO terms identified in (g) enriched with doxorubicin-induced phosphoprotein "hits" identified in (f). Nodes are shaded based on the SEA testing FDR shown in (g) and edge thicknesses correspond to the magnitudes of the gene set overlap coefficients between terms. The identities and numbers of protein "hits" that occur in each GO term are listed.

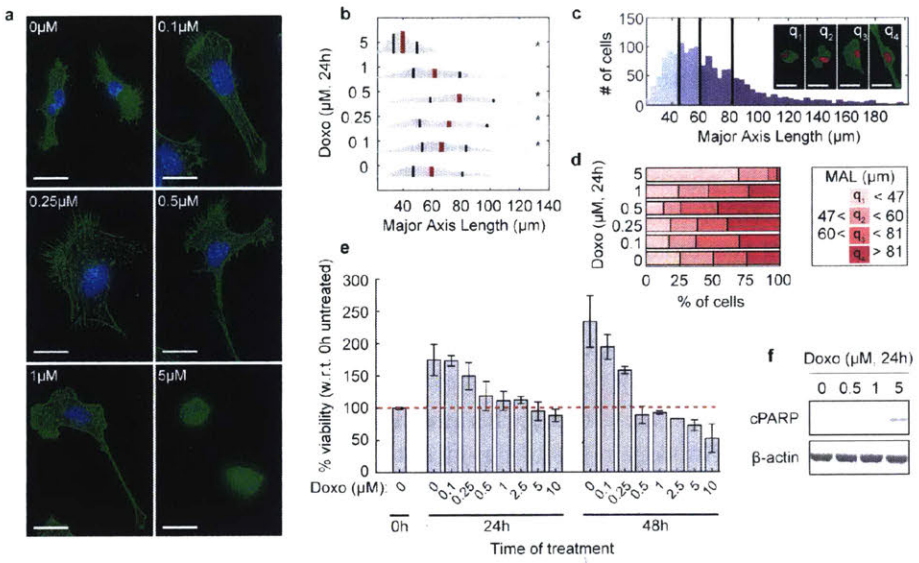

Figure 3-2: Doxorubicin alters cell morphology. **(a)** Representative images of MDA-MB-231 breast cancer cells stained for F-actin (phalloidin, green) and nuclear DNA (DAPI, blue) 24 h after doxorubicin treatment with the indicated doses. Scale bars, 20 μm. **(b-d)** Quantification of cellular morphological elongation (major axis length, MAL) following treatment with different doses of doxorubicin. MDA-MB-231 cells stably expressing actin reporter LifeAct-eGFP and nuclear reporter H2B-mCherry were used. **(b)** shows distributions of cellular major axis lengths under different doxorubicin doses. Red bar, median; left black bar, 25th percentile; right black bar, 75th percentile. Distributions were normalized to have equal areas to aid visual density comparisons. * $p < 0.05$ Wilcoxon rank sum test comparing MALs of cells treated with different doses of doxorubicin with the MALs of untreated cells (Doxo, 0 μM). Limits on x-axis are set to 1st and 95th percentile of the pooled MAL distribution comprising all conditions to aid visual comparisons. Bottom to top, n = 523, 232, 200, 152, 112, 264 cells, each from 3 replicates. **(c)** shows the MAL distribution of cells from all conditions in (b). Purple shading indicates a given quartile (q) of the entire distribution. Representative images of cells in each quartile are shown (green, LifeAct-eGFP; pink, H2B-mCherry). Scale bars, 40 μm. Limits on x-axis are set to 1st and 99th percentile of the pooled distribution of all conditions in (b). **(d)** Stacked bar graph showing the percentage of cells under different doxorubicin dose treatments normalized to each MAL quartile of the untreated (Doxo, 0 μM) cell population (pink shading). Legend indicates the MAL ranges captured by each quartile in the untreated population. **(e)** Cell viability/proliferation dose-response to doxorubicin treatment of MDA-MB-231 cells. Viability/proliferation was measured by SYTO60 cell staining following treatment with doxorubicin for 24 or 48 hrs at the indicated doses. Horizontal red dashed line indicates baseline SYTO60 staining at the start of the experiment (0 h with no doxorubicin treatment). Bars show mean viability values following normalization to untreated control (Doxo, 0 μM at 0 h) of n = 3 replicates for each condition. Error bars, (+/-) s.e.m. **(f)** Western blot of an apoptotic cell death marker, cleaved PARP (cPARP), in MDA-MB-231 cells assayed at 24 hrs following doxorubicin treatment at the doses shown. Assayed lysates include both supernatant (floating cells) and attached cells collected at the 24 hr time point.

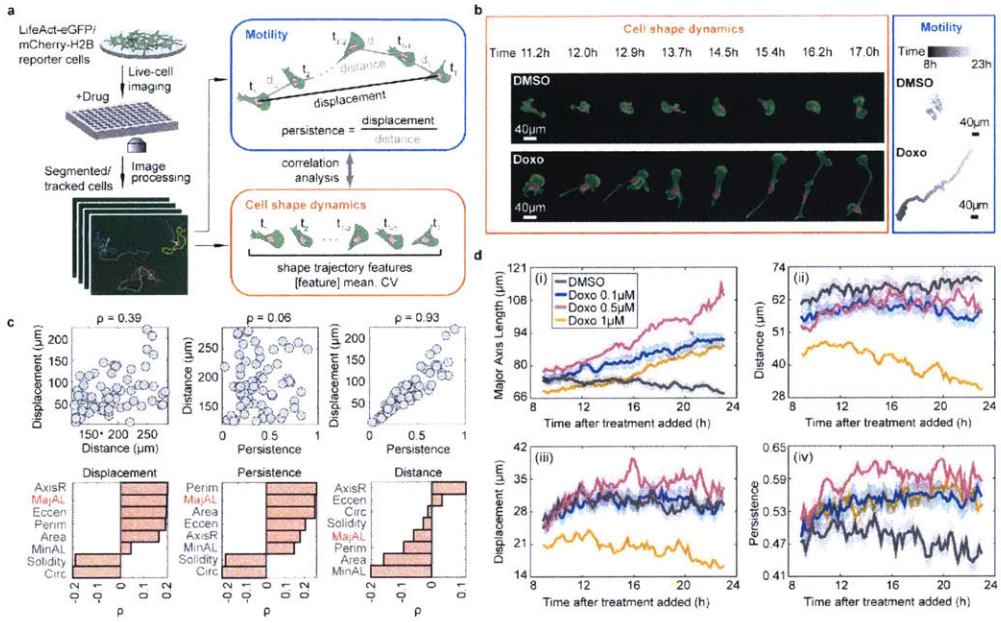

Figure 3-3: Doxorubicin increases directional cell migration that is coupled to morphological elongation. **(a)** Schematic overview of the experimental and computation workflow used to quantify and correlate changes in cell motility and shape dynamics induced by doxorubicin. **(b)** Left, snapshot images showing morphological changes of two representative live MDA-MB-231 cells expressing actin reporter LifeAct-eGFP (green) and nuclear reporter H2B-mCherry (pink) at sequential time points following treatment with DMSO (control) or doxorubicin (Doxo, 0.5 μM). Right, cell migration trajectories of the two cells following treatment. Trajectories were obtained via automated tracking of the cell nuclei using the nuclear reporter. **(c)** Top, correlation (Spearman ρ) between motility metrics shown in (a) of 4 h-long single-cell migration trajectories (gray data points) of cells treated with different doses of doxorubicin (0, 0.1, 0.5, and 1 μM) measured 19 to 23 hrs following treatment. Bottom, correlation between motility metrics and morphological features of the single-cell trajectories, relating average value of the features over time with migratory behavior. Cell elongation (major axis length, MajAL) is highlighted in red. (Perim, perimeter; Eccen, eccentricity; AxisR, axis ratio; MinAL, minor axis length; Circ, circularity, see Table B.1 for shape feature definitions). **(d)** Quantification of morphological elongation (major axis length) and motility (distance, displacement, and persistence) of tracked cells following treatment with different doses of doxorubicin over time, calculated for sequential 1 h-long trajectories. Solid colored lines are the mean feature values (y-axis) of all tracked live cells from n = 8 independent 96-well-plate wells with 3 field of view per well for each treatment condition. Colored shading indicates (+/-) 95% CI of the mean.

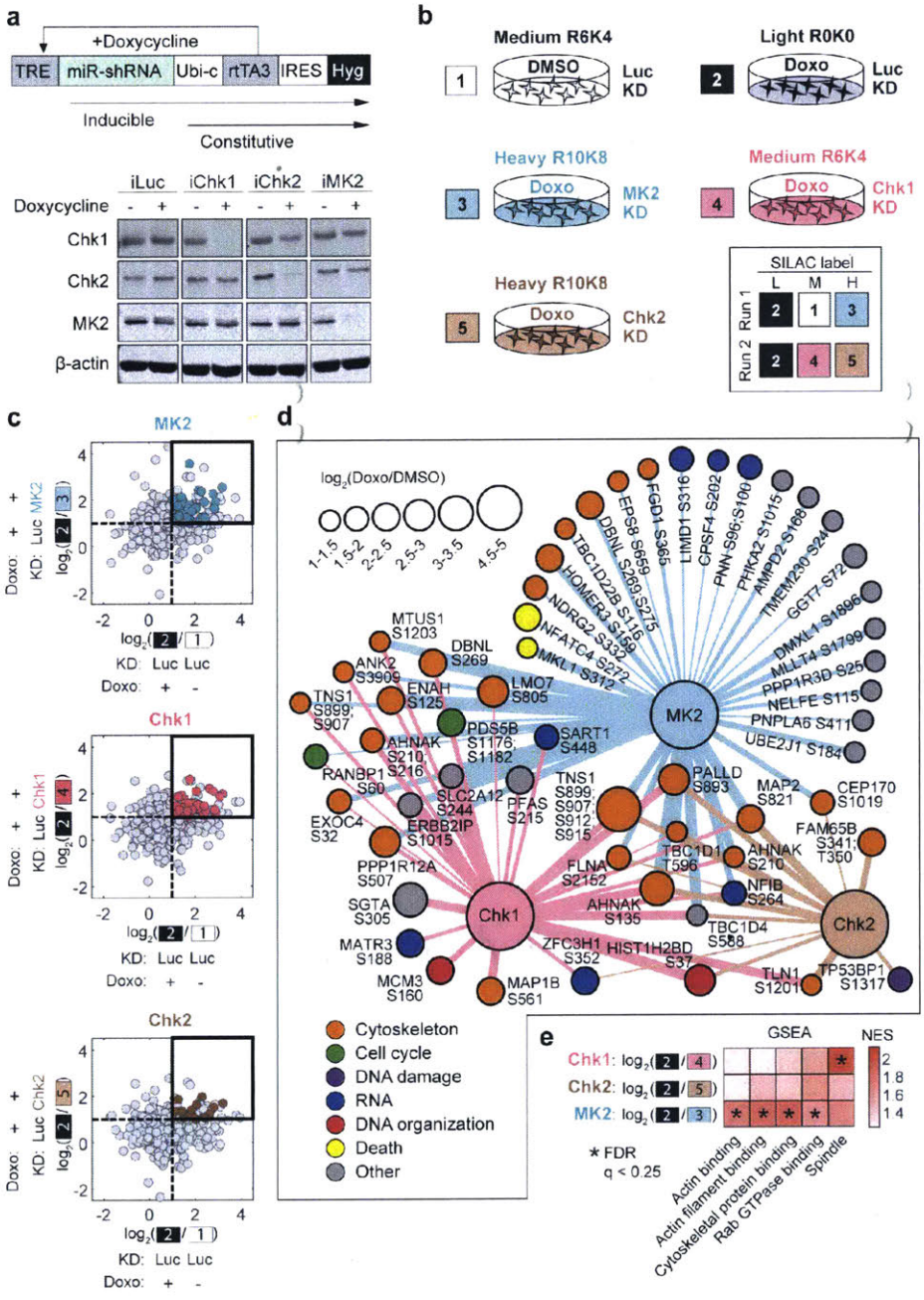
a
+Doxycycline
TRE
miR-shRNA
Ubi-c
rtTA3
IRES
Hyg
Inducible
Constitutive
iLuc
iChk1
iChk2
iMK2
Doxycycline
Chk1
Chk2
MK2
β-actin
b
Medium R6K4
DMSO
Luc KD
Light R0K0
Doxo
Luc KD
Heavy R10K8
Doxo
MK2 KD
Medium R6K4
Doxo
Chk1 KD
Heavy R10K8
Doxo
Chk2 KD
SILAC label
L M H
Run 1
Run 2
c
MK2
Chk1
Chk2
KD: Luc MK2
KD: Luc Chk1
KD: Luc Chk2
KD: Luc Luc
Doxo: + -
d
log2(Doxo/DMSO)
1-1.5
1.5-2
2-2.5
2.5-3
3-3.5
4.5-5
MK2
Chk1
Chk2
Cytoskeleton
Cell cycle
DNA damage
RNA
DNA organization
Death
Other
e
GSEA
NES
Chk1: log2(2/4)
Chk2: log2(2/5)
MK2: log2(2/3)
* FDR q < 0.25
Actin binding
Actin filament binding
Cytoskeletal protein binding
Rab GTPase binding
Spindle

Figure 3-4: The doxorubicin-activated phosphoprotein networks of checkpoint kinases MK2, Chk1, and Chk2 consist of shared and distinct substrates with cytoskeleton-regulatory function. **(a)** Schematic of the hairpin construct used to generate stable cell lines with doxycycline-inducible transient knockdown of each checkpoint kinase. Western blot confirms the efficiency and specificity of checkpoint kinase knockdown with each construct. **(b)** Schematic of the five SILAC labeling conditions used for mass spectrometry, specifying the amino acid label (heavy, medium, or light), treatment (doxorubicin or DMSO), and knockdown (Luciferase, Luc; checkpoint kinases Chk1, Chk2, or MK2). Two mass spectrometry runs, each with 3 SILAC-labeled treatment conditions (bottom, boxed) were performed to assess the dependence of doxorubicin-induced phosphosites on the presence of each checkpoint kinase. **(c)** Phosphosite "hit" identification. Scatterplots of shared phosphosites (data points) identified in all conditions and replicates in (b) plotted as ratios of the conditions shown. "Hits" (cyan, pink , or brown points) are phosphosites at least two-fold upregulated by doxorubicin (x-axis, mean across replicates) and dependent on knockdown target (y-axis, mean across replicates) with FDR q-value < 0.05 (Benjamini-Hochberg multiple test-corrected t-test p-values). The number of "hits" in each knockdown comparison are: MK2, 46; Chk1, 31; Chk2, 15. **(d)** Checkpoint kinase regulation network of phosphosite "hits" identified in (c). Phosphosite node size corresponds to the magnitude of upregulation upon doxorubicin treatment; node color shows the categorical annotation having the largest fraction of GO terms containing the phosphoprotein. Edge thickness indicates dependence of phosphosite upregulation on the connected checkpoint kinase (large pink, brown, or cyan node) upon doxorubicin treatment ($\log_2$(Luc/KD) under doxorubicin). **(e)** GSEA of proteins whose upregulation by doxorubicin was dependent on a given checkpoint kinase. Log_2-transformed fold changes between the SILAC conditions shown (row labels) were used for GSEA input list ranking. Heatmap shows the subset of all GO terms (columns) that were deemed significantly enriched (FDR < 0.25) in at least one condition (row), and the positive normalized enrichment score (NES), out of 470 total GO terms identified in all conditions.

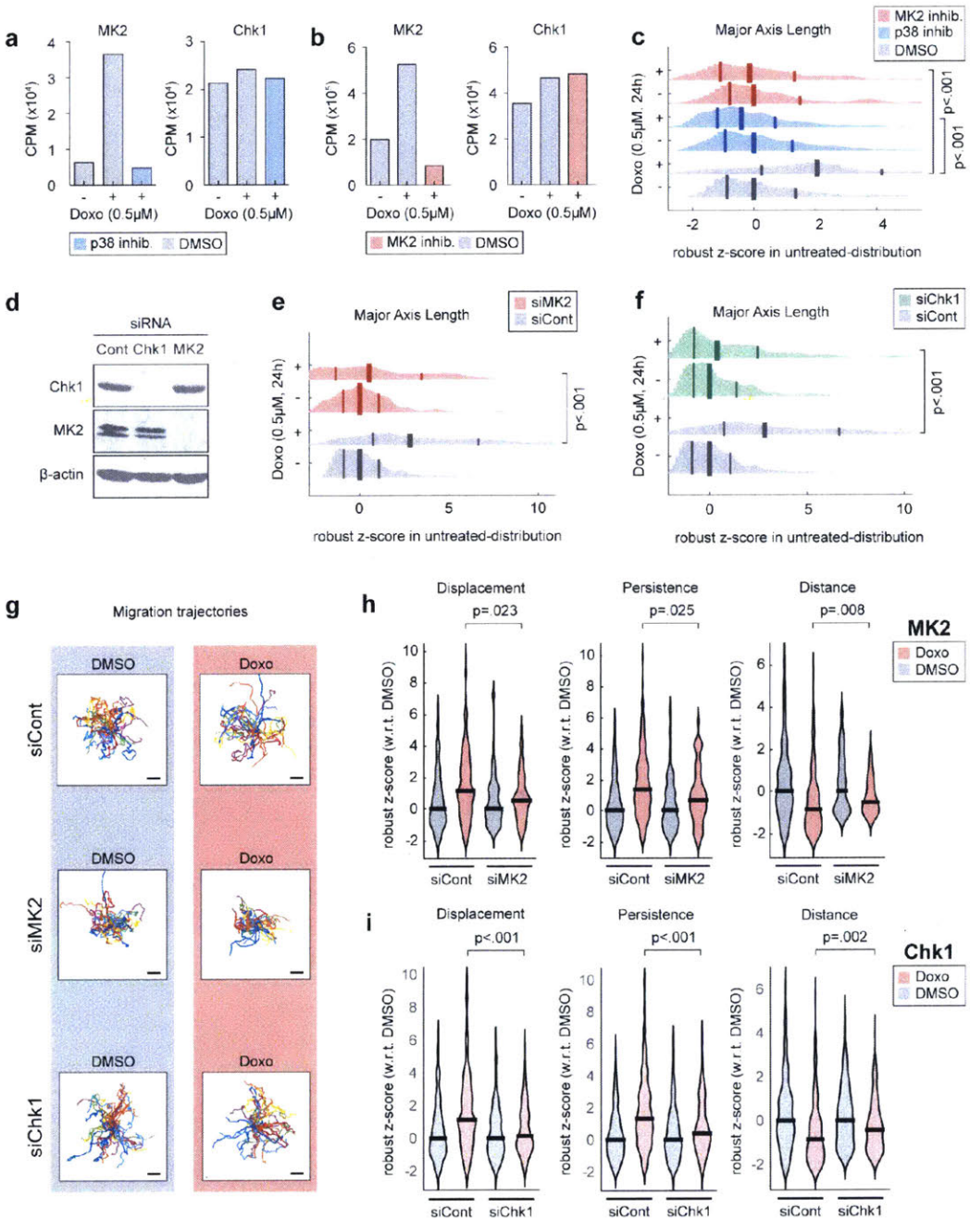
a
MK2
Chk1
CPM (x10⁴)
Doxo (0.5μM)
p38 inhib.
DMSO
b
MK2
Chk1
CPM (x10⁴)
Doxo (0.5μM)
MK2 inhib.
DMSO
c
Major Axis Length
MK2 inhib.
p38 inhib
DMSO
Doxo (0.5μM, 24h)
p<.001
p<.001
robust z-score in untreated-distribution
d
siRNA
Cont Chk1 MK2
Chk1
MK2
β-actin
e
Major Axis Length
siMK2
siCont
Doxo (0.5μM, 24h)
p<.001
robust z-score in untreated-distribution
f
Major Axis Length
siChk1
siCont
Doxo (0.5μM, 24h)
p<.001
robust z-score in untreated-distribution
g
Migration trajectories
DMSO
Doxo
siCont
siMK2
siChk1
h
Displacement
Persistence
Distance
p=.023
p=.025
p=.008
MK2
Doxo
DMSO
robust z-score (w.r.t. DMSO)
siCont
siMK2
i
Displacement
Persistence
Distance
p<.001
p<.001
p=.002
Chk1
Doxo
DMSO
robust z-score (w.r.t. DMSO)
siCont
siChk1

Figure 3-5: MK2 or Chk1 depletion abrogates doxorubicin-induced cell elongation and directional migration. **(a, b)** Effects of pharmacological inhibitors against p38MAPK **(a)** or MK2 **(b)** on MK2 or Chk1 kinase activity in MDA-MB-231 cells based on *in vitro* kinase assays. **(c)** Effects of pharmacological p38MAPK or MK2 inhibition on doxorubicin-induced morphological elongation (major axis length, MAL). MDA-MB-231-LifeAct/H2B cells were treated with a p38MAPK inhibitor (SB202190, 10 μM) or MK2 inhibitor (PF-3644022, 10 μM) with or without doxorubicin (0.5 μM) for 24 hrs, fixed, imaged, and analyzed for morphological changes. In each distribution, the thicker central vertical line is the median, left thinner line is 25th percentile, and right thinner line is 75th percentile. Bottom to top, n = 468, 221, 364, 312, 406, 237 cells, each from 4 replicates. **(d)** Efficacy and specificity of siRNA-based knockdown of MK2 or Chk1. MDA-MB-231 cells were transiently transfected with siRNA targeting control, MK2 or Chk1 for 72 hrs and cell lysates were blotted with an antibody against MK2 or Chk1. **(e)** Effect of RNAi-based knockdown of MK2 on morphological elongation following doxorubicin treatment. MDA-MB-231-LifeAct/H2B cells were transfected with siRNA against non-targeting control (siCont) or MK2 (siMK2) for 72 hrs and treated with doxorubicin (0.5 μM) for 24 hrs and analyzed for changes in morphology as in (c). Bottom to top, n = 395, 153, 216, 116 cells, each from 4 replicates. **(f)** Effect of RNAi-based knockdown of Chk1 on doxorubicin-induced morphological elongation. Cell treatment and analysis same as in (e). Bottom to top, n = 395, 153, 397, 273 cells, each from 4 replicates. **(g)** Migration trajectories (12 hr-long, origin-centered at t = 0 hr) of live MDA-MB-231-LifeAct/H2B cells tracked following doxorubicin treatment (added at t = 0 h, 0.5 μM) with or without MK2 or Chk1 siRNA knockdown for 72 hrs prior to doxorubicin addition. The top 30 cells that travelled the farthest distance under each condition are shown. Trajectories have 72 time steps (cells imaged every 10 min in the time period of 12 to 24 hrs following doxorubicin treatment). **(h)** Effects of doxorubicin treatment on motility (displacement, persistence, and distance) of MDA-MB-231-LifeAct/H2B cells with or without siRNA knockdown of MK2 in the time period of 12 to 24 hrs following doxorubicin treatment. Horizontal black lines in each violin plot distribution are the median values. Left to right within each panel, n = 245, 169, 71, 56 cells, each from 5 replicates. **(i)** Effects of doxorubicin treatment on cell motility (displacement, persistence, and distance) with or without siRNA knockdown of Chk1. Cell treatment and analysis same as in (h). Left to right within each panel, n = 245, 169, 243, 198 cells, each from 5 replicates.

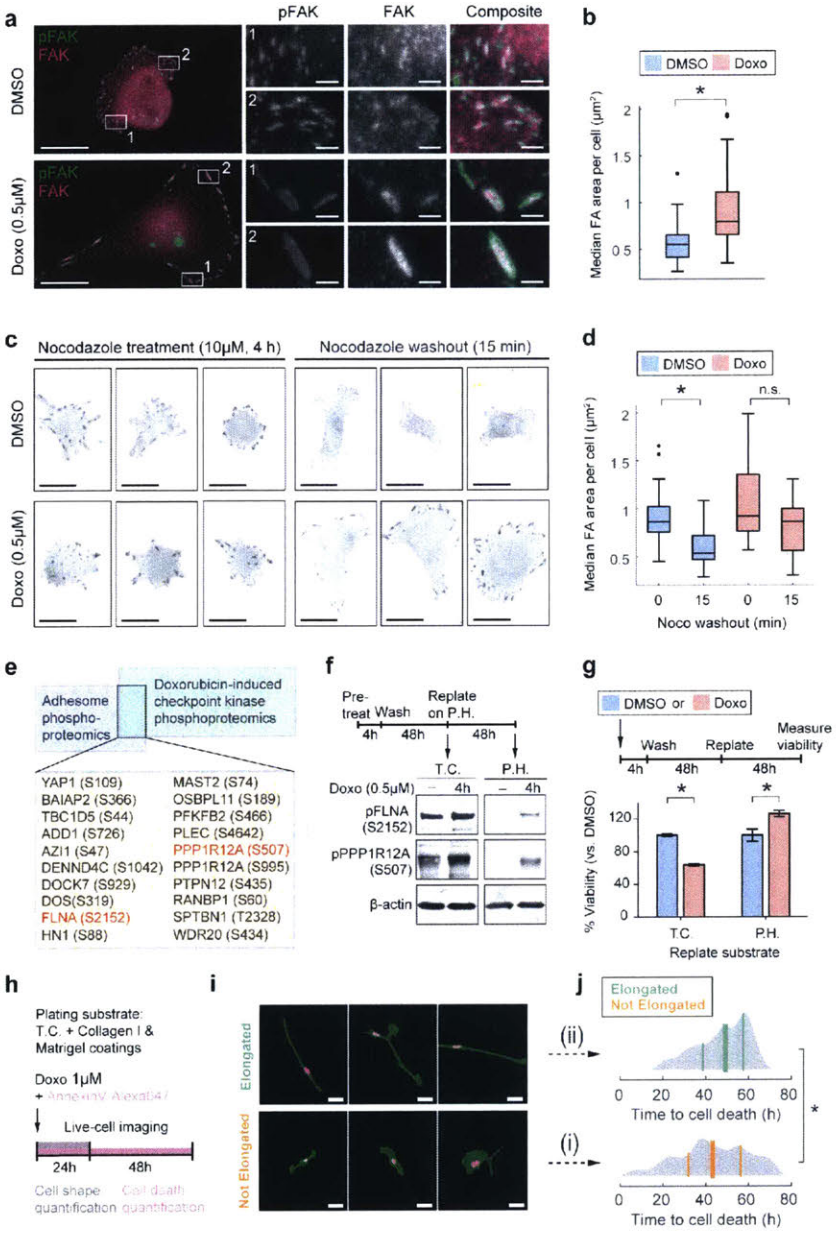
a
pFAK
FAK
Composite
DMSO
Doxo (0.5μM)
b
DMSO
Doxo
Median FA area per cell (μm²)
c
Nocodazole treatment (10μM, 4 h)
Nocodazole washout (15 min)
d
n.s.
Noco washout (min)
e
Adhesome phospho-proteomics
Doxorubicin-induced checkpoint kinase phosphoproteomics
YAP1 (S109)
BAIAP2 (S366)
TBC1D5 (S44)
ADD1 (S726)
AZI1 (S47)
DENND4C (S1042)
DOCK7 (S929)
DOS(S319)
FLNA (S2152)
HN1 (S88)
MAST2 (S74)
OSBPL11 (S189)
PFKFB2 (S466)
PLEC (S4642)
PPP1R12A (S507)
PPP1R12A (S995)
PTPN12 (S435)
RANBP1 (S60)
SPTBN1 (T2328)
WDR20 (S434)
f
Pre-treat
Wash
Replate on P.H.
4h
48h
T.C.
P.H.
Doxo (0.5μM)
pFLNA (S2152)
pPPP1R12A (S507)
β-actin
g
DMSO or Doxo
Measure viability
% Viability (vs. DMSO)
T.C
P.H.
Replate substrate
h
Plating substrate:
T.C. + Collagen I &
Matrigel coatings
Doxo 1μM
+ Annexin V-Alexa647
Live-cell imaging
24h
48h
Cell shape quantification
Cell death quantification
i
Elongated
Not Elongated
j
Elongated
Not Elongated
(ii)
(i)
Time to cell death (h)

Figure 3-6: Doxorubicin alters focal adhesion organization and promotes anoikis resistance. **(a)** Representative images of MDA-MB-231 cells treated with DMSO (control) or doxorubicin (Doxo, 0.5 μM), immunostained for p-FAK (Y347) and total FAK at 24 hrs post-treatment to assess changes in focal adhesion organization. Scale bars: whole-cell images, 20 μm; zoom-in images, 2 μm. Additional images are included in 3-14. **(b)** Quantification of doxorubicin (0.5 μM) effects on focal adhesion area. * $p < 0.05$ Wilcoxon rank sum test. n = 51 and 38 cells analyzed, for DMSO and Doxo, respectively. **(c)** Representative images of focal adhesion organization in DMSO- and doxorubicin-treated cells following nocodazole treatment or 15 min after nocodazole washout. MDA-MB-231 cells were treated with DMSO or doxorubicin (0.5 μM) for 24 hrs, treated with nocodazole for 4 hrs in serum-free media, washed for the indicated lengths of time, fixed and stained for p-FAK (Y397). Three representative images are shown for each condition. Scale bars, 20 μm. **(d)** Quantification of doxorubicin (0.5 μM) effects on focal adhesion area, as performed in (c), at the indicated time points following nocodazole washout. 0 min washout corresponds to the time point at 4 hrs of nocodazole treatment. * $p < 0.05$ Wilcoxon rank sum test. Left to right, n = 24, 39, 18, 23 cells analyzed. **(e)** Phosphosite overlap between the phosphoproteomic data set presented in this work and the consensus adhesome data set of [220]. Sites further assayed in (f) are highlighted red. **(f)** Western blotting of phosphorylated cytoskeleton- and adhesome-associated proteins, FLNA and PPP1R12A (MYPT1), in MDA-MB-231 cells before and after culture on non-adhesive substrate (poly-HEMA, P.H.) following doxorubicin treatment. **(g)** Top, schematic of the experimental design to assess effects of doxorubicin pre-treatment on cell viability when cells are seeded on substrates with low (poly-HEMA, P.H.) or high (tissue culture, T.C.) adhesiveness. Following pre-treatment and washout, cells were re-plated onto 96-well tissue culture plates coated without (T.C.) or with poly-HEMA (P.H.), and cell viability then measured via CellTiterGlo at 48 hrs. Percent viability was normalized to untreated control (DMSO) for each seeding substrate. * $p < 0.05$ Student's t-test comparing mean percent viabilities from n = 3 replicates for each condition. Error bars, (+/-) s.e.m. **(h)** Workflow schematic for simultaneous analysis of morphology and apoptosis of MDA-MB-231-LifeAct/H2B cells. AnnexinV conjugated with AlexaFluor-647 was used for live imaging-based cell death quantification. **(i)** Live-cell snapshots of three representative MDA-MB-231-LifeAct/H2B cells at the time point of maximum elongation over 24 hrs following doxorubicin treatment for the non-elongated and elongated cell subpopulations. In the images, LifeAct-eGFP is green; H2B-mCherry is red. Scale bars, 40 μm. **(j)** Comparison of cell death rates of elongated (ii) and non-elongated (i) cells following 1 μM doxorubicin treatment. Thick center line, median; left thin line, 25th percentile; right thin line, 75th percentile. Distributions (gray) were normalized to have equal areas to aid visual density comparisons. * $p < 0.05$ Wilcoxon rank sum test. n = 412 non-elongated and 53 elongated cells analyzed.

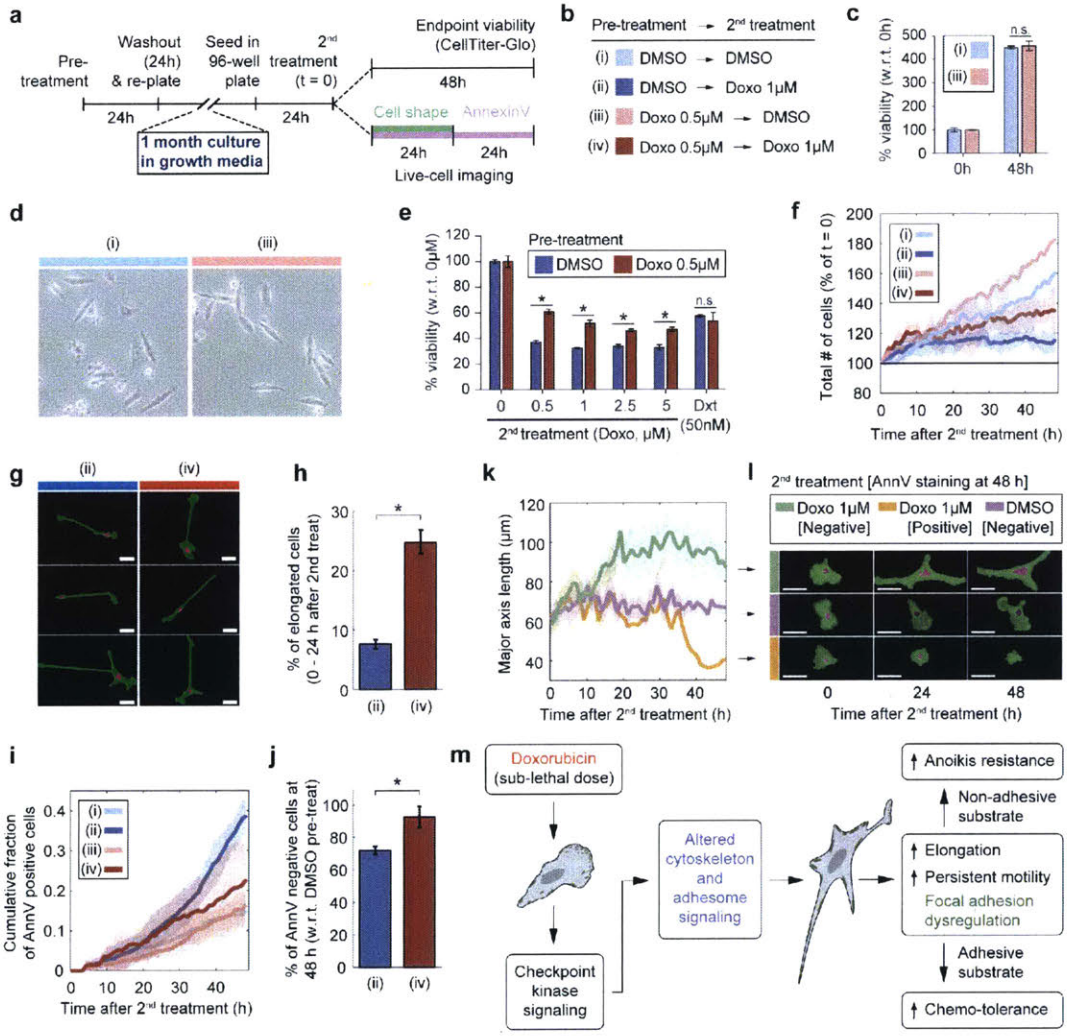
a
Pre-treatment
Washout (24h) & re-plate
Seed in 96-well plate
2nd treatment (t = 0)
Endpoint viability (CellTiter-Glo)
48h
24h
24h
1 month culture in growth media
Cell shape
AnnexinV
24h
24h
Live-cell imaging
b
Pre-treatment → 2nd treatment
(i) DMSO → DMSO
(ii) DMSO → Doxo 1μM
(iii) Doxo 0.5μM → DMSO
(iv) Doxo 0.5μM → Doxo 1μM
c
% viability (w.r.t. 0h)
n.s.
(i)
(iii)
0h
48h
d
(i)
(iii)
e
Pre-treatment
DMSO
Doxo 0.5μM
% viability (w.r.t. 0μM)
n.s.
0
0.5
1
2.5
5
Dxt (50nM)
2nd treatment (Doxo, μM)
f
Total # of cells (% of t = 0)
(i)
(ii)
(iii)
(iv)
Time after 2nd treatment (h)
g
(ii)
(iv)
h
% of elongated cells (0 - 24 h after 2nd treat)
(ii)
(iv)
k
Major axis length (μm)
Time after 2nd treatment (h)
l
2nd treatment [AnnV staining at 48 h]
Doxo 1μM [Negative]
Doxo 1μM [Positive]
DMSO [Negative]
Time after 2nd treatment (h)
i
Cumulative fraction of AnnV positive cells
(i)
(ii)
(iii)
(iv)
Time after 2nd treatment (h)
j
% of AnnV negative cells at 48 h (w.r.t. DMSO pre-treat)
(ii)
(iv)
m
Doxorubicin (sub-lethal dose)
Checkpoint kinase signaling
Altered cytoskeleton and adhesome signaling
Anoikis resistance
Non-adhesive substrate
Elongation
Persistent motility
Focal adhesion dysregulation
Adhesive substrate
Chemo-tolerance

Figure 3-7: Sub-lethal doxorubicin pre-treatment followed by long-term recovery increases cellular tolerance to secondary round of drug exposure. **(a)** Workflow of MDA-MB-231-LifeAct/H2B cell morphology, proliferation, and apoptosis following a two-stage doxorubicin regimen (pre-treatment, 0.5 μM; 2nd treatment, 1 μM). AnnV is AnnexinV conjugated with AlexaFluor-647. **(b)** Legend for panels (c)-(j) indicating treatment conditions and color-coding used throughout the figure. **(c)** Baseline cell proliferation (normalized to 0 hrs) of pre-treated cells after 1 month recovery. **(d)** Representative images of DMSO- or doxorubicin-pretreated cells after 1 month recovery. **(e)** Effect of doxorubicin pre-treatment on cell survival following second treatment with various doxorubicin doses or 50 nM docetaxel (Dxt). Prior to secondary treatment, cells were pre-treated as in (a, b). * $p < 0.05$ Student's t-test comparing means from n = 3 replicates for each condition. Error bars, (+/-) s.e.m. **(f)** Effect of doxorubicin pre-treatment and recovery on proliferation assessed via live-cell imaging over 48 hrs following secondary dose treatment (Doxo, 1 μM). Solid colored lines are the mean values from n = 3 replicates. Colored shading: 95% CI. **(g)** Live-cell snapshots of three randomly chosen elongated cells (rows) at the time point of maximum elongation in each treatment condition (column) labeled (ii) or (iv). Green, LifeAct-eGFP; pink, H2B-mCherry. Scale bars, 40 μm. Intensity was scaled uniformly across all image panels to emphasize cell bodies and nuclei. **(h)** Effect pre-treatment and 1 month recovery on the fraction of elongated cells following treatment with a secondary 1 μM dose of doxorubicin. * $p < 0.05$ Student's t-test comparing means of n = 3 replicates for each condition. Error bars, (+/-) s.e.m. **(i)** Effect of pre-treatment and 1 month recovery on cell death assessed via live-cell imaging over 48 hrs following secondary dose treatment (Doxo, 1 μM). Solid colored lines are the mean values from n = 3 replicates. Colored shading: 95% CI. **(j)** Percentage of viable cells (AnnV negative) at the 48 hr time point after secondary doxorubicin treatment in the right panel plot in (i), relative to DMSO control. * $p < 0.05$ Student's t-test comparing mean percent viabilities. Error bars, (+/-) s.e.m. **(k)** Quantification of morphological elongation (MAL) over time for the subpopulations of doxorubicin pre-treated cells (condition (iv) in (b)) that were either tolerant (green curve) or sensitive (yellow curve) to secondary treatment of 1 μM doxorubicin. Purple curve: baseline morphology of alive (AnnV negative) cells under no drug treatment. Key for colors shown in (l). Solid colored lines are the means. Colored shading: (+/-) 95% CI. The cell subpopulations in the green, purple, and yellow curves comprise n = 189, 432, and 43 cells, respectively. **(l)** Representative morphologies of cells from the tracked subpopulations in (k). Images: green, LifeAct-eGFP; pink, H2B-mCherry. Scale bars, 40 μm. Intensity scaled uniformly across all image panels to emphasize cell bodies and nuclei. **(m)** Summary of major findings and working model of the checkpoint kinase-mediated phospho-signaling and phenotypic responses of cancer cells to sub-lethal doxorubicin chemotherapy presented in this work.

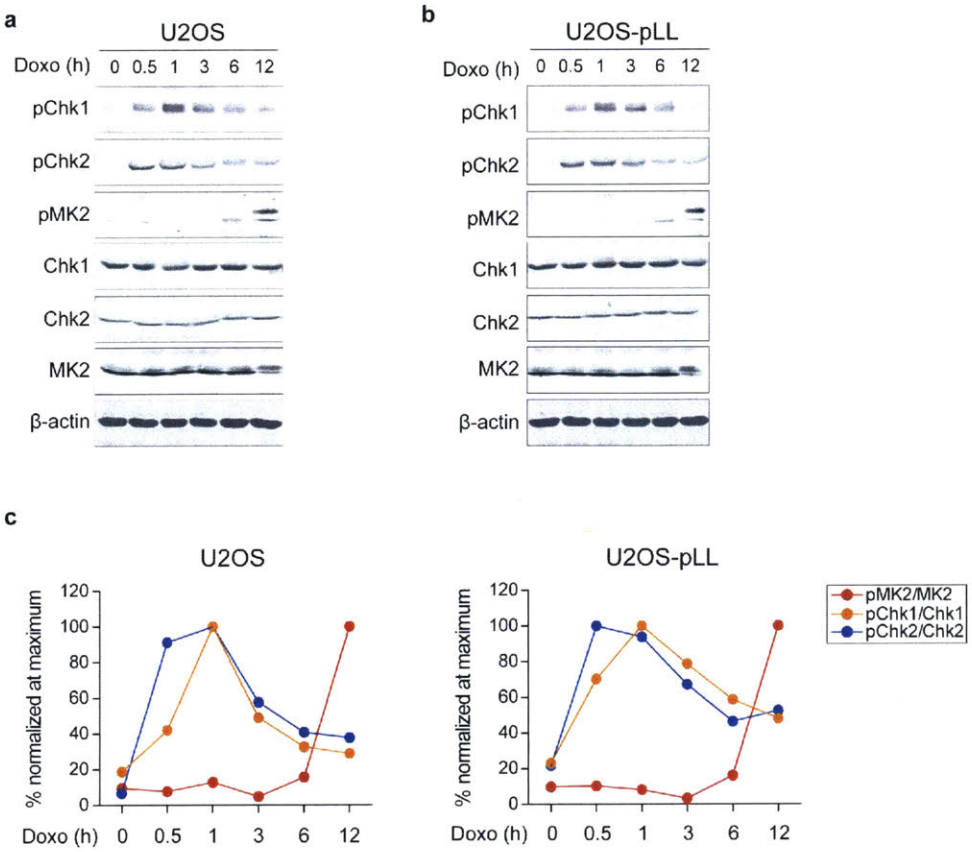

Figure 3-8: Time course of checkpoint kinase signaling response to doxorubicin. U2OS-pLL are the cells used for phosphoproteomic screening in 3-1 (replicate 1) and generated by infecting wild-type U2OS cells with pLL3.7 lentiviral empty vector. U2OS **(a)** or U2OS-pLL **(b)** cells were treated with 5 μM doxorubicin for the indicated lengths of time and lysates were collected for Western blotting. Phosphorylation-specific antibodies against Ser345 of Chk1, T68 of Chk2, and T334 of MK2, were used as surrogate readouts of checkpoint kinase activation. **(c)** Western blot band intensity is determined by quantification of LiCor signal using ImageStudio software. Each checkpoint kinase activity is determined by normalization of phospho-specific signal to its total non-phospho signal. Percent activity of each checkpoint kinase is normalized to the maximum activity of each checkpoint kinase during the time course.

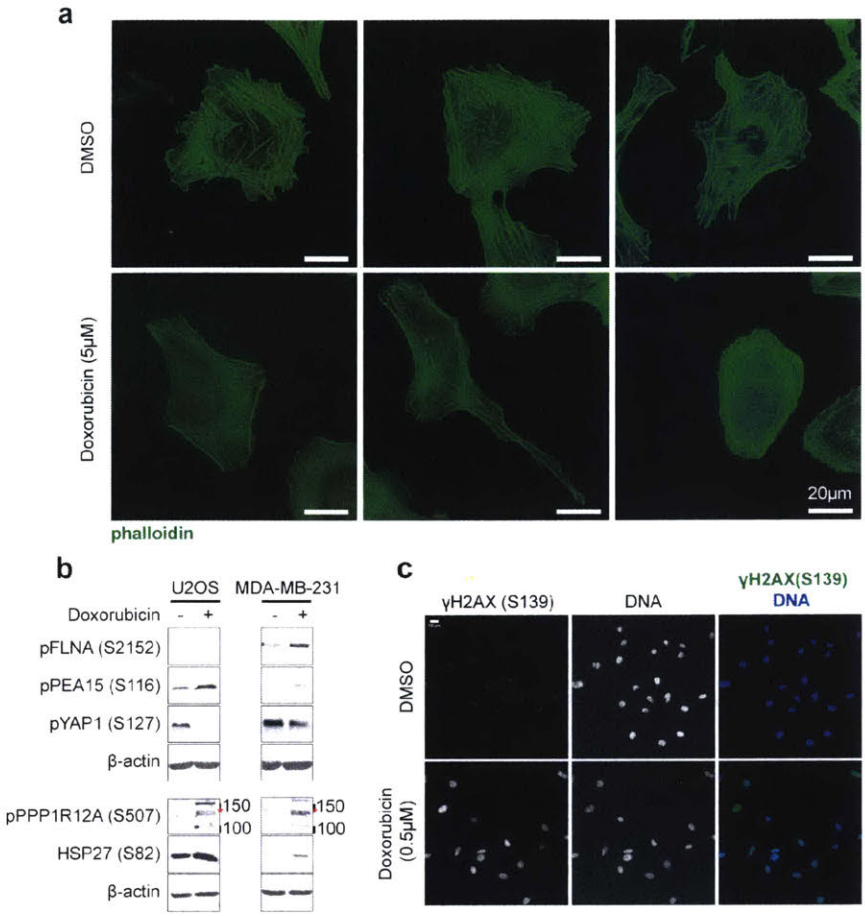

Figure 3-9: Doxorubicin alters actin-cytoskeleton organization and signaling in U2OS cells. **(a)** U2OS cells were treated either with DMSO (control) or 5 μM doxorubicin for 12 hrs, and stained for F-actin (Alexa488-conjugated phalloidin). Two representative images of DMSO- (upper panel) or doxorubicin-treated (lower panel) cells are shown. Scale bars, 20 μm. **(b)** Changes in phosphorylation of selected cytoskeleton-associated phosphoprotein sites identified in the SILAC screen (3-1) validated by Western blotting in both U2OS cells (left panel) and MDA-MB-231 cells (right panel). U2OS cells were treated with 5 μM doxorubicin for 12 hrs, while MDA-MB-231 cells were treated with 0.5 μM doxorubicin for 24 hrs prior to lysate collection. **(c)** MDA-MB-231 cells were treated with DMSO or doxorubicin (0.5 μM) for 24 hrs, and then stained for γH2AX (S139) as a readout of DNA damage (green) and DAPI to delineate nuclei (blue). Representative images for each treatment are shown (left column, DAPI; middle panel, γH2AX (S139); right panel, composite image).

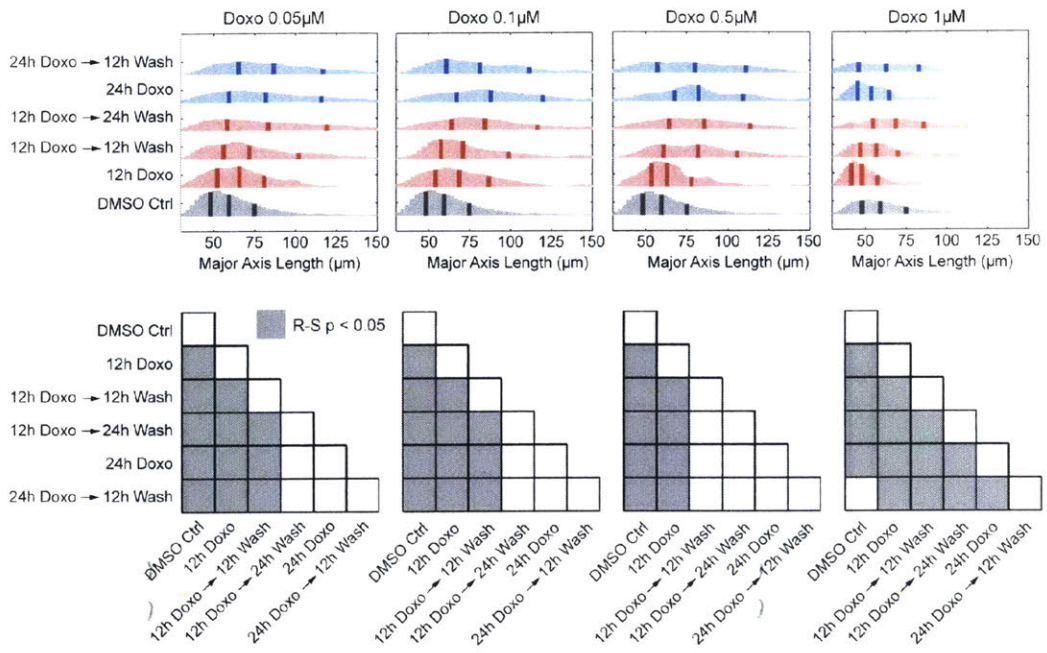

Figure 3-10: Doxorubicin-induced cell elongation is irreversible upon drug washout. **(a)** MDA-MB-231 cells were treated with doxorubicin at the indicated concentrations for 12 hrs (red) or 24 hrs (blue), and changed to new growth media after washing out drug-containing media. Following 12 or 24 hrs of drug washout, cells were fixed and stained with F-actin (Alexa488-conjugated phalloidin). The distributions of major axis lengths of cells is plotted. Vertical bars in each distribution represent the 25th percentile (left bar), median (middle bar), and 75th percentile (right bar). **(b)** Pair-wise statistical comparisons of the major axis length distributions among all treatment conditions using Wilcoxon rank sum test.

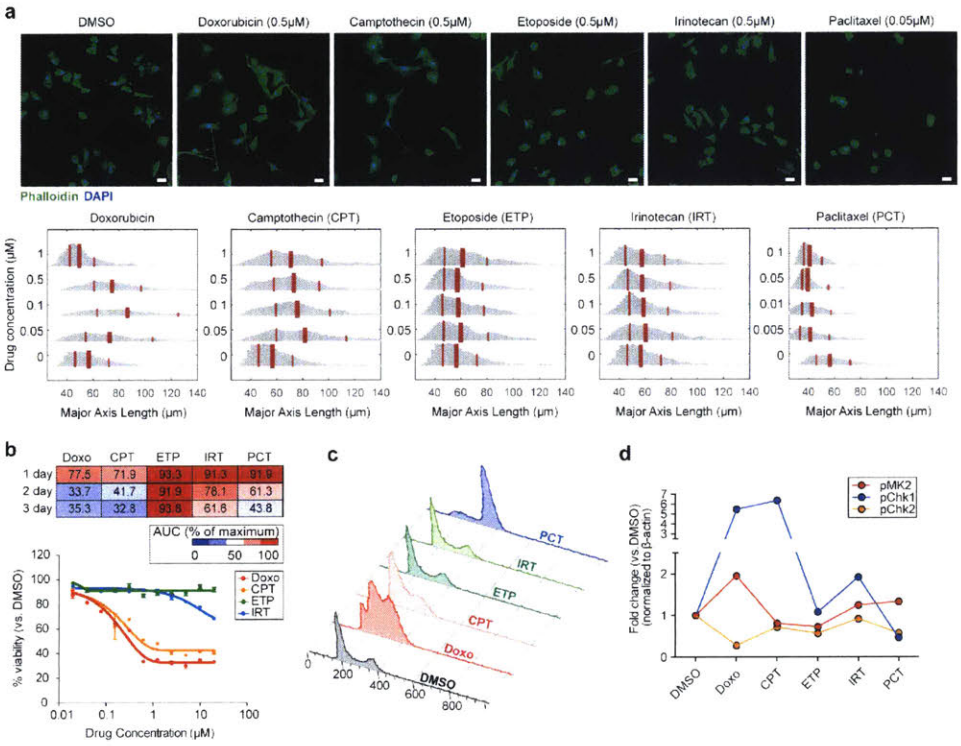
a
DMSO
Doxorubicin (0.5μM)
Camptothecin (0.5μM)
Etoposide (0.5μM)
Irinotecan (0.5μM)
Paclitaxel (0.05μM)
Phalloidin DAPI
Doxorubicin
Camptothecin (CPT)
Etoposide (ETP)
Irinotecan (IRT)
Paclitaxel (PCT)
Drug concentration (μM)
Major Axis Length (μm)
b
Doxo CPT ETP IRT PCT
1 day 77.5 71.9 93.3 91.3 91.9
2 day 33.7 41.7 91.9 78.1 61.3
3 day 35.3 32.8 93.8 61.8 43.8
AUC (% of maximum)
0 50 100
% viability (vs. DMSO)
Drug Concentration (μM)
Doxo
CPT
ETP
IRT
c
PCT
IRT
ETP
CPT
Doxo
DMSO
d
pMK2
pChk1
pChk2
Fold change (vs DMSO)
(normalized to β-actin)
DMSO
Doxo
CPT
ETP
IRT
PCT

Figure 3-11: Different cancer drugs show variable effects on morphology, viability, cell cycle arrest, and checkpoint kinase signaling. **(a)** MDA-MB-231 cells were treated with different classes of chemotherapeutic drugs, including 0.5 μM doxorubicin (Doxo, topoisomerase II inhibitor), camptothecin (CPT, topoisomerase I inhibitor), etoposide (ETP, topoisomerase II inhibitor), or irinotecan (IRT, topoisomerase I inhibitor), or with 0.05 μM paclitaxel (PCT, microtubule stabilizing agent). After 24 hrs of drug treatment, cells were fixed and stained for F-actin (Alexa488-conjugated phalloidin). Scale bars, 40 μm. Distribution of major axis lengths of cell populations treated with different doses of each drug are shown. Thinner vertical red lines in each distribution represent the 25th percentile (left line) and 75th percentile (right line), while the central thicker red line is the median. **(b)** Cell viability dose responses to selected drugs. Top, MDA-MB-231 cells were treated with each drug up to 20 μM, except for PCT, which was used up to 2 μM, and cell viability was assessed at 24, 48, or 72 hrs. Cell viabilities are measured via CellTiterGlo. Bottom, representative dose-response curves with viabilities assessed at 48 hrs of drug treatment. Comparison of differential toxicity of each drug was assessed using area under the curve (AUC), with the percent of maximum AUC (max = 100%) for each drug and each time point calculated (heatmap). **(c)** Effects of different drugs on the cell cycle. MDA-MB-231 cells were treated with each drug for 24 hrs at 0.5 μM except for PCT, which was used at 0.05 μM. Cells were then fixed and stained with propidium iodide (PI). **(d)** Drug effects on checkpoint kinase phosphorylation. MDA-MB-231 cells were treated with each drug for 24 hrs at 0.5 μM except for PCT, which was used at 0.05 μM. Cell lysates were collected and Western blotting with phospho-specific antibodies was used to probe phosphorylation of Chk1, Chk2, or MK2. Line plots show blot quantification of drug effects relative to DMSO control with phospho-checkpoint kinase blot band normalization to total β-actin levels.

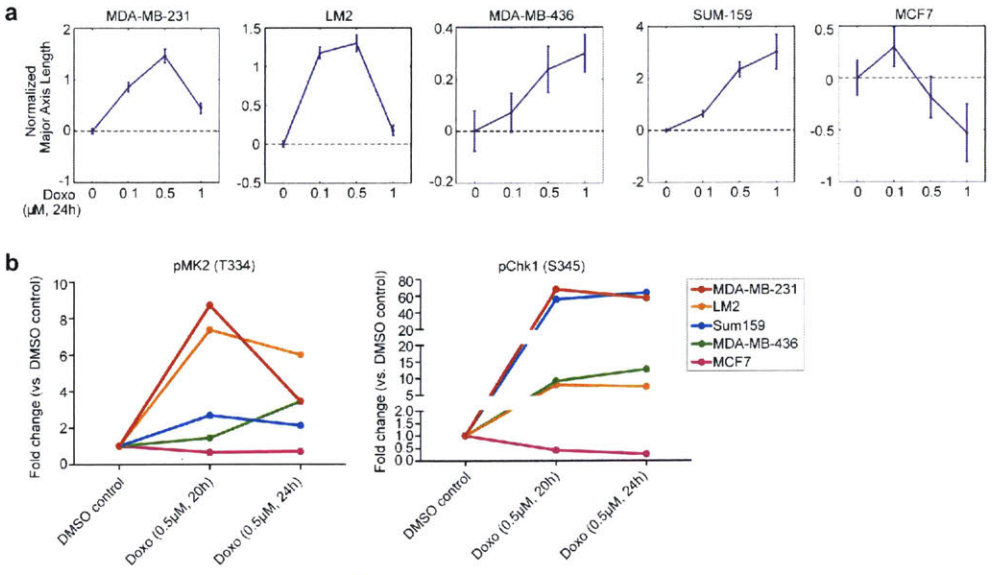

Figure 3-12: Doxorubicin alters the morphology of multiple breast cancer cell lines. **(a)** A panel of five breast cancer cell lines were treated with doxorubicin with the indicated doses for 24 hrs. Cells were then fixed and stained for F-actin (Alexa488-conjugated phalloidin). Effects of multiple doxorubicin doses on average morphological elongation (major axis length) for each cell line are shown, normalized to untreated control (0 μM doxorubicin). **(b)** Comparison of checkpoint kinase signaling activation following doxorubicin treatment in multiple breast cancer cell lines. Cells were treated with doxorubicin (0.5 μM) for either 20 or 24 hrs, and cell lysates were then analyzed with Western blotting to measure phosphorylation of Chk1 and MK2. Western blot bands were quantified using ImageJ after normalization to β-actin, and fold change over untreated (DMSO) control for each cell line is shown.

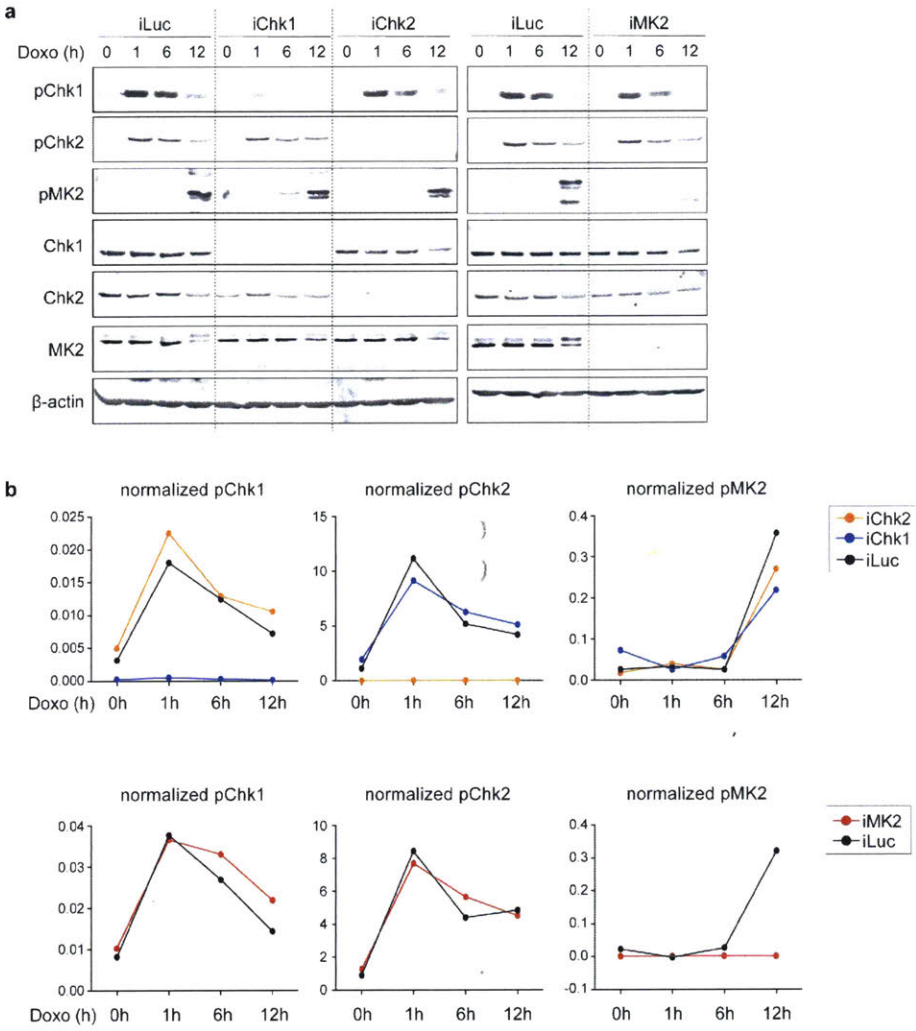
a
iLuc
iChk1
iChk2
iLuc
iMK2
Doxo (h) 0 1 6 12 0 1 6 12 0 1 6 12 0 1 6 12 0 1 6 12
pChk1
pChk2
pMK2
Chk1
Chk2
MK2
β-actin
b
normalized pChk1
normalized pChk2
normalized pMK2
iChk2
iChk1
iLuc
Doxo (h) 0h 1h 6h 12h
normalized pChk1
normalized pChk2
normalized pMK2
iMK2
iLuc
Doxo (h) 0h 1h 6h 12h

Figure 3-13: Time course of checkpoint kinase signaling in U2OS cells following inducible knockdown of individual checkpoint kinases. **(a)** Stable U2OS cell lines with doxycycline-inducible knockdown of Luciferase (iLuc, used as WT control), Chk1 (iChk1), Chk2 (iChk2) or MK2 (iMK2) were generated. Four days after doxycycline addition to induce knockdown, cells were treated with 5 μM doxorubicin for shorter (3 hrs) or longer (12 hrs) periods of time, and cell lysates were collected for Western blot analysis. Phosphorylation-specific antibodies against Ser345 of Chk1, T68 of Chk2, and T334 of MK2, are used as surrogates for checkpoint kinase activation. **(b)** Western blot band intensity determined by quantification of LiCor signal using ImageStudio software. Activity of each checkpoint kinase activity was determined by normalization of phospho-specific signal to its non-phospho signal if the checkpoint kinase is not the one depleted. If the checkpoint kinase is depleted, the activity of that kinase was determined by normalization of phospho-specific signal to β-actin. For example, in the top left graph, normalized pChk1 is calculated by dividing the pChk1 signal intensity to Chk1 in iLuc (black curve) and iChk2 (yellow curve) cells, but in iChk1 (blue curve) cells the normalized pChk1 is calculated by dividing pChk1 signal intensity to β-actin because the Chk1 basal level is too low.

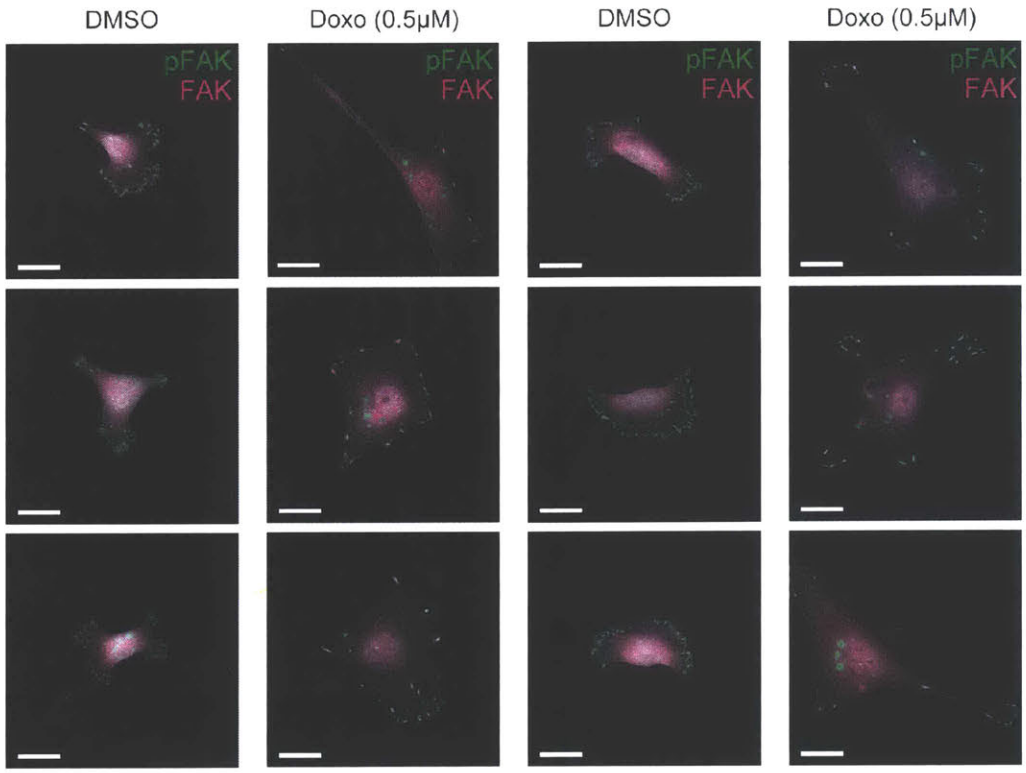

Figure 3-14: Additional images from the same experiment in 3-6a. MDA-MB-231 cells were treated with DMSO (control) or doxorubicin (0.5 μM), immunostained for p-FAK (Y397) and total FAK at 24 hrs post-treatment to assess changes in focal adhesion organization. Scale bars, 20 μm.

Chapter 4

Doxorubicin chemotherapy alters actomyosin signaling that contributes to cell shape determination and survival

4.1 Overview

In Chapter 3, we analyzed the checkpoint kinase-regulated phospho-protein network altered by sub-lethal doxorubicin treatment. This network was highly enriched in dozens of cytoskeleton- and actomyosin-associated proteins that may coordinate the changes in morphology, motility, and survival induced by the drug. In this chapter, we apply the image processing and analysis tools developed in Chapter 2 together with the phosphoproteomics data analyses performed in Chapter 3 to hone in on a putative mechanism of action that regulates these changes. In this chapter, multivariate analysis of cell shape changes induced by doxorubicin and a number of targeted inhibitors of actomyosin cytoskeleton regulators revealed morphological similarities between doxorubicin-treated cells and those treated with Rho associated kinase (ROCK) or Myosin II ATPase inhibitors. Live-cell imaging demonstrated that although both doxorubicin and the ROCK inhibitor promoted morphological cell elongation by 24 hrs of treatment, they achieve this effect with different kinetics. Using a combination of population-level and single-cell assays, measurement of myosin light chain phosphorylation on S19 (pMLC), a site involved in actomyosin contractility regulation, revealed that doxorubicin promotes a biphasic pMLC response over time – levels increased by 12 hrs, but were subsequently reduced below baseline by 24 hrs after start of treatment. Constitutive activation of Rho, an upstream activator of pMLC, increased pMLC levels back to baseline when administered in combination with doxorubicin. Rho activation also reduced cellular tolerance to a higher-dose, secondary round of drug treatment. Additional analyses of cell morphology and contractility in a 3D microenvironment *in vitro* recapitulated the morphological changes observed in 2D and showed that doxorubicin treatment diminished cell-mediated gel contraction.

4.2 Results

4.2.1 Pharmacological inhibition of myosin II and ROCK, but not MLCK, phenocopies sub-lethal dose of doxorubicin treatment

Phosphoproteomics data analysis in Chapter 3 revealed that actomyosin cytoskeleton-associated phosphoproteins were upregulated by 12 hrs of doxorubicin treatment in U2OS osteosarcoma cells (Fig. 3-1 and Fig. 3-4). This altered signaling was accompanied by pronounced changes in cytoskeletal organization and cell shape both in U2OS cells (Fig. 3-9) and, at 24 hrs post-treatment, in the triple-negative breast cancer cell line MDA-MB-231 (Fig. 3-2). In order to converge on a more detailed, putative downstream signaling mechanism that may mediate these morphological changes, we took a high-content, image-based phenotypic profiling approach. Morphological phenotypes induced by pharmacological inhibition of individual actomyosin regulators (Chapter 2) were compared with the morphological changes induced by sub-lethal doxorubicin treatment (Fig. 4-1). These regulators included myosin light-chain kinase (MLCK) and Rho-associated kinase (ROCK), two ubiquitous enzymatic regulators of actomyosin contractility (Chapter 1), as well as the ATPase region of the heads of myosin II heavy chains. F-actin staining at 24 hrs following compound treatment showed visually-discernible morphological elongation of MDA-MB-231 cells following ROCK and myosin II ATPase inhibition with Y-27632 and Blebbistatin, respectively, but not upon MLCK inhibition with ML-7 (Fig. 4-1a). These findings recapitulated the morphological effects induced by these drugs in live-cell experiments discussed in Chapter 2.

Altered cytoskeletal signaling and organization can give rise to a wide variety of complex cellular morphologies that contribute to critical processes such as cell migration and survival. In order to capture and summarize this complexity in our system, we performed a multivariate shape analysis to measure eighteen features that capture various aspects of cell shape (Table B.1). In order to visualize this morphological complexity, we performed dimensionality reduction using principal component analysis (PCA) on the shape feature variables across single-cell observations and represented this PCA "shape space" within a polar coordinate system (Fig. 4-1b). The detailed methods for this approach are described in Appendix A.5. Interestingly, as was also determined in the work described in Chapter 2, cellular major axis length was aligned in the positive (increasing) direction of the first principal component (Fig. 4-1b), indicating that cellular elongation is a key morphological feature that contributes to the observed variability in cell shape under the treatment conditions studied here (actomyosin inhibitors and doxorubicin).

We next projected the cell populations onto the principal component shape space from each treatment condition in order to compare the multivariate shape representations that the treatments induced. As shown in Fig. 4-1c, ROCK and Myosin II ATPase inhibition, as well as doxorubicin treatment, increased the fraction of thinner, elongated cell morphologies in the polar coordinate shape space representation between 0° and 30°, and between 330° and 0° (0° equivalent to 360° in shape space). A key insight from this multivariate analysis is that morphologies with large PC1 values and intermediate-to-low PC2 values differ from larger, rounded morphologies with low aspect ratios, which exhibit larger values of major axis length (PC1) but also have larger values in PC2. Cells with larger PC1 and PC2 values are large flat cells that are frequently not polarized and are non-migratory. In contrast, as discussed in Chapter 3, the cells with thinner, elongated cell bodied exhibit more directionally persistent motility (Fig. 3-3).

Although ROCK inhibition and sub-lethal doxorubicin treatment produced similar elongated morphologies at 24 hours following treatment, we wished to compare the kinetics with which this morphological response is attained under the two treatments. Using MDA-MB-231 cells stably expressing LifeAct-eGFP and Histone H2B-mCherry, we performed live cell imaging under DMSO (control), ROCK inhibitor, and doxorubicin treatments and characterized cellular elongation (major axis length) over approximately 1 day. As shown in Fig. 4-1d, we first confirmed that prior to treatment the cell populations showed similar elongation, but after treatment application at 8 hours after start of imaging, the treatments exhibited diverse morphological responses. The average elongation of DMSO (control) treated cells remained unchanged following treatment. ROCK inhibition produced rapid cellular elongation within minutes of treatment that was maintained over the remaining approximately 20 hours of the live imaging experiment. On the other hand, the morphological elongation of doxorubicin-treated cells steadily increased, on average, after approximately 10 to 12 hours following drug treatment. Both ROCK inhibition and doxorubicin showed similar elongation at the end of the experiment (Fig. 4-1d) as was found from the fixed-cell shape analysis (Fig. 4-1a,c). These findings show that doxorubicin-induced elogation has slower kinetics than the more rapid effects of small-molecule inhibition of ROCK.

4.2.2 pMLC exhibits a biphasic temporal response to doxorubicin

ROCK regulates intracellular actomyosin tension and contractility in part through phosphorylation of the myosin light chain on S19 (pMLC). The observation that ROCK and Myosin II ATPase inhibition produced elongated morphological phenotypes similar to those induced by doxorubicin treatment (Fig. 4-1), led us to ask whether doxorubicin alters pMLC signaling in MDA-MB-231 cells. The SILAC phosphoproteomic screen described in Chapter 2 revealed that pMLC was significantly upregulated upon doxorubicin treatment at 12 hours in U2OS cells (Fig. 4-2a). The SILAC screen that incorporated inducible knockdown of each of the checkpoint kinases we studied, Chk1, Chk2, and MK2, showed that pMLC(S19) phosphopeptide levels were reduced upon knockdown of each kinase in the context of doxorubicin treatment.

Guided by these observations we next assayed for population-average levels of pMLC in MDA-MB-231 cells at 24 hours following treatment, at a time point at which these cells exhibited elongated morphologies (Fig. 3-2 and Fig. 4-1). Intriguingly, pMLC was reduced by doxorubicin treatment by 24 hours following treatment in MDA-MB-231 cells compared with DMSO (control) or Myosin II ATPase inhibtion with Blebbistatin (negative control for pMLC reduction), while total ROCK levels remained unchanged. The pMLC levels decreased with increasing doxorubicin dose, with 1 μM dose producing lower levels than 0.5 μM dose. This decrease in pMLC levels was comparable to that induced by pharmacological inhibition of ROCK and MLCK, which are known positive regulators of pMLC. Interestingly, the doxorubicin-induced decrease in pMLC levels could be reversed and markedly increased by short-term pharmacological inhibition of phosphatases using Calyculin A. This compound blocks the activity of numerous cellular phosphatases, including myosin light chain phosphatase that is involved in pMLC de-phosphorylation and acts in the reverse direction of MLCK- and ROCK-induced upregulation of pMLC. Moreover, although we have previously shown that doxorubicin altered focal adhesion number and organization (Fig. 3-6), doxorubicin treatment did not alter total pFAK (Y397) levels in the cell population by 24 hours compared to DMSO control, while ROCK inhibition led to a marked reduction in total pFAK (Fig. 4-2d).

The potentially discrepant observation that pMLC levels increased at 12 hours in U2OS cells in the SILAC screen (Fig. 4-2a), but decreased at 24 hours following doxorubicin treatment in MDA-MB-231 cells (Fig. 4-2b), led us to perform a time course analysis of pMLC following doxorubicin treatment. We treated multiple MDA-MB-231 cultures with 0.5 μM doxorubicin and assayed for total pMLC and MLC levels by Western blotting at multiple time points (4, 8, 12, 16, 20, and 24 hours) following treatment (Fig. 4-2e). Intriguingly, pMLC levels exhibited a biphasic response over time – levels increased up to 12 hours, and then progressively decreased below DMSO (control) levels from 12 to 24 hours following treatment. Short-term (25 min) treatment of doxorubicin-treated cells at 24 hours with Ionomycin, an ionophore that increases intracellular Calcium that activates MLCK, was able to increase pMLC levels. Collectively, these findings suggest that the progressive decrease in pMLC levels upon sub-lethal doxorubicin treatment between 12 to 24 hours after start of treatment can be reversed by pharmacological manipulation of the actomyosin signaling machinery that regulates the balance of phospho and non-phopsho forms of MLC.

4.2.3 Rho activation diminishes doxorubicin-induced effects on pMLC

The RhoA GTPase is a positive regulator of intracellular actomyosin tension and stress fiber formation that promotes MLC phosphorylation through ROCK activation. We therefore investigated whether constitutive activation of RhoA could reverse doxorubicin-induced reduction in pMLC. To achieve this, we used a Rho activator that is based on a cell-permeant version of the catalytic domain of the bacterial CNF toxin. This activator enters the cell and activates numerous Rho GTPase isoforms by deamidating glutamine-63, which is located in the switch II region of Rho GTPases [69]. This deamination converts glutamine-63 to glutamate, which blocks intrinsic and GAP-stimulated GTPase activity that results in constitutive Rho activation.

We first developed and applied an imaging-based high-content screening assay to simultaneously measure MLC and pMLC levels on a single-cell level. This assay additionally enabled concurrent quantification of cellular morphology of the same cells in which the signals were measured (Fig. 4-3a). In agreement with the previous population-level measurements (Fig. 4-2), image-based characterization revealed that a 0.5 μM sub-lethal dose of doxoubicin decreased pMLC levels (compare gray box plots in Fig. 4-3b). ROCK inhibition with Y-27632 also decreased pMLC levels relative to control, as expected. When administered concurrently with doxorubicin, Rho activator increased pMLC back to baseline levels (compare (a) and (b) distributions in Fig. 4-3b). Although pMLC levels were altered by Rho activation, cellular elongation was not (Fig. 4-3c). This observation suggests that RhoA-mediated increase in pMLC may be decoupled from morphological elongation in our system, but does not necessarily preclude a possible direct relationship between pMLC and cell elongation under the effects of doxorubicin.

4.2.4 Morphological elongation induced by sub-lethal doxorubicin is associated with enhanced cell survival following higher-dose secondary treatment

Having established that doxorubicin promotes changes in cell shape (Fig. 3-2 and Fig. 4-1), we next asked whether these morphological alterations provide a cell survival advantage. To test this, we performed a time course experiment with two sequential rounds of doxorubicin treatment. First, MDA-MB-231 cells expressing LifeAct-eGFP and H2B-mCherry

were pre-treated with a 0.5 μM dose, which, as found earlier, increased cell elongation. After 24 hours of pre-treatment with either DMSO or doxorubicin, we added a higher dose of doxorubicin (2 μM) along with a live-cell apoptosis reporter, fluorophore-conjugated AnnexinV, and concurrently tracked cell shape changes and apoptosis dynamics for 90 hours via fluorescence microscopy (Fig. 4-4a). Interestingly, the death rates of cells pre-treated with doxorubicin were bi-modally distributed, as assessed by Gaussian mixture model fitting (Fig. 4-4b). One cell subpopulation died more quickly, within approximately 44 hours following treatment with the higher 2 μM doxorubicin dose (red subpopulation in Fig. 4-4c), while a second subpopulation died more slowly (blue subpopulation in Fig. 4-4c). Intriguingly, we found that the subpopulation of cells pre-treated with 0.5 μM doxorubicin that died more slowly was, on average, more elongated just prior to higher-dose exposure. On the other hand, cells that were not pre-treated with doxorubicin had similar morphological elongation regardless of cell death rate (Fig. 4-4d,e). Cells that were more elongated following doxorubicin pre-treatment that died more slowly upon higher-dose exposure appeared to lose cell polarity and exhibited abnormal, branched-like morphologies during the course of treatment (Fig. 4-4f). The enhanced tolerance to secondary doxorubicin treatment that was applied immediately after pre-treatment here, is in agreement with the long-term tolerance (Chapter 3) that was potentiated by doxorubicin pre-treatment over 1 month of washout prior to secondary exposure.

4.2.5 Rho activation enhances apoptosis of doxorubicin pre-treated cells following secondary higher-dose treatment

Constitutive Rho activation reversed pMLC reduction induced by doxorubicin (Fig. 4-3b). In an effort to link pMLC reduction with chemo-tolerance conferred by doxorubicin pre-treatment (Fig. 4-4a-f), we investigated the effect of Rho activation during doxorubicin pre-treatment on subsequent cell survival following a second round of drug threatment with a higher dose. Cell survival was not affected by Rho activation in the absense of doxorubicin pre-treatment following secondary drug exposure (compare purple and green curves in Fig. 4-4g left sub-panel). On the other hand, although doxorubicin treatment blocked cell proliferation under all conditions (Fig. 4-4g right sub-panel), MDA-MB-231 cells co-treated with Rho activator and 0.5 μM doxorubicin were more sensitive, on average, to secondary drug treatment than cells that were pre-treated with doxorubicin in the absence of the Rho activator (compare brown and orange curves in Fig. 4-4g left sub-panel).

4.2.6 Doxorubicin increases cell elongation and decreases contractility *in vitro* within 3D Collagen I matrix

Although all of our studies to this point were performed in 2D microenvironments that function as convenient model systems for signaling studies, it is well appreciated that cellular structure and function in 3D better recapitulates the *in vivo* environment. We therefore first sought to assess the effects of sub-lethal doxorubuicin on cellular morphology in 3D. MDA-MB-231 cells stably expressing LifeAct-eGFP and H2B-mCherry were embedded in 3D gels composed of collagen I, a core extracellular matrix component commonly present in the tumor microenvironment *in vivo*. These cells were then treated with DMSO (control) or with sub-lethal doses of doxorubicin, fixed and imaged in the gels using confocal fluorescence microscopy 24 hours after treatment (Fig. 4-5a). Using 3D image processing and analysis tools, isolated (non-touching) cells were then detected and segmented in 3D, enabling us to

quantify morphological changes induced by the drug (Fig. 4-5b). As we found previously in the 2D system (Fig. 4-1), sub-lethal doxorubicin also increased morphological elongation of cells in 3D (Fig. 4-5c).

Finally, because pMLC levels regulate intracellular actomyosin tension and contractility, doxorubicin-induced reduction in pMLC may alter these biophysical processes. To assess whether sub-lethal doxorubicin modulates cellular actomyosin contractility we performed a 3D gel contraction assay. In this assay, cells engage with the extra-cellular matrix through focal adhesions that bridge the actomyosin cytoskeleton with the surrounding matrix. Reduced actomyosin tension will proportedly diminish contraction of the matrix, which can be directly measured via imaging of the gels over time following treatment with compounds of interest (Fig. 4-6a). As expected, pharmacological inhibition of positive regulators of pMLC, ROCK or myosin II ATPase, reduced gel contraction over 60 hours following compound addition (Fig. 4-6b, yellow and pink bars). Interestingly, doxorubicin treatment at 0.5 or 1 μM produced similar gel contraction as DMSO (control) at the 18-hour time point, but subsequently significantly reduced contraction of the gels measured at 42 and 60 hours following treatment (Fig. 4-6b, gray, blue, and green bars). As shown in Fig. 4-6c, at 60 hours after treatment all conditions had comparable cell survival, with the exception of 1 μM doxorubicin that led to a slight decrease in cell viability, suggesting that reduced gel contraction may in part be attributed to altered cellular contractility in the days following doxorubicin exposure.

4.3 Discussion

Here, we studied the effects of sub-lethal doses of doxorubicin chemotherapy on actomyosin signaling and the associated biophysical processes that control cellular contractility and morphology in 3D *in vitro* collagen matrices. Our previous SILAC prosphoproteomic analysis (Chapter 3) revealed that phosphorylation of myosin light chain on S19 (pMLC), a positive regulator of actomyosin contraction, was upregulated in U2OS osteosarcoma cells within 12 hours following sub-lethal doxorubicin treatment (Fig. 4-2a). This effect was recapitulated in MDA-MB-231 breast cancer cells, and a time course experiment showed a biphasic temporal response of pMLC levels following drug exposure, with a pronounced increase at 12 hours and a decrease by 24 hours in pMLC levels following treatment (Fig. 4-2e). This reduction in pMLC was associated with increased cellular elongation both in 2D and 3D, which phenocopied the effects of ROCK and myosin II ATPase inhibition (Figs. 4-1 and 4-5), potentially implicating decreased pMLC in the manifestation of this morphological phenotype. As a potential biophysical consequence of these effects, sub-lethal doxorubicin also reduced cell-mediated contraction of 3D collagen I matrices (Figs. 4-6). In an effort to understand the permanence of these alterations, we further found that constitutive activation of Rho GTPases during doxorubicin treatment reversed the effects on both pMLC levels (Figs. 4-3b) and the enhanced chemo-tolerance to secondary treatment potentiated by a 24-hour pre-treatment with the drug (Figs. 4-4g).

The actomyosin machinery plays a central role in cell shape determination and motility both on planar 2D surfaces and in 3D microenvironments. The two principal modes of cell migration are mesenchymal and amoeboid, whose manifestation in any particular microenvironmental context relies heavily on actomyosin signaling and contractility [78, 38, 195, 201]. Amoeboid migration is characterized by cellular squeezing through pores in the ECM that is mediated in part through periodic actomyosin contractions at the trailing end and periph-

ery of a cell. These contractions propel cells forward in low-adhesion microenvironments; this process is often described as a cell "pushing-off" of the surrounding substrate [155]. In contrast, mesenchymal migration, which occurs in 3D but is the principal mode of motility in 2D, is adhesion-dependent. It is characterized by the motility cycle of leading edge protrusion, adhesion, transcellular contractility, and trailing end retraction [145] (Fig. 1-3). Although mesenchymal motility involves actomyosin contraction, it is less dependent on it than the amoeboid mode. Here, we did not investigate the effects of doxorubicin on these two migration modes directly, but we speculate that doxorubicin-induced reduction in pMLC would hinder actomyosin contractility-dependent amoeboid motility. This effect could alter the metastatic propensity of cancer cells in low-adhesion environments, but it may also adversely affect the motility of other important immune cell types, such as leukocytes. These immune cells, which include neutrophils, T, and B cells, require actomyosin contraction to squeeze their nuclei through matrix pores during migration, suggesting that doxorubicin-induced impairment of this machinery could alter immune function [141].

Interestingly, we found that doxorubicin-induced reduction in pMLC could be reversed rapidly by PP1/PP2a phosphatase inhibition with Calyculin A (Fig. 4-2c,e), by ionophore-mediated increase in intracellular Calcium (Fig. 4-2e), or by Rho activation (Fig. 4-3). As PP1 and PP1a phosphatases act on many substrates, one of which is myosin light chain phosphatase (MLCP) that dephosphorylates MLC [202], it is possible that the resulting increase in pMLC following Calyculin A treatment may be an indirect effect through proteins other than MLCP. Intracellular Calcium promotes myosin light chain kinase (MLCK) activation through CaMKII [202], which increases pMLC levels, suggesting that doxorubicin-induced reduction in pMLC can be reversed by increasing MLCK activity. The GTPase RhoA activates ROCK that leads to MLCP inhibition, demonstrating that doxorubicin effects on pMLC can also be reversed by activation of ROCK signaling (Fig. 4-3b). These findings collectively suggest that doxorubicin may alter actomyosin signaling by shifting the balance from phosphorylated to unphosphorylated MLC, with the core actomyosin regulatory machinery (e.g., MLCK, ROCK, and MLCP) remaining functionally intact.

Although ROCK inhibition expectedly led to rapid cellular elongation and formation of multiple protrusions within minutes of treatment as a result of decreased actomyosin tension, doxorubicin showed a similar, but delayed, response. MDA-MB-231 breast cancer cells started to elongate only at around 12 hours following treatment; this elongation continued to increase through 24 hours (Fig. 4-1d). In temporal alignment with this morphological response, a separate experiment showed that pMLC levels decreased in the same time range from 12 to 24 hours following doxorubicin treatment (Fig. 4-2e). This suggests that reduced pMLC levels may be directly related to the morphological elongation observed in doxorubicin-treated cells. Moreover, cell-mediated gel contraction in 3D collagen matrices was also delayed under doxorubicin treatment compared with ROCK inhibition (Fig. 4-6). These effects further lend support to the possible link between changes in actomyosin signaling, morphological elongation, and cellular contractility that are altered by sub-lethal doses of doxorubicin.

One intriguing possibility is that doxorubicin-induced changes in adhesion-associated substrates of checkpoint kinases (Chapter 3) may result in altered pMLC, morphology, and contractility. Indeed, one checkpoint-kinase substrate phosphosite that we extensively characterized in Chapter 3, PPP1R12A (a.k.a. MYPT1) (S507), is a direct regulator of actomyosin organization. MYPT1 is a myosin phosphatase regulatory subunit that is a canonical substrate of ROCK. ROCK-mediated phosphorylation of MYPT1 on T696 and T853 results in the inhibition of myosin phosphatase and increase in pMLC [236, 202].

Although the role of the checkpoint kinase target residue of pMYPT1 (S507) remains uncharacterized, it is possible that this site may also regulate myosin phosphatase activity, which could be responsible for doxorubicin-induced changes in pMLC. In addition, many other adhesion and actomyosin-associated proteins were differentially phosphorylated in a checkpoint kinase-dependent manner upon doxorubicin treatment, including FLNA, TLN, and TNS1, among others (Chapter 3). It is well established that focal adhesion signaling and remodeling is tightly coupled to the organization and function of the actomyosin cytoskeleton [30, 101, 286, 10, 18], suggesting that altered signaling and/or organization of focal adhesions (Fig. 3-6) may be directly coupled to altered pMLC and actomyosin function in doxorubicin-treated cells. As a result, although checkpoint kinases may directly phosphorylate MLC leading to higher pMLC levels by 12 hours after DNA damage (Fig. 4-1), at later time points (e.g., 24 hours onward) the altered cellular adhesome could be responsible for the decrease in pMLC levels and the associated morphological elongation we observed.

Finally, doxorubicin-induced reduction in pMLC may also explain the increased long- and short-term chemo-tolerance of cells pre-treated with sub-lethal doxorubicin to subsequent treatment with higher doses of the drug. In Chapter 3, we showed that pre-treatment of MDA-MB-231 breast cancer cells with sub-lethal 0.5 μM doxorubicin for 24 hours potentiates increased cell survival upon a second round of treatment even after 1 month of culture in the absence of the drug (Fig. 3-7). We also established that doxorubicin-induced morphological elongation was associated with decreased rates of cell death following higher dose exposure (Figs. 3-6h-j and 4-4a-f). Taken together with the fact that doxorubicin treatment reduced pMLC levels that were also associated with morphological elongation, we speculate that decreased pMLC results in reduced actomyosin contraction that enhances cell survival. Previous studies have shown that ROCK deletion, which reduces pMLC levels, enhances survival of mouse embryonic fibroblasts following doxorubicin treatment [246, 234]. Reduced actomyosin tension is also associated with higher levels of embryonic stem cell (ESC) [44] and induced pluripotent stem cell (iPSC) [279] viability *in vitro*. In these systems, ROCK and Myosin II ATPase inhibitors are commonly supplemented into growth media to improve ESC and iPSC viability during long-term culture. Pharmacological inhibition of ROCK, which leads to reduced pMLC levels, has also been used to immortalize epithelial cells and enhance survival of normal and tumor cells derived from primary human tissue of various origins during *in vitro* culture [152, 56, 39, 153]. We hypothesize that reduced pMLC levels induced by sub-lethal doxorubicin could also enhance breast cancer cell survival in our system. In support of this, constitutive activation of Rho (an upstream positive regulator of ROCK and pMLC) during doxorubicin pre-treatment, enhanced MDA-MB-231 cell death upon treatment with a secondary doxorubicin dose (Fig. 4-4g). As typical doxorubicin regimens in the clinic involve multiple rounds of treatment, these findings highlight the undesirable consequences of sub-maximal tumor eradication at early phases of treatment. Although our studies have established numerous associations, future studies will be necessary to reveal any causative links between doxorubicin-induced checkpoint kinase signaling, pMLC dynamics, cell morphology, contractility, and survival.

4.4 Acknowledgements

This work was funded by grant R01-GM069668 to Profs. Douglas Lauffenburger and Alan Wells. Simon Gordonov was supported by a Whitaker Health Sciences Fund Fellowship.

4.5 Figures

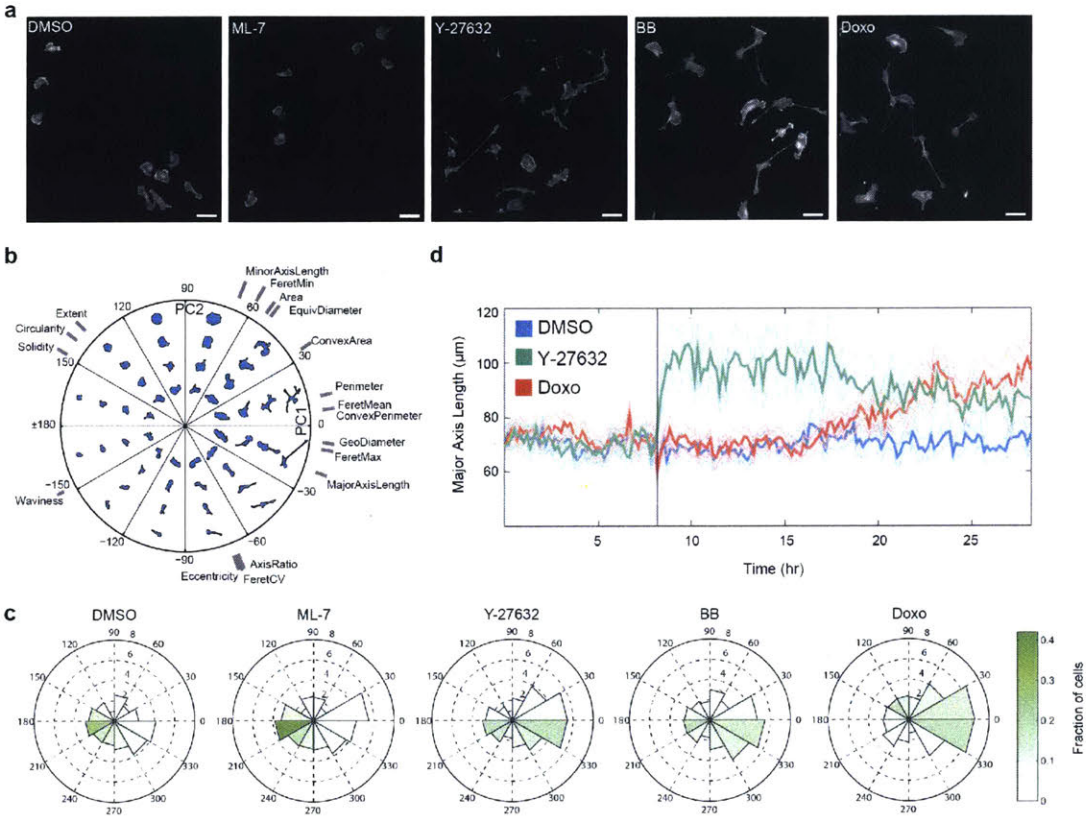
a
DMSO
ML-7
Y-27632
BB
Doxo
b
PC2
PC1
MinorAxisLength
FeretMin
Area
EquivDiameter
ConvexArea
Perimeter
FeretMean
ConvexPerimeter
GeoDiameter
FeretMax
MajorAxisLength
AxisRatio
FeretCV
Eccentricity
Waviness
Extent
Circularity
Solidity
d
DMSO
Y-27632
Doxo
Major Axis Length (μm)
Time (hr)
c
DMSO
ML-7
Y-27632
BB
Doxo
Fraction of cells

Figure 4-1: Doxorubicin-induced changes in cell shape phenocopy the effects of pharmacological ROCK and myosin II inhibition. **(a)** Representative images of MDA-MB-231 cells stained for F-actin (fluorophore-conjugated phalloidin) 24 hrs after treatment with DMSO (control), ML-7 (MLCK inhibitor, 20 μM), Y-27632 (ROCK inhibitor, 10 μM), BB (Blebbistatin, myosin II ATPase inhibitor, 10 μM), Doxo (Doxorubicin, 0.5 μM). Scale bars, 60 μm. **(b)** Polar visualization of principal component analysis (PCA) of cellular morphologies from treatments in (a). PC1 and PC2 correspond to the first and second principal component axes, respectively. Orientation and location of shape features used for PCA signify directions in which the features increase in magnitude. Analysis was performed as in Fig. 2-3C. Shape feature descriptions are specified in Table B.1. **(c)** Rose plot quantification of morphological changes induced by treatments in (a) within the polar PCA shape space in (b). Each angular bin (petal) represents a slice of PCA shape space spanning the angular range of 30° intervals. Petal length corresponds to the average distance of cells in the bin from the origin (center of PCA shape space circle), signifying the average magnitude of the features in a given direction in (b). Petal shading corresponds to the fraction of cells within the measured cell population in each treatment condition that falls with a particular angular bin in PCA shape space. **(d)** Comparison of morphological elongation dynamics following doxorubicin treatment or ROCK inhibition. Vertical black line within the plot indicates time when treatment was added (DMSO, 10 μM Y-27632, or 0.5 μM doxorubicin). Thick colored lines correspond to the means, shading is the (+/-) 95% CI from all tracked cells per condition.

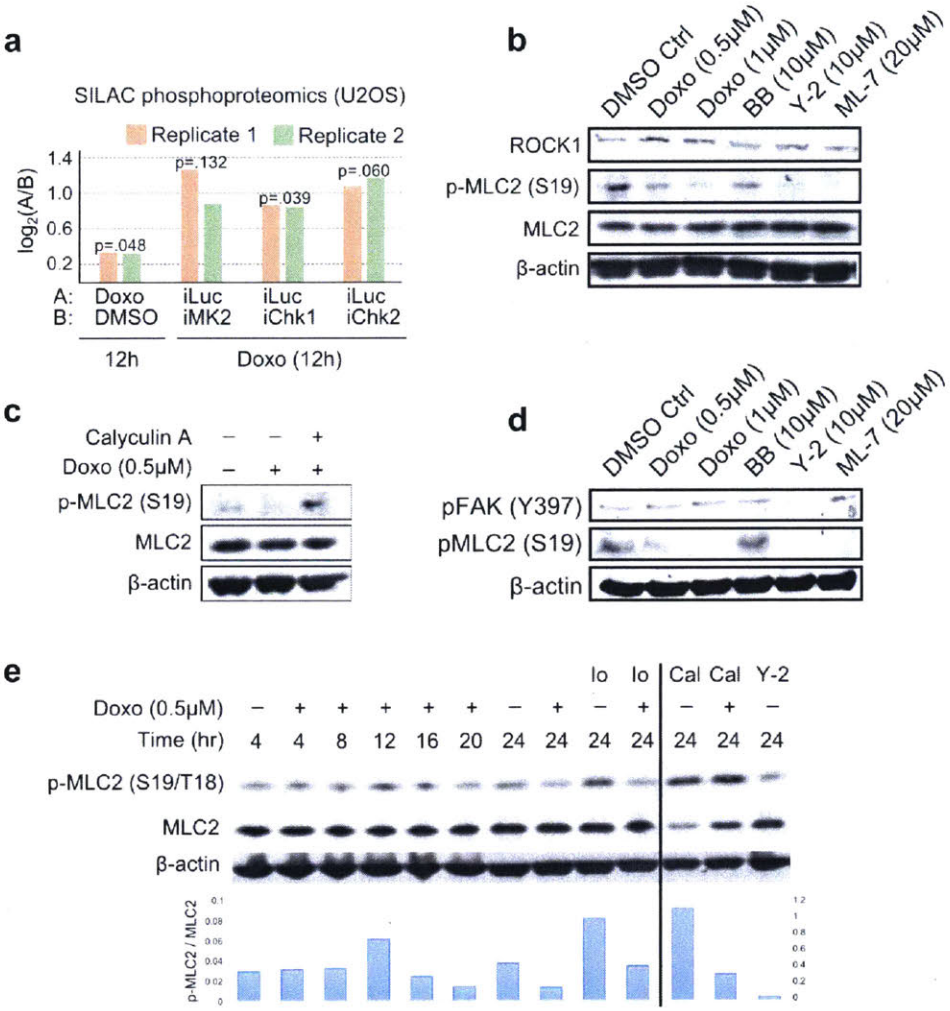
a
SILAC phosphoproteomics (U2OS)
Replicate 1
Replicate 2
log2(A/B)
1.4
1.0
0.6
0.2
p=.048
p=.132
p=.039
p=.060
A: Doxo
B: DMSO
iLuc
iMK2
iLuc
iChk1
iLuc
iChk2
12h
Doxo (12h)
b
DMSO Ctrl
Doxo (0.5μM)
Doxo (1μM)
BB (10μM)
Y-2 (10μM)
ML-7 (20μM)
ROCK1
p-MLC2 (S19)
MLC2
β-actin
c
Calyculin A
Doxo (0.5μM)
p-MLC2 (S19)
MLC2
β-actin
d
DMSO Ctrl
Doxo (0.5μM)
Doxo (1μM)
BB (10μM)
Y-2 (10μM)
ML-7 (20μM)
pFAK (Y397)
pMLC2 (S19)
β-actin
e
Io
Io
Cal
Cal
Y-2
Doxo (0.5μM)
Time (hr)
4 4 8 12 16 20 24 24 24 24 24 24 24
p-MLC2 (S19/T18)
MLC2
β-actin
p-MLC2 / MLC2

Figure 4-2: Doxorubicin promotes biphasic temporal phosphorylation of myosin light chain. **(a)** Effect of doxorubicin treatment (5 μM) in the presence or absence of inducible shRNA-based checkpoint kinase knockdown on myosin light chain phosphopeptide (pMLC on S19) in U2OS osteosarcoma cells. Data was derived from the SILAC phosphoproteomic screen analyzed in Chapter 3. The two technical replicates from the screen are shown in orange and green. Positive values correspond to upregulation of pMLC under condition "A" relative to condition "B" shown. The "i" in front of Luc (Luciferase, control), and the checkpoint kinases Chk1, Chk2, and MK2 corresponds to inducible knockdown. *P*-values correspond to one-sample *t*-test assessing the deviation of the two replicates in each condition from zero (no change in pMLC under condition "A" and "B"). **(b)** Effects of doxorubicin treatment on myosin light chain (MLC) phosphorylation on the actomyosin contractility-activating S19 residue, with pharmacological inhibitors of ROCK (Y-27632, abbreviated Y-2) and MLCK (ML-7) known to reduce pMLC as positive controls, assayed 24 hrs post-treatment. The direct mechanism of Blebbistatin (BB)-induced inhibition of myosin II activity is independent of pMLC. **(c)** Effects of doxorubicin and actomyosin inhibitors on focal adhesion kinase (FAK) phosphorylation on the Y397 residue after 24 hrs of treatment. **(d)** Effects of PP1/PP2A phosphatase inhibition using Calyculin A on pMLC following doxorubicin treatment. Cells were treated with doxorubicin for 24 hrs, followed by 10 nM Calyculin A for 25 mins prior to cell lysis and Western blot analysis. **(e)** Time course of pMLC following sub-lethal doxorubicin treatment. Ionomycin (Io, 4 μM), an ionophore used to increase intracellular Calcium, and Calyculin A (Cal, 10 nM) were added for 25 mins following 24 hrs of treatment with doxorubicin or control, prior to cell lysis and blot analysis. Bar graph shows blot densitometry analysis of pMLC (S19/T18) using the dual-site antibody normalized to total MLC levels.

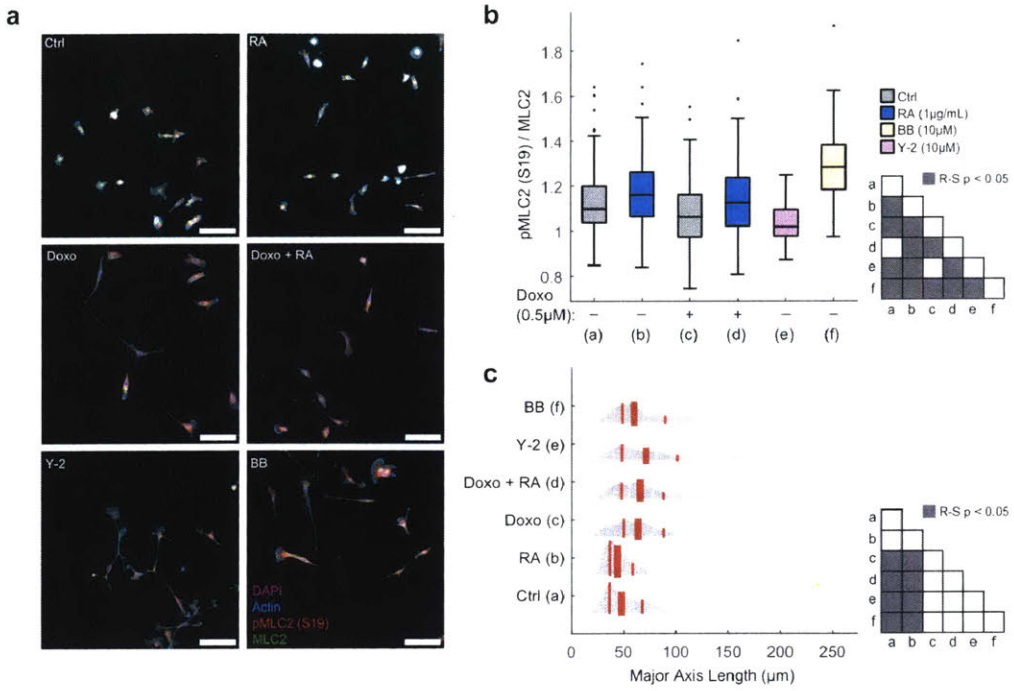

Figure 4-3: Constitutive Rho activation reverses doxorubicin-induced reduction in myosin light chain phosphorylation 24 hrs following treatment. **(a)** Representative composite images showing overlay of nuclear DNA (DAPI), F-actin (phalloidin), pMLC (S19), and total MLC. Cells were treated with doxorubicin (Doxo) or media control alone or in combination with pharmacological agent (RA) that constitutively activates Rho. BB, Blebbistatin (myosin II ATPase inhibitor); Y-2, Y-27632 (ROCK inhibitor). Scale bars, 100 μm. **(b)** Image-based quantification of single-cell levels of pMLC (S19) normalized to total MLC per cell. R-S, two-tailed Wilcoxon rank-sum test. Data shown is from n = 4 replicates. **(c)** Quantification of morphological elongation (major axis length) of cells in (a, b). In each distribution, thicker center line is the median, left and right thinner red lines are the 25th and 75th percentiles, respectively. R-S, two-tailed Wilcoxon rank-sum test.

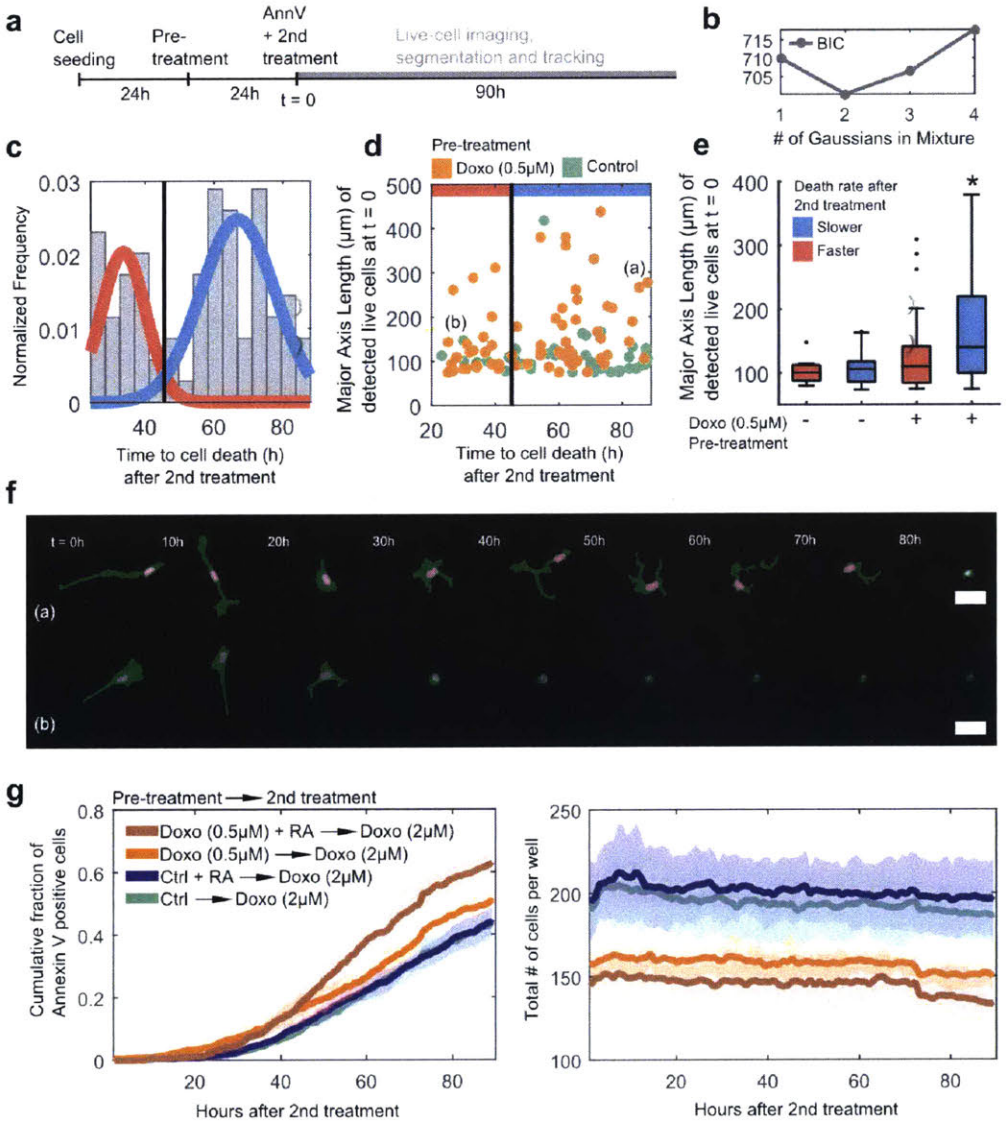
a
Cell seeding
Pre-treatment
AnnV + 2nd treatment
Live-cell imaging, segmentation and tracking
24h
24h
t = 0
90h
b
BIC
715
710
705
1
2
3
4
# of Gaussians in Mixture
c
Normalized Frequency
0.03
0.02
0.01
0
40
60
80
Time to cell death (h) after 2nd treatment
d
Pre-treatment
Doxo (0.5μM)
Control
Major Axis Length (μm) of detected live cells at t = 0
500
400
300
200
100
0
(a)
(b)
20
40
60
80
Time to cell death (h) after 2nd treatment
e
Major Axis Length (μm) of detected live cells at t = 0
400
300
200
100
Death rate after 2nd treatment
Slower
Faster
*
Doxo (0.5μM) Pre-treatment
-
-
+
+
f
t = 0h
10h
20h
30h
40h
50h
60h
70h
80h
(a)
(b)
g
Pre-treatment → 2nd treatment
Doxo (0.5μM) + RA → Doxo (2μM)
Doxo (0.5μM) → Doxo (2μM)
Ctrl + RA → Doxo (2μM)
Ctrl → Doxo (2μM)
Cumulative fraction of Annexin V positive cells
0.8
0.6
0.4
0.2
0
20
40
60
80
Hours after 2nd treatment
Total # of cells per well
250
200
150
100
20
40
60
80
Hours after 2nd treatment

Figure 4-4: Doxorubicin-induced cell elongation is associated with reduced rate of cell death upon higher dose exposure. **(a)** Schematic of the live-cell imaging workflow for concurrent analysis of cell morphology and death under sequential rounds of drug treatment. Pre-treatment was either media control or 0.5 μM doxorubicin. 2^{nd} treatment was 2 μM doxorubicin. AnnV is fluorophore-conjugated AnnexinV used as an apoptosis marker. **(b)** Bayesian information criterion (BIC) of Gaussian mixture model (GMM) fitting with different numbers of mixtures used in the models. Models were fit to the times to cell death of doxorubicin pre-treated cells. **(c)** Distribution of times to cell death with the best-fitting (2-state) model in (b). **(d)** Major axis length (MAL) of tracked cells at the time of 2^{nd} treatment addition (t = 0) plotted against their time to death (AnnexinV positive) after 2^{nd} treatment. Cells are grouped into subpopulations that died faster (red) or slower (blue), as categorized by the best-fitting 2-state GMM in (c). **(e)** Comparison of major axis lengths prior to cell death of cells that died more slowly (blue) or more quickly (red), in the presence or absence of sub-lethal (0.5 μM) doxorubicin pre-treatment. * $p < 0.05$ two-tailed Wilcoxon rank-sum test of pair-wise comparisons with all other conditions individually. **(f)** Representative images of doxorubicin pre-treated MDA-MB-231 cells tracked over time following 2^{nd} treatment, which exhibited varying degrees of elongation labeled (a) and (b) in panel (d). **(g)** Left, effects of constitutive Rho activation (RA, Rho activator) in combination with sub-lethal (0.5 μM) doxorubicin pre-treatment on cell death dynamics following higher-dose exposure with 2 μM doxorubicin. Thick lines correspond to the means, shading is (+/-) 95% CI, of n = 4 replicates. Right, total number of cells (alive and dead) per well of a 96-well plate of the same cell population tracked in the left sub-panel.

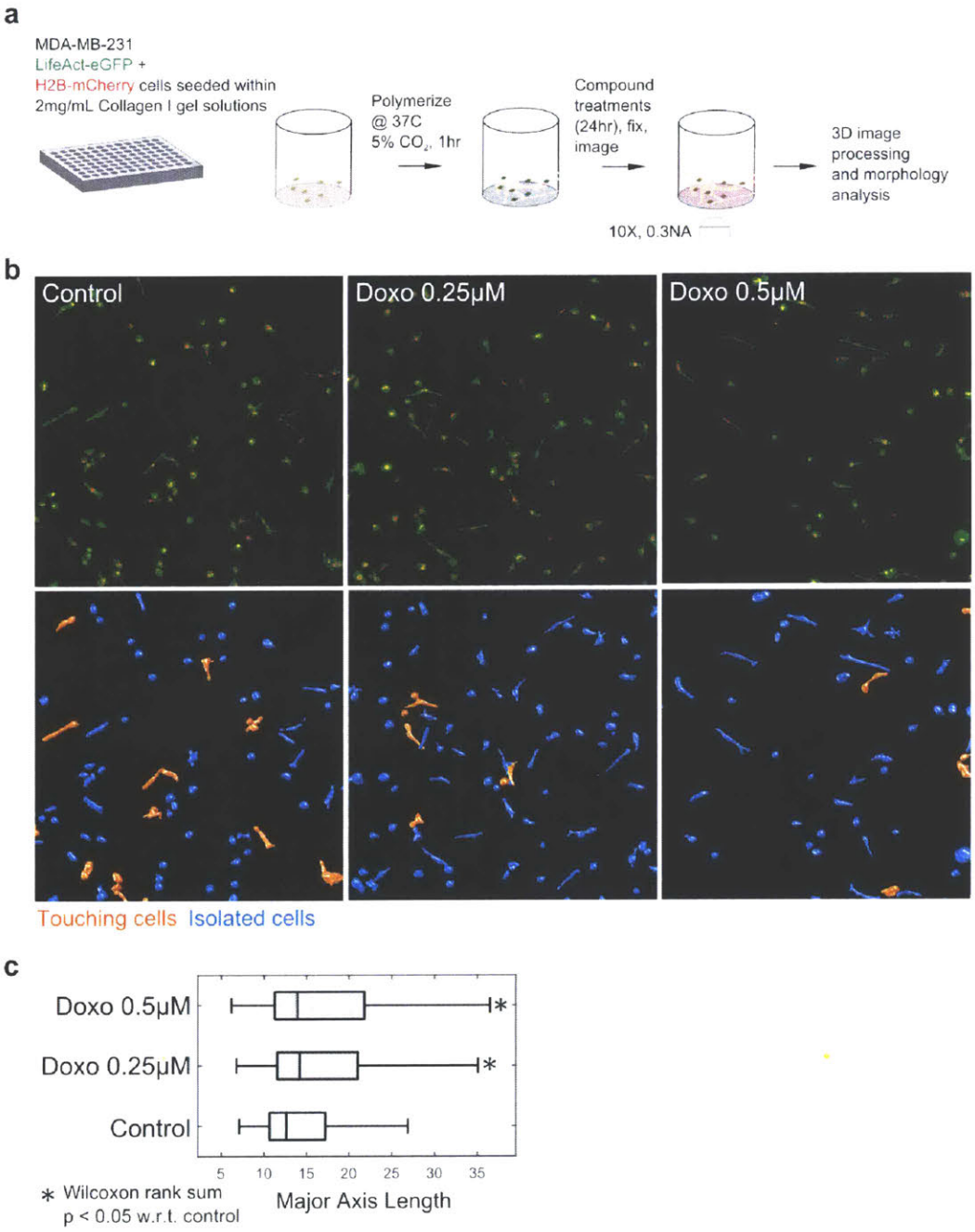

Figure 4-5: Doxorubicin increases morphological cell elongation in 3D. **(a)** Workflow schematic of cell morphology characterization in 3D Collagen I gels. **(b)** Top row: representative images of maximum (x-y) intensity projections of z-stacks acquired 24 hrs after treatment of MDA-MB-231 cells with media control or with doxorubicin at the two doses indicated. Bottom row: smoothed 3D isosurfaces of cells segmented in 3D with automated detection of touching (orange) and isolated (cyan) cells. **(c)** Effects of doxorubicin treatment on cell elongation in 3D Collagen I gels. Data shown are from n = 3 replicates for each condition. Touching cells (orange in (b)) were excluded from morphological analysis.

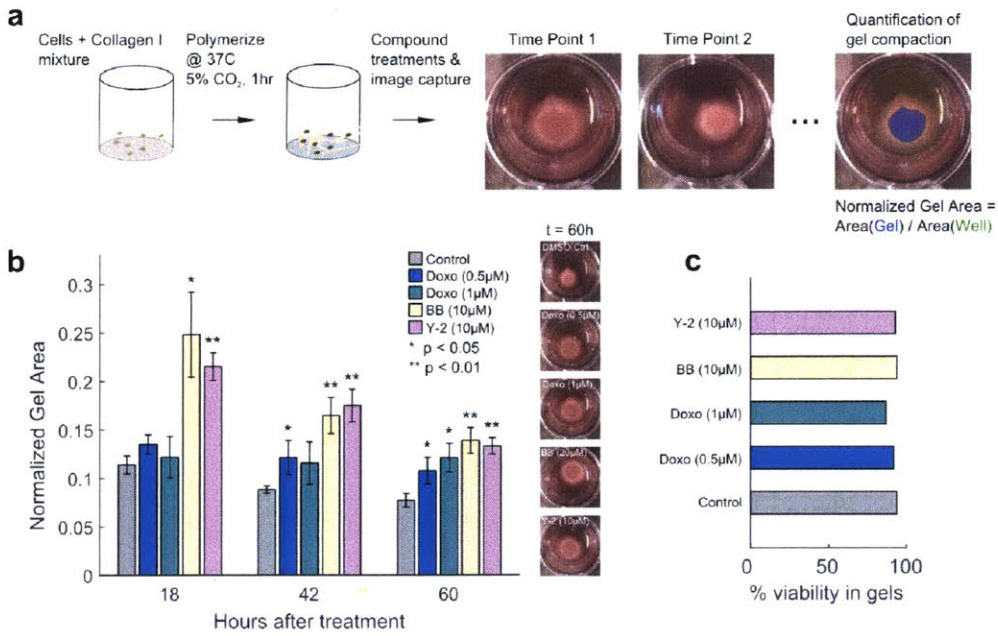

Figure 4-6: Doxorubicin reduces cell-mediated contraction of 3D collagen gels. **(a)** Workflow diagram depicting cell-mediated contraction and analysis over time of floating 3D collagen I gels. **(b)** Quantification of cell-mediated collagen I gel contraction, imaged at 3 time points following treatment with the conditions indicated. Representative gel images following 60 hrs of contraction under each condition are shown to the right of the graph. Bar height is the mean of n = 3 replicates, and error bars correspond to 95% CI. *P*-values, Student's *t*-test at 5% FDR. BB, Blebbistatin; Y-2, Y-27632; Doxo, doxorubicin. **(c)** Viability of MDA-MB-231 cells grown within the floating collagen I gels in (b) 60 hrs after start of treatment. Three gels per treatment condition were pooled for measurement. Percent viability was analyzed using the Trypan-blue exclusion assay following enzymatic gel dissociation.

Chapter 5

Multiplexed confocal and super-resolution fluorescence imaging of cytoskeletal and neuronal synapse proteins with diffusible probes

5.1 Overview

The preceding chapters demonstrated the quantification of cellular structure and function, such as morphology, migration, and apoptosis dynamics, within the same cellular population. In this chapter, I describe a generally-applicable framework that enables multiplexed fluorescence imaging of close to a dozen subcellular targets within the same sample using diffusible nucleic acid probes. Multiplexing can be achieved in either super-resolution mode, or using standard confocal microscopy. Although this chapter presents the methodology within the context of rodent-derived neurons in culture, it is directly extendable to other cellular systems for measuring multiple cytoskeletal and molecular signaling species within the same cells, including in cancer cells that are studied in this thesis. This approach is prospectively compatible with prior live-cell imaging followed by end-point, fixed-cell multiplexed imaging of subcellular signals and structural proteins. This enables linking of multiple signals (e.g., actomyosin- and adhesion-associated phosphoproteins) with phenotype (e.g., morphology, migration, apoptosis dynamics) on an individual-cell basis.

The contents of this chapter were published as:

S.-M. Guo, R. Veneziano, S. Gordonov, L. Li, D. Park, A. B. Kulesa, P. C. Blainey, J. R. Cottrell, E. S. Boyden, and M. Bathe. Multiplexed confocal and super-resolution fluorescence imaging of cytoskeletal and neuronal synapse proteins. *bioRxiv*, 2017.

Contributions

Syuan-Ming Guo (S-M.G.), Remi Veneziano (R.V.), and the author of this thesis (S.G.) contributed equally to this work. S-M.G., S.G., R.V., Edward S. Boyden (E.S.B.), and Mark Bathe (M.B.) conceived of and designed the DNA-PRISM study. S-M.G. and M.B. conceived of the LNA-PRISM study. S-M.G., Li Li (L.L.), Jeffrey R. Cottrell (J.R.C.), and M.B. designed the LNA-PRISM study. R.V. designed and implemented the antibody conjugation protocols for DNA- and LNA-PRISM. S-M.G and S.G. designed and implemented the DNA-PRISM experiments. S-M.G analyzed the DNA-PRISM data. Demian Park (D.P.) and L.L. prepared primary neuronal cultures. S-M.G., S.G., and R.V. designed and implemented the DNA-PRISM fixation, blocking, staining, probe exchange, and imaging protocols. S-M.G. and L.L. adapted the DNA-PRISM protocol for LNA-PRISM. S-M.G., L.L., and S.G. analyzed the LNA-PRISM data. S.G., Anthony B. Kulesa (A.B.K), and Paul C. Blainey (P.C.B.) designed the microfluidic device for DNA-PRISM. M.B. designed and supervised the overall project including DNA-PRISM and LNA-PRISM. J.R.C. supervised the LNA-PRISM project. S-M.G., S.G., and M.B. interpreted the DNA-PRISM results. S-M.G., S.G., L.L., J.R.C., and M.B. interpreted the LNA-PRISM results.

5.2 Abstract

Neuronal synapses contain dozens of different protein species whose spatially heterogeneous expression levels are key determinants of synaptic plasticity and signal transmission. Here, we introduce PRISM: **P**robe-based **I**maging for **S**equential **M**ultiplexing, to overcome both the spectral and spatial resolution limits of conventional light microscopy, enabling multichannel confocal and super-resolution imaging in the same cellular sample. To achieve this, we use high-affinity Locked Nucleic Acid imaging probes that specifically bind antibodies and peptides in high-throughput, confocal-based imaging, and low affinity DNA imaging probes for localization, reconstruction-based super-resolution imaging of the same protein targets with PAINT. We use our approach to quantify the 66 co-expression levels of one dozen cytoskeletal and synaptic proteins within individual neuronal synapses, as well as resolve their single-synapse-level nanometer-scale organization. Our approach is scalable to dozens of target proteins and is compatible with imaging-based screening of genetic and drug perturbations for interrogating both fundamental and disease-associated biological processes in a variety of cellular systems.

5.3 Introduction

Neuronal synapses are the fundamental sites of electrochemical signal transmission in the brain and the primary cellular loci of plasticity that underlie learning and memory. Synapses are composed of dozens of proteins, whose expression levels, structural organization, and turnover govern diverse aspects of brain development and neuronal circuit function [65, 51]. Because numerous synaptic protein genes have been implicated in psychiatric and neurological diseases [99, 219, 84] and synaptic protein expression levels are known to vary widely across organisms, brain regions, and neuronal cell subtypes, characterizing synaptic protein composition *in situ* is of major importance to both basic and translational neuroscience. While fluorescence imaging offers the opportunity to characterize the heterogeneity in synaptic protein expression levels and localizations within intact neuronal samples6, it

has been limited by its inability to visualize more than four protein species in any given neuronal sample using conventional imaging approaches.

Multiplexed imaging strategies that are used to overcome the spectral limit of conventional fluorescence microscopy typically involve multiple rounds of antibody staining and imaging achieved either by antibody elution [278, 175] or fluorophore inactivation using photo- and/or chemical bleaching [85, 150, 229]. Array Tomography (AT) applied volumetric imaging of synapses within intact brain tissues by sequentially staining and stripping ultrathin tissue sections with different antibodies [175, 174, 52]. More recently, gel embedding and expansion of whole intact organs has been used with sequential antibody loading and stripping to generate 13-channel fluorescence imaging datasets [140]. Cyclic Immunofluorescence (CycIF) was applied to generate 9-channel diffraction-limited images of cancer cell lines using repetitive antibody loading-bleaching cycles. In each case, multiple antibody staining rounds are used together with harsh and time-consuming wash-steps that limit both epitope accessibility compared with simultaneous antibody loading, as well as potentially alter epitope reactivity with disruptive chemical or photobleaching treatment. Further, these preceding approaches are not readily amenable to super-resolution imaging within the same intact sample, and are therefore unable to resolve sub-synaptic protein structural organization. While electron microscopy (EM) has been integrated with AT to facilitate correlative light and EM imaging, EM is limited in its ability to resolve multiple molecular species in the same sample [7, 42], and requires complex sample fixation, embedding, and processing steps.

In contrast, the use of diffusible fluorescent imaging probes that target specific protein markers or antibodies *in situ* can in principle overcome each of the preceding limitations by offering (1) simultaneous antibody loading prior to imaging; (2) rapid probe-exchange using mild buffer treatment and (3) super-resolution imaging using PAINT (Points Accumulation In Nanoscale Topography) [233]. Originally introduced by Sharonov and Hochstrasser [233], PAINT was first used to perform super-resolution imaging of reconstituted lipid membranes with diffusible dye molecules. Subsequently, several variants of this approach [233, 88, 134] were introduced including uPAINT [88] that employs diffusible fluorescent antibodies and DNA-PAINT [127, 126] that uses diffusible fluorescent single-stranded DNA (ssDNA) molecules (imaging probes) that transiently bind to complementary ssDNA oligos (docking strands) attached to target DNA nanostructures or antibodies to generate 10- or 4-channel data [126], respectively. Protein-fragment-based probes have alternatively been used to generate multiplexed cytoskeletal and focal adhesion super-resolution images with higher labeling density compared with antibody-based approaches [134]. However, this strategy requires identification of highly specific, transiently binding peptides for each target molecular species, which may be challenging to generalize to other proteins, particularly those with lower expression levels than cytoskeletal proteins. Critically, each of the preceding super-resolution approaches relies on time-consuming and low-throughput time-lapse imaging followed by fluorophore localization and reconstruction employed in the conventional single-molecule localization microscopy approaches PALM [19] and STORM [222]. Moreover, diffusible fluorescent probes generate non-specific, high background fluorescence signals that prevents their application to rapid, high-throughput confocal imaging used in phenotypic cellular profiling of genomic and drug perturbations.

To overcome this limitation, here we introduce **P**robe-based **I**maging for **S**equential **M**ultiplexing (PRISM) that offers multiplexed protein imaging either with high-throughput confocal or super-resolution fluorescence imaging in the same cellular samples. Fluorescently labeled ssLNA (LNA-PRISM) and conventional ssDNA (DNA-PRISM) oligos are

used differentially as high- and low-affinity imaging probes to realize either diffraction-limited confocal or PAINT-based super-resolution imaging with the same ssDNA-labeled antibodies or peptides. The design of high specificity and affinity ssLNA probes offers reversible, tight binding to target proteins with significantly reduced background fluorescence of unbound, diffusible imaging probes. We apply LNA-PRISM to 13-channel confocal imaging of 7 synaptic proteins imaged simultaneously with 5 cytoskeletal proteins that have been shown to interact with each *in vivo* [104]. These multiplexed imaging data facilitate the quantitative analysis of 66 protein co-expression profiles extracted from thousands of individual synapses within the same intact neuronal culture, revealing strong correlations amongst subsets of synaptic proteins, as well as heterogeneity in synapse sub-types. We additionally apply DNA-PRISM using the same ssDNA-antibody and -peptide conjugates to resolve the 20 nm-scale structural organization of 8 synaptic proteins together with filamentous actin and dendritic microtubules *in situ*. Our super-resolution imaging data reveal the nanometer-scale structural organization of 9 targets within single synapses that is consistent with EM [269] and average synaptic structure previously assayed using STORM [57].

5.4 Results

5.4.1 Overview of LNA- and DNA-PRISM

The PRISM workflow employs neuronal cultures that are fixed, permeabilized, and stained simultaneously using ssDNA-conjugated antibodies or peptides, collectively termed "markers", which specifically label cellular targets. Markers are barcoded with single-stranded nucleic acid oligonucleotides ("docking strands"), rationally designed to optimize orthogonality between complementary fluorescently labeled ssLNA or DNA imaging probes used for confocal or super-resolution imaging (Fig. 5-1a). To maximize the multiplexing capacity of the assay, primary rather than secondary antibodies are labeled with docking strands whenever possible so that labeling of distinct targets is not limited by the number of secondary antibodies reacting with different species. Extensive validation of each marker and fluorescently labeled ssLNA/ssDNA imaging probe is performed to ensure that markers retain their target-specific recognition properties following conjugation with nucleic acid docking strands, and that imaging strands target cognate docking strands with high affinity and specificity without cross-talk (Fig. 5-1b). Following marker and imaging probe validation, multiplexed imaging is performed using sequential labeling and washing out of individual imaging probes, with wash-steps in between used to clear the sample of imaging probes (Fig. 5-1c). Diffraction-limited, confocal images are acquired using LNA-PRISM, whereas single-molecule time-lapse imaging followed by image reconstruction, drift correction, and image alignment is performed with DNA-PRISM using PAINT.

5.4.2 Design and validation of markers for PRISM

To apply multiplexed neuronal imaging in either confocal or super-resolution modes using the same protein markers, we conjugated distinct ssDNA docking strands using either SMCC linkers or site-specific chemoenzymatic labeling to synaptic and cytoskeletal markers validated in neuronal cell culture (Appendix A.4) (see Fig. S1 in [100]). Whereas SMCC conjugates docking strands to surface-accessible primary amines through NHS chemistry, site-specific labeling conjugates ssDNA docking strands to four conserved glycan chains on

the Fc region of the antibody (see Fig. S2 and Fig. S3 in [100]), thereby minimizing the likelihood of disrupting the antibody paratope. In generating PRISM antibodies, SMCC was first attempted for ssDNA conjugation, and site-specific conjugation was alternatively applied to antibodies that changed localization patterns after SMCC-based conjugation. In cases where staining patterns were disrupted with both SMCC and site-specific conjugation, or the fluorescence signal of the primary antibody conjugate was too low for high quality imaging, ssDNA-conjugated secondary antibodies were instead employed to visualize the target.

Because conjugation of antibodies and peptides with ssDNA may alter their affinity and/or specificity, we validated each marker-docking-strand conjugate individually in neuronal culture using indirect immunofluorescence (IF) to ensure the same staining patterns were obtained compared with the reference, unconjugated marker. However, most markers were found to exhibit strong nuclear localization following SMCC or site-specific conjugation with ssDNA, suggesting that the observed change in affinity of the ssDNA-conjugated antibody to its target is not solely due to the possible modification of paratopes by ssDNA (Fig. 5-2a, and see Fig. S4 and Fig. S5 in [100]).

To eliminate off-target nuclear localization of the ssDNA-conjugated antibodies, we screened several nuclear blocking agents and found that salmon sperm DNA commonly used in Southern blotting successfully blocked the nuclear localization of ssDNA-conjugated antibodies (Fig. 5-2a) and see Fig. S6 in [100]). Interestingly, conjugating antibodies with single-stranded Peptide Nucleic Acid (ssPNA) [223] docking strands instead of ssDNA also eliminated nuclear localization in the absence of any blocking (Fig. 5-2a), supporting the hypothesis that overall charge of the nucleic acid docking strands present on antibodies was responsible for their non-specific nuclear localization. Nevertheless, salmon sperm blocking was performed in all experiments to minimize cost and complexity associated with generating a full library of ssPNA docking strands. Image cross-correlation analysis showed that ssDNA-conjugated antibodies produced staining patterns similar to those of unmodified antibodies, as assessed through indirect IF when samples were blocked with salmon sperm DNA prior to immunostaining (Fig. 5-2b and see Fig. S7 in [100]).

5.4.3 Imaging probe design for LNA-PRISM

To enable high-throughput confocal imaging of neurons with high signal-to-noise and low background fluorescence in multi-well plate format, we designed high affinity ssLNA imaging strands of 11 nt length that target the same 11 nt ssDNA docking strands used in DNA-PAINT imaging with high specificity [126]. Similar to ssDNA, ssLNA binding affinity to complementary ssDNA is salt-dependent, thereby enabling rapid probe exchange via imaging probe wash-out using low salt concentration buffer (see Fig. S8 in [100]). RNase was used to eliminate off-target binding of ssLNA imaging probes to cellular RNA (see Fig. S9 in [100]), a treatment that did not affect antibody marker localization (see Fig. S10 in [100]). Orthogonality of each imaging probe was validated individually using a cell-based crosstalk assay that resembles the staining and imaging conditions in a multiplexed PRISM experiment. Results of this cross-talk assay showed less than 10% crosstalk between each of the docking-imaging-strand pairs for our staining and imaging conditions (see Fig. S11 and Fig. S12 in [100]). Typical imaging strand incubation and wash-out times for LNA-PRISM are 5-10 minutes each, which is considerably faster than existing multiplexed imaging approaches that require multiple rounds of antibody staining and elution that can require up to hours or days to complete [175, 150, 174]. PRISM washing conditions consist

of 0.01x phosphate buffered saline (PBS), which is also milder than alternative multiplexed imaging methods that utilize oxidizing reagents or high-pH buffer [175, 150, 174]. In addition to reducing the risk of altering epitopes over the course of multiple wash cycles, mild buffer conditions minimize the possibility of the disruption of delicate cellular structures, which may be particularly crucial for preserving the integrity of neuronal synapses. RNase-treated cells produced target staining patterns using LNA-PRISM that were indistinguishable from those with conventional indirect IF (see Fig. S13 in [100]).

5.4.4 LNA-PRISM: 13-channel confocal neuronal imaging

13-channel imaging of cultured rat hippocampal neurons using 10 ssLNA imaging probes and three non-PRISM fluorescent markers was performed to characterize the synaptic and cytoskeletal protein-protein network that is core to the regulation of synapse formation and plasticity (Fig. 5-3a). This network includes the cytoskeletal proteins actin, Tuj-1, MAP2, ARPC2, and cortactin, the pre-synaptic proteins synapsin-I, bassoon, and VGLUT1, the post-synaptic density proteins PSD-95, Homer-1b/c, and SHANK3, and the receptor NMDAR2B. The canonical synaptic markers synapsin-I, bassoon, VGLUT1, PSD-95, Homer-1b/c, and SHANK3 exhibited a high degree of co-localization, with punctate patterns, whereas Tuj-1 and MAP2 yielded clear cytoskeletal morphologies (Fig. 5-3b), and see Fig. S14 in [100]). Noticeably, ARPC2 and cortactin displayed punctate patterns that also co-localized with other synaptic markers, in agreement with previous results [104]. To assess whether multiple rounds of imaging probe wash-out and probe application steps physically distorted the sample or noticeably stripped markers from their epitopes, synapsin-I was imaged twice, once in the middle and once at the end of the PRISM experiment, which revealed highly reproducible localization patterns (Fig. 5-3a).

LNA-PRISM offers nearly an order of magnitude increase in the ability to detect co-localization/co-expression patterns *in situ*, with 66 protein-protein co-localizations using 12 protein labels compared with only 6 from conventional 4-channel imaging. While synaptic proteins generally showed co-localization patterns, examination of individual synapses revealed variations in co-localization patterns across different proteins and synapses (Fig. 5-4a). To characterize the co-localization/ co-expression patterns of each protein pair, individual synaptic features including size and intensity were extracted for each target from PRISM images using an image-processing pipeline optimized for synapse segmentation (see Fig. S15 in [100], and Appendix A.4). Correlations between distinct synaptic features were computed across all synapses, with a high correlation score between two synaptic proteins indicating a higher functional association. The correlation scores showed expression levels of most synaptic proteins were highly correlated in synapses, with the exception of the cytoskeletal proteins Tuj-1 and MAP2, in agreement with previous image cross-correlation analyses that showed that tubulin is largely excluded from synapses [104] (Fig. 5-4b, and see Fig. S17 in [100]). In addition, the post-synaptic density proteins Homer-1b/c, PSD-95, and SHANK3 strongly correlated with one another in their expression levels, which may be attributed to their dense and compact protein distributions within the PSD [263, 107]. The Arp2/3 complex subunit ARPC2, which has been shown to interact with SHANK3 within synapses [104], also correlated in its expression level with other PSD proteins. In agreement with the expected separation of pre- and post- synaptic proteins, synapsin-I and VGLUT1 that are associated with pre-synaptic vesicles were highly correlated with the pre-synaptic scaffolding protein bassoon, but were only weakly correlated with most post-synaptic proteins (Fig. 5-4b). Interestingly, bassoon and VGLUT1 exhibited moderate correlation

in expression with PSD95, suggesting a coordination of pre- and post-synaptic structures across the synaptic cleft. NR2B exhibited correlation with both pre- and post-synaptic markers, consistent with previous observation of both pre- and post- synaptic localizations of NMDAR [143, 89].

Large-scale profiling of synapses also enabled us to use the rich protein co-expression feature profiles assayed with LNA-PRISM to classify synapse subtypes. To identify putative sub-categories of synapse types in this high-dimensional feature space that consists of 24 dimensions, we applied t-Distributed Stochastic Neighbor Embedding (t-SNE), a tool commonly used to visualize high-dimensional single-cell data (Fig. 5-4c) [6]. t-SNE transforms high dimensional data into two dimensions, aiming to preserve the local high dimensional data structure within the lower dimensional space. t-SNE analysis of 10,000 randomly subsampled synaptic profiles revealed a cluster of synapses contain most of the synaptic proteins that we measured, which, given that our antibody panel consisted mostly of excitatory proteins, also likely corresponded to conventional excitatory synapses. In addition, smaller sub-type clusters were identified, showing an absence of one or more synaptic proteins, which may correspond to conventional inhibitory synapses or additional synapse subtypes. Hierarchical clustering of protein feature profiles corroborated findings of the preceding correlation and t-SNE analyses, namely that pre-synaptic proteins are highly clustered with one another, whereas PSD proteins and ARPC2 form a separate sub-cluster (Fig. 5-4d). Features of synapsin-I from two imaging rounds were tightly clustered together, confirming clustering results reflected the similarities between features. These findings suggest that protein associations derived from PRISM data recapitulate the molecular composition and structural properties of excitatory synapses, and can do so for one dozen targets simultaneously in thousands of synapses within the same intact sample imaged within hours in multi-well plate format.

5.4.5 DNA-PRISM: Super-resolution imaging using low affinity ssDNA imaging strands and PAINT

The same antibody-ssDNA conjugates offered the ability to also super-resolve molecular targets within individual synapses in primary mouse neuronal cultures using DNA-PRISM (DNA-PAINT) [127, 126]. Neuronal cultures were assembled into flow cells in which fluid exchange was controlled by an automated fluidics handling system to ensure gentle buffer washing and imaging probe application designed to minimize sample distortion. Super-resolution DNA-PRISM images of microtubules and F-actin in neurons were first compared with widefield IF images. Super-resolved microtubules formed bundles within neuronal processes, whereas F-actin exhibited linear, filamentous structures within these regions, but showed punctae within dendritic spines (Fig. 5-5a-d). Subcellular structures imaged with DNA-PRISM correlated well with the corresponding widefield images, but with significantly improved spatial resolution (Fig. 5-5b,d). A Gaussian fit to the cross-sectional profile of a single microtubule produced a full-width at half-maximum (FWHM) of 46.5 nm (5-5g), which is consistent with previous PAINT measurements in HeLa cells [126]. In addition to microtubules and F-actin, DNA-PRISM imaging of neuronal synapses also corresponded well with the widefield IF images, but with significantly improved resolution, as expected, revealing closely apposed pre- and post-synaptic sites (Fig. 5-5e-f). We quantified the average synapse size defined by synapsin-I and PSD-95 punctae using the radial cross-correlation function between synapsin-I and PSD-95, with the decay length of the correlation function revealing an average synapse size of 200 nm (Fig. 5-5i) [174]. The spatial decay

of the DNA-PRISM correlation curve occurred at a smaller spatial scale than the widefield imaging curve, indicating the smaller synapse size revealed by DNA-PRISM due to enhanced resolution relative to widefield imaging.

We next applied DNA-PRISM imaging to super-resolve the nanoscale pre- and post-synaptic organization of 9 targets within individual synapses, including Tuj-1, F-actin, cortactin, PSD-95, synapsin-I, NMDAR2B, SHANK3, Homer-1b/c, and bassoon (Fig. 5-6a). Due to differences in synapse orientations with respect to the imaging plane, individual synapses varied in their degree of overlap among proteins within each synapse. For a subset of synapses with the proper orientation relative to the imaging plane, we identified clear separation between pre-synaptic proteins (synapsin-I and bassoon) and post-synaptic proteins (PSD-95, SHANK3, Homer-1b/c) (Fig. 5-6b). Pre- and post-synaptic proteins were localized to opposing regions of the synaptic cleft, cytoskeletal proteins (Tuj-1, actin, cortactin) and NMDAR2B were observed in both sides of the cleft. Moreover, PSD proteins (PSD-95, SHANK3, Homer-1b/c) showed narrow, overlapping distributions in expression levels, suggesting physical interaction of these proteins in the PSD (Fig. 5-6c) that is consistent with the correlation analysis applied to the preceding confocal imaging results. In contrast, synapsin-I exhibited a broader spatial distribution compared with the distributions of scaffolding proteins, in agreement with the more diffuse distributions expected for vesicle-associated proteins (Fig. 5-6c). These spatial distributions of synaptic proteins were consistent with the average distributions previously measured from multiple synapses and distinct cultures using three-channel STORM26 and EM [269]. However, in stark contrast to these previous studies that relied on reference markers, our imaging and analysis of sub-synaptic proteins resolved all measured targets of interest within the same synapse simultaneously. Integration of our approach with 3D super-resolution imaging systems would offer its application to dozens or hundreds of synapses *in situ*.

5.5 Discussion

PRISM offers a powerful, versatile approach to multiplexed fluorescence imaging of cellular protein targets for both phenotypic profiling and high-resolution structural analysis of cellular cultures. LNA-PRISM uses diffusible high-affinity ssLNA imaging probes to realize high-throughput confocal imaging for rapid, large-scale phenotypic screening of more than one-dozen cytoskeletal and synaptic protein targets across tens of thousands of individual neuronal synapses in triplicate. Alternately, DNA-PRISM utilizes the same antibody/peptide reagents with ssDNA imaging probes to perform super-resolution synaptic imaging with PAINT. In future studies, large-scale morphological screens may first be performed in multi-well plate format using LNA-PRISM, followed by super-resolution imaging of a sub-set of synapses or neuronal sub-regions with DNA-PRISM to resolve synaptic ultrastructure. Compared with previous multiplexed diffraction-limited imaging approaches that utilize sequential antibody labeling and stripping or bleaching [175, 150, 174], LNA-PRISM offers simultaneous staining of all protein targets, which reduces the risk of "masking" antigens, as well as substantially increasing assay throughput. The use of physiological wash buffers additionally minimizes the possibility of sample or epitope disruption, which may be crucial for high-resolution structural and co-localization studies requiring high sample fidelity, such as in the profiling of synapses within cultured neuronal samples.

Application of our primary antibody conjugation strategy together with the use of libraries of orthogonal ssDNA sequences [290] offers the potential for future application of

PRISM to neuronal and other cellular systems exceeding substantially the approximately one dozen targets realized here. Genetic and drug perturbation screens aimed at discovering subtle alterations in neuronal phenotype should additionally benefit substantially from the large-scale protein association networks within synapses that are derived from the 12 synaptic targets examined in this study, which offer 66 pair-wise synaptic co-localizations within the same neuronal culture. While single-color imaging probes were used to demonstrate the robustness of our probe-exchange strategy, which yielded reproducible protein localization even after 10 successive probe exchanges, future applications that utilize multiple laser lines to simultaneously image 3 distinct fluorophores in any given imaging cycle renders our approach viable for multiplexing at least 30 molecular targets *in situ*. The significant increase in phenotypic information captured by our approach offers major potential for both basic and translational neuroscience research, including high-content screening of phenotypic variation due to genetic and compound perturbations, as well as super-resolution ultrastructural synaptic imaging with nanometer-scale resolution. Future application of PRISM to 3D super-resolution imaging may also enable multiplexed analysis of neuronal morphology and nanoscale protein organization within fixed human and diverse model organism tissues and organoids, including cancer and immunology models.

5.6 Acknowledgments

Funding from NIH BRAIN Initiative Award 1U01MH106011 to M.B. and E.S.B. is gratefully acknowledged. Funding from the NSF Physics of Living Systems program NSF PoLS 1305537 to M.B. is additionally acknowledged. E.S.B. additionally acknowledges the HHMI-Simons Faculty Scholars Program, the Open Philanthropy Project, U.S. Army Research Laboratory and the U.S. Army Research Office under contract/grant number W911NF1510548, the New York Stem Cell Foundation-Robertson Award, and NIH grants 1RM1HG008525, 1R24MH106075, and 1R01NS087950. J.R.C. acknowledges funding from the Stanley Center for Psychiatric Research. Dr. Ralf Jungmann is acknowledged for helpful discussions on DNA-PAINT at the outset of this work. We acknowledge the Koch Institute Swanson Biotechnology Center, specifically Microscopy and Biopolymers and Proteomics core facilities, as well as the Whitehead Institute W.M. Keck Microscopy Facility, for technical support.

5.7 Figures

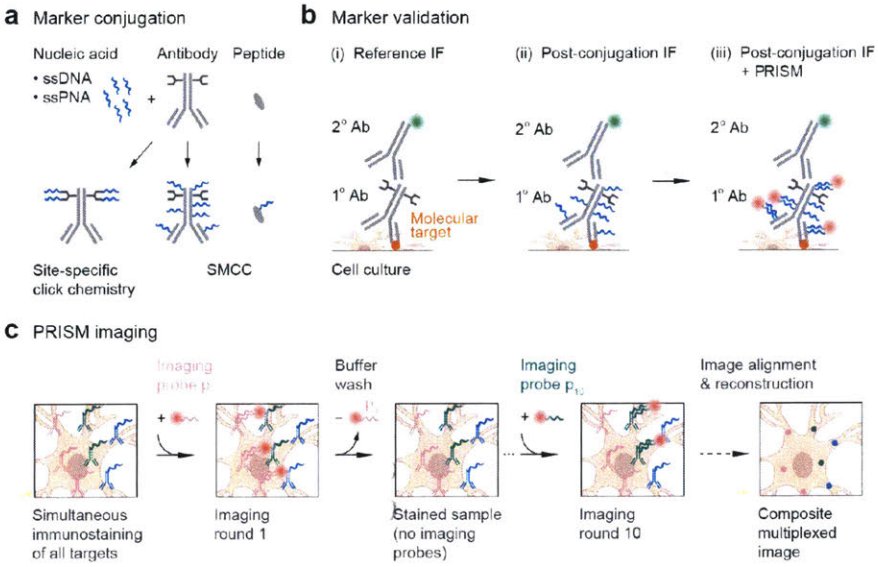

Figure 5-1: Schematic of the PRISM framework for highly-multiplexed imaging of molecular targets in neurons. **(a)** Reagents ("markers", shown in gray) for detecting subcellular targets include antibodies or peptides that are conjugated with unique oligonucleotide barcodes ("docking strands", shown in blue). A barcoded marker is imaged using the complementary fluorophore-conjugated oligonucleotides (imaging probes) that bind to the docking strands on the marker (see (iii) in (b), fluorophores shown as red circles). Binding affinity of the imaging probes to the docking strands can be varied by changing the sequence and type of the oligonucleotides, which thereby enables either diffraction-limited (high affinity) or super-resolution microscopy (low affinity). Conjugation of docking strands to markers using site-specific click chemistry enables stoichiometric control of the number of nucleic acids bound to a whole antibody, while SMCC enables conjugation of docking strands to free amine groups on a variety of markers. **(b)** The reagent testing and validation phase consists of: (i) generating reference staining patterns of all molecular targets of interest using standard immunofluorescence (IF), (ii) Specificity and staining quality of markers conjugated with docking strands compared to those in the reference IF, and (iii) co-localization of PRISM-imaged staining patterns using imaging probes (red circles, which correspond to fluorophores conjugated to the probes) with standard IF staining patterns (green circles). **(c)** Overview of the main steps in the PRISM imaging workflow. All molecular targets of interest are immunostained at once using docking strand-conjugated markers (e.g., antibodies shown in green, blue, and pink). Nucleic acid imaging probes specific to each marker (e.g., p1–p10) are applied and imaged sequentially, with each imaging strand washed out after image acquisition at each step. This approach enables imaging a dozen or more distinct molecular targets in the same sample. Images of different markers are drift-corrected and overlaid to generate a pseudo-colored, multiplexed image. For super-resolution PRISM, prior to drift correction, the super-resolved image of each marker is reconstructed from the temporal image stack of binding/unbinding events of the imaging probes to/from the docking strands on the marker.

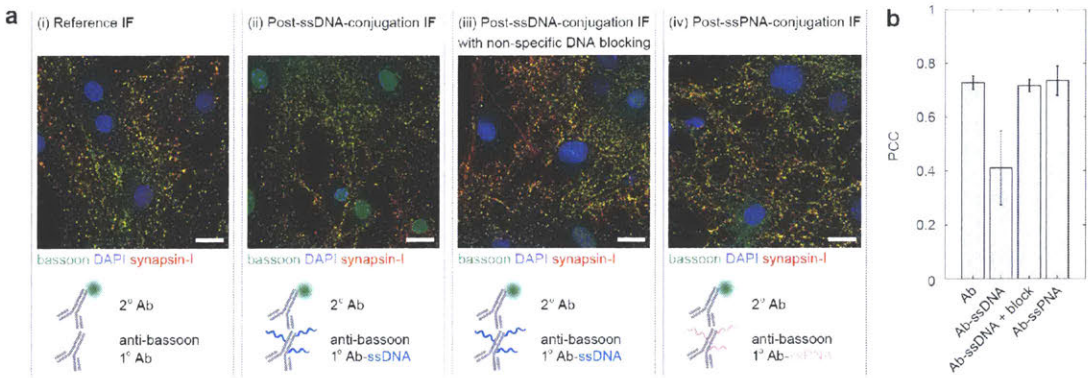

Figure 5-2: Blocking off-target nuclear localization of ssDNA-conjugated antibodies. **(a)** Neurons were stained with native or ssDNA-conjugated anti-bassoon antibody, anti-synapsin-I antibody, and DAPI. ssDNA-conjugated anti-bassoon antibody exhibited strong off-target nuclear localization (ii, green staining inside the nuclei) compared to the native antibody (i). This nuclear localization was reduced by blocking the fixed sample with non-specific (salmon sperm) DNA prior to immunostaining (iii), or when the anti-bassoon antibody used for staining was conjugated with ssPNA instead of ssDNA (iv). Scale bar, 20 μm. **(b)** Cross-correlation analysis of the IF images in (a). Pearson correlation coefficient (PCC) of the bassoon channel (green in (a)) with the synapsin-I channel (red in (a)) for each image. Differences in PCC indicate changes in antibody staining patterns. Error bars represent 95% confidence intervals.

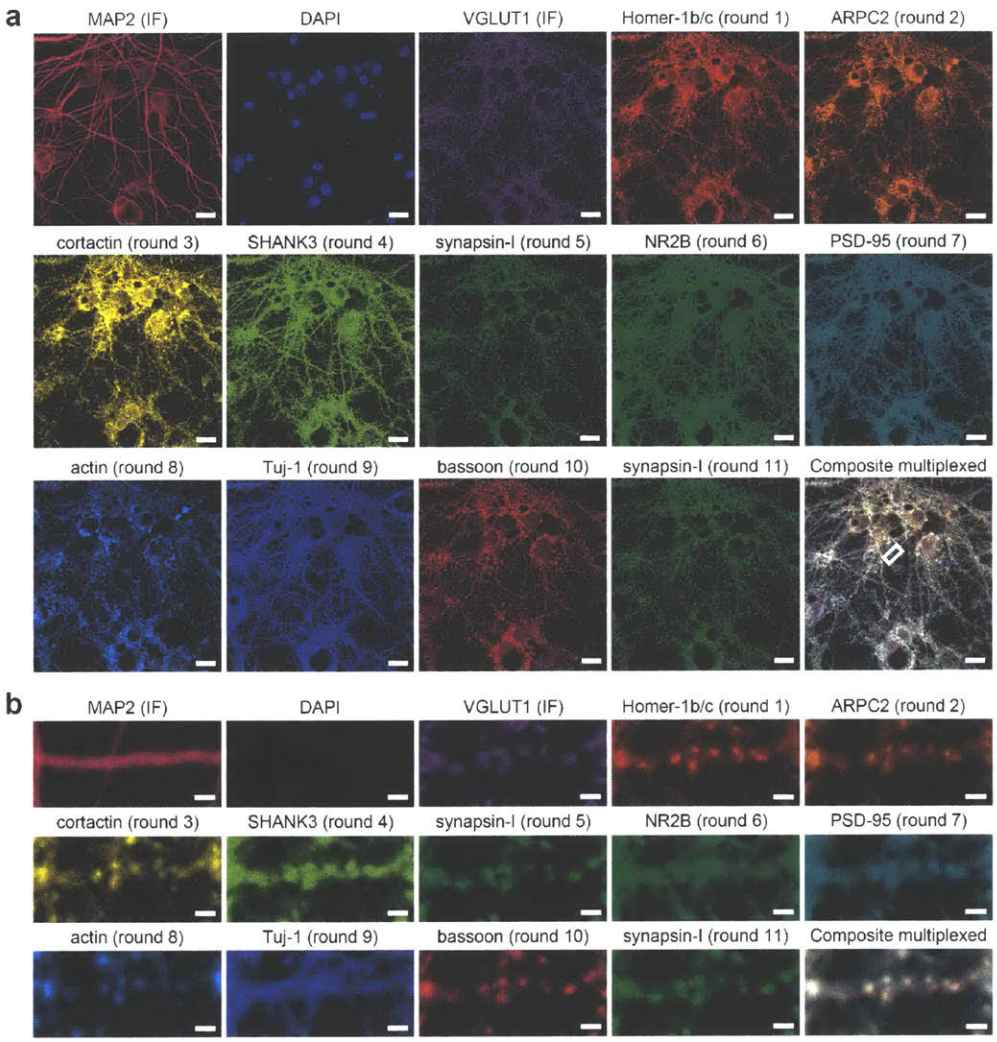

Figure 5-3: Confocal LNA-PRISM image of rat hippocampal neuronal synapses. **(a)** 13-channel images of 21 days *in vitro* (DIV) rat hippocampal neuronal culture. The composite image is shown in the top-left corner, followed by the image of each individual channel. MAP2 and VGLUT1 were visualized using fluorescently labeled secondary antibodies, and nuclei were visualized using DAPI, while other targets were visualized using ssLNA imaging probes. Synapsin-I was imaged twice, once in the middle and once at the end of the experiment. **(b)** Zoom-in view of a single dendrite indicated by the white box in (a). Scale bars: (a) 20 μm; (b) 2 μm.

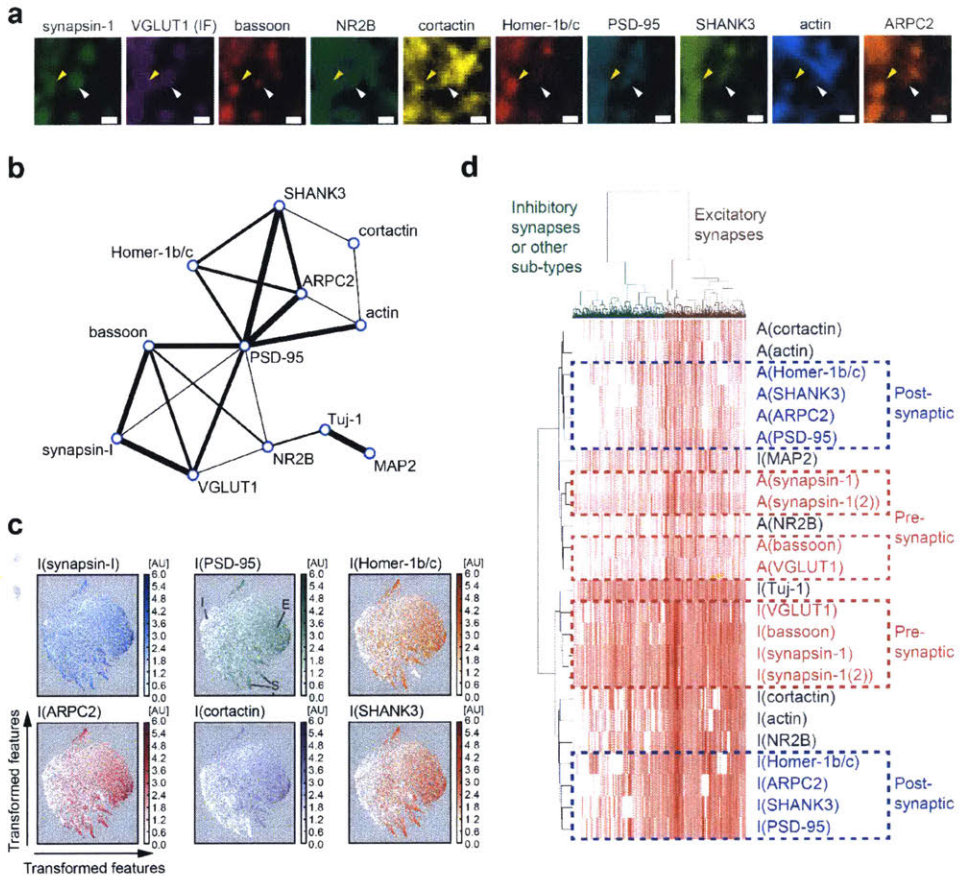

Figure 5-4: Analysis of single-synapse profiles from multiplexed confocal imaging data acquired using LNA-PRISM. **(a)** LNA-PRISM images of a conventional excitatory synapse (yellow arrow) with co-localization of every synaptic marker measured, and a synapse (white arrow) with only a subset of markers present. **(b)** Network representation of correlations between intensity levels of synaptic proteins within synapses (n=178,528 synapses from 3 cell culture batches). The thickness of each edge represents the relative correlation strength between the respective nodes. **(c)** t-Distributed Stochastic Neighbor Embedding (t-SNE) maps of n=10,000 synapses from a single culture batch; each with 20 features (intensity levels and punctae sizes of 10 synaptic proteins). Each point in each t-SNE map represents a single synapse with its (x,y) coordinates corresponding to the transformed features that best preserve the distribution of synapses in the original high dimensional feature space. Intensity levels of individual proteins are color-coded in each map. E: cluster of conventional excitatory synapses with the presence of most synaptic markers; I: cluster of possible inhibitory synapses with the absence of most synaptic markers; S: cluster of possible sub-type synapses with the presence of only a subset of synaptic markers. **(d)** Hierarchical clustering analysis of synapse profiles. Each column in the heat map represents a profile of a single synapse with 24 synaptic features (rows). "I" and "A" denote image intensity level and punctum size, respectively (n=53,698 synapses from a single culture batch).

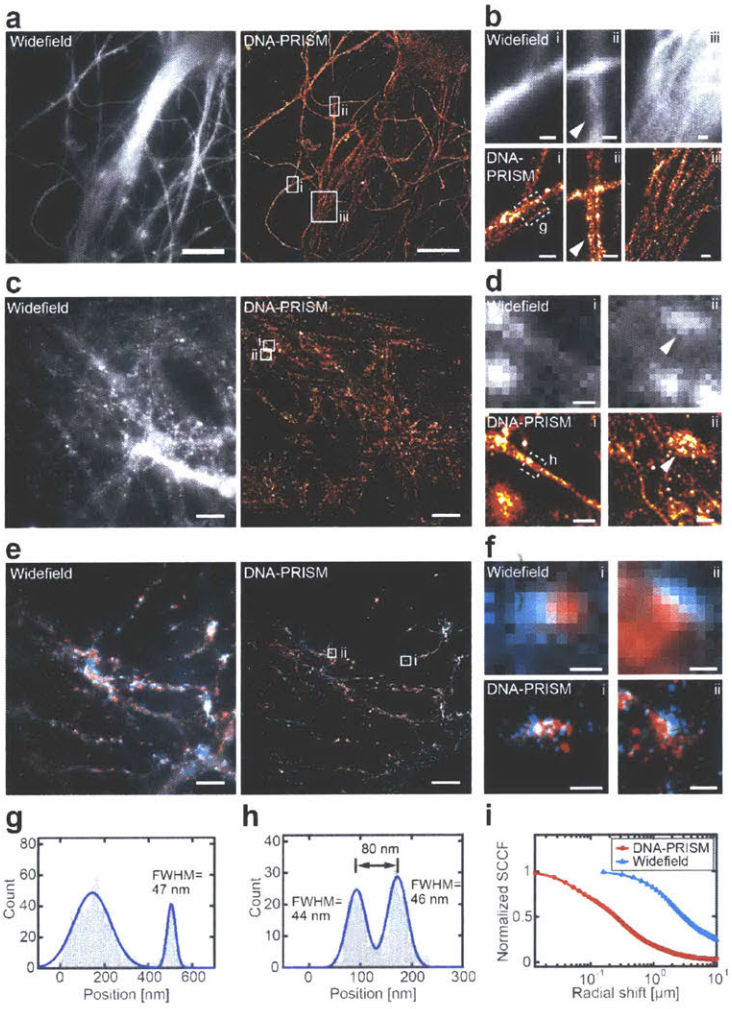
a
Widefield
DNA-PRISM
ii
i
iii
b
Widefield i
ii
iii
DNA-PRISM i
ii
iii
g
c
Widefield
DNA-PRISM
i
ii
d
Widefield i
ii
DNA-PRISM i
ii
h
e
Widefield
DNA-PRISM
ii
i
f
Widefield i
ii
DNA-PRISM i
ii
g
Count
FWHM= 47 nm
Position [nm]
h
Count
80 nm
FWHM= 44 nm
FWHM= 46 nm
Position [nm]
i
Normalized SCCF
DNA-PRISM
Widefield
Radial shift [μm]

Figure 5-5: Super-resolution DNA-PRISM imaging of primary neuronal cultures. **(a)** Widefield and DNA-PRISM images of neuronal microtubules stained using the DNA-conjugated anti-Tuj-1 antibody. **(b)** Zoom-in view of the boxed areas in (a) show resolution enhancement of DNA-PRISM images compared with widefield images. The arrowhead indicates distinct microtubule bundles that are not resolved in the widefield image **(c)** Widefield and DNA-PRISM images of filamentous actin stained using DNA-conjugated phalloidin. **(d)** Zoom-in views of the boxed areas in (c) show two actin filaments (left) and the synaptic actin punctae with sub-synaptic structures (right, arrow head) that are not resolved in widefield images. **(e)** Widefield and DNA-PRISM images of pre-synaptic marker synapsin-I (red) and post-synaptic marker PSD-95 (cyan) of the same field of view. **(f)** Zoom-in view of single synapses indicated by boxes in (e). **(g)** Cross-sectional profile of the boxed region in (b) shows a microtubule bundle next to a possible single microtubule with FWHM = 47 nm. **(h)** Cross-sectional profile of the boxed region in (d) shows two actin filaments or small filament bundles that are 80 nm apart. **(i)** The average size of synapses defined by synapsin-I and PSD-95 is quantified using the normalized radial cross-correlation function. The decay at the smaller radial shift of the DNA-PRISM curve (red) indicates the smaller synapse size in the DNA-PRISM image due to the improved spatial resolution. Scale bar: (a,c,e) 10 μm; (b,d,f) 0.5 μm.

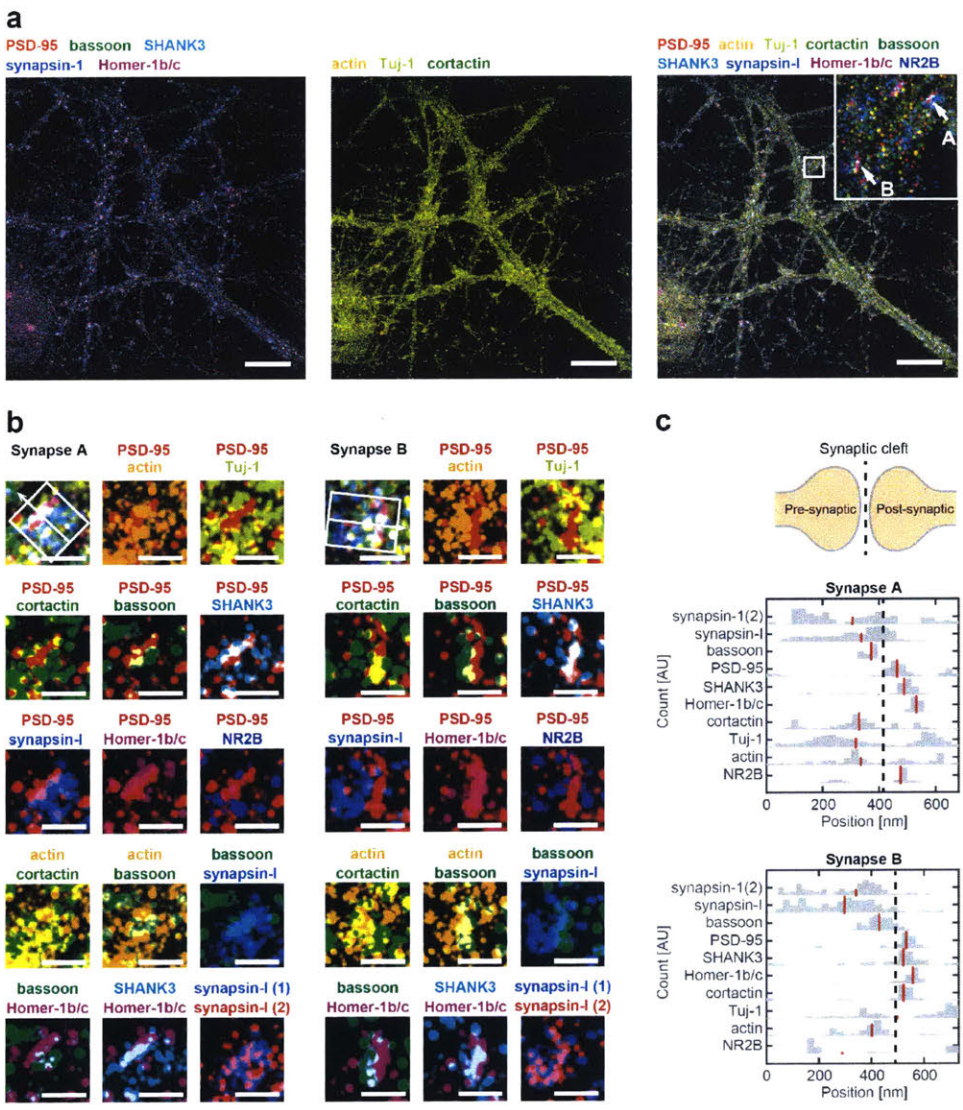
a
PSD-95 bassoon SHANK3
synapsin-1 Homer-1b/c
actin Tuj-1 cortactin
PSD-95 actin Tuj-1 cortactin bassoon
SHANK3 synapsin-I Homer-1b/c NR2B
A
B
b
Synapse A
Synapse B
PSD-95 actin
PSD-95 Tuj-1
PSD-95 cortactin
PSD-95 bassoon
PSD-95 SHANK3
PSD-95 synapsin-I
PSD-95 Homer-1b/c
PSD-95 NR2B
actin cortactin
actin bassoon
bassoon synapsin-I
bassoon Homer-1b/c
SHANK3 Homer-1b/c
synapsin-I (1) synapsin-I (2)
c
Synaptic cleft
Pre-synaptic
Post-synaptic
Synapse A
Synapse B
synapsin-1(2)
synapsin-I
bassoon
PSD-95
SHANK3
Homer-1b/c
cortactin
Tuj-1
actin
NR2B
Count [AU]
0
200
400
600
Position [nm]

Figure 5-6: Multiplexed DNA-PRISM image shows distributions of synaptic proteins within individual synapses. **(a)** DNA-PRISM images of neurons showing the subset channels of synaptic proteins (left), the subset channels of cytoskeletal proteins (middle), and all the channels (right). **(b)** Zoom-in view of two individual synapses in (a) shows the separation of pre-synaptic proteins (synapsin-I and bassoon) and post-synaptic proteins (PSD-95, SHANK3, Homer-1b/c). For each synapse, the nine-target image is shown in the top-left corner, with distinct pairs of synaptic proteins shown in the remaining images. Synapsin-I was imaged twice, once at the beginning and once at the end of the experiment. **(c)** Cross-sectional profiles of protein distributions along trans-synaptic axes (white boxes with arrows in (b)) of the two synapses in (b). Red lines indicate the medians of the distributions. Scale bars: 10 μm in full field views; 500 nm in zoom-in views.

Chapter 6

Conclusions and future directions

6.1 The convergence of -omics data analysis with image-based profiling of cellular structure and function

The post-genomic era has ushered in a new wave of -omics technologies that now enable systems-level interrogation of cellular processes at numerous levels, including the genome, epigenome, transcriptome, metabolome, and proteome [4]. At the same time, advancements in microscopy now enable detailed characterization of cellular structure and function largely by using fluorescent reporters to study the regulation of specific molecules in space and time [114]. -Omics techologies are principally used to measure hundred to thousands of molecular species and generate hypotheses about which species are most interesting to use as biomarkers, or which species to follow-up on with more detailed mechanistic studies. Such technologies, however, typically miss the spatiotemporal features of the species. In contrast, microscopy studies often characterize only a few molecular species, but do so with high spatial and temporal resolution. Microscopy is used to capture cellular signaling and phenotype – morphology, migration, proliferation, apoptosis, signaling dynamics, subcellular localization of proteins, etc. Importantly, "blind" phenotypic screens that attempt to quantify thousands of features of a set of general markers (e.g., F-actin, nucleus, microtubules, membrane-bound organelles) have largely been inferior in drug discovery efforts compared to target-based drug design, as general markers likely fail to capture phenotypes relevant to many diseases [181, 26]. As a result, more targeted, mechanism-specific phenotypic screening is needed. How can one leverage both -omics and quantitative imaging technologies to hone in on such targeted screens that can reveal molecular mechanisms important to the biological process under study?

This thesis demonstrates one such approach for identifying putative mechanisms of drug action, in this case for doxorubicin chemotherapy, a non-targeted therapy with multiple modes of action. Bioinformatics analyses were first applied to phosphoproteomics measurements to identify the general class of signaling processes and functions altered by the drug. The results of this analysis were then used to design an imaging-based phenotypic assay to captures these processes and functions with finer spatiotemporal detail to converge on a putative mechanism. Specifically, in Chapter 3, gene ontology analysis of checkpoint kinase phospho-substrates revealed a novel role for the DNA-damage response in regulating cytoskeleton- and adhesion-associated processes. Dozens of phosphoproteins associated with these processes were upregulated by doxorubicin (Fig. 3-4). The drug also altered cellular morphology (Fig. 3-2) and migration (Fig. 3-3). A key question remained

as to whether one of the dozens of phosphoproteins contributed most to these phenotypic changes. Guided by the phosphoproteomic analysis, a small-scale phenotypic screen was applied to characterize morphological changes under doxorubicin and a number of targeted inhibitors of various actomyosin components (Chapter 4), using both fixed- and live-cell image processing and analysis tools (Chapter 2). The screen revealed that ROCK and myosin II, but not MLCK, inhibition phenocopied doxorubicin treatment, which led to the finding that myosin light chain phosphorylation on S19 (pMLC) may be contributing to the doxorubicin-induced changes in cell shape and migration (Chapter 4).

A key insight was gained into the value of integrating phosphoproteomic and phenotypic screens during the course of experiments and data analyses presented in this thesis. Large changes in magnitude (i.e., upregulation or downregulation) of a measured signal do not necessarily correspond to a biologically meaningful response. For instance, pMLC, which we found may largely contribute to doxorubicin-induced changes in cellular elogation, was ranked 510 out of 711 phosphosites in its magnitude of doxorubicin-induced upregulation. This phosphosite would likely never have been studied further in this work if not for the convergence of gene ontology and pathway analysis with the rationally-designed, image-based phenotypic screen. This work demonstrates the power of combining -omics and phenotypic profiling in mechanism discovery, particularly when one uses information from one to inform the other. In this thesis, the phosphoproteomic analysis suggested the relevance of a phenotypic screen centered around cell morphology and actomyosin organization. However, other -omics studies may generate hypotheses in which processes and functions other than actomyosin/adhesions play an important role. A multitude of other cellular processes can be studied with higher spatiotemporal resolution using quantitative imaging. In such cases, one can use fixed- and live-cell fluorescent reporters to phenotypically profile mitochonodria, lysosomes, endoplasmic reticulum, nuclear structure, and activation of Erk, Jnk, or Akt signaling, for example, or generate highly specific fluorescently-tagged protein constructs whose expression and localization can be microscopically analyzed.

6.2 Future studies for linking multiplexed molecular signals with changes in cell phenotype using latent variable models

The key findings from Chapters 3 and 4 suggested that doxorubicin-induced changes in focal adhesion and actomyosin signaling were associated with altered cellular morphology through separate experiments, but relationships between cell signaling and cell shape were not firmly established within the same cells. The phosphoproteomics studies in Chapter 3 showed that dozens of cytoskeletal and signaling proteins may contribute to doxorubicin-induced changes in cell shape and motility. Conventional microscopy systems are typically limited to 4 fluorescence channels, making it impossible to realistically measure more than 2-3 signals in the same sample. The multiplexed fluorescence imaging methodology presented in Chapter 5 enables us to overcome this limit. Future studies should focus on building relational models between multiplexed sub-cellular signaling and morphological alteration on a single-cell level. These models will reveal, for instance, whether levels of pMLC and numerous adhesion associated phosphoproteins altered by doxorubicin are directly related to morphological elongation (as opposed to other shape features we measured, see Appendix A.5) within the same population of cells. Provided that the putative phosphoproteins have primary antibodies compatible with immunofluorescence staining (e.g., as does pMLC that was

used in Chapter 4), one would simultaneously stain against, for instance, pFLNA (S2152), pMYPT1 (S508), pMLC (S19), and F-actin, using antibodies and phalloidin conjugated to nucleic acid barcodes to enable simultaneous measurement in the same cell culture (Chapter 5). Using image processing and analysis techniques discussed in this thesis, quantitative metrics of the signals and cytoskeletal organization would be extracted, and relational (e.g., regression) models built to predict cell shape features from the signal features, or vice versa. What types of relational models would be useful for this task?

In the relational model we wish to build, the goal is to explain the variance in morphological responses between cells using measurements of signal levels/distributions. In other words, we want to establish relationships in a predictive sense – how signals can predict morphology. The key hypothesis that establishes the variable relationships in the model and guides its specification is that expression levels and organization of subcellular molecular signals and cytoskeletal regulators positively correlate with cell shape. One would then need to transcribe the hypothesis into a formalized relational model, defining variables and the relationships between them that will be estimated. Importantly, the variables in this case are expression levels and subcellular organization features of molecules and the morphological characteristics of cells. In Chapter 4 and in Appendix A.5 I showed how such multivariate features can be extracted, using the tools developed in Chapter 2. Notice that we are presented with a multivariate data set in which each variable (i.e. signal or shape) can be described by multiple features that are extracted from the corresponding images. Some of these features will be meaningful and informative in the sense of explaining variance among the properties, while others will not. Therefore, a relevant approach is to represent signal and shape variables as latent variables, which leads us to the use of latent variable (LV) modeling (discussed below). Latent variables, also called latent constructs, are those that cannot be directly measured or observed – they are constructed from a combination of other, measurable, manifest variables (MVs) that can be directly extract from images. We can regard LVs as data reduction devices in which a set of MVs are linearly combined to form a particular LV.

Latent variable modeling is a well-established and widely used multivariate technique popular in the fields of chemometrics, social science, and marketing research [102, 45, 275]. Similar approaches have also been successfully applied in the biological domain on population-level measurements to relate molecular signals with phenotypic responses, such as migration, proliferation, and apoptosis in a variety of *in vitro* and *in vivo* models [121, 177, 144]. This framework is used to establish causal relationships between variables that cannot be directly observed or quantified, but are composed of multiple measurable (manifest) variables. As an example, take "morphological polarization" as a latent variable, which can be used to describe the degree to which a migratory cell is directionally polarized (Fig. 3-3). One cannot measure this variable directly, but must instead use various image features of cell shape and cytoskeletal organization in order to put a number to the measure of polarization. Therefore, we can formalize the model as a multiple regression using the latent variable approach. Two popular latent variable modeling frameworks are covariance-based structural equation modeling (CV-SEM) [45, 102], and partial least squares structural equation modeling, also called partial least squares path modeling (PLS-PM) [275]. Both approaches are used to estimate the relationships between latent variables: CV-SEM seeks to find the parameters that minimize the residual covariance between the latent variables in the model estimates in comparison with the data. On the other hand, PLS-PM seeks to maximize the variance explained by the causal latent variables and the explanatory latent variables in the model.

The PLS-PM algorithm is iterative, alternating between estimating the relationships between LVs and their corresponding MVs, first, which describes the measurement, or outer, model, and, second, the relationship between LVs, which describes the structural, or inner, model. The relationships between LVs and MVs and among LVs themselves are a series of simple or multiple linear regressions. The representation of LVs by their indicators, or MVs, can take the form of formative or reflective relationships. The selection of formative versus reflective relationship between a LV and its MVs depends on the underlying theory of the causal directionality of the LV and its associated MVs. In addition, one must consider whether the MVs are describing the same underlying property, or, conversely, they are not expected to be correlated. If the MVs describe different, uncorrelated, aspects of a particular property of a cell represented by a LV, then the formative measurement model would be appropriate. If, on the other hand, the MVs are expected to correlate in the same direction, they are assumed to be regulated by the same underlying latent construct, and therefore a reflective measurement model would be appropriate. As an example, consider a PLS path model relating pMLC to the morphological polarization. In this case, we treat "pMLC" and "morphological polarization" as two latent constructs, each of which is associated with three formative MVs, for instance. The MVs are measurable image features in a cell image that is stained for pMLC and has a defined cell shape outline, as was done in Chapter 4 (see Fig. 4-3).

One could conceive a formative relationship between LVs and their MVs by theorizing that three MVs, say asymmetry of pMLC distribution, overall levels, and distance of pMLC signal from the cell edge are separate, possibly uncorrelated, measures. These three MVs would together form their LV, which would correspond to a generalized "pMLC" construct derived from the multiple MVs, or image features, from a given cell. Similarly, morphological polarization can be described by image features (MVs) that are also not necessarily correlated, but could be, such as "Major Axis Length", "Area", and "Axis Ratio". The relationship in the structural model relating the two LVs is captured by an arrow drawn between the "pMLC" and "morphological polarization" LVs in the PLS path model. The PLS-PM framework thus enables flexibility in formulating relationships between LVs and their associated MVs in terms of directionality through which we can incorporate *a priori* knowledge of the biological system at hand. PLS-PM also leads to the structural model relating LVs themselves, each of which can be flexibly associated with its own MVs in a formative or reflective sense. The goal of the PLS-PM algorithm, not detailed here, would be to compute weights and loadings relating MVs with their LVs, and path coefficients relating the LVs among each other.

A separate PLS-PM model can be derived for each of many drug pertubations (e.g. doxorubicin and ROCK inhibitors in the system studied in this thesis). For each drug's model, the MV weights inform which MV in the measurement model contributes most to the explanatory relationship between the LVs, while the path coefficients will inform on the variance of the predicted LV ("morphological polarization") by the predictor LV ("pMLC"). This model can be extended to include a larger set of signaling and structural proteins and phenotypic constructs for broadening the scope of associations between molecular signaling and cell shape on a single-cell level. These PLS-PM models can then be used to objectively compare and contrast not just the effects of different drug perturbations on cell signaling or cell phenotype (e.g. morphology) as was done in this thesis, but also on the *relationships* between signaling and phenotype. These relationships will help establish, in a statistically formalized way, direct associations between cellular signaling, structure, and function that would provide a deeper understanding into how exogenous perturbations, like doxorubicin

chemotherapy, alter these associations.

6.3 Clinical implications of tumor adaptation to chemotherapy treatment

For decades, selecting the course of breast cancer treatment has been largely phenomenological and empirical – accumulated knowledge from clinical trials and medical records spanning hundreds of thousands of patients have generated insights, rationale, and structure into courses of treatment [198, 105, 253]. The post-genomic era has led to an explosion in biological data derived from -omics technologies that reveals the molecular underpinnings of tumor etiology [4]. Integrative analysis of this data provides for concrete therapeutic strategies that can specifically target the signaling pathways that tumor cells rely on to survive, proliferate, and disseminate. This thesis has shown that doses of doxorubicin chemotherapy that fail to induce cell death can have the counterproductive effects of altering cytoskeletal phosphosignaling regulated by checkpoint kinases that promote changes in cell shape, migration, and chemo-tolerance. In essence, this work bridges the fields of DNA damage and cytoskeletal biology. Studies of DNA damage pathways have largely focused on cell cycle inhibition and apoptosis – this thesis demonstrated a new link between these pathways and mechanisms of cell shape and motility regulation. Although gene expression profiling has been largely used to define prognostic and theragnostic signatures [49], the majority of cellular processes responsible for drug resistance and metastasis are regulated by protein-level signaling networks. As a result, proteomic and phosphoproteomic assays will be critical in defining the mechanisms that drive cancer progression and optimizing therapeutic strategies.

Many studies have focused on the genetic basis of drug resistance, applying experimental and computational methods to formulate potential therapeutic strategies to counteract the forces of evolution in cancer progression [204]. These forces remain an important area of study, but this thesis suggests that, at least for doxorubicin, non-genetic forces may also play a role. Future work remains to thoroughly understand the contributions of epigenetic and transcriptional changes induced by doxorubicin, and to what extent these changes contribute to altered cytoskeletal signaling and phenotypic alterations that were observed in Chapters 3 and 4. Interestingly, the majority of discussions pertaining to resistance to chemotherapy, as opposed to targeted therapies, lie mainly in the domain of multi-drug resistance mechanisms and buffering of reactive oxygen through anti-oxidant enzymes [23]. These mechanisms may effectively reduce drug concentrations within tumor cells to sub-lethal levels, but they do not directly explain the downstream changes in signaling and phenotype that result in altered morphology, motility, and viability that were characterized in this thesis. Consequently, the findings in this thesis are not in disagreement with the current understanding of cellular response to chemotherapy, but expand our knowledge of the consequences of sub-lethal doses that alter the signaling and phenotypic landscape of surviving cancer cells following drug treatment. Despite the mechanisms involved, pharmacokinetic properties inevitably result in heterogeneity of drug dose within the tumor under almost all scenarios during the course of treatment. Pockets of the tumor with sub-lethal dose exposure lead to residual survivors, which, as this thesis has shown, may have important implications on subsequent treatment response and disease progression.

As discussed in Chapter 3, the enhanced chemo-tolerance induced by low-dose doxorubicin could constitute an adaptive response to therapy, a form of acquired resistance

that may influence the course of multi-round doxorubicin monotherapies in the clinic (Fig. 6-1). Sub-lethal doses of chemotherapy could result from reduced drug penetration into a tumor mass, in which peripheral cells die off while cell at the core survive under low-dose exposure while still activating DNA damage pathways. Acquired resistance is particularly problematic because the resistant population often attains additional traits that can make constituent cells more invasive. This is particularly likely in our system, given altered cytoskeletal and actomoysin changes induced by the drug, which directly regulate cell motility. It is intriguing to speculate that the large body of clinical evidence demonstrating acquired resistance to doxorubicin, as discussed in Section 1.1, may be in part due to the mechanisms characterized in this thesis. Much work still remains to assess whether cells that survive primary doxorubicin treatment become more resistant to subsequent rounds of treatment to support the clinical evidence showing that patients with prior chemotherapy exposure are less responsive to secondary treatments with the same drug.

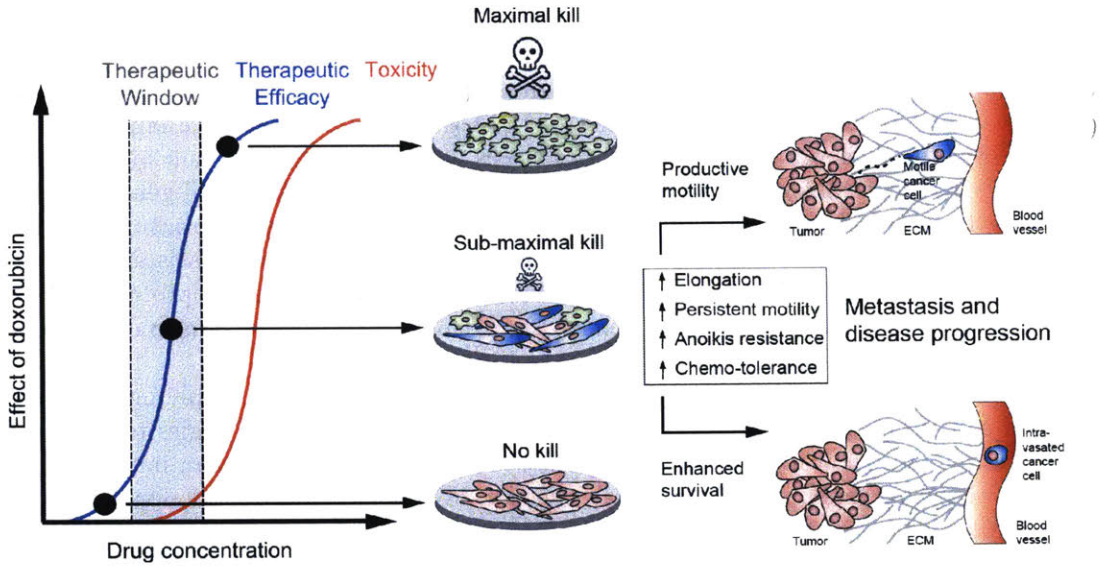

Figure 6-1: Sub-maximal tumor killing resulting from sub-lethal doxorubicin doses promotes phenotypic changes in cancer cells *in vitro* that are typically associated with metastasis and disease progression *in vivo*.

In addition to changes in cytoskeletal signaling, alternative mechanisms not studied here could also contribute to the phenotypic changes induced by sub-lethal doxorubicin. Future studies should focus on ROS, which, as discussed in Section 1.1, are increased by doxorubicin. Sub-lethal ROS levels could activate pro-migratory signaling through p38 MAPK or inhibition of tyrosine phosphatases that regulate RTK signal transduction pathways. Additional studies should also assess whether sub-lethal ROS levels induced by the drug result in increased production of antioxidant co-factors and enzymes, such as glutathione, catalase, thioredoxin, among others, which could negate the pro-apoptotic effects of subsequent chemotherapy.

One promising approach toward addressing drug resistance is to leverage the phenomenon of collateral sensitivity. Collateral sensitivty refers to the hypersensitive state of cancer cells to a different drug that have acquired resistance to a primary treatment [253]. Combination therapy with multiple drugs at once could address intrinsic resistance,

while sequential application could better target acquired resistance. For instance, Lee et al. have shown that sequential administration of a targeted inhibitor of EGFR and doxorubicin enhances cancer cell death compared with simultaneous administration with the two drugs [146]. More generally, the phenomenon of collateral sensitivity emphasizes the value of studying the dynamics of tumor cell function to guide optimization of combination treatment scheduling [297].

Indeed, this thesis has shown the importance of perhaps unintuitive, and complex, temporal regulation of molecular signaling and the critical role it plays in determining cell phenotype. Although the phosphoproteomic screen in Chapter 3 showed that pMLC levels increased at 12 hrs following doxorubicin treatment, subsequent site-specific assays in Chapter 4 showed that pMLC exhibits a biphasic response, with a subsequent decrease in pMLC levels below baseline by 24 hours. This biphasic response not only suggests a complex spatiotemporal interplay between DNA damage networks, focal adhesion signaling, and actomyosin regulation, but a potential temporal "window" of intervention into these processes. For instance, as discussed in Chapters 3 and 4, sub-lethal doxorubicin potentiates a chemotolerant state to MDA-MB-231 breast cancer cells that makes them less sensitive to subsequent doxorubicin chemotherapy treatment. Since an increase in pMLC achieved through Rho GTPase activation resulted in reduced tolerance to doxorubicin, modulation of the actomyosin machinery may be a novel way to counteract doxorubicin-induced chemo-tolerance. The timing, however, may be critical – re-activation of actomyosin within 12 hours may be counterproductive, while re-activation following 24 hours could be more effective, as this is the time point when pMLC levels dropped below baseline. Future studies should explore in greater detail the signaling mechanisms that regulate the doxorubicin-induced biphasic temporal response in pMLC, and relate this regulatory machinery to changes in morpholgoy, motility, and drug tolerance.

6.4 Toward the use of model systems with improved translational relevance

Although the findings presented in this thesis suggest counterproductive features of sublethal chemotherapy that may exacerbate clinically-relevant characteristics of the disease like metastasis and drug tolerance, the 2-D *ex vivo* model system used has clear limitations. Future work should focus on characterizing cellular signaling and phenotype in more physiologically-relevant systems with more direct translational relevance. These include 3-D culture systems, co-cultures of cancer cells with stromal cells, and *in vivo* mouse models to capture the important roles of extracellular matrix dimensionality and composition, heterotypic intercellular interactions, and tissue architecture on cellular response to chemotherapy.

Three-dimensional model systems are increasingly being used in the study of physiological parameters that influence cancer cell response to drugs [133, 291]. First, extracellular matrix architecture and composition can substantially affect cellular mode of motility [59, 200, 201]. The 2-D systems used in this thesis constitute an environment in which mesenchymal migration dominates, whereby cells rely on cytoskeletal reorganization through focal adhesion-matrix engagement to migrate. Actomyosin stress fibers, a dominant cytoskeletal feature altered by doxorubicin (Chapter 3), are preferentially observed in 2-D, but are frequently absent in 3-D. Although this thesis has shown that doxorubicin induces morphological elongation in 2-D and 3-D (Fig. 3-2 and Fig. 4-5) future studies are needed

to investigate effects of doxorubicin on cancer cell motility in 3-D. In addition to mesenchymal motility, in 3-D environments cells can also migrate through the amoeboid mode, which relies on the actomyosin machinery to squeeze cellular organelles through matrix pores. As a result, impairment of actomyosin contraction induced by doxorubicin (Chapter 4) may block amoeboid migration, which may lead to mesenchymal migration as the dominant mode. With regard to toxicity, doxorubicin-induced inhibition of actomyosin contraction could also potentially impair the migration of immune cells, such as neutrophils, which have been shown to migrate through amoeboid motion [76, 110]. This possibility presents an exciting direction for future investigation into the effects of chemotherapy on the immune system.

Additionally, matrix composition and architecture can influence cell survival [27, 218]. Numerous studies have shown that cancer cells in 3-D display reduced sensitivity to pharmacological treatments, demonstrating the importance of extending signaling and phenotypic studies beyond 2-D culture. Moreover, tumor-stroma interactions can substantially affect cancer cell signaling and behavior through paracrine and juxtacrine engagement. The contributions of tumor-associated macrophages and mesenchymal stem cells to cancer cell motility and survival have been extensively studied [235, 137, 210], and are therefore an important element of follow-on work to this thesis.

Finally, breast cancer xenograph mouse models can be used to study the metastatic process directly [77]. This thesis has shown that sub-lethal doxorubicin enhances survival of MDA-MB-231 breast cancer cells on both adherent and non-adherent substrates (Fig. 3-6 and Fig. 3-7), suggesting enhanced survival during primary tumor escape and in the vasculature following intravasation. These findings set the stage for the use of orthotopic xenograft mouse models to investigate the effects of sub-lethal doxorubicin on survival of MDA-MB-231 cancer cells in various stages of metastasis to the lung, liver, bone, or brain (e.g., through tail, portal, intracarotid or intracardiac vein injections of human cells in the mouse). Additional studies measuring intratumor drug concentration following systemic drug administration are also warranted, in order to assess whether the *in vitro* concentrations used in this thesis can be observed at the cores of growing tumors [179]. Furthermore, it would be relevant to investigate how sensitive doxorubicin pre-treated cells are to secondary treatment in the mouse model by measuring tumor growth following a doxorubicin treatment regimen. Xenograft models also provide a useful system for intravital imaging studies using two-photon microscopy to track fluorescently-labeled cancer cell survival, morphology, and motility under doxorubicin *in vivo*. The application of 3-D (co)culture systems and mouse models will contribute critical features of *in vivo* context to the study of DNA damaging chemotherapy effects on cancer cell signaling, structure, and function.

Appendix A

A.1 Materials and Methods (Chapter 2)

A.1.1 Software and image data availability

The files necessary to run SAPHIRE are available as a software package that can be downloaded in its latest version at http://saphire-hcs.org. A demo with sample cell image data, instructions, and scripts is provided for using the trajectory editing GUI tool, time series modeling, phenotypic profile computation for groups of cells, and visualization of SAPHIRE outputs.

A.1.2 Generation of fluorescent reporter cells

Cells were generated with fluorescent reporters for both actin to provide for cell shape and histones to label nuclei. A pBABE-HistoneH2B-mCherry retroviral plasmid was a gift from Dr Iain Cheeseman (MIT Whitehead Institute). LifeAct-eGFP was inserted between the XhoI-EcoRI sites in pMSCV-puro vector using standard molecular biology techniques. Replication-incompetent virus was purified from HEK-293T cells using standard protocols. Supernatants containing LifeAct-eGFP or H2B-mCherry packaged virus were harvested at 48-72 h after transfection, and passed through 0.45 μm filter prior to use for transduction of target cells (Pall Corp., Cortland, NY). MDA-MB-231 cells were transduced with LifeAct-eGFP and H2B-mCherry filtered viral supernatants containing 8 μg/ml polybrene (Millipore). Selection and propagation of transduced MDA-MB-231 cells was performed by culture in 1 μg/ml Puromycin (Sigma) in complete DMEM media. To make the stable fluorescent cell population more uniform in the expression of the two reporters, cells were sorted for double-positive intensities in the 80–90 percentile of the population using a MoFlo3 flow cytometer (Beckman Coulter, Inc.).

A.1.3 Cell culture, live-cell imaging, and drug perturbations

The triple negative breast cancer cell line MDA-MB-231 (ATCC) stably expressing LifeAct-eGFP and histone H2B-mCherry was used in all experiments. Cells were cultured in high-glucose Dulbecco's Modified Eagle Medium (DMEM) (Life Technologies) supplemented with 10% HyClone fetal bovine serum (Thermo Scientific), 1% penicillin/streptomycin (Gibco), and 1% GlutaMAX (Life Technologies) at 37 °C and 5% CO_2. For drug perturbation imaging experiments, Nunclon Delta 96-well optical bottom plates (Thermo Scientific) were coated with 5 μg/cm^2 pH-neutralized, acid-extracted, nonpepsin digested collagen I (BD Biosciences) for 1 hour at 37 °C and 5% CO_2. All wells were then washed twice with PBS and once with culture media prior to cell seeding. Following plate

coating with collagen, cells were seeded at a density of 1000 cells per cm2 in culture medium and incubated at 37 °C and 5% CO_2 for 24 hours. Following the 24 hour incubation, the culture media was replaced with drug-containing imaging culture media and the plates were immediately transferred to the microscope for live imaging. The time delay between drug addition and start of image acquisition was approximately 30 minutes to 1 hour.

Two imaging experiments were performed: for the experiment with the expanded panel of drugs cells were imaged on an IncuCyte ZOOM system incubated at 37 °C and 5% CO_2 under a standard scanning protocol (Essen Bioscience) in drug-containing DMEM growth media (see above). Cells were imaged over approximately 18 hours at 20 minute intervals, with three wells per drug condition and four fields of view per well, producing an image data set of 84 fields (4452 time series image frames), from which 293 individual cell trajectories, with an average of 53 time frames, were obtained for further analyses. For the other experiment, which contained the experimental controls, cells were imaged in Leibovitz's L-15 media (Life Technologies) supplemented with the same additives as the DMEM culture media above, on a Nikon Eclipse Ti microscope equipped with an Andor Zyla sCMOS camera. Cells were imaged over approximately 18 hours at 8 minute intervals, with three wells per drug condition and four fields of view per well, producing an image data set of 96 fields (16,128 time series image frames), from which 435 individual cell trajectories, with an average of 100 time frames, were obtained for further analyses. All inhibitor stocks were dissolved in dimethyl sulfoxide (DMSO) (Sigma), other than Y-27632, which was dissolved in high-purity water. All final concentrations of inhibitors in culture media used for imaging were at 0.1% v/v DMSO or lower. In both experiments cells were imaged using a 0.30 NA Nikon Plan Fluor 10x air objective. The inhibitors used in this work and their vendor sources were as follows: AZD6244 (MEK inhibitor; Selleck Chem.), ML-7 (MLCK inhibitor; Enzo Life Sciences), Blebbistatin(+/-) (non-muscle myosin II inhibitor; Enzo Life Sciences); Gefitinib (EGFR inhibitor; LC Labs), PD0325901 (MEK inhibitor; LC Labs), Y-27632 (ROCK inhibitor; Enzo Life Sciences), PD150606 (Calpain inhibitor; EMD Millipore).

A.1.4 Image processing

Time series stacks were exported as monochrome images from the red and green channel for LifeAct-eGFP (actin) and histone H2B-mCherry (nuclei) reporters, respectively. All images were batch processed using a custom pipeline written in MATLAB (Mathworks, Inc.). First, time series images were drift-corrected with the StackReg plugin in ImageJ using the nuclear reporter channel relative to the first time frame and cropped to maintain identical field of view regions in the nuclei and actin reporter image stacks for each field individually. Nuclei in each image were then segmented using point-source detection [3]. User-assisted cell body segmentation from the actin reporter channel was performed for the first frame of each time series stack. Otsu intensity and Canny edge detection thresholds were set by the user for the first frame of a time series for each field of view, with the cell masks generated by combining the binary Otsu foreground and Canny edge pixels. The thresholds were modified through time for each field of view automatically for the second frame onward using a parameter gradient search that minimized the sum of the difference in area, perimeter, and solidity of foreground objects between a previous and subsequent frame. For each connected foreground object, nuclei centers were used to form holes in the binary object mask that enabled detection of touching cells by computing the Euler number

for the object. Segmented cell body regions without spatial overlap with segmented nuclei were removed. Segmented nuclei were tracked over time using the IDL tracking method implementation [55]. To avoid bias of cell–cell interaction effects on morphology, touching cells were automatically identified as two or more segmented nuclei within a segmented cell body region in a given frame, and subsequently flagged for removal. A graphical user interface was developed to correct cell body segmentation inaccuracies and to label dividing or dying cells (Fig. 2-2). Continuous cell trajectories with no division, death, or intercellular spatial interactions were retained for both imaging experiments and subsequent analyses.

A.1.5 Cell shape quantification and shape-space definition

Eighteen whole-cell shape features were computed from the binary masks of each cell at every time point in both imaging experiments (Table B.1). Here, we call a temporal snapshot of a cell a "cell object". For each imaging experiment separately, the raw shape features from all cell objects were combined into an $n \times m$ matrix A, where n is the total number of cell objects and m is the number of shape features. The matrix was z-score normalized across cell objects for each feature (along columns). For the imaging experiment where the expanded panel of drugs was tested, we performed dimensionality reduction using PCA onto a two-dimensional basis from the covariance matrix of A, making the PCs linear combinations of the shape features with points in PC space corresponding to cell objects. The PCA coefficients derived from cells imaged in the expanded drug panel experiment were then used to project the shape features from the other experiment (with drug doses and controls) onto the same two-dimensional PC basis. Reducing data dimensionality using PCA dampens the effects of features in the model that contribute little to shape variability across cells and removes correlations between features used for subsequent modeling steps. With this projection, the shape trajectory of a cell is converted from a $T \times m$ matrix, where T is the number of time points, to a $T \times 2$ matrix, where the two columns correspond to the two linearly independent PCs. The $T \times 2$ matrices for each cell represent bivariate temporal trajectories in the two-dimensional PC space that we define as the "shape-space". The bivariate temporal trajectories are then used for subsequent shape state identification and time series modeling. GMM using expectation maximization and Bayesian information criterion (BIC) for model selection were used for GMM analyses of simulated and experimental data and implemented using the `mclust` package in R.

A.1.6 Probabilistic time series modeling

The methods in this section were adapted from prior work applying time-series modeling to infer modes of motion for particles in biological systems [184]. For additional mathematical and methodological details, refer to the PhD thesis of Nilah Monnier cited in [184]. Below I walk through the implementationn of these methods to the annotation of cellular morphological states.

A bivariate temporal trajectory for an individual cell whose shape dynamics we wish to model is comprised of T time points each with an (x_t, y_t) coordinate at each time point $t \in \{1, ..., T\}$ in two-dimensional PC shape-space. We model the coordinates as emissions $e_t = (x_t, y_t)$ from K number of "hidden" shape states, $\{s_i\}_{i=1}^{K}$, $K = \{1, 2, 3, ...\}$. We represent each shape state as a symmetric, bivariate Gaussian distribution with mean $\mu_i = (\mu_{x,i}, \mu_{y,i})$ and standard deviation along both PC coordinates, $\sigma_i = \sigma_{x,i} = \sigma_{y,i}$. The covariance matrix

of x and y is diagonal, and we write the probability of the point e_t in shape-space coming from shape state s_i as:

$$p_{s_i}(e_t) = \frac{1}{2\pi\sigma_i^2} \exp\left(-\frac{(x_t - \mu_{x,i})^2 + (y_t - \mu_{y,i})^2}{2\pi\sigma_i^2}\right) \tag{A.1}$$

We next consider the set of points e_t for the entire cell trajectory ($e_t \forall t \in \{1, ..., T\}$), resulting in a $T \times 2$ matrix, $\mathbf{e}$. Because the number of hidden shape states, and the parameters μ_i and σ_i for each state s_i that lead to the emissions $\mathbf{e}$ are unknown, we test models M_k with different numbers of hidden states, $k \in K$, and select the model that best fits the cell trajectory shape-space data, $\mathbf{e}$. Bayesian model selection is used to evaluate how well each model fits the data in order to select the best model, inherently penalizing increased model complexity (i.e., increasing number of states),

$$P(M_k|\mathbf{e}) = \frac{P(\mathbf{e}|M_k)P(M_k)}{P(\mathbf{e})} \propto P(\boldsymbol{e}|M_k) \tag{A.2}$$

with the proportionality holding since we consider the prior probabilities of all models M_k to be equal. Importantly, points in $\mathbf{e}$ are not independent as they represent a temporal evolution in shape of the same cell. A hidden Markov model in the framework is used to incorporate the temporal dependencies in $\mathbf{e}$ and infer parameters that describe the dynamic properties (state transitions). Therefore, for each model, $\mathbf{e}$, its full set of parameters that must be inferred from the data are

$$\Theta = \left[\{\mu_{x,i}, \mu_{y,i}, \sigma_i\}_{i=1}^K, \{\pi_i\}_{i=1}^K, \{\Phi_{ij}\}_{i,j=1}^K\right] \tag{A.3}$$

where for each shape state (bivariate Gaussian distribution) μ_i and σ_i correspond to the state mean and standard deviation in shape-space, respectively, ϕ_{ij} is the probability of transitioning from state s_i to state s_j within the state transition probability matrix, ϕ, and π_i is the probability of the cell starting in state s_i at the first time point. Models are compared amongst each other independent of a particular realization, or values, of the parameters, as well as of the possible hidden shape state sequences. Therefore, the likelihood $P(\mathbf{e}|M_k)$ is marginalized over all the parameters Θ and hidden state sequences $\mathbf{s}_k = \{s_t\}$ for $t \in \{1, ..., T\}$ to obtain the total marginalized likelihood of the model M_k,

$$P(\mathbf{e}|M_k) = \int \sum_{s_k} (\pi_{s_1} \prod_{t=2}^{T} \phi_{s_{t-1}s_t} \prod_{t=1}^{T} p_{s_t}(e_t))] Pr(\boldsymbol{\Theta}_k|M_k) d\boldsymbol{\Theta}_k \tag{A.4}$$

The summation over states in brackets, $[\cdot]$, is the probability, $P(\mathbf{e}|M_k, \boldsymbol{\Theta}_k)$, of the observed temporal sequence of coordinates in shape-space of the cell trajectory, $\mathbf{e}$, conditioned on a particular model with k hidden shape states, M_k, and its parameters, $\boldsymbol{\Theta}_k$. Summation over the hidden state sequences is performed using the forward algorithm. Metropolis Markov Chain Monte Carlo (MCMC) with importance sampling is used to sample parameter space in order to integrate the marginalized likelihood, with the prior probability of the parameters given the model, $P(\boldsymbol{\Theta}_\mathbf{k}, M_k)$, taken as constant [184]. The resulting MCMC integration yields the total marginalized likelihood of each model, $P(\mathbf{e}|M_k, \boldsymbol{\Theta}_k)$, and its maximum likelihood (ML) parameters, $\hat{\boldsymbol{\Theta}}_k$. The model with the highest marginalized likelihood is chosen to describe the shape dynamics of the cell, with the most likely hidden shape state sequence calculated by the Viterbi algorithm using the ML parameters.

A.1.7 SAPHIRE model-derived phenotypic profiles for drug comparisons

Annotated shape state sequences of individual trajectories from identically treated cells were combined to generate a phenotypic profile for that treatment condition. A phenotypic profile is a 48-element numerical vector composed of four types of histograms that capture shape dynamics: state radial distances and state dwell times, collectively called "state location features", as well as state transition magnitudes and state transition dwell times, collectively called "state transition features". These features are derived as follows (see illustration in Fig. 2-5A).

For each inferred Gaussian state s_i in shape-space from a temporally annotated sequence, we convert the coordinates of the state mean value in the Cartesian PCA axes $(\mu_{x,s_i}, \mu_{y,s_i})$ to polar coordinates $(\mu_{r,s_i}, \mu_{\theta,s_i})$. As a result, $\mathbf{r}_{s_i}$ becomes the location vector of the state in shape-space and $|\mathbf{r}_{s_i}|$ is the radial distance of the state from the origin, where $|\cdot|$ denotes vector magnitude. θ is the angle $\mathbf{r}_{s_i}$ makes in the counterclockwise direction with the positive PC1 axis for state s_i. For each state s_i the state radial distance is described by $|\mathbf{r}_{s_i}|$, or equivalently $\sqrt{\mu_{x,s_i}^2 + \mu_{y,s_i}^2}$. The normalized state dwell time for s_i is calculated as $\sum_{t=1}^{T} \delta_{t,s_i}/T$, where $\delta_{t,s_i} = 1$ if the state is s_i in the model-annotated state sequence at time t, and 0 otherwise, with T equal to the number of elements in the sequence (i.e. number of time frames in the cell trajectory). For a given cell trajectory, we derive an angular histogram with twelve bins on the range of 0 to 360 degrees, with the first bin 0 to 30 degrees, second bin 30 to 60 degrees, and so on until the twelfth bin that ranges from 330 to 360 degrees. For all states $s_i \in S$ in the cell sequence, the state radial distance value of each bin is computed as $\langle|\mathbf{r}_{s_i}|\rangle$ where $\langle\cdot\rangle$ denotes the mean, for all states s_i with μ_{θ,s_i} falling within the angular range of the bin, to generate a histogram of state radial distances. A state radial distance profile for a treatment condition is then computed as the average within each bin in the twelve-bin state radial distance histograms for all cells in that treatment condition. The state dwell time profile of the treatment condition is similarly computed except averaging normalized state dwell time values for states of each cell instead of the state radial distances for twelve angular bins.

We additionally derive state transition profiles for each treatment condition. Consider for a given cell a state transition from s_i to s_j. The state transition direction $\theta_{s_{ji}}$ for s_j from state s_i is the angle that the vector $\mathbf{r}_{s_j} - \mathbf{r}_{s_i}$ makes in the counterclockwise direction with the positive PC1 axis in shape-space. The state transition magnitude for s_j from state s_i is computed as $|\mathbf{r}_{s_j} - \mathbf{r}_{s_i}|$ scaled by the normalized state transition dwell time. The normalized state transition dwell time for s_j from state s_i is calculated as the number of time points a cell spends in state s_j after transitioning to it from state s_j, divided by the sequence length, T . The state transition dwell time value of each of the twelve angular bins is the mean of the normalized state transition dwell times of all states whose means $(\mu_{r,s_i}, \mu_{\theta,s_i})$ are in the bin. For transition directions $\theta_{s_{ji}}$ for all $i \neq j$ and a given cell, the state transition magnitude value of each of the twelve angular bins is computed as $|\mathbf{r}_{s_j} - \mathbf{r}_{s_i}|$ for all $\theta_{s_{ji}}$ falling within the angular range of each bin, to produce a histogram of state transition magnitudes. A state transition magnitude profile for a treatment condition is then calculated as the average within each bin in the twelve-bin state transition histograms for all cells in that treatment condition. A state transition dwell time profile is similarly computed except averaging normalized state transi-

tion dwell times across cells for the twelve angular bins instead of the transition magnitudes.

To quantify similarities in effects of treatment conditions on cell shape dynamics, clustering using average linkage of Euclidean distances between phenotypic profiles was performed for treatment pairs to generate cluster dendrograms. Internal nodes were re-sorted into optimal leaf order without dividing the clusters or changing overall tree connectivity so that treatments with similar profiles are next to each other by maximizing the sum of similarities ($\max_{ij}(d_{ij}) - d_{ij}$, where i is a leaf adjacent to leaf j) between adjacent tree leaves.

Permutation testing was used to assess significance of Euclidean distances (similarities) between all pairs of treatments as follows. Dynamic phenotype profiles (48-element vectors) based on state locations and state transitions and corresponding dwell times (see above) of individual cells within any two treatment conditions being compared were randomly reassigned into the two treatments while preserving the number of cells and their signatures. Signature values were averaged between the randomly-assigned cells for a given treatment to generate a treatment profile. A permutation test p-value for similarity between two treatment profiles was quantified by comparing the actual Euclidean distance between the treatment profiles relative to the null distribution of distances between profiles that were obtained by repeating the cell assignment randomizations and distance calculations 10,000 times for each pair of treatments.

A.1.8 Drug classification and comparison with existing methods

To compare between various image-based profiling methods for classifying treatment conditions, we followed an analysis procedure similar to the one described previously [157]. Four existing state-of-the-art methods for generating treatment profiles from fixed-cell measurements were implemented for comparison with the temporal modeling framework presented in this work: "Means" [249], "K-S Statistic" [197], "Factor Analysis + Means" [296], and "Gaussian Mixture" [238], all of which were previously compared in an HCI drug classification performance study [157]. For each method, all cellular image snapshots were extracted from the time series movies for all treatment conditions at 1, 4, 8, 12, and 16 hours following treatment addition, as if a researcher would make fixed-cell imaging measurements at these time points in an HCI experiment.

Briefly, the "Means" approach averages each of the 18 cell shape features for each treatment condition for the five time points to generate a phenotypic profile for a treatment. For the "K-S Statistic", the cumulative distribution function (cdf) is compared between the treatment and DMSO control cells for each shape feature separately. A signed Kolmogorov-Smirnov (K-S) statistic is then computed for each treatment, which is equal to the maximum distance between the two cdfs and set to positive if the treatment cdf is above the control cdf and negative otherwise. A "K-S Statistic" profile for a treatment is a vector of concatenated signed K-S statistics for each shape feature. For the "Factor Analysis + Means" method we first performed factor analysis on cells from all treatments at the five time points, selecting the number of factors using the Kaiser criterion, and then computed the average value of the scores of each factor for the cells in each treatment condition to generate a profile for that treatment. Finally, for the "Gaussian Mixture" method, a GMM with no covariance matrix constraints was fit to cell

observations from all treatments at each time point separately using all shape features as variables, testing models with 2 to 30 mixtures, and selecting the best-fitting model using BIC. For each treatment, the posterior probability of each cell under that treatment belonging to each of the mixtures was computed and averaged across cells for each mixture to generate a profile at a given time point. The averaged posterior probabilities of all mixtures and time points were combined to generate a phenotypic profile for each treatment.

Treatment classification accuracy was assessed for each of the profiling methods described above, as well as using the profiles derived from the single-cell temporal modeling using SAPHIRE. To assess the value of the HMM in treatment classification, treatment profiles extracted from shape-space analyses of cellular dynamics without the HMM annotations were generated identically as for SAPHIRE but by treating each time point in a cell trajectory as a separate "state" (i.e. no modeling of PCA coordinates from underlying hidden Gaussian states). Treatment condition classification accuracy was assessed by computing pair-wise Euclidean distances between phenotypic profiles of treatments using each of the profiling approaches separately. A treatment was designated as being correctly classified if its phenotypic profile was closest, in terms of distance, to that of the same treatment at a different dose, compared to the profiles from other treatments [157].

A.1.9 Abbreviations

BIC	Bayesian information criterion
EGFR	epidermal growth factor receptor
GMM	Gaussian mixture modeling
HCI	high-content imaging
HMM	hidden Markov modeling
PC	principal component
PCA	principal component analysis
MEK	mitogen-activated protein kinase kinase
MLCK	myosin light chain kinase
ROCK	Rho-associated protein kinase
SAPHIRE	Stochastic Annotation of Phenotypic Individual-cell Responses

A.2 Materials and Methods (Chapter 3)

A.2.1 Cell Culture

U2OS, HEK-293T, HEK-293FS, MDA-MB-231, LM2, MCF7, and MDA-MB-436 cells were maintained in Dulbecco's Modified Eagle's Medium (DMEM) supplemented with 10% fetal bovine serum (FBS). SUM159 cells were cultured in HAM-F12 medium supplemented with 5% FBS, 5 μg/ml Insulin, 1 μg/ml Hydrocortisone, and 20 ng/ml EGF. HEK-293FS cells were a gift from Tyler Jacks' lab (MIT, USA). MDA-MB-231 cells, SUM 159 and LM2 cells lines are maintained in the authors' laboratories and re-authenticated (Genetica, Inc., Burlington, NC, USA). Other cell lines were purchased from ATCC.

A.2.2 Reagents

Doxorubicin (Catalog# D-1515), hygromycin (Catalog# 10687010), doxycycline (Catalog# D-9891), PF-3644022 (MK2 inhibitor; Catalog# PZ-0188), SB202190 (p38MAPK inhibitor), camptothecin (Catalog# C-9911), etoposide (Catalog# E-1383), irinotecan (Catalog# I-1406), nocodazole (Catalog# M-1404), propidium iodide (Catalog# P-4170), and anti-β-actin (Catalog# A-2228) antibody were purchased from Sigma (St. Louis, MO, USA). Paclitaxel (Catalog# S-1150) was purchased from Selleckchem (Houston, TX, USA). Antibodies against pChk1 (S345; Catalog# 2348), pChk2 (T68; Catalog 2661), pMK2 (T334; Catalog# 3007), Chk2 (Catalog# 2662), MK2 (Catalog# 3042), cleaved PARP (Catalog# 5625), pFLNA (S2152; Catalog# 4761), and pPPP1R12A (S507; Catalog# 3040) were purchased from Cell Signaling Technology (Danvers, MA, USA) and used for Western blot at 1:1000 dilution. Antibody against Chk1 (Western blot, 1:2000; Catalog# 8408) was purchased from Santa Cruz Biotechnology (Dallas, TX, USA). Antibodies against pFAK (Y397; Catalog# 44-624G) and γH2AX (S139; Catalog# 05-636) were from Millipore (Billerica, MA, USA), and FAK (Catalog# 610082) was from BD Biosciences (San Jose, CA, USA) were used for immunofluorescence at 1:200 dilution. Phalloidin-AlexaFluor488 (Catalog# A12379), Phalloidin-AlexaFluor594 (Catalog# A12381), SYTO60 (Catalog# S12342) dye, and DAPI (Catalog# D1306) were purchased from Invitrogen (Waltham, MA, USA), with the Phalloidin conjugates used for immunofluorescence at 1:300 dilution. AlexaFluor647 AnnexinV (Catalog# 640943) was purchased from BioLegend (San Diego, CA, USA), and used for live-cell imaging of apoptosis dynamics at 0.25 μg/ml.

A.2.3 Virus production and generation of stable cell lines

For retrovirus production, 293T cells were transfected with GFP-LifeAct and mCherry-H2B along with packaging and structural vectors VSVG and GAG/POL using Fugene 6 transfection reagents (Promega, Madison, WI, USA, Catalog# E2691) following manufacturer instructions. Supernatants containing virus were used to transduce target cells in the presence of 8 μg/ml polybrene (Millipore; Catalog# TR-1003-G) for three rounds of infection. Successfully transduced cells are selected by sorting GFP- and mCherry-positive cells using an Aria3 cell sorter (BD Biosciences).

A.2.4 Generation of inducible knockdown cell lines

pSLIK containing Tet-inducible miR30-based hairpins were developed for single viral infection method to conditionally knock down target genes [237]. To generate pSLIK-

hygromycin-shLuc, pSLIK-hygromycin-shMK2, pSLIK-hygromycin-shChk1 and pSLIK-hygromycin-shChk2, gateway recombination between the pSLIK-hygromycin destination vector and a pEN-TTmiRc2 entry vector harboring either shLuc, shMK2, shChk1, or shChk2, were performed using LR clonase (Invitrogen; Catalog# 11791-020) following manufacturer instructions. pSLIK-hygromycin and pEN-TTmiRc2 vectors are obtained from Tyler Jacks' lab (MIT, USA). Vector information can be found on the Addgene website (Catalog# 25737 for pSLIK-hygromycin; Catalog# 25752 for pEN-TTmiRc2). shRNA sequences were designed using the Cold Spring Harbor web portal:
`http://codex.cshl.org/RNAi_central/RNAi.cgi?type=shRNA`
and 97mer oligonucleotides were used as templates (see sequences below). For lentivirus production, 293FS cells were transfected with either pSLIK-hygromycin-shLuc, pSLIK-hygromycin-shMK2, pSLIK-hygromycin-shChk1 or pSLIK-hygromycin-shChk2 along with lentiviral packaging and structural vectors delta8.2 and GAG/POL using Fugene 6 transfection reagents (Promega) following manufacturer instructions. Supernatants containing virus were then used to transduce target cells in the presence of 8 μg/ml polybrene (Millipore) for three rounds of infection. Successfully transduced cells are selected using 50 μg/ml Hygromycin.

MK2, human: GAGCGAAATTGTCTTTACTAAA
Chk1, human: GAGACACTTCCTGAAGATTAAA
Chk2, human: AGCTCTCAATGTTGAAACAGAA
Luciferase: CCCGCCTGAAGTCTCTGATTAA

A.2.5 siRNA oligonucleotides and siRNA transfection

MK2 siRNA and non-targeting control siRNA were purchased from Ambion (Foster City, CA, USA). siRNA transfection was performed using Lipofectamine RNAiMAX (Invitrogen; Catalo# 13778150) following manufacturer instructions using a final siRNA concentration of 10 nM.

A.2.6 SILAC cell labeling and sample preparation for phosphoproteomics

U2OS cells were grown in Arginine- and Lysine-depleted DMEM supplemented with 10% dialyzed FBS (Invitrogen; Catalog# 26400). For Light SILAC amino acid labeling, cells were labeled with L-Arginine (Sigma; Catalog# A6969) and L-Lysine (Sigma; Catalog# L5751). For Medium SILAC amino acids labeling, cells were labeled with L-Arginine-U-13C6 (Cambridge Isotope Laboratories, Tewksbury, MA, USA; Catalog# CLM-2265-H-0.25) and L-lysine-4,4,5,5-D4 (Cambridge Isotope Laboratories; Catalog# DLM-2640-0.5). For Heavy SILAC amino acids labeling, cells were labeled with L-arginine-U-13C6;U15N4 (Cambridge Isotope Laboratories; Catalog# CNLM-539-H-0.25) and L-lysine-U-13C6;U-15N2 (Cambridge Isotope Laboratories; Catalog# CNLM-291-H-0.25). After 5 passages in SILAC medium, cells were confirmed to have proteins fully converted to SILAC amino acids. To induce DNA damage, SILAC amino acids-labeled cells were treated with DMSO or doxorubicin (5 μM) for 12 hrs. Supernatants are discarded, and the attached cells were washed with PBS and lysed with buffer (20 mM HEPES pH 8.0, 9 M UREA, 1 mM Sodium orthovanadate, 2.5 mM Sodium pyrophosphate, 1 mM β-glycerophosphate). Lysates were sonicated and cleared by centrifugation at 17,000 x g for 15 min at 4 °C. Protein concentration was measured using Bradford reagents (Bio-Rad Laboratories, Hercules, CA, USA)

following manufacturer instructions. The same amounts of protein (5 mg) from cells with differentially labeled SILAC amino acids were then mixed in a 1:1 ratio. Proteins were reduced with 1 mM dithiothreitol at 60 °C for 20 min and alkylated with 5.5 mM iodoacetamide at room temperature for 15 min. For digestion, protein extracts were diluted in 20 mM HEPES pH 8.0 to a final concentration of 2 M Urea, and protease was then added. Proteins were digested with endoproteinase Lys-C (Wako Chemicals, Richmond, VA, USA; Catalog# 129-02541) overnight at room temperature, rather than trypsin, to protect checkpoint kinase substrate motif sequences. Complete digestion was subsequently confirmed by SDS-PAGE. Digested peptides were purified using Sep-Pak C18 columns (Waters, Milford, MA, USA; Catalog# WAT-051910) and lyophilized.

A.2.7 Enrichment of phosphopeptides using immunoaffinity purification (IAP) and analysis by LC-MS/MS

To enrich for checkpoint kinase substrates, immunoaffinity purification was performed. Lyophilized peptides were dissolved in IAP buffer (50 mM MOPS/NaOH, pH7.2; 10 mM Na_2HPO_4; 50 mM NaCl; Cell Signaling Technology, Catalog# 9992), and incubated with bead-conjugated motif antibodies detecting RxxS*/T* sequences, where S* denotes phosphoserine and T* denotes phosphothreonine (Cell Signaling Technology, Catalog# 1978). The immobilized antibody beads were washed three times with IAP buffer and twice with water, while supernatants were incubated with a secondary bead-conjugated motif antibody detecting LxRxxS*/T* sequences (Cell Signaling Technology, Catalog# 5760). The immobilized antibody beads were washed three times with IAP buffer and twice with water. Peptides were eluted from the beads by incubation with 0.15% TFA. The eluents were purified using C18 microtips (Stage Tips; VWR, Radnor, PA, USA; Catalog# 55004-098), and then digested post-IP with trypsin (Promega, Catalog# V5113) at a final concentration of 25 ng/ml.

A.2.8 Peptide identification

Eluted peptides were loaded onto a C18 resin column and analyzed on an LTQ ion trap mass spectrometer (Thermo Fisher Scientific, Waltham, MA, USA). Tandem MS spectra were analyzed using MASCOT software to identify peptides (Matrix Science, London, UK). Readouts with MASCOT scores below 25 were filtered out, and the remainder of the phosphosites identified by MASCOT software are confirmed using PhosphoRS [251]. Only the phosphosites that were assigned by both MASCOT and PhosphoRS were used for further analysis.

A.2.9 Gene set enrichment analysis

Enrichment for gene ontology terms was performed on pre-ranked lists of genes from the phosphoproteomics data sets comparing fold changes between two experimental conditions using GSEA v2.0 [245]. First, phosphosites detected in at least one of two replicates for both experimental conditions were taken and gene names were extracted. Phosphosites were then ranked based on their $\log_2$-transformed fold change values between the two experimental conditions. The rank value for proteins with multiple phosphorylation sites was obtained by taking the maximum absolute fold change among all sites, while retaining the sign of the fold change (positive or negative). Because GSEA is agnostic to post-translational modifications, the identities of the phosphorylation sites were removed, producing unique

gene names with associated rank values, which were used as input for pre-ranked GSEA [245]. Enrichment for ontology terms was performed using the C5 GO gene sets from the MSigDB collections, using the classic enrichment statistic and no gene symbol collapse, while keeping other parameters at their default values.

A.2.10 Gene ontology singular enrichment analysis

Singular enrichment analysis (SEA) was used to quantify over-representation of phosphoprotein "hits" within ontology term gene sets related to molecular function, cellular component, and biological process. Unlike GSEA, SEA does not take gene list rank values into account, but assesses statistical over-representation of the input gene list within a GO term gene set. The degree of over-representation of genes in the input list of hits, A, within each GO term gene set, B, was computed with the Fisher's exact test using the command-line version of Lists2Networks that is part of the Expression2Kinases tool suite [43], implemented in headless mode using in-house MATLAB (Mathworks Inc., Natick, MA, USA) scripts. The SEA p-values derived from Fisher's exact test for over-representation within each gene set were corrected for multiple hypothesis testing using the Benjamini-Hochberg method [17] to generate FDR q-values for each gene set tested. To further account for over-representation of phosphoproteins categorized as "non-hits" that may occur by chance, we performed permutation testing as follows. Consider all genes in the phosphoproteomic data set, S, composed of two non-overlapping subsets: hits, A, and non-hits, C, where $|A|$ is the number of hits. Permutation testing was performed by randomly sampling $|A|$ genes from gene list C and running SEA on this randomly-sampled gene list of non-hits for over-representation with each GO term gene set, B. An empirical permutation test p-value was computed for over-representation of A in each gene set B by generating a null distribution of over-representation p-values from 1000 random, non-hit gene samples from C for each set B. The permutation p-value for each gene set B was computed as the fraction of the 1000 random samples that had over-representation p-values smaller (i.e. larger extent of over-representation) than the SEA p-value of A.

A.2.11 Network visualization of enrichment analyses

GSEA results were represented as enrichment networks, in which nodes correspond to enriched GO terms and edges to the similarity between two gene sets. Node sizes correspond to binned values of the number of genes in the GO term gene sets that also occur in the fold-change ranked gene input list. The edge weights correspond to binned values of the overlap coefficients between all pairwise GO term gene set comparisons. For two gene sets A and B, the overlap coefficient was computed as $\text{overlap}(A,B) = |A \cap B|/\min(|A|,|B|)$, where $|.|$ represents the number of genes. GSEA results were processed using custom scripts written in MATLAB to generate .graphml files with specified network properties. Networks were visualized and arranged using a combination of manual positioning and automated layout functions in yEd Graph Editor (yWorks GmBH, Tübingen, Germany). SEA results were visualized in a network format similar to that of GSEA results, with the exception that node sizes were kept constant with the number of genes in a GO term overlapping with the phosphoproteomic data set directly specified in node text labels. Nodes were colored based on the FDR q-value obtained from the SEA testing of "hits" over-representation within each GO term gene set.

A.2.12 Immunoblot analysis

Cells were lysed in lysis buffer (20 mM Tris-HCl pH 7.5, 150 mM NaCl, 1 mM Na_2EDTA, 1 mM EGTA, 1% Triton X-100, 1 mM PMSF) containing protease (Catalog# 4693159001) and phosphatase (Catalog# 4906837001) inhibitor tablets (Roche, Basel, Switzerland). Protein concentration was measured using BCA kit (Pierce Biotechnology, Waltham, MA, USA; Catalog# 23225). Cell extracts containing the same amount of protein in every condition were mixed with 6X reducing sample buffer (34 mM Tris-HCl pH6.8, 7% glycerol, 500 mM β-mercaptoethanol, 1.6% SDS, 120 mg/ml bromophenol blue). Samples were boiled at 95 °C for 5 min, and subjected to electrophoresis using the standard SDS-PAGE method. For LICOR-based blotting, proteins were transferred to nitrocellulose membranes (Bio-Rad; Catalog# 162-0115) and blocked with Odyssey blocking buffer (LICOR Biosciences, Lincoln, NE, USA; Catalog# 927-40000) for 1 hr. Membranes were then incubated with primary antibodies for 2 hrs at room temperature, then incubated for 1 hr at room temperature with secondary antibodies conjugated with LICOR fluorophores. Blots were scanned with a LICOR/Odyssey infrared imaging system (LICOR Biosciences), and bands quantified by densitometry using LI-COR ImageStudio. For ECL-based blotting, proteins were transferred to methanol-activated PVDF membranes (Bio-Rad; Catalog# 162-0177) and blocked with 5% nonfat dried milk for 1 hr. Membranes were then incubated with primary antibodies for 2 hrs at room temperature, incubated for 1 hr at room temperature with secondary antibodies conjugated with HRP, and imaged using enhanced chemiluminescence (ECL reagent kit, PerkinElmer, Waltham, MA, USA; Catalog# NE105001EA). Bands were quantified by densitometry using ImageJ.

A.2.13 IP kinase assay

Cells were treated with doxorubicin in the presence or absence of inhibitors against p38MAPK (SB202190, 10 μM) or MK2 (PF-3644022, 10 μM) and lysed in IP lysis buffer (20 mmol/L Tris-HCl (pH 7.4), 1 mmol/L EDTA, 150 mmol/L NaCl, 1 mmol/L EGTA, 1% Triton X-100, 1 mmol/L β-glycerophosphate, 1 mg/ml leupeptin, 1 mmol/L Na_3VO_4, 1 mmol/L phenylmethylsulfonyl fluoride). 500 μg of protein lysates were incubated with 2 μg of antibody against MK2 or Chk1 for 4 hrs, and subsequently with 50% slurry of protein A/G agarose beads overnight. Immunoprecipitates were washed with wash buffer (50 mmol/L Tris-HCl pH 7.5, 5 mmol/L EDTA, 150 mmol/L NaCl, 1 mmol/L DTT, 0.01% NP-40, 0.02 mmol/L PMSF) three times and then resuspended in 50 μL of kinase buffer (20 mmol/L MOPS pH 7.2, 25 mmol/L β-glycerol phosphate, 5 mmol/L EGTA, 1 mmol/L Na_3VO_4, 1 mmol/L DTT). 2 μL of [γ-32P]ATP and 2.5 μL peptide substrate (50 μM final concentration) were added and the kinase reaction proceeded at 30 °C for 30 min. 10 μL of reaction mixture was spotted onto p81 paper, air-dried, and washed with 0.5% H_3PO_4 three times. After being allowed to air-dry, the blotted p81 paper was submerged in 10 mL scintillation cocktail and radioactivity measured using a scintillation counter (LS-6500; Beckman Coulter, Brea, CA, USA).

A.2.14 Fluorescence live- and fixed-cell imaging

For live cell imaging experiments, MDA-MB-231 cells stably expressing LifeAct-eGFP and Histone H2B-mCherry were used (see "Generation of fluorescent reporter cells" in Materials and Methods section of ref. [96]). Cells were seeded at a density of 1000 cells/well in Nunclon Delta optical bottom black-wall 96-well plates (Thermo Fisher Scientific) precoated with

pH-neutralized, acid-extracted, nonpepsin digested collagen I (BD Biosciences, 50 mg/ml in 0.02N acetic acid, for 1 hr at 37 °C and 5% CO_2) and matrigel (0.2% in serum-free DMEM media, for 1 hour at 37 °C and 5% CO_2), and grown overnight at 37 °C and 5% CO_2. In live cell imaging experiments, Leibovitz's L-15 media ("imaging media"; Life Technologies, Carlsbad, CA, USA) supplemented with the same additives as DMEM culture media was used because of its superior buffering ability in the absence of 5% CO_2. Prior to imaging, DMEM media was removed from the plates, cells were washed with pre-warmed imaging media, compounds diluted in imaging media were added to the cells, and cells were incubated at 37 °C, without CO_2 infusion. Cells were then imaged live on a Nikon Eclipse Ti microscope equipped with an Andor Zyla sCMOS camera and temperature housing (37°C, no CO_2 infusion), using a 0.30 NA Nikon Plan Fluor 10X air objective. Processing and analysis of live-cell imaging data, including fluorescent cell segmentation, tracking, and shape feature extraction, were performed using the SAPHIRE software package, as described previously [96].

For tracking apoptosis dynamics, AlexaFluor647 AnnexinV was diluted to 0.25 μg/mL in imaging media containing experimental compounds and applied to cells immediately prior to imaging. AnnexinV mean intensity for each tracked cell at every time point was measured within the segmented nuclei regions defined by the H2B-mCherry signal. The elbow method applied to the histogram of AnnexinV intensities from all cells and time points was used to define the threshold to categorize cells as AnnexinV positive (dead) or negative (alive) at each point in time. Drug-treated cells were classified as "elongated" or "non-elongated" in live-cell imaging studies by defining a threshold at the 95th percentile of the major axis length distribution of DMSO-treated (control) cells. Drug-treated cells with major axis lengths above this threshold were considered "elongated", whereas those below the threshold were considered "not-elongated".

For fixed-cell analyses, non-fluorescent MDA-MB-231 cells were seeded as described above for live-cell imaging experiments, except DMEM culture media was used for all compound dilutions and cells were incubated at 37 °C with 5% CO_2. To characterize morphology following treatment, cells were fixed with 4% paraformaldehyde diluted in PHEM fixation buffer (60 mM PIPES pH 7.0, 25 mM HEPES pH 7.0, 10 mM EGTA pH 8.0, 2 mM $MgCl_2$, 0.12 M Sucrose) from a 16% solution (Electron Microscopy Sciences, Hatfield, PA, USA; Catalog# 15710) for 20 min at room temperature, permeabilized with 0.2% Triton X-100/PBS for 5 min, and stained with AlexaFluor488 phalloidin (1:300 in 1% BSA in PBS) for 30 min at room temperature and DAPI (1:1000 dilution in PBS) for 5 min at room temperature. Cells were imaged on a Cellomics ArrayScan VTI (Thermo Fisher Scientific) HCS Reader, equipped with a Hamamatsu Orca-ER digital camera (C4742-80) using a 0.30 NA Zeiss Plan-NEOFLUAR 10X air objective. An automated in-house image processing and analysis pipeline written in MATLAB was used to segment cells; any cell that touched another cell or the image border was removed and object segmentation quality control for each image was performed prior to morphology quantification.

A.2.15 Immunofluorescence

Cells were seeded onto glass coverslips in 6 well plates that were coated in the same way as the 96-well plates for high-throughput imaging. Following compound treatment, cells were fixed with 4% paraformaldehyde for 20 min at room temperature, and permeabilized with 0.2% Triton X-100/PBS for 5 min. Cells were blocked with 10% BSA/PBS for 30 min at 37 °C, incubated with primary antibodies (1:300 dilution in 1% BSA/PBS solution)

for 2 hrs at 37 °C, followed by secondary antibodies conjugated with fluorophore (1:200 dilution in 1% BSA/PBS) for 1 hr. Cells were stained with DAPI (1:1000 dilution in PBS) for 5 min before mounting onto glass slides, which were then imaged on a Delta-Vision II microscopy system equipped with an EDGE/sCMOS camera (Applied Precision, Issaquah, WA, USA). For high-resolution actin imaging (Fig. 3-2a and Fig. 3-9a) and focal adhesion imaging (Fig. 3-6a,c), a 1.40 NA Plan Apo Olympus 60X oil objective was used. For lower-resolution γH2AX imaging, a 0.75 NA U Apo 340 Olympus 20X objective was used.

A.2.16 Cell viability

Cells were seeded in 96-well plates at a density of 0.6 x 10^4 cells/mL (100 μL/well). After overnight incubation, cells were treated with compounds for indicated times. Cells were then fixed with 4% paraformaldehyde for 20 min at room temperature, and stained with SYTO60 dye (Invitrogen, 1 μM final concentration in PBS) for 1 hr at room temperature. After washing with PBS, fluorescence intensity was measured with a LI-COR/Odyssey infrared imaging system (LI-COR Biosciences) using the 700 nm channel.

A.2.17 Anoikis

Poly-HEMA (Sigma; Catalog# P-3932) was dissolved in 95% Ethanol at 37 °C by overnight incubation at a final concentration of 10 mg/mL. Cell culture plates were coated with poly-HEMA solution at 37 °C and allowed to air dry. For viability measurements, cells were seed in either poly-HEMA-coated or uncoated 96-well tissue culture plates at a density of 10 x 10^4 cells/mL (100 μL/well). After 48 hrs post-seeding, cell viability was measured using CellTiterGlo (Promega) following manufacturer instructions. Relative luminescence was measured using a microplate reader (Tecan Inc., Männedorf, Switzerland). For Western blotting, cells were seeded on polyHEMA-coated plates at a density of 50 x 10^4 cells/dish (100 mm dish). Forty eight hours post-seeding, cells are collected and lysed in lysis buffer, followed by Western blotting and immunoblot analysis as described above.

A.2.18 Focal adhesion disassembly

Cells were seeded onto glass coverslips in 6 well plates that were coated with 50 mg/ml collagen I and 0.2% matrigel. Cells were then treated with doxorubicin for 24 hrs, washed with serum-free media, and incubated in serum-free media containing 10 μM nocodazole for 4 hrs. Cells were fixed after 4 hr nocodazole incubation (no washout), or washed with serum-free media and released into complete growth media for 15 min, prior to fixation with 4% paraformaldehyde for 20 min. Focal adhesions were visualized by immunofluorescence staining using antibodies against phospho-FAK (Y397).

A.2.19 Cell cycle analysis

After 24 hrs of drug treatment, cells were trypsinized, fixed with cold 70% Ethanol in PBS, and stored at -20 °C until analysis. For flow cytometric analysis, fixed cells were washed with PBS and resuspended in PBS containing 0.5% BSA and 10 μg/mL RNAse A for 30 min at 37 °C followed by the addition of 25 μg/mL propidium iodide. DNA content was measured by flow cytometry (Calibur, BD Biosciences), and cell cycle profiles analyzed using FlowJo software.

A.2.20 Generation of regrown cell populations after doxorubicin treatment

MDA-MB-231 cells were treated with doxorubicin (0.5 μM) for 24 hrs. The drug was washed out by a media change, and cells incubated for an additional 24 hrs to allow recovery. Cells were then trypsinized and replated at 50 x 10^4 cells per 10 cm dish. Growth media was replaced every 3 to 4 days. Following 1 month of culture, the surviving proliferative cells had visibly repopulated the culture plate and formed colonies. These cells were then pooled and used as the regrown population for two-round doxorubicin treatment experiments.

A.3 Materials and methods (Chapter 4)

Unless otherwise specified in the sections below, experimental and computational procedures were performed, and reagents were prepared, as described in Appendices A.1 and A.2.

A.3.1 Reagents

Primary antibodies used for immunofluorescence and Western blotting from Cell Signaling Technology, Inc., were used at the following dilutions (WB = Western blotting, IF = immunofluorescence): ROCK1 (cat# 4035, WB 1:1000), MLC2 (cat# 8505, WB 1:1000, IF 1:100), pMLC2(S19) (cat# 3671, WB 1:1000, IF 1:200), pMLC2(T18/S19) (cat# 3674, WB 1:1000). β-actin antibody was from Sigma (cat# A1978, WB 1:5000), and pFAK(Y397) antibody was from Life Technologies (cat# 44-624G, WB and IF 1:1000). The inhibitors used in this work and their vendor sources were as follows: ML-7 (MLCK inhibitor; Enzo Life Sciences), Blebbistatin(+/-) (non-muscle myosin II inhibitor; Enzo Life Sciences); Y-27632 (ROCK inhibitor; Enzo Life Sciences); Calyculin A (cat# C-3987, LC Labs), Ionomycin (cat# I-6800, LC Labs). Rho activator II was from Cytoskeleton Inc. (cat# CN03 and used at 2μg/mL final concentration). The pH-neutralized, acid-extracted, nonpepsin digested collagen I used for 3D gels and 2D coating was from BD Biosciences.

A.3.2 Immunofluorescence

MDA-MB-231 cells were seeded on glass-bottom (#1.5) 96-well black plates pre-coated with 5 μg/cm^2 Collagen I, allowed to attach overnight, and then treated with compounds or DMSO (control). Following 24 hours of treatment, cells were fixed with 4% paraformalehyde. Cells were permeabilized with 0.5% TritonX-100 in PBS for 10 minutes, and then stained overnight with primary antibodies at 4°C, followed by secondary antibodies + 1:200 phalloidin for 1 hour at room temperature, and finally counterstained with DAPI (1:1000 in PBS) for 10 minutes at room temperature. Cells were imaged on a Nikon Eclipse Ti microscope equipped with an Andor Zyla sCMOS camera using a 0.30 NA Nikon Plan Fluor 10X air objective.

A.3.3 Imaging and morphology analysis in 3D gels

MDA-MB-231 cells stably expressing LifeAct-eGFP and H2B-mCherry were seeded within Collagen I gels (2 mg/mL final concentration) and allowed to polymerize at 37°C and 5% CO_2 for 30 minutes according to manufacturer instructions (50 μL of cell+gel suspension was added per well in a polymer-base optical bottom 96-well plate, 200,000 cells/mL final cell concentration). Compounds (100 μL) at desired final concentrations (accounting for the gel volume) were added and cells were incubated at 37°C and 5% CO_2 for 24 hours. Cells were then fixed with 4% (final) paraformaldehyde and washed once with PBS prior to imaging. Laser scanning confocal microscopy using a Nikon Eclipse Ti microscope using a 0.30 NA Nikon Plan Fluor 10X air objective was used to acquires approximately 300 μm z-stacks for each field-of-view. Images were processed and analyzed using a custom MATLAB script. Briefly, 3D Gaussian filtering was applied to localize cell nuclei in the stacks. Otsu thresholding was applied to each 2D slice to create a foreground mask of the cells and reconstruct 3D cell objects. For each connected foreground object, nuclei centers were used to form holes in the binary object cell body mask that enabled detection of touching cells by

computing the Euler number for each object. Segmented cell body regions without spatial overlap with segmented nuclei were categorized as debris and removed.

A.3.4 Gel contraction assay

Tissue culture-bottom 24-well plates were coated with 10% bovine serum albumin (BSA) PBS solution for 1 hour at 37°C and 5% CO_2. BSA solution was then removed and wells were washed once with PBS and allowed to air-dry. Cells were embedded in 1mg/mL Collagen I gels at a cell concentration of 1 million cells/mL and 400 μL of cell+gel suspensions were added to each well, and allowed to polymerize at 37°C and 5% CO_2 for 90 minutes. Compounds diluted in growth media were then added to each well (500 μL per well) to achieve final desired concentration, taking into account gel volume. Gels were gently released from the well bottom and sides using a sterile metal spatula and floating gels with cells + compounds were incubated at 37°C and 5% CO_2. A cell phone camera was used to take pictures of the gels at designated time points, and contraction area of each gel was analyzed using ImageJ.

To evaluate endpoint cell viability within the gels, and Trypan-blue assay was used. Briefly, gels were washed once with PBS and digested with 600 μL per well of Liberase solution (purchased from Sigma, 6 μL Liberase + 594 μL Liberase Calcium buffer was used). Gels in Liberase solution were transferred to eppendorf tubes and incubated with agitation for 90 minutes at 37°C. After dissociation, 300 μL of growth media was added to each tube and suspension was passed through a 40 μm pore-size cell strainer to remove undigested gel and cell clumps. Viability was then measured using Trypan-blue on a ViCell instrument (Beckman Coulter, Inc.).

A.4 Materials and methods (Chapter 5)

A.4.1 SMCC (succinimidyl 4-(N-maleimidomethyl)cyclohexane-1-carboxylate) ssDNA conjugation of antibodies and phalloidin

Twenty five nanomoles of thiolated single-stranded DNA (ssDNA)(Integrated DNA Technologies, Inc., Coralville, IA) was reduced using Dithiothreitol (DTT, 50 mM) for 2 h, purified using a NAP-5 column (GE Healthcare Life Sciences, Inc., Marlborough, MA), and quantified using a NanoDrop 2000 (Thermo Fisher Scientific, Inc., Waltham, MA). In parallel, 100 μg of antibody was concentrated to 1 mg/mL using an Amicon Ultra 0.5 mL centrifugal column (100 kDa, EMD Millipore, Inc., Billerica, MA) and purified from additive chemicals such as sodium azide using a Zeba spin desalting column (7 kDa, Thermo Fisher Scientific). A freshly prepared solution of SMCC with 5% DMF in PBS (Sigma-Aldrich, Inc., St. Louis, MO) was then added to react for 1.5 h with the antibody solution at a molar ratio of 7.5:1. Unreacted SMCC was removed using a 7 kDa Zeba column. In a subsequent reaction, antibodies were mixed in a 1:15 molar ratio with the reduced thiolated ssDNA strands and incubated overnight at 4°C to form stable thioether bonds. ssDNA-conjugated antibodies were then purified using an Amicon Ultra 0.5 mL column (100 kDa). The final protein concentration of the antibody was measured using a Nanodrop 2000 and the antibodies were stored at -20°C in 1x PBS with 50% glycerol. Amino-modified phalloidin (Bachem AG, Bubendorf, Switzerland) was conjugated using the protocol described above with an extra step of HPLC purification to separate unreacted thiolated ssDNA and ssDNA-conjugated peptides. See Table S1 in [100] for antibody information.

A.4.2 Site-specific ssDNA conjugation of antibodies

The SiteClick antibody labeling system (Thermo Fisher Scientific) enables site-specific conjugation to four conserved glycan sites present on the Fc region of the heavy chains using copper-free click chemistry. Briefly, 100 μg of each antibody was concentrated to 2-4 mg/mL in azide-free Tris buffer and treated with β-galactosidase enzyme to modify carbohydrate domains. In a second step, azide modified sugars were attached to the modified glycan chain using β-1,4-galactosyltransferase. After overnight incubation and purification of antibodies using an Amicon Ultra 0.5 mL centrifugal column (100 kDa), DBCO-modified ssDNA docking strands (Integrated DNA Technologies, Inc.) were mixed at a 40x molar ratio with azide-modified antibodies and incubated overnight at 25°C. ssDNA conjugated antibodies were then purified using an Amicon Ultra 0.5 mL (100 kDa). Final concentration was measured using a Nanodrop 2000 and antibodies were stored in 1x PBS (Sigma-Aldrich) with 50% glycerol. For PNA-antibody conjugation, DBCO-modified mini-PEG-γ-PNA strands27 (PNA Innovations, Inc., Woburn, MA) were used as the docking strands. See Table S1 in [100] for antibody information.

A.4.3 Design of ssLNA imaging probes

Same ssDNA sequences used for DNA-PAINT were used for ssLNA imaging probes with two modification to increase the melting temperatures of the sequences: (1) two adenine were added the 3' end of each sequence so that the imaging probes to maximize the hybridization of the imaging probes with the corresponding docking strands. (2) Three DNA nucleotides in each sequence were replaced with LNA nucleotides. Since introducing LNA nucleotides could possibly introduce unwanted cross-hybridization (or crosstalk) between

docking strands and imaging probes, an empirical algorithm was used to determine the optimal positions to replace the DNA nucleotides. Briefly, BLAST was performed for each docking strand and imaging probe pair to identify the partially complementary regions for each pair. An empirical cost function was then used to calculate the cost of every possible LNA substitution scheme with each docking strand. The cost function penalized LNA substitution in the partially complementary regions, with increasing penalty for more LNA substitution in the partially complementary regions, and bigger partially complementary regions. For each LNA substitution scheme, the highest cost within all the costs with different docking strands was assigned as the cost for the given substitution scheme. Finally, for each LNA sequence, the substitution scheme with the minimal cost was then selected for our LNA imaging probe sequence design. The algorithm was implemented in Python 3.5. Blast was performed using Biopython 1.66 in Python 3.5.

A.4.4 Fluorophore conjugation of ssLNA imaging probes

3'-amino ssLNA strands were purchased from Exiqon A/S and conjugated with ATTO 655-NHS (ATTO-TEC GmbH, Siegen, Germany). Briefly, 10 nmoles of ssLNA were mixed with ATTO 655-NHS in 1:5 molar ratio in 500 μL PBS (Sigma-Aldrich), incubated for 2 h at room temperature and then overnight at 4°C. Prior to purification with HPLC, isopropanol precipitation was performed to remove free dyes: 50 μL of 3M sodium acetate solution was first added to the ssLNA solution followed by adding 550 μL of isopropanol (-20°C). The mixed solution was thoroughly vortexed and incubated for 30 min at –20°C, and then immediately centrifuged at 10,000 g and 4°C for 1 h. The supernatant was delicately removed from the pellet. 500 μL of cold ethanol (-20°C) was carefully added to the pellet and centrifuged at 10,000g and 4°C for 15 min. The supernatant was removed, and the pellet was dried at 37°C for 2 h. The pellet was then resuspended in 500 uL PBS (Sigma-Aldrich), purified with HPLC, and lyophilized. See Table S2 in [100] for ssLNA probe sequences.

A.4.5 SDS-PAGE and mass spectrometry validation of conjugated antibodies

ssDNA-modified antibody solutions were reduced with 10 mM Tris-HCl complemented with DTT (20 mM) for 2 h at 37°C. Reduced antibody solutions were then run on an SDS-PAGE gel (10% acrylamide/bis-acrylamide), for 90 min at 110 V. Staining was performed using EZBlue™ gel staining reagent (Sigma-Aldrich). SiteClick conjugation efficiency and the ssDNA to antibody ratio (DAR) were determined using MALDI-TOF mass spectrometry. Briefly, 20 μL of modified antibody solutions in 1x PBS (Sigma-Aldrich) (0.5–1 mg/mL) were purified and concentrated using ZipTip pipette tips C4 resin (EMD Millipore) and then eluted in 10 μL of 80% ACN 0.1% TFA, dried down, and re-constituted in 1 μL of sinapinic acid matrix solution. The samples were then spotted and analyzed with microflex MALDI-TOF (Bruker Daltonics, Inc., Billerica, MA).

A.4.6 Primary mouse and rat neuronal cultures

Procedures for mouse neuronal culture preparation were approved by the Massachusetts Institute of Technology Committee on Animal Care. Hippocampal and cortical mouse neuronal cultures were prepared from postnatal day 0 or day 1 Swiss Webster (Taconic, Inc.,

Germantown, NY) mice as previously described [104, 135] but with the following modifications: dissected hippocampal and cortical tissues were digested with 50 units of papain (Worthington Biochem, Inc., Lakewood, NJ) for 6-8 min, and the digestion was stopped with ovomucoid trypsin inhibitor (Worthington Biochem). Cells were plated at a density of 10,000 per well in a glass-bottom 96-well plate coated with 50 μl Matrigel (BD Biosciences, Inc., San Jose, CA). Neurons were seeded in 50 μl Plating Medium containing MEM (Life Technologies, Carlsbad, CA), glucose (33 mM, Sigma-Aldrich), transferrin (0.01%, Sigma-Aldrich), Hepes (10 mM), Glutagro (2 mM, Corning, Inc., Corning, NY), Insulin (0.13%, EMD Millipore), B27 supplement (2%, Thermo Fisher Scientific), heat inactivated fetal bovine serum (7.5%, Corning). After cell adhesion, additional Plating Medium was added. AraC (0.002 mM, Sigma-Aldrich) was added when glia density was 50-70%. Neurons were grown at 37°C and 5% CO2 in a humidified atmosphere.

Procedures for rat neuronal culture were reviewed and approved for use by the Broad Institutional Animal Care and Use Committee. For rat hippocampal neuronal cultures, E18 embryos were collected from CO2 euthanized pregnant Sprague Dawley rats (Taconic). Embryo hippocampi were dissected in ice-cold Hibernate E supplemented with 2% B27 supplements and 100U/mL Pen/Strep (Thermo Fisher Scientific). Hippocampal tissues were digested in Hibernate E containing 20 U/mL papain, 1 mM L-cysteine, 0.5 mM EDTA (Worthington Biochem) and 0.01% DNAse (Sigma-Aldrich) for 8 min, and the digestion was stopped with 0.5% ovomucoid trypsin inhibitor (Worthington Biochem) and 0.5% bovine serum albumin (BSA)(Sigma-Aldrich). Neurons were dissociated and plated at a density of 15,000 cells/well onto poly-D-lysine coated, black-walled, thin-bottomed 96-well plates (Greiner Bio-One, Inc., Kremsmünster, Austria). Neurons were seeded and maintained in NbActiv1 (BrainBits, Inc., Springfield, IL). Cells were grown at 37°C in a 95% air with 5% CO2 humidified incubator for 21 days before use. All procedures involving animals were in accordance with the US National Institutes of Health Guide for the Care and Use of Laboratory Animals.

subsectionImmunostaining and analysis for validation of ssDNA-conjugated antibodies and phalloidin

To test whether the binding specificities of antibodies were affected by ssDNA conjugation, immunostaining patterns of unconjugated and ssDNA-conjugated antibodies were compared in each case. Cells were fixed at room temperature for 15 min with 4% paraformaldehyde (PFA) (Electron Microscopy Sciences, Inc., Hatfield, PA) and 4% wt/vol sucrose (Sigma-Aldrich) in PBS (Sigma-Aldrich), and then washed three times with PBS. Cells were permeabilized for 10 min at room temperature with 0.25% Triton-X100 in PBS and washed twice with PBS. For staining with unconjugated primary antibody or fluorescently labeled phalloidin, cells were blocked for 1 hr at room temperature with the regular blocking buffer (5% BSA (Sigma-Aldrich) in PBS). Cells were then incubated with primary antibodies or fluorescently labeled phalloidin diluted in the blocking buffer overnight at 4°C. For staining with ssDNA-conjugated primary antibodies, the nuclear blocking buffer (5% BSA and 1 mg/mL salmon sperm DNA (Sigma-Aldrich) in PBS) was used instead of regular blocking buffer for blocking and antibody dilution. After primary antibody staining, the sample was then washed three times with PBS, incubated for 1 hr at room temperature with secondary antibodies in 5% BSA in PBS, and washed again three times with PBS. For validation of ssDNA-conjugated secondary antibodies, the fluorescently labeled secondary antibodies of the same species were added to the samples after 30 min incubation with ssDNA-conjugated secondary antibodies to reduce the competition of binding of fluorescently labeled secondary antibodies with ssDNA-conjugated secondary antibodies. See

Table S1 in [100] for antibody information. Comparison of antibody staining patterns before and after ssDNA conjugation were performed using the Pearson Correlation Coefficient (PCC). Colocalization of each antibody being tested with synapsin-I signal was performed before and after ssDNA conjugation. Specifically, three confocal images were acquired of neurons stained with unconjugated and conjugated antibodies separately. Each image was split into four quadrants, and the PCC between the synapsin-I channel and the channel of the other synaptic antibody for each quadrant was calculated and then averaged to obtain the mean PCC.

A.4.7 Immunostaining for LNA- and DNA-PRISM

Cells were fixed and permeabilized as described in the previous section. For LNA-PRISM, cells were additionally incubated in RNase solution (50 μg/mL RNase A (Thermo Fisher Scientific) and 230 U/mL RNase T1 (Thermo Fisher Scientific) in 1x PBS (Sigma-Aldrich)) at 37°C for 1 h to reduce the fluoresce background caused by ssLNA-RNA binding, and washed 3 times with PBS. Cells were then blocked for 1 h at room temperature with the regular blocking buffer (5% BSA (Sigma-Aldrich) in PBS). The following unconjugated primary antibodies were diluted in the regular blocking buffer and used for LNA- or DNA-PRISM: MAP2, VGLUT1, PSD-95, and NMDAR2B (LNA-PRISM); PSD-95 and NMDAR2B (DNA-PRISM). Cells were incubated in diluted primary antibodies overnight at 4°C, washed 3 times with PBS, and then incubated in the nuclear blocking buffer for 1 h at room temperature. Next, the following secondary antibodies were diluted in the nuclear blocking buffer and used for LNA- or DNA-PRISM: goat-anti-chicken-Alexa 488, goat-anti-guinea pig-Alexa555 and goat-anti-rabbit-p1, goat-anti-mouse-p12 (LNA-PRISM); goat-anti-rabbit-p1 and goat-anti-mouse-p12 (DNA-PRISM). Cells were incubated at room temperature for 1 h in the secondary antibody solution. Cells were washed 3 times with PBS, post-fixed for 15 min with 4% PFA and 4% wt/vol sucrose in PBS. This step was used to prevent cross-binding of the secondary antibodies to the primary antibodies in the following round of staining. Cells were washed 3 times with PBS and incubated again in the nuclear blocking buffer for 30 min at room temperature. Cells were then incubated overnight at 4°C in the following primary antibody/peptide solution diluted in the nuclear blocking buffer for LNA- or DNA-PRISM: phalloidin-p2, Tuj-1-p3, cortactin-p4, SHANK3-p6, ARPC2-p7, bassoon-p8, synapsin-I-p9, Homer-1b/c-p10 (LNA-PRISM); phalloidin-p2, Tuj-1-p3, cortactin-p4, SHANK3-p6, bassoon-p5 (PNA), synapsin-I-p9, Homer-1b/c-p10 (DNA-PRISM). Cells were then washed 3 times with PBS. For LNA-PRISM, cells were incubated in diluted DAPI or Hoechst for 15 min. For DNA-PRISM, cells were incubated at room temperature for 1 h in donkey-anti-goat-Alexa488 diluted in the regular blocking buffer, washed 3 times with PBS, and then incubated with 10 nM of 100 nm diameter gold nanoparticle (Sigma-Aldrich) in PBS for 15 min. Cells were then washed 3 times with PBS prior to imaging. See Table S1 in [100] for antibody information.

A.4.8 Multiplexed confocal imaging of neurons using LNA-PRISM

LNA-PRISM imaging was performed on an Opera Phenix High-Content Screening System (PerkinElmer, Waltham, MA) equipped with a fast laser-based autofocus system, high NA water immersion objective (63x, numerical aperture=1.15), two large format scientific complementary metal-oxide semiconductor (sCMOS) cameras and spinning disk optics. 405 nm, 488 nm and 561 nm lasers were used as excitation for DAPI, MAP2, and VGLUT1

channels respectively. PRISM images were acquired using a 640 nm laser (40 mW), sCMOS camera with 1-2 s exposure time, and effective pixel size of 187 nm. Before each imaging round, the corresponding imaging probe was freshly diluted to 10 nM in imaging buffer (500 mM NaCl in 1x PBS (Sigma-Aldrich), pH 8). Neurons were incubated with 10 nM imaging probes for 5 min, and then washed twice manually with imaging buffer to remove the free imaging probe. For each field, a stack of 3 images was acquired with a step of 0.5 μm. After imaging, cells were washed three times with wash buffer (0.01x PBS), and incubated in the wash buffer for 5 min after the last wash before the next round of imaging.

A.4.9 LNA-PRISM confocal image processing and analysis

The flat-field correction was performed to correct the uneven illumination in the images due to the laser beam profile [191]. Briefly, each image was filtered by morphological opening filter with a disk structural element of 100 pixels to estimate the background of each image. For each 96-well plate, all background images from the same channel were then averaged to obtain the illumination profile for each channel for each plate. Note that the illumination profile can vary across experiments; therefore the illumination profile for each plate needs to be estimated separately. Images from the same channel were then divided by the illumination profile of the channel to obtain the corrected images. Next, lateral (x,y) drift between LNA-PRISM images from different imaging rounds was corrected by aligning the MAP2 channel in each imaging round. The (x,y) drift was estimated by locating the peak of the spatial cross-correlation function between two MAP2 images. For segmentation of synaptic punctae, the contrast of the image was first adjusted by saturating the highest and lowest 1% of pixels in the intensity histogram. The image was then denoised using a 5x5 Wiener filter, and filtered again with a top-hat operator with a disk structural element of 8 pixels to enhance the punctae in the image. The optimal threshold for each image was determined using an object-feature-based thresholding algorithm adapted from the thresholding algorithm previously used for single-molecule tracking [183]. The threshold producing the maximum number of objects was chosen as the optimal threshold. We found thresholding based on the features of objects was more robust to the intensity variations across different channels than the intensity-based approach for synapse segmentation. Connected synapses in the thresholded image were then separated using a watershed transform to obtain the final segmentation mask for each image of each synaptic target. Following Micheva et al. [174], synapses were identified using synapsin-I as the synapse marker. Synapsin-I punctae in the nuclei were mostly not synapses and therefore excluded from segmentation [174]. Each segmented synapsin-I punctum larger than 0.42 μm^2 was considered to be a synapse. For other synaptic proteins, only punctae that were colocalized (intensity weighted centroid distance less than 1 μm) with synapsin-I punctae were considered to be synapses and therefore retained. For each identified synapse, the average intensity and area of the segmented punctum in each synaptic channel were measured; zero was assigned when no colocalized punctum was detected. For non-synaptic targets (MAP2 and Tuj-1), the intensity was estimated by averaging the intensity within the synapsin-I puncta and no area measurement was performed. The Pearson Correlation Coefficient between each pair of synaptic intensity measurement was computed for each cell culture batch. The average correlation coefficients over 3 cell culture batches (total 178,528 synapses) were represented using a network diagram. An edge was shown between two nodes if the corresponding correlation was greater than 0.35, with the thickness of each edge representing the strength of the correlation. t-Distributed Stochastic Neighbor Embedding (t-SNE) was used to visualize

the distributions of synapses in high-dimensional feature space. 10,000 synapses were randomly subsampled from each replicate. 24 features (intensity levels from 13 channels and punctae sizes from 11 channels) of single synaptic profiles were used as the input to t-SNE. Each feature was log-transformed and normalized to have standard deviation of one and minimum of zero before applying t-SNE. t-SNE analysis was performed using scikit-learn 0.18.1 in Python 3.5 with the exact method, perplexity parameter equal to 40, and PCA initialization. The resulting t-SNE maps were similar for perplexity of 10-100. Hierarchical clustering of single-synapse profiles was performed by first normalizing the distribution of each feature to have a minimum of zero and a standard deviation of one using all synapses as input. 24 features (intensity levels 13 channels and punctae sizes from 11 channels) were used as input for the clustering analysis. Clustering was performed using the "clustermap" function from Seaborn 0.7.1 in Python 3.5 with the Euclidean metric and Ward's linkage.

A.4.10 Multiplexed super-resolution imaging of neurons using DNA-PRISM

Single and dual channel PAINT imaging was performed on an inverted Nikon Eclipse Ti microscope (Nikon Instruments, Inc., Melville, NY) with the Perfect Focus System and oil-immersion objective (Plan Apo TIRF 100x, numerical aperture (NA) 1.49). A 642 nm wavelength laser (100 mW nominal) was used for excitation. Images were acquired using an Electron-Multiplying Charge-Coupled Device (EMCCD) camera (iXon DU-897, Andor Technology, Belfast, UK) with 100 ms exposure time, 100 EM gain, and effective pixel size of 160 nm. Nine-channel DNA-PAINT imaging was performed on an inverted Nikon Eclipse Ti microscope (Nikon Instruments) with the Perfect Focus System and oil-immersion objective (Plan Apo TIRF 100x, numerical aperture (NA) 1.49). 640 nm laser (45 mW nominal) was used for excitation. Images were acquired using a Zyla 4.2 sCMOS camera (Andor Technology) with 100 ms exposure time, 2x2 binning, and effective pixel size of 130 nm. Cells were imaged using Highly Inclined and Laminated Optical illumination (HILO). The same imaging probe sequences labeled with Atto655 (Eurofins, Luxembourg) and imaging/washing buffer (1x PBS (Sigma-Aldrich), 500 mM NaCl, pH 8) as previously published [126] were used (see Table S2 in [100]). Probe exchange was performed using a home-built fluid control system (see Fig. S18 in [100]). Depending on the labeling density, typically 0.5-3 nM imaging probe diluted in the imaging buffer was used in order to achieve optimal spot density for single-molecule imaging. 5,000-20,000 image frames were typically acquired for each target.

A.4.11 Super-resolution image reconstruction and localization analysis

Localization of the center of each diffraction-limited spot corresponding to a single-molecule in the acquired movies was performed using DAOSTORM [8, 112]. The super-resolution image was reconstructed by computing a 2D histogram of the (x,y) coordinates of the localized spots with bin size 5.4x5.4 nm, followed by smoothing with a 2D Gaussian filter. Non-specifically bound gold nanoparticles were used as fiduciary markers to estimate the drift and align images of distinct targets. Drift was estimated by fitting splines to the x- and y-coordinates separately of each fiduciary marker as a function of time using LOESS regression, and averaging over splines of all the fiduciary markers. 1D cross-sectional profiles of protein distributions were generated by projecting the 2D (x,y) coordinates of the localized spots onto the 1D coordinates along the trans-synaptic axes, and followed by

computing a 1D histogram of the 1D coordinates. All image reconstruction and analysis procedures except for single-molecule localization were performed using MATLAB R2015a (The MathWorks, Inc.).

A.5 Multivariate analysis of cell shape

A.5.1 Data dimensionality reduction using principal component analysis

The complexity of morphological characteristics attained by cells in different phenotypic states necessitates a framework for describing shape using morphological features. To facilitate interpretation and visualization of these shape characteristics requires a summarization method that reduced the space of feature dimensions while maximizing the variability inherent in the original high-dimensional data. In developing the framework, we aim to address the following:

1. Standardization of cell shape measurements to account for undesirable batch effects and inter-experimental variability during cell plating, culture, and imaging.

2. Many of the shape features are correlated (positively and negatively), which leads to information redundancy and unnecessary complexity.

3. Shape states (see Chapter 2) explored by cells must be uniquely described and grouped in the shape feature domain. This is challenged by the continuous nature of morphological state transitions (e.g. for a cell going from round to elongated, it goes through an "in between" shape), which occur in highly dynamic cytoskeleton-mediated processes like cell migration.

4. High dimensional feature space is hard to visualize for biophysical interpretation.

Consider n cells imaged at a certain snapshot in time. Each cell can be described by m shape features. In our case, $m = 18$ for a set of commonly used shape features that use the object silhouette (binary shape of foreground pixels) for feature computation (Table B.1). These features are popular for shape description in high-content screening assays (HCS). The idea is that each of the m features captures some aspect of cell morphology that puts a number to properties of shape states. These features do not necessarily capture unique aspects of shape, and it is not necessary to know *a priori* if they do, to what extent, or which aspect of shape they describe. Conveniently, "shape" can be treated as an overarching unobservable construct that is described by the m observable and measurable shape features, or indicators. The cell shape data for the population at a given point in time therefore comprises the $m \times n$ data matrix X. Each row of X corresponds to a shape feature and each column corresponds to a single cell (observation).

Batch effects and systematic, passage-dependent variability in cell populations in experiments performed on different days requires a standardization technique for making shape measurements directly comparable between experiments. Here, we choose to standardize shape features in all treatment conditions to the distribution of shape features of cells in untreated control samples. In brief, each imaged plate contains untreated control wells that serve as the standardization reference distribution. Consider the vector $\mathbf{m}_i$ of shape feature i for all cells in the untreated control, and the same feature for a given cell, c_i, in another treatment condition. We perform the standardization by asking where in the distribution of $\mathbf{m}_i$ the sample c_i falls. Therefore, we compute a sample z-score using the untreated control population's distribution for all m features individually as: $[c_i - \text{mean}(\mathbf{m}_i)] \,/\, \text{std}(\mathbf{m}_i)$. As a

result, all c_i comprising the individual elements of matrix X are standardized to untreated control such that shape feature matrices X's assembled from different plates and experiments can be directly merged and compared in subsequent analyses. We now replace the feature matrix X with the standardized values. However, despite the standardization of shape features relative to untreated control, the features still have different variances. We therefore re-scale, or normalize, the feature values across the entire set of observation so that the variances and means of each feature in the cell population in all treatment conditions are identical. This involved calculating the z-score: for each standardized row of X, $\mathbf{m}_i$, we replace the standardized row with its z-score normalized version: $[\mathbf{m}_i - \text{mean}(\mathbf{m}_i)]$ / $\text{std}(\mathbf{m}_i)$, producing the standardized and normalized feature data matrix X. Note that standardization is necessary to account for batch effects and day-to-day experimental variability, while normalization is used to bring shape features to similar scale and making all the features contribute equally, in terms of variance scale, to cell shape description across the population.

Next, given the standardized and normalized feature matrix X we turn to PCA for summarizing and visualizing cell shape, with the goal of accounting for the redundancy among features and reducing the dimensionality of the matrix to facilitate interpretation and visualization of the shape space. We perform PCA on the matrix X using the eigenvalue decomposition of the covariance matrix of X (for details see any review on PCA analysis on normalized data). Briefly, our goal is to transform the basis of X such that individual shape features are combined linearly into orthogonal (non-redundant) principal components (PCs) that maximally capture the variability in the features between cells. We wish to find the $m \times m$ transformation matrix P that re-represents the data in X into an orthogonal shape feature basis Y in a linear fashion: $Y = PX$. Since our goal is to generate a basis with orthogonal PCs, implies that the covariance matrix of Y is a diagonal matrix. The matrix P contains the orthonormal basis vectors, or principal components, of X. The diagonal values in the covariance matrix of Y correspond to the variance of X along each principal component. A key utility, and useful assumption, in this transformation is that by transforming the basis of X into Y we capture the features that contribute to biologically relevant shape information that dominates the variance in the feature data, while de-emphasizing the variance that is contributed by measurement noise. A key source of noise in shape feature data often observed in HCS lies in the segmentation error during image processing to get cell outlines. However, in our case we manually QC every cell that is processed by segmentation prior to feature calculation, so the issue of noise from artifactual sources such as segmentation is negligible.

A.5.2 Polar visualization of principal component space

Recall our original goal of partitioning the shape space so that we can define morphological states. One way to describe a state is to discretize the shape space into regions that define particular morphological classes. One popular approach to do this is through data clustering, which aims to partition the data into coherent groups minimizing intra-group distance and maximizing inter-group distance. This approach was taken by Sailem et al. to define morphological states in 3D PCA space [224]. The authors used silhouette analysis to define the optimal number of clusters that partitions the data based on different values of desired clusters k using k-means clustering. Briefly, for each number of clusters k we define for each cluster i two values: a_i and b_i, which define the average intra- and inter-cluster dissimilarity, respectively, using Euclidean distance. The value b_i is calculated for points

in the cluster that is closest to the cluster containing sample i, while a_i is the intra-cluster Euclidean distance between the samples. The silhouette value for each sample is calculated as $s_i = (b_i - a_i)/\max(a_i,b_i)$, with $-1 < s_i < 1$. A higher value of s_i indicates good clustering of a sample in its cluster relative to its closest neighboring cluster, since b_i is larger and a_i is smaller. Using this approach, the authors achieve an optimal average silhouette value of close to 0.8. We performed the same analysis on our shape data, but generally find monotonic decrease in average silhouette values for morphological of MDA-MB-231 cells, which is considered worse clustering (Fig. 2-3D). The cluster analysis through silhouette values therefore suggests that our data does not partition well into discrete clusters, or states. This is not surprising, given the continuous nature of morphology for highly dynamic cytoskeleton-regulated processes like cell migration. Consequently, during shape state transitions, cells explore in-between morphologies that smoothly transform one morphology into another. This also suggests that cells do not necessarily stay in particular states very long, as shape space is sampled continuously without many "gaps" in the PCA scatterplot (Fig. 2-3D).

Given the relatively poor clustering of our data in PCA shape space, we present an alternative discretization of the shape space using angular partitioning. If we consider the structure of the data in the 2 PCs shown in (Fig. 2-3A), we can define two useful properties for an observation: (1) distance a point is away from the mean shape (r), and (2) angle the point makes with the two PCs (θ). This is essentially a polar transformation of the PC1 and PC2 coordinates, which enables us to define discrete "slices" of PC space, as shown by the polar separating lines in Figures 2-3B and 4-3b. This discretization is convenient because of the slice relation to the PC axes relative to the mean. For example, the 0° to 30° slice generally captures high positive values of PC1 and low to intermediate values of PC2, which, given their orthogonality, capture different and non-redundant aspects of shape space.

Given the discretization of the PC space into slices, we can calculate a "morphological signature" for a given treatment condition j as the fraction of observation f_j that fall into slice s, with the slices starting at angle of 0° along PC1 and going counterclockwise (Fig 4-3c). These fractions can be visualized for each treatment condition to assess the proportion of cells in a given condition that fall into a particular morphological state using a rose plot. In the polar visualization of Figures 2-3B and 4-3b we also capture the values of the PC coefficients, in front of each shape feature, which collectively comprise the linear combination that produces the PC basis. The lengths of the line ticks next to feature names indicate the magnitudes of the coefficients and the orientation shows the direction along which a particular feature increases. This visualization enables us to assess how particular features contribute to the formation of the PCA shape space and the shape parameters of cells that drug treatments enrich. We also see that many of the shape features are correlated, such as `Major Axis Length`, `Geodesic Diameter`, and `Feret Max` for example, but none of the features points in the same direction as another feature, meaning that each feature contributes some unique shape information in describing cell morphology.

Appendix B

Tables

Table B.1: List and descriptions of image-derived cell shape features.

Feature #	Feature Name	Feature Description
1	Area	Number of pixels in the cell region.
2	Perimeter	Length of the cell region's boundary.
3	Equivalent Diameter	The diameter of a circle that has the same area as in the cell region.
4	Major Axis Length	Length of major axis of an ellipse that has the same normalized second central moments as the cell region.
5	Minor Axis Length	Length of the minor axis of an ellipse that has the same normalized second central moments as the cell region.
6	Eccentricity	The eccentricity of an ellipse that has the same second moments as the cell region.
7	Solidity	The ratio of the area of the cell region to the area of cell region's convex hull.
8	Extent	The ratio of the area of the cell region to the area of cell region's bounding box.
9	Convex Area	The area of the convex hull of the cell region.
10	Axis Ratio	The ratio of the major axis length to the minor axis length of the cell region.
11	Circularity	For the cell region, computed as: $(4 * \pi * \text{Perimeter})/(\text{Area}^2)$
12	Waviness	The ratio of the perimeter of the cell region's convex hull to the perimeter of the cell region.
13	Geodesic Diameter	The length of the longest geodesic path between all pairs of points on the boundary of the cell region. A geodesic path is the shortest path that connects two points on the cell region boundary that cannot traverse outside of the cell region.
14	Convex Perimeter	Length of the cell region's convex hull's boundary.
15	Feret Max	The maximum of the Feret lengths of the cell region over 180 directions sampled uniformly 0–360 degrees. Feret length is the measure of the cell region's size (length) along a specified direction, as would be measured with calipers.
16	Feret Min	The minimum of the Feret lengths of the cell region over 180 directions sampled uniformly 0–360 degrees.
17	Feret Mean	The mean of the Feret lengths of the cell region over 180 directions sampled uniformly 0–360 degrees.
18	Feret CV	The coefficient of variation (standard deviation divided by the mean) of Feret lengths of the cell region from 180 directions sampled uniformly 0–360 degrees.

Bibliography

[1] S. AbuHammad and M. Zihlif. Gene expression alterations in doxorubicin resistant MCF7 breast cancer cell line. *Genomics*, 101(4):213–220, Apr. 2013.

[2] B. Adamson, A. Smogorzewska, F. D. Sigoillot, R. W. King, and S. J. Elledge. A genome-wide homologous recombination screen identifies the RNA-binding protein RBMX as a component of the DNA-damage response. *Nature Cell Biology*, 14(3):318–328, Feb. 2012.

[3] F. Aguet, C. N. Antonescu, M. Mettlen, S. L. Schmid, and G. Danuser. Advances in Analysis of Low Signal-to-Noise Images Link Dynamin and AP2 to the Functions of an Endocytic Checkpoint. *Developmental Cell*, 26(3):279–291, Aug 12 2013.

[4] B. Al-Lazikani, U. Banerji, and P. Workman. Combinatorial drug therapy for cancer in the post-genomic era. *Nature Biotechnology*, 30(7):679–92, Jul 2012.

[5] J. Alanko, A. Mai, G. Jacquemet, K. Schauer, R. Kaukonen, M. Saari, B. Goud, and J. Ivaska. Integrin endosomal signalling suppresses anoikis. *Nature Cell Biology*, 17(11):1412–1421, Nov. 2015.

[6] E. D. Amir, K. L. Davis, M. D. Tadmor, E. F. Simonds, J. H. Levine, S. C. Bendall, D. K. Shenfeld, S. Krishnaswamy, G. P. Nolan, and D. Pe'er. viSNE enables visualization of high dimensional single-cell data and reveals phenotypic heterogeneity of leukemia. *Nature Biotechnology*, 31(6):545–552, Jun 2013.

[7] C. P. Arthur, D. B. Serrell, M. Pagratis, D. L. Potter, D. S. Finch, and M. H. B. Stowell. Electron tomographic methods for studying the chemical synapse. *Methods in Cell Biology*, 79(79):241–57, Jan 2007.

[8] H. Babcock, Y. M. Sigal, and X. Zhuang. A high-density 3D localization algorithm for stochastic optical reconstruction microscopy. *Optical Nanoscopy*, 1(6):6, jan 2012.

[9] C. Bakal, J. Aach, G. Church, and N. Perrimon. Quantitative morphological signatures define local signaling networks regulating cell morphology. *Science*, 316(5832):1753–1756, Jun 22 2007.

[10] N. Q. Balaban, U. S. Schwarz, D. Riveline, P. Goichberg, G. Tzur, I. Sabanay, D. Mahalu, S. Safran, A. Bershadsky, L. Addadi, and B. Geiger. Force and focal adhesion assembly: a close relationship studied using elastic micropatterned substrates. *Nature Cell Biology*, 3(5):466–472, May 2001.

[11] T. Balla. Phosphoinositides: tiny lipids with giant impact on cell regulation. *Physiological Reviews*, 93(3):1019–137, July 2013.

[12] S. Barrientos, O. Stojadinovic, M. S. Golinko, H. Brem, and M. Tomic-Canic. Growth factors and cytokines in wound healing. *Wound Repair and Regeneration*, 16(5):585–601, 2008.

[13] D. J. Barry, C. H. Durkin, J. V. Abella, and M. Way. Open source software for quantification of cell migration, protrusions, and fluorescence intensities. *Journal of Cell Biology*, 209(1):163–180, Apr 13 2015.

[14] J. Bartek and J. Lukas. Chk1 and Chk2 kinases in checkpoint control and cancer. *Cancer Cell*, 3(5):421–429, May 2003.

[15] J. E. Bear and J. M. Haugh. Directed migration of mesenchymal cells: where signaling and the cytoskeleton meet. *Current Opinion in Cell Biology*, 30:74–82, Oct 2014.

[16] P. Beli, N. Lukashchuk, S. A. Wagner, B. T. Weinert, J. V. Olsen, L. Baskcomb, M. Mann, S. P. Jackson, and C. Choudhary. Proteomic Investigations Reveal a Role for RNA Processing Factor THRAP3in the DNA Damage Response. *Molecular Cell*, pages 1–14, Mar. 2012.

[17] Y. Benjamini and Y. Hochberg. Controlling the False Discovery Rate: A Practical and Powerful Approach to Multiple Testing. *Journal of the Royal Statistical Society Series B*, 1995.

[18] A. D. Bershadsky, N. Q. Balaban, and B. Geiger. Adhesion-Dependent Cell Mechanosensitivity. *Annual Review of Cell and Developmental Biology*, 19(1):677–695, Nov 2003.

[19] E. Betzig, G. H. Patterson, R. Sougrat, O. W. Lindwasser, S. Olenych, J. S. Bonifacino, M. W. Davidson, J. Lippincott-Schwartz, and H. F. Hess. Imaging intracellular fluorescent proteins at nanometer resolution. *Science*, 313(5793):1642–1645, 2006.

[20] L. Blanchoin, R. Boujemaa-Paterski, C. Sykes, and J. Plastino. Actin Dynamics, Architecture, and Mechanics in Cell Motility. *Physiological Reviews*, 94(1):235–263, Jan. 2014.

[21] M. Blasius, J. V. Forment, N. Thakkar, S. A. Wagner, C. Choudhary, and S. P. Jackson. A phospho-proteomic screen identifies substrates of the checkpoint kinase Chk1. *Genome Biology*, 12(8):R78, Aug. 2011.

[22] M. Blasius, S. A. Wagner, C. Choudhary, J. Bartek, and S. P. Jackson. A quantitative 14-3-3 interaction screen connects the nuclear exosome targeting complex to the DNA damage response. *Genes & Development*, Sept. 2014.

[23] A. Bon Avid and B. Amin. *Molecular mechanisms of tumor cell resistance to chemotherapy.* Springer, 2014.

[24] G. Bonadonna, U. Veronesi, C. Brambilla, L. Ferrari, A. Luini, M. Greco, C. Bartoli, G. C. D. Yoldi, R. Zucali, F. Rilke, S. Andreola, R. Silvestrini, G. D. Fronzo, and P. Valagussa. Primary chemotherapy to avoid mastectomy in tumors with diameters of three centimeters or more. *Journal of the National Cancer Institute*, 82(19):1539–1545, Oct 1990.

[25] L. Bosgraaf and P. J. M. Van Haastert. Quimp3, an automated pseudopod-tracking algorithm. *Cell Adhesion & Migration*, 4(1):46–55, Jan 2010.

[26] M. Bredel and E. Jacoby. Chemogenomics: an emerging strategy for rapid target and drug discovery. *Nature Reviews Genetics*, 5(4):262–75, Apr 2004.

[27] S. Breslin and L. O'Driscoll. The relevance of using 3d cell cultures, in addition to 2d monolayer cultures, when evaluating breast cancer drug sensitivity and resistance. *Oncotarget*, 7(29):45745, 2016.

[28] S.-A. Brown, N. Sandhu, and J. Herrmann. Systems biology approaches to adverse drug effects: the example of cardio-oncology. *Nature Reviews Clinical Oncology*, 12(12):718–731, Dec. 2015.

[29] V. G. Brunton and M. C. Frame. Src and focal adhesion kinase as therapeutic targets in cancer. *Current Opinion in Pharmacology*, 8(4):427–432, Aug. 2008.

[30] K. Burridge and M. Chrzanowska-Wodnicka. Focal Adhesions, Contractility, and Signaling. *Annual Review of Cell and Developmental Biology*, 12(1):463–519, Nov 1996.

[31] A. M. Calcagno, C. D. Salcido, J. P. Gillet, C. P. Wu, J. M. Fostel, M. D. Mumau, M. M. Gottesman, L. Varticovski, and S. V. Ambudkar. Prolonged Drug Selection of Breast Cancer Cells and Enrichment of Cancer Stem Cell Characteristics. *JNCI Journal of the National Cancer Institute*, 102(21):1637–1652, Nov. 2010.

[32] J. Candia, R. Maunu, M. Driscoll, A. Biancotto, P. Dagur, J. P. McCoy, Jr., H. N. Sen, L. Wei, A. Maritan, K. Cao, R. B. Nussenblatt, J. R. Banavar, and W. Losert. From Cellular Characteristics to Disease Diagnosis: Uncovering Phenotypes with Supercells. *PLoS Computational Biology*, 9(9), Sep 2013.

[33] I. G. Cannell, K. A. Merrick, S. Morandell, C.-Q. Zhu, C. J. Braun, R. A. Grant, E. R. Cameron, M.-S. Tsao, M. T. Hemann, and M. B. Yaffe. A Pleiotropic RNA-Binding Protein Controls Distinct Cell Cycle Checkpoints to Drive Resistance of p53-Defective Tumors to Chemotherapy. *Cancer Cell*, 28(5):623–637, Nov. 2015.

[34] F. Cardoso, N. Harbeck, L. Fallowfield, S. Kyriakides, and E. Senkus. Locally recurrent or metastatic breast cancer: ESMO clinical practice guidelines for diagnosis, treatment and follow-up. *Annals of Oncology*, 23(SUPPL. 7):vii11–vii19, Oct 2012.

[35] N. O. Carragher, V. J. Fincham, D. Riley, and M. C. Frame. Cleavage of focal adhesion kinase by different proteases during SRC-regulated transformation and apoptosis. Distinct roles for calpain and caspases. *The Journal of Biological Chemistry*, 276(6):4270–4275, Feb. 2001.

[36] N. O. Carragher and M. C. Frame. Focal adhesion and actin dynamics: a place where kinases and proteases meet to promote invasion. *Trends in Cell Biology*, 14(5):241–249, May 2004.

[37] N. O. Carragher, B. Levkau, and R. Ross. Degraded collagen fragments promote rapid disassembly of smooth muscle focal adhesions that correlates with cleavage of pp125FAK, paxillin, and talin. *Journal of Cell Biology*, 1999.

[38] N. O. Carragher, S. M. Walker, L. a. Scott Carragher, F. Harris, T. K. Sawyer, V. G. Brunton, B. W. Ozanne, and M. C. Frame. Calpain 2 and Src dependence distinguishes mesenchymal and amoeboid modes of tumour cell invasion: a link to integrin function. *Oncogene*, 25(42):5726–40, Sep 2006.

[39] S. Chapman, X. Liu, C. Meyers, R. Schlegel, and A. A. McBride. Human keratinocytes are efficiently immortalized by a Rho kinase inhibitor. *Journal of Clinical Investigation*, 120(7):2619–2626, 2010.

[40] E. Charafe-Jauffret, C. Ginestier, F. Monville, P. Finetti, J. Adélaïde, N. Cervera, S. Fekairi, L. Xerri, J. Jacquemier, D. Birnbaum, and F. Bertucci. Gene expression profiling of breast cell lines identifies potential new basal markers. *Oncogene*, 25(15):2273–2284, Apr. 2006.

[41] P. G. Charest and R. A. Firtel. Feedback signaling controls leading-edge formation during chemotaxis. *Current Opinion in Genetics & Development*, 16(4):339–47, Aug. 2006.

[42] B. Chen, Q. Zong, R. Cibotti, C. Morris, J. Castaneda, B. Naiman, D. Liu, A. Glodek, G. P. Sims, R. Herbst, S. K. Horrigan, P. A. Kiener, D. Soppet, A. J. Coyle, and L. Audoly. Genomic-based high throughput screening identifies small molecules that differentially inhibit the antiviral and immunomodulatory effects of IFN-alpha. *Molecular Medicine*, 14(7-8):374–382, 2008.

[43] E. Y. Chen, H. Xu, S. Gordonov, M. P. Lim, M. H. Perkins, and A. Ma'ayan. Expression2Kinases: mRNA profiling linked to multiple upstream regulatory layers. *Bioinformatics*, 28(1):105–111, Nov. 2011.

[44] G. Chen, Z. Hou, D. R. Gulbranson, and J. A. Thomson. Actin-myosin contractility is responsible for the reduced viability of dissociated human embryonic stem cells. *Cell Stem Cell*, 7(2):240–248, 2010.

[45] W. W. Chin. The partial least squares approach to structural equation modeling. *Modern Methods for Business Research*, 295(2):295–336, 1998.

[46] J. Chou, N. a. Burke, A. Iwabu, S. C. Watkins, and A. Wells. Directional motility induced by epidermal growth factor requires Cdc42. *Experimental Cell Research*, 287(1):47–56, July 2003.

[47] J. Chou, D. B. Stolz, N. a. Burke, S. C. Watkins, and A. Wells. Distribution of gelsolin and phosphoinositol 4,5-bisphosphate in lamellipodia during EGF-induced motility. *The International Journal of Biochemistry & Cell Biology*, 34(7):776–90, July 2002.

[48] A. Ciccia and S. J. Elledge. The DNA Damage Response: Making It Safe to Play with Knives. *Molecular Cell*, 40(2):179–204, Oct. 2010.

[49] G. Ciriello, M. Gatza, A. Beck, M. Wilkerson, S. Rhie, A. Pastore, H. Zhang, M. McLellan, C. Yau, C. Kandoth, R. Bowlby, H. Shen, S. Hayat, R. Fieldhouse, S. Lester, G. Tse, R. Factor, L. Collins, K. Allison, Y.-Y. Chen, K. Jensen, N. Johnson, S. Oesterreich, G. Mills, A. Cherniack, G. Robertson, C. Benz, C. Sander, P. Laird, K. Hoadley, T. King, C. M. Perou, R. Akbani, J. Auman, M. Balasundaram, S. Balu, T. Barr, A. Beck, C. Benz, S. Benz, M. Berrios, R. Beroukhim, T. Bodenheimer, L. Boice, M. Bootwalla, J. Bowen, R. Bowlby, D. Brooks, A. Cherniack, L. Chin, J. Cho, S. Chudamani, G. Ciriello, T. Davidsen, J. Demchok, J. Dennison, L. Ding, I. Felau, M. Ferguson, S. Frazer, S. Gabriel, J. Gao, J. Gastier-Foster, M. Gatza, N. Gehlenborg, M. Gerken, G. Getz, W. Gibson, D. Hayes, D. Heiman, K. Hoadley, A. Holbrook, R. Holt, A. Hoyle, H. Hu, M. Huang, C. Hutter, E. Hwang, S. Jefferys, S. Jones, Z. Ju, J. Kim, P. Lai, P. Laird, M. Lawrence, K. Leraas, T. Licht-

enberg, P. Lin, S. Ling, J. Liu, W. Liu, L. Lolla, Y. Lu, Y. Ma, D. Maglinte, E. Mardis, J. Marks, M. Marra, C. McAllister, M. McLellan, S. Meng, M. Meyerson, G. Mills, R. Moore, L. Mose, A. Mungall, B. Murray, R. Naresh, M. Noble, S. Oesterreich, O. Olopade, J. Parker, C. Perou, T. Pihl, G. Saksena, S. Schumacher, K. Shaw, N. Ramirez, W. Rathmell, S. Rhie, J. Roach, A. Robertson, G. Saksena, C. Sander, J. Schein, N. Schultz, H. Shen, M. Sheth, Y. Shi, J. Shih, C. Shelley, C. Shriver, J. Simons, H. Sofia, M. Soloway, C. Sougnez, C. Sun, R. Tarnuzzer, D. Tiezzi, D. Van?Den?Berg, D. Voet, Y. Wan, Z. Wang, J. Weinstein, D. Weisenberger, M. Wilkerson, R. Wilson, L. Wise, M. Wiznerowicz, J. Wu, Y. Wu, L. Yang, C. Yau, T. Zack, J. Zenklusen, H. Zhang, J. Zhang, and E. Zmuda. Comprehensive Molecular Portraits of Invasive Lobular Breast Cancer. *Cell*, 163(2):506–519, Oct 2015.

[50] M. L. Citron. Dose-dense chemotherapy: principles, clinical results and future perspectives. *Breast Care*, 3(4):251–255, 2008.

[51] M. O. Collins, H. Husi, L. Yu, J. M. Brandon, C. N. G. Anderson, W. P. Blackstock, J. S. Choudhary, and S. G. N. Grant. Molecular characterization and comparison of the components and multiprotein complexes in the postsynaptic proteome. *Journal of Neurochemistry*, 97 Suppl 1:16–23, Apr 2006.

[52] F. Collman, J. Buchanan, K. D. Phend, K. D. Micheva, R. J. Weinberg, and S. J. Smith. Mapping synapses by conjugate light-electron array tomography. *The Journal of Neuroscience*, 35(14):5792–807, Apr 2015.

[53] J. Condeelis, R. H. Singer, and J. E. Segall. The great escape: when cancer cells hijack the genes for chemotaxis and motility. *Annual Review of Cell and Developmental Biology*, 21:695–718, Jan. 2005.

[54] L. Cong, F. A. Ran, D. Cox, S. Lin, R. Barretto, N. Habib, P. D. Hsu, X. Wu, W. Jiang, L. A. Marraffini, and F. Zhang. Multiplex Genome Engineering Using CRISPR/Cas Systems. *Science*, 339(6121):819–823, Feb 15 2013.

[55] J. Crocker and D. Grier. Methods of digital video microscopy for colloidal studies. *Journal of Colloid and Interface Science*, 179(1):298–310, Apr 15 1996.

[56] A. Dakic, K. DiVito, S. Fang, F. Suprynowicz, A. Gaur, X. Li, N. Palechor-Ceron, V. Simic, S. Choudhury, S. Yu, C. M. Simbulan-Rosenthal, D. Rosenthal, R. Schlegel, and X. Liu. ROCK inhibitor reduces Myc-induced apoptosis and mediates immortalization of human keratinocytes. *Oncotarget*, 7(41):66740–66753, 2016.

[57] A. Dani, B. Huang, J. Bergan, C. Dulac, and X. Zhuang. Superresolution imaging of chemical synapses in the brain. *Neuron*, 68(5):843–856, 2010.

[58] G. Danuser. Computer vision in cell biology. *Cell*, 147(5):973–8, Nov 2011.

[59] A. D. Doyle, R. J. Petrie, M. L. Kutys, and K. M. Yamada. Dimensions in cell migration. *Current Opinion in Cell Biology*, pages 1–8, July 2013.

[60] M. K. Driscoll, W. Losert, K. Jacobson, and M. Kapustina. Spatiotemporal relationships between the cell shape and the actomyosin cortex of periodically protruding cells. *Cytoskeleton*, 72(6):268–281, Jun 2015.

[61] M. K. Driscoll, C. McCann, R. Kopace, T. Homan, J. T. Fourkas, C. Parent, and W. Losert. Cell Shape Dynamics: From Waves to Migration. *PLoS Computational Biology*, 8(3), Mar 2012.

[62] S. Ebinger, E. Z. Özdemir, C. Ziegenhain, S. Tiedt, C. Castro Alves, M. Grunert, M. Dworzak, C. Lutz, V. A. Turati, T. Enver, H.-P. Horny, K. Sotlar, S. Parekh, K. Spiekermann, W. Hiddemann, A. Schepers, B. Polzer, S. Kirsch, M. Hoffmann, B. Knapp, J. Hasenauer, H. Pfeifer, R. Panzer-Grümayer, W. Enard, O. Gires, and I. Jeremias. Characterization of Rare, Dormant, and Therapy-Resistant Cells in Acute Lymphoblastic Leukemia. *Cancer Cell*, 30(6):849–862, Dec. 2016.

[63] M. Eitaki, T. Yamamori, S. Meike, H. Yasui, and O. Inanami. Vincristine enhances amoeboid-like motility via GEF-H1/RhoA/ROCK/Myosin light chain signaling in MKN45 cells. *BMC Cancer*, 12(1):1–1, Oct. 2012.

[64] H. Elliott, R. S. Fischer, K. A. Myers, R. A. Desai, L. Gao, C. S. Chen, R. S. Adelstein, C. M. Waterman, and G. Danuser. Myosin II controls cellular branching morphogenesis and migration in three dimensions by minimizing cell-surface curvature. *Nature Cell Biology*, 17(2):137+, Feb 2015.

[65] R. D. Emes and S. G. N. Grant. Evolution of synapse complexity and diversity. *Annual Review of Neuroscience*, 35:111–31, Jan 2012.

[66] E. J. Ezratty, E. J. Ezratty, M. A. Partridge, M. A. Partridge, G. G. Gundersen, and G. G. Gundersen. Microtubule-induced focal adhesion disassembly is mediated by dynamin and focal adhesion kinase. *Nature Cell Biology*, 7(6):581–590, May 2005.

[67] J. Fan, S. Guan, C.-F. Cheng, M. Cho, J. W. Fields, M. Chen, M. F. Denning, D. T. Woodley, and W. Li. PKCdelta clustering at the leading edge and mediating growth factor-enhanced, but not ecm-initiated, dermal fibroblast migration. *The Journal of Investigative Dermatology*, 126(6):1233–43, June 2006.

[68] S. Fang, L. Yu, H. Mei, J. Yang, T. Gao, A. Cheng, W. Guo, K. Xia, and G. Liu. Cisplatin promotes mesenchymal-like characteristics in osteosarcoma through Snail. *Oncology Letters*, 12(6):5007–5014, Dec. 2016.

[69] G. Flatau, E. Lemichez, M. Gauthier, P. Chardin, et al. Toxin-induced activation of the g protein p21 rho by deamidation of glutamine. *Nature*, 387(6634):729, 1997.

[70] S. R. Floyd, M. E. Pacold, Q. Huang, S. M. Clarke, F. C. Lam, I. G. Cannell, B. D. Bryson, J. Rameseder, M. J. Lee, E. J. Blake, A. Fydrych, R. Ho, B. A. Greenberger, G. C. Chen, A. Maffa, A. M. Del Rosario, D. E. Root, A. E. Carpenter, W. C. Hahn, D. M. Sabatini, C. C. Chen, F. M. White, J. E. Bradner, and M. B. Yaffe. The bromodomain protein Brd4 insulates chromatin from DNA damage signalling. *Nature*, 498(7453):246–250, June 2013.

[71] B. S. Fogh, H. a. B. Multhaupt, and J. R. Couchman. Protein Kinase C, Focal Adhesions and the Regulation of Cell Migration. *The Journal of Histochemistry and Cytochemistry*, Jan. 2014.

[72] M. Fokkelman, H. E. Balcıoğlu, J. E. Klip, K. Yan, F. J. Verbeek, E. H. J. Danen, and B. van de Water. Cellular adhesome screen identifies critical modulators of focal

adhesion dynamics, cellular traction forces and cell migration behaviour. *Nature*, 6:31707, Aug. 2016.

[73] R. Fossati, C. Confalonieri, V. Torri, E. Ghislandi, A. Penna, V. Pistotti, A. Tinazzi, and A. Liberati. Cytotoxic and hormonal treatment for metastatic breast cancer: a systematic review of published randomized trials involving 31,510 women. *Journal of Clinical Oncology*, 16(10):3439–3460, Oct 1998.

[74] C. Fraley and A. Raftery. Model-based clustering, discriminant analysis, and density estimation. *Journal of the American Statistical Association*, 97(458):611–631, Jun 2002.

[75] S. Franco and A. Huttenlocher. Regulating cell migration: calpains make the cut. *Journal of Cell Science*, 118(17):3829–3838, Sep 1 2005.

[76] J. Francois, R. Meili, J. C. del Alamo, R. Firtel, and J. C. Lasheras. Understanding the mechanics of neutrophil migration in three-dimensional extracellular matrices. *Biophysical Journal*, 112(3):125a, 2017.

[77] K. K. Frese and D. A. Tuveson. Maximizing mouse cancer models. *Nature Reviews Cancer*, 7(9):654, 2007.

[78] P. Friedl and K. Wolf. Tumour-cell invasion and migration: diversity and escape mechanisms. *Nature Reviews Cancer*, 3(5):362–374, May 2003.

[79] S. M. Frisch, K. Vuori, E. Ruoslahti, and P. Y. Chan-Hui. Control of adhesion-dependent cell survival by focal adhesion kinase. *Journal of Cell Biology*, 134(3):793–799, Aug. 1996.

[80] F. Fuchs, G. Pau, D. Kranz, O. Sklyar, C. Budjan, S. Steinbrink, T. Horn, A. Pedal, W. Huber, and M. Boutros. Clustering phenotype populations by genome-wide RNAi and multiparametric imaging. *Molecular Systems Biology*, 6, Jun 2010.

[81] P. Fumoleau, P. Kerbrat, P. Romestaing, P. Fargeot, A. Brémond, M. Namer, S. Schraub, M. J. Goudier, J. Mihura, A. Monnier, P. Clavère, D. Serin, P. Seffert, C. Pourny, T. Facchini, J. P. Jacquin, J. F. Sztermer, J. Datchary, R. Ramos, and E. Luporsi. Randomized trial comparing six versus three cycles of epirubicin-based adjuvant chemotherapy in premenopausal, node-positive breast cancer patients: 10-Year follow-up results of the French Adjuvant Study Group 01 trial. *Journal of Clinical Oncology*, 21(2):298–305, Jan 2003.

[82] M. J. Garnett, E. J. Edelman, S. J. Heidorn, C. D. Greenman, A. Dastur, K. W. Lau, P. Greninger, I. R. Thompson, X. Luo, J. Soares, Q. Liu, F. Iorio, D. Surdez, L. Chen, R. J. Milano, G. R. Bignell, A. T. Tam, H. Davies, J. A. Stevenson, S. Barthorpe, S. R. Lutz, F. Kogera, K. Lawrence, A. McLaren-Douglas, X. Mitropoulos, T. Mironenko, H. Thi, L. Richardson, W. Zhou, F. Jewitt, T. Zhang, P. O'Brien, J. L. Boisvert, S. Price, W. Hur, W. Yang, X. Deng, A. Butler, H. G. Choi, J. Chang, J. Baselga, I. Stamenkovic, J. A. Engelman, S. V. Sharma, O. Delattre, J. Saez-Rodriguez, N. S. Gray, J. Settleman, P. A. Futreal, D. A. Haber, M. R. Stratton, S. Ramaswamy, U. McDermott, and C. H. Benes. Systematic identification of genomic markers of drug sensitivity in cancer cells. *Nature*, 483(7391):570–U87, Mar 29 2012.

[83] J. Gehl, M. Boesgaard, T. Paaske, J. Vittrup, and P. Dombernowsky. Combined

doxorubicin and paclitaxel in advanced breast cancer: effective and cardiotoxic. *Ann.Oncol.*, 7(7):687–693, Sep 1996.

[84] G. Genovese, M. Fromer, E. A. Stahl, D. M. Ruderfer, K. Chambert, M. Landen, J. L. Moran, S. M. Purcell, P. Sklar, P. F. Sullivan, C. M. Hultman, and S. A. McCarroll. Increased burden of ultra-rare protein-altering variants among 4,877 individuals with schizophrenia. *Nature Neuroscience*, 19(11):1433–1441, Nov 2016.

[85] M. J. Gerdes, C. J. Sevinsky, A. Sood, S. Adak, M. O. Bello, A. Bordwell, A. Can, A. Corwin, S. Dinn, R. J. Filkins, D. Hollman, V. Kamath, S. Kaanumalle, K. Kenny, M. Larsen, M. Lazare, Q. Li, C. Lowes, C. C. McCulloch, E. McDonough, M. C. Montalto, Z. Pang, J. Rittscher, A. Santamaria-Pang, B. D. Sarachan, M. L. Seel, A. Seppo, K. Shaikh, Y. Sui, J. Zhang, and F. Ginty. Highly multiplexed single-cell analysis of formalin-fixed, paraffin-embedded cancer tissue. *Proceedings of the National Academy of Sciences*, 110(29):11982–11987, Jul 2013.

[86] D. Ghersi, N. Wilcken, J. Simes, and E. Donoghue. Taxane containing regimens for metastatic breast cancer, Apr 2003.

[87] L. Gianni, E. Munzone, G. Capri, F. Fulfaro, E. Tarenzi, F. Villani, C. Spreafico, A. Laffranchi, A. Caraceni, C. Martini, M. Stefanelli, P. Valagussa, and G. Bonadonna. Paclitaxel by 3-hour infusion in combination with bolus doxorubicin in women with untreated metastatic breast cancer: High antitumor efficacy and cardiac effects in a dose-finding and sequence-finding study. *Journal of Clinical Oncology*, 13(11):2688–2699, Nov 1995.

[88] G. Giannone, E. Hosy, F. Levet, A. Constals, K. Schulze, A. I. Sobolevsky, M. P. Rosconi, E. Gouaux, R. Tampé, D. Choquet, and L. Cognet. Dynamic superresolution imaging of endogenous proteins on living cells at ultra-high density. *Biophysical Journal*, 99(4):1303–1310, 2010.

[89] I. Gill, S. Droubi, S. Giovedi, K. N. Fedder, L. A. D. Bury, F. Bosco, M. P. Sceniak, F. Benfenati, and S. L. Sabo. Presynaptic NMDA receptors – dynamics and distribution in developing axons in vitro and in vivo. *Journal of Cell Science*, 128(4):768 LP – 780, Feb 2015.

[90] A. P. Gilmore. Anoikis. *Cell Death and Differentiation*, 12 Suppl 2:1473–1477, Nov. 2005.

[91] A. Glading, D. Lauffenburger, and A. Wells. Cutting to the chase: calpain proteases in cell motility. *Trends in Cell Biology*, 12(1):46–54, Jan 2002.

[92] E. Glory and R. F. Murphy. Automated subcellular location determination and high-throughput microscopy. *Developmental Cell*, 12(1):7–16, Jan 2007.

[93] S. A. Glynn, P. Gammell, M. Heenan, R. O'Connor, Y. Liang, J. Keenan, and M. Clynes. A new superinvasive in vitro phenotype induced by selection of human breast carcinoma cells with the chemotherapeutic drugs paclitaxel and doxorubicin. *British Journal of Cancer*, 91(10):1800–1807, Nov. 2004.

[94] A. Goldhirsch, W. C. Wood, R. D. Gelber, A. S. Coates, B. Thürlimann, and H. J. Senn. Meeting highlights: Updated international expert consensus on the primary

therapy of early breast cancer. *Journal of Clinical Oncology*, 21(17):3357–3365, Sep 2003.

[95] A. Goldman, B. Majumder, A. Dhawan, S. Ravi, D. Goldman, M. Kohandel, P. Majumder, and S. Sengupta. Temporally sequenced anticancer drugs overcome adaptive resistance by targeting a vulnerable chemotherapy-induced phenotypic transition. *Nature Communications*, 6:6139, 2015.

[96] S. Gordonov, M. K. Hwang, A. Wells, F. B. Gertler, D. A. Lauffenburger, and M. Bathe. Time series modeling of live-cell shape dynamics for image-based phenotypic profiling. *Integrative Biology*, 8(1):73–90, 2016.

[97] J. Grahovac and A. Wells. Matrikine and matricellular regulators of EGF receptor signaling on cancer cell migration and invasion. *Laboratory Investigation*, pages 1–10, Nov. 2013.

[98] B. T. Grys, D. S. Lo, N. Sahin, O. Z. Kraus, Q. Morris, C. Boone, and B. J. Andrews. Machine learning and computer vision approaches for phenotypic profiling. *Journal of Cell Biology*, 216(1):65–71, 2017.

[99] S. Gulsuner, T. Walsh, A. C. Watts, M. K. Lee, A. M. Thornton, S. Casadei, C. Rippey, H. Shahin, V. L. Nimgaonkar, R. C. P. Go, R. M. Savage, N. R. Swerdlow, R. E. Gur, D. L. Braff, M.-C. King, and J. M. McClellan. Spatial and temporal mapping of de novo mutations in schizophrenia to a fetal prefrontal cortical network. *Cell*, 154(3):518–29, Aug 2013.

[100] S.-M. Guo, R. Veneziano, S. Gordonov, L. Li, D. Park, A. B. Kulesa, P. C. Blainey, J. R. Cottrell, E. S. Boyden, and M. Bathe. Multiplexed confocal and super-resolution fluorescence imaging of cytoskeletal and neuronal synapse proteins. *bioRxiv*, 2017.

[101] S. L. Gupton and C. M. Waterman-Storer. Spatiotemporal Feedback between Actomyosin and Focal-Adhesion Systems Optimizes Rapid Cell Migration. *Cell*, 125(7):1361–1374, Jun 2006.

[102] J. F. Hair Jr and G. T. M. Hult. *A primer on partial least squares structural equation modeling (PLS-SEM)*. Sage Publications, 2016.

[103] M. E. H. Hammond, D. F. Hayes, A. C. Wolff, P. B. Mangu, and S. Temin. American Society of Clinical Oncology/College of American Pathologists Guideline Recommendations for Immunohistochemical Testing of Estrogen and Progesterone Receptors in Breast Cancer. *Journal of Oncology Practice*, 6(4):195–197, Jul 2010.

[104] K. Han, J. L. Holder Jr., C. P. Schaaf, H. Lu, H. Chen, H. Kang, J. Tang, Z. Wu, S. Hao, S. W. Cheung, P. Yu, H. Sun, A. M. Breman, A. Patel, H. C. Lu, and H. Y. Zoghbi. SHANK3 overexpression causes manic-like behaviour with unique pharmacogenetic properties. *Nature*, 503(7474):72–77, 2013.

[105] M. Hassan, J. Ansari, D. Spooner, and S. Hussain. Chemotherapy for breast cancer (Review). *Oncology Reports*, 25(5):223–230, Nov 2011.

[106] J. M. Haugh. Live-cell fluorescence microscopy with molecular biosensors: what are we really measuring? *Biophysical Journal*, 102(9):2003–11, May 2012.

[107] M. K. Hayashi, C. Tang, C. Verpelli, R. Narayanan, M. H. Stearns, R. M. Xu, H. Li, C. Sala, and Y. Hayashi. The postsynaptic density proteins Homer and Shank form a polymeric network structure. *Cell*, 137(1):159–171, 2009.

[108] M. Held, M. H. A. Schmitz, B. Fischer, T. Walter, B. Neumann, M. H. Olma, M. Peter, J. Ellenberg, and D. W. Gerlich. CellCognition: time-resolved phenotype annotation in high-throughput live cell imaging. *Nature Methods*, 7(9):747–U118, Sep 2010.

[109] S. J. Henry, J. C. Crocker, and D. A. Hammer. Ligand density elicits a phenotypic switch in human neutrophils. *Integrative Biology*, 6(3):348–356, 2014.

[110] L. E. Hind, W. J. Vincent, and A. Huttenlocher. Leading from the back: the role of the uropod in neutrophil polarization and migration. *Developmental Cell*, 38(2):161–169, 2016.

[111] K. S. Hoek, O. M. Eichhoff, N. C. Schlegel, U. Döbbeling, N. Kobert, L. Schaerer, S. Hemmi, and R. Dummer. In vivo switching of human melanoma cells between proliferative and invasive states. *Cancer Research*, 68(3):650–656, Feb. 2008.

[112] S. J. Holden, S. Uphoff, and A. N. Kapanidis. DAOSTORM: an algorithm for high-density super-resolution microscopy. *Nature Methods*, 8(4):279–280, 2011.

[113] C. Holohan, S. Van Schaeybroeck, D. B. Longley, and P. G. Johnston. Cancer drug resistance: an evolving paradigm. *Nature Reviews Cancer*, 13(10):714–726, Sep 2013.

[114] P. Horvath, N. Aulner, M. Bickle, A. M. Davies, E. D. Nery, D. Ebner, M. C. Montoya, P. Östling, V. Pietiäinen, L. S. Price, S. L. Shorte, G. Turcatti, C. von Schantz, and N. O. Carragher. Screening out irrelevant cell-based models of disease. *Nature Reviews Drug Discovery*, 15(11):751–769, 2016.

[115] C. Hudis, A. Seidman, J. Baselga, G. Raptis, D. Lebwohl, T. Gilewski, M. Moynahan, N. Sklarin, D. Fennelly, J. P. A. Crown, A. Surbone, M. Uhlenhopp, E. Riedel, T. J. Yao, and L. Norton. Sequential dose-dense doxorubicin, paclitaxel, and cyclophosphamide for resectable high-risk breast cancer: Feasibility and efficacy. *Journal of Clinical Oncology*, 17(1):93–100, Jan 1999.

[116] T. R. Hurd, M. DeGennaro, and R. Lehmann. Redox regulation of cell migration and adhesion. *Trends in Cell Biology*, 22(2):107–15, Feb 2012.

[117] K. E. Hurov, C. Cotta-Ramusino, and S. J. Elledge. A genetic screen identifies the Triple T complex required for DNA damage signaling and ATM and ATR stability. *Genes & Development*, 24(17):1939–1950, Sept. 2010.

[118] S. A. Hussain, D. H. Palmer, A. Stevens, D. Spooner, C. J. Poole, and D. W. Rea. Role of chemotherapy in breast cancer. *Expert Review of Anticancer Therapy*, 5(6):1095–110, Dec 2005.

[119] A. Iwabu, K. Smith, F. D. Allen, D. a. Lauffenburger, and A. Wells. Epidermal growth factor induces fibroblast contractility and motility via a protein kinase C delta-dependent pathway. *The Journal of Biological Chemistry*, 279(15):14551–60, Apr. 2004.

[120] S. P. Jackson and J. Bartek. The DNA-damage response in human biology and disease. *Nature*, 461(7267):1071–1078, Oct. 2009.

[121] K. A. Janes, J. R. Kelly, S. Gaudet, J. G. Albeck, P. K. Sorger, and D. A. Lauffenburger. Cue-signal-response analysis of TNF-induced apoptosis by partial least squares regression of dynamic multivariate data. *Journal of Computational Biology*, 11(4):544–61, Aug 2004.

[122] H. E. Johnson and J. M. Haugh. Quantitative analysis of phosphoinositide 3-kinase (PI3K) signaling using live-cell total internal reflection fluorescence (TIRF) microscopy. *Current Protocols in Cell Biology*, 61(December):14.14.1–14.14.24, Jan. 2013.

[123] T. R. Jones, A. E. Carpenter, M. R. Lamprecht, J. Moffat, S. J. Silver, J. K. Grenier, A. B. Castoreno, U. S. Eggert, D. E. Root, P. Golland, and D. M. Sabatini. Scoring diverse cellular morphologies in image-based screens with iterative feedback and machine learning. *Proceedings of the National Academy of Sciences*, 106(6):1826–1831, Feb 10 2009.

[124] T. R. Jones, I. H. Kang, D. B. Wheeler, R. a. Lindquist, A. Papallo, D. M. Sabatini, P. Golland, and A. E. Carpenter. CellProfiler Analyst: data exploration and analysis software for complex image-based screens. *BMC Bioinformatics*, 9:482, Jan. 2008.

[125] M. A. Jordan and L. Wilson. Microtubules as a target for anticancer drugs. *Nature*, 4(4):253–265, Apr. 2004.

[126] R. Jungmann, M. S. Avendano, J. B. Woehrstein, M. J. Dai, W. M. Shih, and P. Yin. Multiplexed 3D cellular super-resolution imaging with DNA-PAINT and Exchange-PAINT. *Nature Methods*, 11(3):313–U292, 2014.

[127] R. Jungmann, C. Steinhauer, M. Scheible, A. Kuzyk, P. Tinnefeld, and F. C. Simmel. Single-molecule kinetics and super-resolution microscopy by fluorescence imaging of transient binding on DNA origami. *Nano Letters*, 10(11):4756–4761, 2010.

[128] R. Kafri, J. Levy, M. B. Ginzberg, S. Oh, G. Lahav, and M. W. Kirschner. Dynamics extracted from fixed cells reveal feedback linking cell growth to cell cycle. *Nature*, 494(7438):480–483, Feb 28 2013.

[129] C. Karlsson-Rosenthal and J. B. A. Millar. Cdc25: mechanisms of checkpoint inhibition and recovery. *Trends in Cell Biology*, 16(6):285–292, June 2006.

[130] K. Kemper, P. L. de Goeje, D. S. Peeper, and R. van Amerongen. Phenotype switching: tumor cell plasticity as a resistance mechanism and target for therapy. *Cancer Research*, 74(21):5937–5941, Nov. 2014.

[131] K. Keren, Z. Pincus, G. M. Allen, E. L. Barnhart, G. Marriott, A. Mogilner, and J. A. Theriot. Mechanism of shape determination in motile cells. *Nature*, 453(7194):475–U1, May 22 2008.

[132] S. Kharait, S. Hautaniemi, S. Wu, A. Iwabu, D. a. Lauffenburger, and A. Wells. Decision tree modeling predicts effects of inhibiting contractility signaling on cell motility. *BMC Systems Biology*, 1:9, Jan. 2007.

[133] J. B. Kim, R. Stein, and M. J. O'hare. Three-dimensional in vitro tissue culture models of breast cancer—a review. *Breast Cancer Research and Treatment*, 85(3):281–291, 2004.

[134] T. Kiuchi, M. Higuchi, A. Takamura, M. Maruoka, and N. Watanabe. Multitarget super-resolution microscopy with high-density labeling by exchangeable probes. *Nature Methods*, 12(8):743–746, Jul 2015.

[135] N. C. Klapoetke, Y. Murata, S. S. Kim, S. R. Pulver, A. Birdsey-Benson, Y. K. Cho, T. K. Morimoto, A. S. Chuong, E. J. Carpenter, Z. Tian, J. Wang, Y. Xie, Z. Yan, Y. Zhang, B. Y. Chow, B. Surek, M. Melkonian, V. Jayaraman, M. Constantine-Paton, G. K.-S. Wong, and E. S. Boyden. Independent optical excitation of distinct neural populations. *Nature Methods*, 11(3):338–46, Mar 2014.

[136] N. Komatsu, K. Aoki, M. Yamada, H. Yukinaga, Y. Fujita, Y. Kamioka, and M. Matsuda. Development of an optimized backbone of FRET biosensors for kinases and GTPases. *Molecular Biology of the Cell*, 22(23):4647–4656, Dec 1 2011.

[137] Y. Komohara, Y. Fujiwara, K. Ohnishi, and M. Takeya. Tumor-associated macrophages: potential therapeutic targets for anti-cancer therapy. *Advanced Drug Delivery Reviews*, 99:180–185, 2016.

[138] M. Krause and A. Gautreau. Steering cell migration: lamellipodium dynamics and the regulation of directional persistence. *Nature Reviews Molecular Cell Biology*, 15(9):577–590, Aug. 2014.

[139] C.-J. Ku, Y. Wang, O. D. Weiner, S. J. Altschuler, and L. F. Wu. Network Crosstalk Dynamically Changes during Neutrophil Polarization. *Cell*, 149(5):1073–1083, May 25 2012.

[140] T. Ku, J. Swaney, J.-Y. Park, A. Albanese, E. Murray, J. H. Cho, Y.-G. Park, V. Mangena, J. Chen, and K. Chung. Multiplexed and scalable super-resolution imaging of three-dimensional protein localization in size-adjustable tissues. *Nature Biotechnology*, 34(9):973–981, Sep 2016.

[141] T. Lämmermann and M. Sixt. Mechanical modes of 'amoeboid' cell migration. *Current Opinion in Cell Biology*, 21(5):636–644, Oct 2009.

[142] W. D. Landry and T. G. Cotter. ROS signalling, NADPH oxidases and cancer. *Biochemical Society Transactions*, 42(4):934–8, Aug 2014.

[143] R. S. Larsen, R. J. Corlew, M. A. Henson, A. C. Roberts, M. Mishina, M. Watanabe, S. A. Lipton, N. Nakanishi, I. Perez-Otano, R. J. Weinberg, and B. D. Philpot. NR3A-containing NMDARs promote neurotransmitter release and spike timing-dependent plasticity. *Nature Neuroscience*, 14(3):338–344, Mar 2011.

[144] K. S. Lau, A. M. Juchheim, K. R. Cavaliere, S. R. Philips, D. A. Lauffenburger, and K. M. Haigis. In vivo systems analysis identifies spatial and temporal aspects of the modulation of TNF-α-induced apoptosis and proliferation by MAPKs. *Science Signaling*, 4(165):ra16, Mar 2011.

[145] D. A. Lauffenburger and A. F. Horwitz. Cell migration: a physically integrated molecular process. *Cell*, 84(3):359–369, Feb. 1996.

[146] M. J. Lee, A. S. Ye, A. K. Gardino, A. M. Heijink, P. K. Sorger, G. MacBeath, and M. B. Yaffe. Sequential application of anticancer drugs enhances cell death by rewiring apoptotic signaling networks. *Cell*, 149(4):780–94, May 2012.

[147] L. Leloup, H. Shao, Y. H. Bae, B. Deasy, D. Stolz, P. Roy, and A. Wells. m-calpain Activation Is Regulated by Its Membrane Localization and by Its Binding to Phosphatidylinositol 4,5-Bisphosphate. *Journal of Biological Chemistry*, 285(43):33549–33566, Oct 22 2010.

[148] M. A. Lemmon and J. Schlessinger. Cell signaling by receptor tyrosine kinases. *Cell*, 141(7):1117–34, June 2010.

[149] Q. Q. Li, J. D. Xu, W. J. Wang, X. X. Cao, Q. Chen, F. Tang, Z. Q. Chen, X. P. Liu, and Z. D. Xu. Twist1-Mediated Adriamycin-Induced Epithelial-Mesenchymal Transition Relates to Multidrug Resistance and Invasive Potential in Breast Cancer Cells. *Clinical Cancer Research*, 15(8):2657–2665, Apr. 2009.

[150] J.-R. Lin, M. Fallahi-Sichani, and P. K. Sorger. Highly multiplexed imaging of single cells using a high-throughput cyclic immunofluorescence method. *Nature Communications*, 6, Sep 2015.

[151] Q. Liu, S. Guntuku, X.-S. Cui, S. Matsuoka, D. Cortez, K. Tamai, G. Luo, S. Carattini-Rivera, F. DeMayo, A. Bradley, L. A. Donehower, and S. J. Elledge. Chk1 is an essential kinase that is regulated by ATR and required for the G2/M DNA damage checkpoint. *Genes & Development*, 2000.

[152] X. Liu, E. Krawczyk, F. A. Suprynowicz, N. Palechor-Ceron, H. Yuan, A. Dakic, V. Simic, Y.-L. Zheng, P. Sripadhan, C. Chen, J. Lu, T.-W. Hou, S. Choudhury, B. Kallakury, D. Tang, T. Darling, R. Thangapazham, O. Timofeeva, A. Dritschilo, S. H. Randell, C. Albanese, S. Agarwal, and R. Schlegel. Conditional reprogramming and long-term expansion of normal and tumor cells from human biospecimens. *Nature Protocols*, 12(2):439–451, 2017.

[153] X. Liu, V. Ory, S. Chapman, H. Yuan, C. Albanese, B. Kallakury, O. A. Timofeeva, C. Nealon, A. Dakic, V. Simic, B. R. Haddad, J. S. Rhim, A. Dritschilo, A. Riegel, A. McBride, and R. Schlegel. ROCK Inhibitor and Feeder Cells Induce the Conditional Reprogramming of Epithelial Cells. *The American Journal of Pathology*, 180(2):599–607, Feb 2012.

[154] X. Liu, E. S. Welf, and J. M. Haugh. Linking morphodynamics and directional persistence of T lymphocyte migration. *Journal of the Royal Society Interface*, 12(106), May 6 2015.

[155] Y. J. Liu, M. Le Berre, F. Lautenschlaeger, P. Maiuri, A. Callan-Jones, M. Heuzé, T. Takaki, R. Voituriez, and M. Piel. Confinement and low adhesion induce fast amoeboid migration of slow mesenchymal cells. *Cell*, 160(4):659–672, 2015.

[156] C. A. Livasy, G. Karaca, R. Nanda, M. S. Tretiakova, O. I. Olopade, D. T. Moore, and C. M. Perou. Phenotypic evaluation of the basal-like subtype of invasive breast carcinoma. *Modern Pathology*, 19(2):264–271, Feb 2006.

[157] V. Ljosa, P. D. Caie, R. ter Horst, K. L. Sokolnicki, E. L. Jenkins, S. Daya, M. E. Roberts, T. R. Jones, S. Singh, A. Genovesio, P. A. Clemons, N. O. Carragher, and A. E. Carpenter. Comparison of Methods for Image-Based Profiling of Cellular Morphological Responses to Small-Molecule Treatment. *Journal of Biomolecular Screening*, 18(10, SI):1321–1329, Dec 2013.

[158] J. G. Lock, M. J. Mamaghani, H. Shafqat-Abbasi, X. Gong, J. Tyrcha, and S. Stromblad. Plasticity in the Macromolecular-Scale Causal Networks of Cell Migration. *PLoS One*, 9(2), Feb 28 2014.

[159] L.-H. Loo, L. F. Wu, and S. J. Altschuler. Image-based multivariate profiling of drug responses from single cells. *Nature Methods*, 4(5):445–453, May 2007.

[160] S. S. Lou, A. Diz-Munoz, O. D. Weiner, D. A. Fletcher, and J. A. Theriot. Myosin light chain kinase regulates cell polarization independently of membrane tension or Rho kinase. *Journal of Cell Biology*, 209(2):275–288, Apr 27 2015.

[161] S. Luria and M. Delbrück. Mutations of Bacteria from Virus Sensitivity to Virus Resistance. *Genetics*, 28(6):491–511, Nov 1943.

[162] L. v. d. Maaten and G. Hinton. Visualizing data using t-sne. *Journal of Machine Learning Research*, 9(Nov):2579–2605, 2008.

[163] M. Machacek and G. Danuser. Morphodynamic profiling of protrusion phenotypes. *Biophysical Journal*, 90(4):1439–1452, Feb 2006.

[164] M. Machacek, L. Hodgson, C. Welch, H. Elliott, O. Pertz, P. Nalbant, A. Abell, G. L. Johnson, K. M. Hahn, and G. Danuser. Coordination of Rho GTPase activities during cell protrusion. *Nature*, 461(7260):99–103, Sept. 2009.

[165] P. Mali, L. Yang, K. M. Esvelt, J. Aach, M. Guell, J. E. DiCarlo, J. E. Norville, and G. M. Church. RNA-Guided Human Genome Engineering via Cas9. *Science*, 339(6121):823–826, Feb 15 2013.

[166] I. A. Manke, A. Nguyen, D. Lim, M. Q. Stewart, A. E. H. Elia, and M. B. Yaffe. MAPKAP kinase-2 is a cell cycle checkpoint kinase that regulates the G2/M transition and S phase progression in response to UV irradiation. *Molecular Cell*, 17(1):37–48, Jan. 2005.

[167] M. Mann. Functional and quantitative proteomics using SILAC. *Nature Reviews Molecular Cell Biology*, 7(12):952–958, Dec. 2006.

[168] S. Matsuoka, B. A. Ballif, A. Smogorzewska, E. R. McDonald, K. E. Hurov, J. Luo, C. E. Bakalarski, Z. Zhao, N. Solimini, and Y. Lerenthal. ATM and ATR Substrate Analysis Reveals Extensive Protein Networks Responsive to DNA Damage. *Science*, 316(5828):1160–1166, May 2007.

[169] M. Mattiazzi Usaj, E. B. Styles, A. J. Verster, H. Friesen, C. Boone, and B. J. Andrews. High-Content Screening for Quantitative Cell Biology. *Trends in Cell Biology*, 26(8):598–611, Aug 2016.

[170] D. Q. Matus, L. L. Lohmer, A. J. Kelley, Laura C Schindler, A. Q. Kohrman, M. Barkoulas, W. Zhang, Q. Chi, and D. R. Sherwood. Invasive Cell Fate Requires G1 Cell-Cycle Arrest and Histone Deacetylase-Mediated Changes in Gene Expression. *Developmental Cell*, 35(2):162–174, Oct. 2015.

[171] A. Mazumder, L. Q. Pesudo, S. McRee, M. Bathe, and L. D. Samson. Genome-wide single-cell-level screen for protein abundance and localization changes in response to DNA damage in S-cerevisiae. *Nucleic Acid Research*, 41(20):9310–9324, Nov 2013.

[172] H. R. Mellor, A. R. Bell, J. P. Valentin, and R. R. A. Roberts. Cardiotoxicity associated with targeting kinase pathways in cancer. *Toxicological Sciences*, 120(1):14–32, Mar 2011.

[173] M. P. Menden, F. Iorio, M. Garnett, U. McDermott, C. H. Benes, P. J. Ballester, and J. Saez-Rodriguez. Machine Learning Prediction of Cancer Cell Sensitivity to Drugs Based on Genomic and Chemical Properties. *PLoS One*, 8(4), Apr 30 2013.

[174] K. D. Micheva, B. Busse, N. C. Weiler, N. O'Rourke, and S. J. Smith. Single-synapse analysis of a diverse synapse population: proteomic imaging methods and markers. *Neuron*, 68(4):639–653, 2010.

[175] K. D. Micheva and S. J. Smith. Array tomography: a new tool for imaging the molecular architecture and ultrastructure of neural circuits. *Neuron*, 55(1):25–36, 2007.

[176] E. Middleman, J. Luce, and E. Frei. Clinical trials with adriamycin. *Cancer*, 28(4):844–850, Oct 1971.

[177] M. A. Miller, A. S. Meyer, M. T. Beste, Z. Lasisi, S. Reddy, K. W. Jeng, C.-H. Chen, J. Han, K. Isaacson, L. G. Griffith, and D. A. Lauffenburger. ADAM-10 and -17 regulate endometriotic cell migration via concerted ligand and receptor shedding feedback on kinase signaling. *Proceedings of the National Academy of Sciences*, 110(22):E2074–83, May 2013.

[178] M. A. Miller, R. J. Sullivan, and D. A. Lauffenburger. Molecular pathways: Receptor ectodomain shedding in treatment, resistance, and monitoring of cancer. *Clinical Cancer Research*, 23(3):623–629, Feb 2017.

[179] M. A. Miller and R. Weissleder. Imaging of anticancer drug action in single cells. *Nature Reviews Cancer*, 17(7):399–414, Jun 2017.

[180] S. K. Mitra, D. A. Hanson, and D. D. Schlaepfer. Focal adhesion kinase: in command and control of cell motility. *Nature Reviews Molecular Cell Biology*, 6(1):56–68, 2005.

[181] J. G. Moffat, J. Rudolph, and D. Bailey. Phenotypic screening in cancer drug discovery - past, present and future. *Nature Reviews Drug discovery*, 13(8):588–602, Aug 2014.

[182] A. Mogilner and K. Keren. The Shape of Motile Cells. *Current Biology*, 19(17):R762–R771, Sept. 2009.

[183] N. Monnier. *Bayesian Inference Approaches for Particle Trajectory Analysis in Cell Biology*. PhD thesis, Harvard University, 2013.

[184] N. Monnier, Z. Barry, H. Y. Park, K.-C. Su, Z. Katz, B. P. English, A. Dey, K. Pan, I. M. Cheeseman, R. H. Singer, and M. Bathe. Inferring transient particle transport dynamics in live cells. *Nature Methods*, 12(9):838–840, 2015.

[185] Y. Mosesson, G. B. Mills, and Y. Yarden. Derailed endocytosis: an emerging feature of cancer. *Nature Reviews Cancer*, 8(11):835–850, Nov. 2008.

[186] G. Mouneimne, V. DesMarais, M. Sidani, E. Scemes, W. Wang, X. Song, R. Eddy, and J. Condeelis. Spatial and temporal control of cofilin activity is required for directional sensing during chemotaxis. *Current Biology*, 16(22):2193–205, Dec. 2006.

[187] K. Mross, B. Niemann, U. Massing, J. Drevs, C. Unger, R. Bhamra, and C. E. Swenson. Pharmacokinetics of liposomal doxorubicin (TLC-D99; Myocet) in patients with solid tumors: An open-label, single-dose study. *Cancer Chemotherapy and Pharmacology*, 54(6):514–524, Dec 2004.

[188] M. Nagano, D. Hoshino, N. Koshikawa, T. Akizawa, and M. Seiki. Turnover of focal adhesions and cancer cell migration. *International Journal of Cell Biology*, 2012:310616, 2012.

[189] A. Y. J. Ng, J. C. Rajapakse, R. E. Welsch, P. T. Matsudaira, V. Horodincu, and J. G. Evans. A Cell Profiling Framework for Modeling Drug Responses from HCS Imaging. *Journal of Biomolecular Screening*, 15(7):858–868, Aug 2010.

[190] D. X. Nguyen, P. D. Bos, and J. Massagué. Metastasis: from dissemination to organ-specific colonization. *Nature Reviews Cancer*, 9(4):274–84, Apr. 2009.

[191] T. J. F. Nieland, D. J. Logan, J. Saulnier, D. Lam, C. Johnson, D. E. Root, A. E. Carpenter, and B. L. Sabatini. High content image analysis identifies novel regulators of synaptogenesis in a high-throughput RNAi screen of primary neurons. *PLoS ONE*, 9(3):e91744, mar 2014.

[192] M. Niepel, M. Hafner, E. A. Pace, M. Chung, D. H. Chai, L. Zhou, B. Schoeberl, and P. K. Sorger. Profiles of Basal and Stimulated Receptor Signaling Networks Predict Drug Response in Breast Cancer Lines. *Science Signaling*, 6(294), Sep 24 2013.

[193] J. Niu, Y. Shi, G. Tan, C. H. Yang, M. Fan, L. M. Pfeffer, and Z.-H. Wu. DNA damage induces NF-κB-dependent microRNA-21 up-regulation and promotes breast cancer cell invasion. *Journal of Biological Chemistry*, 287(26):21783–21795, June 2012.

[194] D. Páez, M. J. Labonte, P. Bohanes, W. Zhang, L. Benhanim, Y. Ning, T. Wakatsuki, F. Loupakis, and H.-J. Lenz. Cancer dormancy: a model of early dissemination and late cancer recurrence. *Clinical Cancer Research*, 18(3):645–653, Feb. 2012.

[195] M. Parri and P. Chiarugi. Rac and Rho GTPases in cancer cell motility control. *Cell Communication and Signaling*, 8:23, Jan 2010.

[196] R. D. Paulsen, D. V. Soni, R. Wollman, A. Hahn, M.-C. Yee, A. Guan, J. A. Hesley, S. C. Miller, E. F. Cromwell, D. E. Solow-Cordero, T. Meyer, and K. A. Cimprich. A Genome-wide siRNA screen reveals diverse cellular processes and pathways that mediate genome stability. *Molecular Cell*, 35(2):228–239, July 2009.

[197] Z. Perlman, M. Slack, Y. Feng, T. Mitchison, L. Wu, and S. Altschuler. Multidimensional drug profiling by automated microscopy. *Science*, 306(5699):1194–1198, Nov 12 2004.

[198] M. C. Perry, D. C. Doll, and C. E. Freter. *Perry's the Chemotherapy Source Book*. Lippincott Williams & Wilkins, 2012.

[199] R. J. Petrie, A. D. Doyle, and K. M. Yamada. Random versus directionally persistent cell migration. *Nature Reviews Molecular Cell Biology*, 10(8):538–49, Aug. 2009.

[200] R. J. Petrie, N. Gavara, R. S. Chadwick, and K. M. Yamada. Nonpolarized signaling reveals two distinct modes of 3D cell migration. *Journal of Cell Biology*, 197(3):439–55, Apr. 2012.

[201] R. J. Petrie and K. M. Yamada. At the leading edge of three-dimensional cell migration. *Journal of Cell Science*, 125(Pt 24):5917–26, Dec 2012.

[202] G. Pfitzer, O. O. Adeoye, V. Bouthors, M. C. Hubbell, J. M. Williams, J. William, A. M. Prasad, D. W. Nuno, O. M. Koval, P. Ketsawatsomkron, W. Li, H. Li, F. Y. Shen, M.-l. A. Joiner, W. Kutschke, R. M. Weiss, D. Curt, M. E. Anderson, K. G. Lamping, I. M. Grumbach, S. M. Butler, A. Semotiuk, M. James, W. J. Pearce, A. J. Physiol, and C. Physiol. Regulation of myosin phosphorylation in smooth muscle. *Journal of Applied Physiology*, pages 497–503, 2014.

[203] Z. Pincus and J. A. Theriot. Comparison of quantitative methods for cell-shape analysis. *Journal of Microscopy*, 227(Pt 2):140–56, Aug. 2007.

[204] O. Podlaha, M. Riester, S. De, and F. Michor. Evolution of the Cancer Genome, Apr 2012.

[205] K. Polyak and R. A. Weinberg. Transitions between epithelial and mesenchymal states: acquisition of malignant and stem cell traits. *Nature Reviews Cancer*, 9(4):265–273, 2009.

[206] D. Posada and T. Buckley. Model selection and model averaging in phylogenetics: Advantages of akaike information criterion and Bayesian approaches over likelihood ratio tests. *Systematic Biology*, 53(5):793–808, Oct 2004.

[207] A. Prat, B. Adamo, M. C. U. Cheang, C. K. Anders, L. A. Carey, and C. M. Perou. Molecular Characterization of Basal-Like and Non-Basal-Like Triple-Negative Breast Cancer. *The Oncologist*, 18(2):123–133, Feb 2013.

[208] M. Quintavalle, L. Elia, J. H. Price, S. Heynen-Genel, and S. A. Courtneidge. A Cell-Based High-Content Screening Assay Reveals Activators and Inhibitors of Cancer Cell Invasion. *Science Signaling*, 4(183):ra49–ra49, July 2011.

[209] A. E. Raftery. Bayesian model selection in social research. *Sociological Methodology*, pages 111–163, 1995.

[210] C. Raggi, H. Mousa, M. Correnti, A. Sica, and P. Invernizzi. Cancer stem cells and tumor-associated macrophages: a roadmap for multitargeting strategies. *Oncogene*, 35(6):671–682, 2016.

[211] P. Rämö, R. Sacher, B. Snijder, B. Begemann, and L. Pelkmans. CellClassifier: supervised learning of cellular phenotypes. *Bioinformatics*, 25(22):3028–30, Nov. 2009.

[212] A. C. Ranganathan, A. P. Adam, L. Zhang, and J. A. Aguirre-Ghiso. Tumor cell dormancy induced by p38SAPK and ER-stress signaling: an adaptive advantage for metastatic cells? *Cancer Biology & Therapy*, 5(7):729–735, Oct. 2014.

[213] H. C. Reinhardt, A. S. Aslanian, J. A. Lees, and M. B. Yaffe. p53-Deficient Cells Rely on ATM- and ATR-Mediated Checkpoint Signaling through the p38MAPK/MK2 Pathway for Survival after DNA Damage. *Cancer Cell*, 11(2):175–189, Feb. 2007.

[214] H. C. Reinhardt, P. Hasskamp, I. Schmedding, S. Morandell, M. A. T. M. van Vugt, X. Wang, R. Linding, S.-E. Ong, D. Weaver, S. A. Carr, and M. B. Yaffe. DNA Damage Activates a Spatially Distinct Late Cytoplasmic Cell-Cycle Checkpoint Network

Controlled by MK2-Mediated RNA Stabilization. *Molecular Cell*, 40(1):34–49, Oct. 2010.

[215] H. C. Reinhardt and M. B. Yaffe. Kinases that control the cell cycle in response to DNA damage: Chk1, Chk2, and MK2. *Current Opinion in Cell Biology*, 21(2):245–255, Apr. 2009.

[216] H. C. Reinhardt and M. B. Yaffe. Phospho-Ser/Thr-binding domains: navigating the cell cycle and DNA damage response. *Nature Reviews Molecular Cell Biology*, 14(9):563–580, Sept. 2013.

[217] A. J. Ridley. Life at the leading edge. *Cell*, 145(7):1012–22, June 2011.

[218] G. Rijal and W. Li. 3d scaffolds in breast cancer research. *Biomaterials*, 81:135–156, 2016.

[219] S. Ripke, C. O'Dushlaine, K. Chambert, J. L. Moran, A. K. Kähler, S. Akterin, S. E. Bergen, A. L. Collins, J. J. Crowley, M. Fromer, Y. Kim, S. H. Lee, P. K. E. Magnusson, N. Sanchez, E. A. Stahl, S. Williams, N. R. Wray, K. Xia, F. Bettella, A. D. Borglum, B. K. Bulik-Sullivan, P. Cormican, N. Craddock, C. de Leeuw, N. Durmishi, M. Gill, V. Golimbet, M. L. Hamshere, P. Holmans, D. M. Hougaard, K. S. Kendler, K. Lin, D. W. Morris, O. Mors, P. B. Mortensen, B. M. Neale, F. A. O'Neill, M. J. Owen, M. P. Milovancevic, D. Posthuma, J. Powell, A. L. Richards, B. P. Riley, D. Ruderfer, D. Rujescu, E. Sigurdsson, T. Silagadze, A. B. Smit, H. Stefansson, S. Steinberg, J. Suvisaari, S. Tosato, M. Verhage, J. T. Walters, D. F. Levinson, P. V. Gejman, C. Laurent, B. J. Mowry, M. C. O'Donovan, A. E. Pulver, S. G. Schwab, D. B. Wildenauer, F. Dudbridge, J. Shi, M. Albus, M. Alexander, D. Campion, D. Cohen, D. Dikeos, J. Duan, P. Eichhammer, S. Godard, M. Hansen, F. B. Lerer, K.-Y. Liang, W. Maier, J. Mallet, D. A. Nertney, G. Nestadt, N. Norton, G. N. Papadimitriou, R. Ribble, A. R. Sanders, J. M. Silverman, D. Walsh, N. M. Williams, B. Wormley, M. J. Arranz, S. Bakker, S. Bender, E. Bramon, D. Collier, B. Crespo-Facorro, J. Hall, C. Iyegbe, A. Jablensky, R. S. Kahn, L. Kalaydjieva, S. Lawrie, C. M. Lewis, D. H. Linszen, I. Mata, A. McIntosh, R. M. Murray, R. A. Ophoff, J. Van Os, M. Walshe, M. Weisbrod, D. Wiersma, P. Donnelly, I. Barroso, J. M. Blackwell, M. A. Brown, J. P. Casas, A. P. Corvin, P. Deloukas, A. Duncanson, J. Jankowski, H. S. Markus, C. G. Mathew, C. N. A. Palmer, R. Plomin, A. Rautanen, S. J. Sawcer, R. C. Trembath, A. C. Viswanathan, N. W. Wood, C. C. A. Spencer, G. Band, C. Bellenguez, C. Freeman, G. Hellenthal, E. Giannoulatou, M. Pirinen, R. D. Pearson, A. Strange, Z. Su, D. Vukcevic, C. Langford, S. E. Hunt, S. Edkins, R. Gwilliam, H. Blackburn, S. J. Bumpstead, S. Dronov, M. Gillman, E. Gray, N. Hammond, A. Jayakumar, O. T. McCann, J. Liddle, S. C. Potter, R. Ravindrarajah, M. Ricketts, A. Tashakkori-Ghanbaria, M. J. Waller, P. Weston, S. Widaa, P. Whittaker, M. I. McCarthy, K. Stefansson, E. Scolnick, S. Purcell, S. A. McCarroll, P. Sklar, C. M. Hultman, and P. F. Sullivan. Genome-wide association analysis identifies 13 new risk loci for schizophrenia. *Nature Genetics*, 45(10):1150–9, Oct 2013.

[220] J. Robertson, G. Jacquemet, A. Byron, M. C. Jones, S. Warwood, J. N. Selley, D. Knight, J. D. Humphries, and M. J. Humphries. Defining the phospho-adhesome through the phosphoproteomic analysis of integrin signalling. *Nature Communications*, 6:6265, 2015.

[221] N. Ronkina, J. Lafera, A. Kotlyarov, and M. Gaestel. Stress-dependent phosphorylation of myocardin-related transcription factor A (MRTF-A) by the p38MAPK/MK2 axis. *Nature*, 6(1):1301, Aug. 2016.

[222] M. J. Rust, M. Bates, and X. Zhuang. Sub-diffraction-limit imaging by stochastic optical reconstruction microscopy (STORM). *Nature Methods*, 3(10):793–796, 2006.

[223] B. Sahu, I. Sacui, S. Rapireddy, K. J. Zanotti, R. Bahal, B. A. Armitage, and D. H. Ly. Synthesis and characterization of conformationally-preorganized, miniPEG-containing γPNAs with superior hybridization properties and water solubility. *The Journal of Organic Chemistry*, 76(14):5614–5627, Jul 2011.

[224] H. Sailem, V. Bousgouni, S. Cooper, and C. Bakal. Cross-talk between Rho and Rac GTPases drives deterministic exploration of cellular shape space and morphological heterogeneity. *Open Biology*, 4(1), Jan 2014.

[225] H. Z. Sailem, S. Cooper, and C. Bakal. Visualizing quantitative microscopy data: History and challenges. *Critical Reviews in Biochemistry and Molecular Biology*, 51(2):96–101, 2016.

[226] V. A. Sardão, P. J. Oliveira, J. Holy, C. R. Oliveira, and K. B. Wallace. Morphological alterations induced by doxorubicin on H9c2 myoblasts: nuclear, mitochondrial, and cytoskeletal targets. *Cell Biology and Toxicology*, 25(3):227–243, June 2009.

[227] S. K. Sastry and K. Burridge. Focal Adhesions: A Nexus for Intracellular Signaling and Cytoskeletal Dynamics. *Experimental Cell Research*, 261(1):25–36, Nov. 2000.

[228] U. Schnell, F. Dijk, K. A. Sjollema, and B. N. G. Giepmans. Immunolabeling artifacts and the need for live-cell imaging. *Nature Methods*, 9(2):152–158, Feb 2012.

[229] W. Schubert, B. Bonnekoh, A. J. Pommer, L. Philipsen, R. Bockelmann, Y. Malykh, H. Gollnick, M. Friedenberger, M. Bode, and A. W. M. Dress. Analyzing proteome topology and function by automated multidimensional fluorescence microscopy. *Nature Biotechnology*, 24(10):1270–1278, Oct 2006.

[230] J. Schwermann, C. Rathinam, M. Schubert, S. Schumacher, F. Noyan, H. Koseki, A. Kotlyarov, C. Klein, and M. Gaestel. MAPKAP kinase MK2 maintains self-renewal capacity of haematopoietic stem cells. *The EMBO Journal*, 28(10):1392–1406, Apr. 2009.

[231] A. S. Sebag, S. Plancade, C. Raulet-Tomkiewicz, R. Barouki, J.-P. Vert, and T. Walter. A generic methodological framework for studying single cell motility in high-throughput time-lapse data. *Bioinformatics*, 31(12):320–328, Jun 15 2015.

[232] J. E. Sero, H. Z. Sailem, R. C. Ardy, H. Almuttaqi, T. Zhang, and C. Bakal. Cell shape and the microenvironment regulate nuclear translocation of NF-kappa B in breast epithelial and tumor cells. *Molecular Systems Biology*, 11(3), Mar 2015.

[233] A. Sharonov and R. M. Hochstrasser. Wide-field subdiffraction imaging by accumulated binding of diffusing probes. *Proceedings of the National Academy of Sciences*, 103(50):18911–18916, 2006.

[234] J. Shi, M. Surma, L. Zhang, and L. Wei. Dissecting the roles of ROCK isoforms in stress-induced cell detachment. *Cell Cycle*, 12(10):1492–1500, May 2013.

[235] Y. Shi, L. Du, L. Lin, and Y. Wang. Tumour-associated mesenchymal stem/stromal cells: emerging therapeutic targets. *Nature Reviews Drug Discovery*, 16(1):35–52, 2017.

[236] K. Shibata, H. Sakai, Q. Huang, H. Kamata, Y. Chiba, M. Misawa, R. Ikebe, and M. Ikebe. Rac1 regulates myosin II phosphorylation through regulation of myosin light chain phosphatase. *Journal of Cellular Physiology*, 2014.

[237] K.-J. Shin, E. A. Wall, J. R. Zavzavadjian, L. A. Santat, J. Liu, J.-I. Hwang, R. Rebres, T. Roach, W. Seaman, M. I. Simon, and I. D. C. Fraser. A single lentiviral vector platform for microRNA-based conditional RNA interference and coordinated transgene expression. *Proceedings of the National Academy of Sciences*, 103(37):13759–13764, Sept. 2006.

[238] M. D. Slacka, E. D. Martineza, L. F. Wu, and S. J. Altschuler. Characterizing heterogeneous cellular responses to perturbations. *Proceedings of the National Academy of Sciences*, 105(49):19306–19311, Dec 9 2008.

[239] D. J. Slamon. Studies of the HER-2/neu Proto-oncogene in Human Breast Cancer. *Cancer Investigation*, 8(2):253–254, May 1990.

[240] D. J. Slamon, G. M. Clark, S. G. Wong, W. J. Levin, A. Ullrich, and W. L. McGuire. Nucleic Acids Research. *Science (New York, N.Y.)*, 235(4785):177–82, Jan 1987.

[241] G. W. Sledge, E. P. Mamounas, F. Health, G. N. Hortobagyi, and H. J. Burstein. Past, Present, and Future Challenges in Breast Cancer Treatment. *Journal of Clinical Oncology*, 32(19):15–19, 2017.

[242] G. W. Sledge, D. Neuberg, P. Bernardo, J. N. Ingle, S. Martino, E. K. Rowinsky, and W. C. Wood. Phase III trial of doxorubicin, paclitaxel, and the combination of doxorubicin and paclitaxel as front-line chemotherapy for metastatic breast cancer: An Intergroup trial (E1193). *Journal of Clinical Oncology*, 21(4):588–592, Feb 2003.

[243] R. V. Smalley, J. Lefante, A. Bartolucci, J. Carpenter, C. Vogel, and S. Krauss. A comparison of cyclophosphamide, adriamycin, and 5-fluorouracil (CAF) and cyclophosphamide, methotrexate, 5-fluorouracil, vincristine, and prednisone (CMFVP) in patients with advanced breast cancer - A Southeastern Cancer Study Group Project. *Breast Cancer Research and Treatment*, 3(2):209–220, Aug 1983.

[244] J. A. Sparano. Doxorubicin/taxane combinations: cardiac toxicity and pharmacokinetics. *Seminars in Oncology*, 26(3 Suppl 9):14–9, Jun 1999.

[245] A. Subramanian, P. Tamayo, V. K. Mootha, S. Mukherjee, B. L. Ebert, M. A. Gillette, A. Paulovich, S. L. Pomeroy, T. R. Golub, and E. S. Lander. Gene set enrichment analysis: a knowledge-based approach for interpreting genome-wide expression profiles. *Proceedings of the National Academy of Sciences*, 102(43):15545–15550, 2005.

[246] M. Surma, C. Handy, J. Chang, R. Kapur, L. Wei, and J. Shi. ROCK1 deficiency enhances protective effects of antioxidants against apoptosis and cell detachment. *PLoS One*, 9(3):e90758, 2014.

[247] M. A. Sussman, S. F. Hamm-Alvarez, P. M. Vilalta, S. Welch, and L. Kedes. Involvement of phosphorylation in doxorubicin-mediated myofibril degeneration. An immunofluorescence microscopy analysis. *Circulation Research*, 80(1):52–61, Jan. 1997.

[248] Z. Symon, A. Peyser, D. Tzemach, O. Lyass, E. Sucher, E. Shezen, and A. Gabizon. Selective delivery of doxorubicin to patients with breast carcinoma metastases by stealth liposomes. *Cancer*, 86(1):72–78, Jul 1999.

[249] M. Tanaka, R. Bateman, D. Rauh, E. Vaisberg, S. Ramachandani, C. Zhang, K. Hansen, A. Burlingame, J. Trautman, K. Shokat, and C. Adams. An unbiased cell morphology-based screen for new, biologically active small molecules. *PLoS Biology*, 3(5):764–776, May 2005.

[250] J. H. Taube, J. I. Herschkowitz, K. Komurov, A. Y. Zhou, S. Gupta, J. Yang, K. Hartwell, T. T. Onder, P. B. Gupta, K. W. Evans, B. G. Hollier, P. T. Ram, E. S. Lander, J. M. Rosen, R. A. Weinberg, and S. A. Mani. Core epithelial-to-mesenchymal transition interactome gene-expression signature is associated with claudin-low and metaplastic breast cancer subtypes. *Proceedings of the National Academy of Sciences*, 107(35):15449–15454, Aug. 2010.

[251] T. Taus, T. Köcher, P. Pichler, C. Paschke, A. Schmidt, C. Henrich, and K. Mechtler. Universal and confident phosphorylation site localization using phosphoRS. *Journal of Proteome Research*, 10(12):5354–5362, Dec. 2011.

[252] B. Tavora, L. E. Reynolds, S. Batista, F. Demircioglu, I. Fernandez, T. Lechertier, D. M. Lees, P.-P. Wong, A. Alexopoulou, G. Elia, A. Clear, A. Ledoux, J. Hunter, N. Perkins, J. G. Gribben, and K. M. Hodivala-Dilke. Endothelial-cell FAK targeting sensitizes tumours to DNA-damaging therapy. *Nature*, 514(7520):112–116, Oct. 2014.

[253] B. A. Teicher. *Cancer Drug Resistance*. Springer Science & Business Media, 2007.

[254] M. A. X. Tollenaere, B. H. Villumsen, M. Blasius, J. C. Nielsen, S. A. Wagner, J. Bartek, P. Beli, N. Mailand, and S. Bekker-Jensen. p38- and MK2-dependent signalling promotes stress-induced centriolar satellite remodelling via 14-3-3-dependent sequestration of CEP131/AZI1. *Nature Communications*, 6:10075, Nov. 2015.

[255] F. M. Torti, M. R. Bristow, A. E. Howes, D. Aston, F. E. Stockdale, S. K. Carter, M. Kohler, B. W. Brown, and M. E. Billingham. Reduced cardiotoxicity of doxorubicin delivered on a weekly schedule. Assessment by endomyocardial biopsy. *Annals of Internal Medicine*, 99(6):745–749, Dec 1983.

[256] P. A. Toste, A. H. Nguyen, B. E. Kadera, M. Duong, N. Wu, I. Gawlas, L. M. Tran, M. Bikhchandani, L. Li, S. G. Patel, D. W. Dawson, and T. R. Donahue. Chemotherapy-Induced Inflammatory Gene Signature and Protumorigenic Phenotype in Pancreatic CAFs via Stress-Associated MAPK. *Molecular Cancer Research*, 14(5):437–447, Mar. 2016.

[257] G. Totsukawa, Y. Wu, Y. Sasaki, D. Hartshorne, Y. Yamakita, S. Yamashiro, and F. Matsumura. Distinct roles of MLCK and ROCK in the regulation of membrane protrusions and focal adhesion dynamics during cell migration of fibroblasts. *Journal of Cell Biology*, 164(3):427–439, Feb 2 2004.

[258] M. D. Treiser, E. H. Yang, S. Gordonov, D. M. Cohen, I. P. Androulakis, J. Kohn, C. S. Chen, and P. V. Moghe. Cytoskeleton-based forecasting of stem cell lineage fates. *Proceedings of the National Academy of Sciences*, 107(2):610–615, Jan 12 2010.

[259] S.-H. Tsou, T.-M. Chen, H.-T. Hsiao, and Y.-H. Chen. A critical dose of doxorubicin

is required to alter the gene expression profiles in MCF-7 cells acquiring multidrug resistance. *PLoS One*, 10(1):e0116747, 2015.

[260] Y. Tsukada, K. Aoki, T. Nakamura, Y. Sakumura, M. Matsuda, and S. Ishii. Quantification of Local Morphodynamics and Local GTPase Activity by Edge Evolution Tracking. *PLoS Computational Biology*, 4(11), Nov 2008.

[261] D. Tsygankov, C. G. Bilancia, E. A. Vitriol, K. M. Hahn, M. Peifer, and T. C. Elston. CellGeo: A computational platform for the analysis of shape changes in cells with complex geometries. *Journal of Cell Biology*, 204(3):443–460, Feb 3 2014.

[262] D. Tsygankov, P.-H. Chu, H. Chen, T. C. Elston, and K. Hahn. User-friendly tools for quantifying the dynamics of cellular morphology and intracellular protein clusters. *Methods in Cell Biology*, 123:409, 2014.

[263] J. C. Tu, B. Xiao, S. Naisbitt, J. P. Yuan, R. S. Petralia, P. Brakeman, A. Doan, V. K. Aakalu, A. A. Lanahan, M. Sheng, and P. F. Worley. Coupling of mGluR/Homer and PSD-95 complexes by the Shank family of postsynaptic density proteins. *Neuron*, 23(3):583–592, Jul 1999.

[264] N. J. Turton, D. J. Judah, J. Riley, R. Davies, D. Lipson, J. A. Styles, A. G. Smith, and T. W. Gant. Gene expression and amplification in breast carcinoma cells with intrinsic and acquired doxorubicin resistance. *Oncogene*, 20(11):1300–1306, Mar. 2001.

[265] R. Tyson, D. Epstein, K. Anderson, and T. Bretschneider. High resolution tracking of cell membrane dynamics in moving cells: an electrifying approach. *Mathematical Modelling of Natural Phenomena*, 5:34–55, 1 2010.

[266] M. Valcovici, F. Andrica, C. Serban, and S. Dragan. Cardiotoxicity of anthracycline therapy: Current perspectives. *Archives of Medical Science*, 12(2):428–435, Apr 2016.

[267] V. Valero, A. U. Buzdar, R. L. Theriault, N. Azarnia, G. A. Fonseca, J. Willey, M. Ewer, R. S. Walters, B. Mackay, D. Podoloff, D. Booser, L. W. Lee, and G. N. Hortobagyi. Phase II trial of liposome-encapsulated doxorubicin, cyclophosphamide, and fluorouracil as first-line therapy in patients with metastatic breast cancer. *Journal of Clinical Oncology*, 17(5):1425–1434, May 1999.

[268] T. Vallenius. Actin stress fibre subtypes in mesenchymal-migrating cells. *Open Biology*, 3(6):130001, 2013.

[269] J. G. Valtschanoff and R. J. Weinberg. Laminar organization of the NMDA receptor complex within the postsynaptic density. *Journal of Neuroscience*, 21(4):1211–1217, 2001.

[270] J. van Rheenen, X. Song, W. van Roosmalen, M. Cammer, X. Chen, V. Desmarais, S.-C. Yip, J. M. Backer, R. J. Eddy, and J. S. Condeelis. EGF-induced PIP2 hydrolysis releases and activates cofilin locally in carcinoma cells. *Journal of Cell Biology*, 179(6):1247–59, Dec. 2007.

[271] S. L. Vega, A. Dhaliwal, V. Arvind, P. J. Patel, N. R. M. Beijer, J. de Boer, N. S. Murthy, J. Kohn, and P. V. Moghe. Organizational metrics of interchromatin speckle factor domains: integrative classifier for stem cell adhesion & lineage signaling. *Integrative Biology*, 7(4):435–446, Apr 2015.

[272] M. Veronika, R. Welsch, A. Ng, P. Matsudaira, and J. C. Rajapakse. Correlation of cell membrane dynamics and cell motility. *BMC Bioinformatics*, 12(13), Nov 30 2011.

[273] M. Vicente-Manzanares, M. A. Koach, L. Whitmore, M. L. Lamers, and A. F. Horwitz. Segregation and activation of myosin IIB creates a rear in migrating cells. *Journal of Cell Biology*, 183(3):543–554, Nov 3 2008.

[274] M. Vicente-Manzanares, J. Zareno, L. Whitmore, C. K. Choi, and A. F. Horwitz. Regulation of protrusion, adhesion dynamics, and polarity by myosins IIA and IIB in migrating cells. *Journal of Cell Biology*, 176(5):573–580, Feb 2007.

[275] V. E. Vinzi, L. Trinchera, and S. Amato. Pls path modeling: from foundations to recent developments and open issues for model assessment and improvement. *Handbook of Partial Least Squares*, pages 47–82, 2010.

[276] L. Volk-Draper, K. Hall, C. Griggs, S. Rajput, P. Kohio, D. DeNardo, and S. Ran. Paclitaxel Therapy Promotes Breast Cancer Metastasis in a TLR4-Dependent Manner. *Cancer Research*, 74(19):5421–5434, Oct. 2014.

[277] A. V. Vorotnikov. Chemotaxis: movement, direction, control. *Biochemistry*, 76(13):1528–55, Dec. 2011.

[278] C. Wählby, F. Erlandsson, E. Bengtsson, and A. Zetterberg. Sequential immunofluorescence staining and image analysis for detection of large numbers of antigens in individual cell nuclei. *Cytometry*, 47(1):32–41, Jan 2002.

[279] A. Walker, H. Su, M. A. Conti, N. Harb, R. S. Adelstein, and N. Sato. Non-muscle myosin II regulates survival threshold of pluripotent stem cells. *Nature Communications*, 1(6):71, 2010.

[280] M. J. Wawer, K. Li, S. M. Gustafsdottir, V. Ljosa, N. E. Bodycombe, M. A. Marton, K. L. Sokolnicki, M.-A. Bray, M. M. Kemp, E. Winchester, B. Taylor, G. B. Grant, C. S.-Y. Hon, J. R. Duvall, J. A. Wilson, J. A. Bittker, V. Dancik, R. Narayan, A. Subramanian, W. Winckler, T. R. Golub, A. E. Carpenter, A. F. Shamji, S. L. Schreiber, and P. A. Clemons. Toward performance-diverse small-molecule libraries for cell-based phenotypic screening using multiplexed high-dimensional profiling. *Proceedings of the National Academy of Sciences*, 111(30):10911–10916, Jul 29 2014.

[281] M. C. Weiger, S. Ahmed, E. S. Welf, and J. M. Haugh. Directional Persistence of Cell Migration Coincides with Stability of Asymmetric Intracellular Signaling. *Biophysical Journal*, 98(1):67–75, Jan 6 2010.

[282] M. C. Weiger, C.-C. Wang, M. Krajcovic, A. T. Melvin, J. J. Rhoden, and J. M. Haugh. Spontaneous phosphoinositide 3-kinase signaling dynamics drive spreading and random migration of fibroblasts. *Journal of Cell Science*, 122(3):313–323, Feb 1 2009.

[283] C. M. Welch, H. Elliott, G. Danuser, and K. M. Hahn. Imaging the coordination of multiple signalling activities in living cells. *Nature Reviews Molecular Cell Biology*, 12(11):749–756, Nov 2011.

[284] A. Wells. *Cell Motility in Cancer Invasion and Metastasis*, volume 8. Springer, 2006.

[285] T. R. Wilson, J. Fridlyand, Y. Yan, E. Penuel, L. Burton, E. Chan, J. Peng, E. Lin, Y. Wang, J. Sosman, A. Ribas, J. Li, J. Moffat, D. P. Sutherlin, H. Koeppen, M. Merchant, R. Neve, and J. Settleman. Widespread potential for growth-factor-driven resistance to anticancer kinase inhibitors. *Nature*, 487(7408):505–509, Jul 2012.

[286] H. Wolfenson, A. Bershadsky, Y. I. Henis, and B. Geiger. Actomyosin-generated tension controls the molecular kinetics of focal adhesions. *Journal of Cell Science*, 124(9), 2011.

[287] M. A. Wozniak, K. Modzelewska, L. Kwong, and P. J. Keely. Focal adhesion regulation of cell behavior. *Biochimica et Biophysica Acta*, 1692(2-3):103–119, July 2004.

[288] C. Wu, S. B. Asokan, M. E. Berginski, E. M. Haynes, N. E. Sharpless, J. D. Griffith, S. M. Gomez, and J. E. Bear. Arp2/3 is critical for lamellipodia and response to extracellular matrix cues but is dispensable for chemotaxis. *Cell*, 148(5):973–87, Mar. 2012.

[289] S. Wu, A. Wells, L. G. Griffith, and D. A. Lauffenburger. Controlling multipotent stromal cell migration by integrating "course-graining" materials and "fine-tuning" small molecules via decision tree signal-response modeling. *Biomaterials*, 32(30):7524–31, Oct. 2011.

[290] Q. Xu, M. R. Schlabach, G. J. Hannon, and S. J. Elledge. Design of 240,000 orthogonal 25mer DNA barcode probes. *Proceedings of the National Academy of Sciences*, 106(7):2289–2294, Feb 2009.

[291] K. M. Yamada and E. Cukierman. Modeling tissue morphogenesis and cancer in 3d. *Cell*, 130(4):601–610, 2007.

[292] J. Yang, S. A. Mani, J. L. Donaher, S. Ramaswamy, R. A. Itzykson, C. Come, P. Savagner, I. Gitelman, A. Richardson, and R. A. Weinberg. Twist, a master regulator of morphogenesis, plays an essential role in tumor metastasis. *Cell*, 117(7):927–939, June 2004.

[293] J. Yang and R. A. Weinberg. Epithelial-mesenchymal transition: at the crossroads of development and tumor metastasis. *Developmental Cell*, 14(6):818–829, June 2008.

[294] Z. Yin, A. Sadok, H. Sailem, A. McCarthy, X. Xia, F. Li, M. A. Garcia, L. Evans, A. R. Barr, N. Perrimon, C. J. Marshall, S. T. C. Wong, and C. Bakal. A screen for morphological complexity identifies regulators of switch-like transitions between discrete cell shapes. *Nature Cell Biology*, 15(7):860–871, Jun 2013.

[295] Z. Yin, H. Sailem, J. Sero, R. Ardy, S. T. C. Wong, and C. Bakal. How cells explore shape space: A quantitative statistical perspective of cellular morphogenesis. *Bioessays*, 36(12):1195–1203, Dec 2014.

[296] D. W. Young, A. Bender, J. Hoyt, E. McWhinnie, G.-W. Chirn, C. Y. Tao, J. A. Tallarico, M. Labow, J. L. Jenkins, T. J. Mitchison, and Y. Feng. Integrating high-content screening and ligand-target prediction to identify mechanism of action. *Nature Chemical Biology*, 4(1):59–68, Jan 2008.

[297] B. Zhao, J. C. Sedlak, R. Srinivas, P. Creixell, J. R. Pritchard, B. Tidor, D. A. Lauffenburger, and M. T. Hemann. Exploiting Temporal Collateral Sensitivity in Tumor Clonal Evolution. *Cell*, 165(1):234–246, Mar 2016.

[298] Q. Zhong, A. G. Busetto, J. P. Fededa, J. M. Buhmann, and D. W. Gerlich. Unsupervised modeling of cell morphology dynamics for time-lapse microscopy. *Nature Methods*, 9(7):711–U267, Jul 2012.

[299] C. Zhou, A. E. H. Elia, M. L. Naylor, N. Dephoure, B. A. Ballif, G. Goel, Q. Xu, A. Ng, D. M. Chou, R. J. Xavier, S. P. Gygi, and S. J. Elledge. Profiling DNA damage-induced phosphorylation in budding yeast reveals diverse signaling networks. *Proceedings of the National Academy of Sciences*, 113(26):E3667–E3675, June 2016.